SOFiSTiK

DIRECT. ALIGNED. TO THE POINT.
2024

VERiFiCATiON

Mechanical Benchmarks

SOFiSTiK | 2024

VERiFiCATiON

VERiFiCATiON Manual, Service Pack 2024-3 Build 7

Copyright © 2024 by SOFiSTiK AG, Nuremberg, Germany.

SOFiSTiK AG

HQ Nuremberg
Flataustraße 14
90411 Nürnberg
Germany

T +49 (0)911 39901-0
F +49(0)911 397904

Office Garching
Parkring 2
85748 Garching bei München
Germany

T +49 (0)89 315878-0
F +49 (0)89 315878-23

info@sofistik.com
www.sofistik.com

This manual is protected by copyright laws. No part of it may be translated, copied or reproduced, in any form or by any means, without written permission from SOFiSTiK AG. SOFiSTiK reserves the right to modify or to release new editions of this manual.

The manual and the program have been thoroughly checked for errors. However, SOFiSTiK does not claim that either one is completely error free. Errors and omissions are corrected as soon as they are detected.

The user of the program is solely responsible for the applications. We strongly encourage the user to test the correctness of all calculations at least by random sampling.

Front Cover

6th Street Viaduct, Los Angeles Photo: Tobias Petschke

Contents

Introduction 3

1 About this Manual 3
1.1 Layout and Organization of a Benchmark 3
1.2 Finding the Benchmark of interest 3
1.3 Symbols 5

2 Index by Categories 7
2.1 Mechanical Benchmarks 7

I SOFiSTiK Software Quality Assurance (*SQA*) 9

3 SOFiSTiK SQA Policy 11
3.1 Objectives 11
3.1.1 About SOFiSTiK 11
3.1.2 Innovation and Reliability 11
3.2 Organisation 11
3.2.1 Software Release Schedule 11
3.2.2 SQA Modules - Classification 12
3.2.3 Responsibilities 12
3.2.4 Software Release Procedure 13
3.3 Instruments 14
3.3.1 CRM System 14
3.3.2 Tracking System (internal) 14
3.3.3 Continuous Integration – Continuous Testing 14
3.4 Additional Provisions 15
3.4.1 Training 15
3.4.2 Academia Network 15
3.5 Disclaimer 16

II Mechanical Benchmarks 17

4 BE1: Joint Deflection of Plane Truss 19
4.1 Problem Description 19
4.2 Reference Solution 19
4.3 Model and Results 19
4.4 Conclusion 20
4.5 Literature 20

5 BE2: Kinematic Coupling Conditions 23
5.1 Problem Description 23
5.2 Reference Solution 23
5.3 Model and Results 24
5.4 Conclusion 27

5.5 Literature 27

6 **BE3: Beam Stresses and Deflections** **29**
6.1 Problem Description 29
6.2 Reference Solution 29
6.3 Model and Results 30
6.4 Conclusion 31
6.5 Literature 31

7 **BE4: Tie Rod with Lateral Loading** **33**
7.1 Problem Description 33
7.2 Reference Solution 33
7.3 Model and Results 34
7.4 Conclusion 35
7.5 Literature 35

8 **BE5: Bending of a T-beam** **37**
8.1 Problem Description 37
8.2 Reference Solution 37
8.3 Model and Results 37
8.4 Conclusion 38
8.5 Literature 38

9 **BE6: Warping Torsion Bar** **39**
9.1 Problem Description 39
9.2 Reference Solution 39
9.3 Model and Results 41
9.4 Conclusion 42
9.5 Literature 42

10 **BE7: Large Deflection of Cantilever Beams I** **43**
10.1 Problem Description 43
10.2 Reference Solution 43
10.3 Model and Results 44
10.4 Conclusion 46
10.5 Literature 46

11 **BE8: Large Deflection of Cantilever Beams II** **47**
11.1 Problem Description 47
11.2 Reference Solution 47
11.3 Model and Results 47
11.4 Conclusion 49
11.5 Literature 49

12 **BE9: Verification of Beam and Section Types I** **51**
12.1 Problem Description 51
12.2 Reference Solution 52
12.3 Model and Results 53
12.3.1 Comparison of numerical approaches for thick walled cross sections 55
12.3.2 Convergence of the thick walled sections (FEM-BEM) in regard to the thin-walled theory 56
12.4 Conclusion 58
12.5 Literature 58

13 **BE10: Verification of Beam and Section Types II** **61**

13.1 Problem Description . . . 61
13.2 Reference Solution . . . 61
13.3 Model and Results . . . 62
13.4 Conclusion . . . 64
13.5 Literature . . . 64

14 BE11: Plastification of a Rectangular Beam 65
14.1 Problem Description . . . 65
14.2 Reference Solution . . . 65
14.3 Model and Results . . . 66
14.4 Conclusion . . . 67
14.5 Literature . . . 67

15 BE12: Cantilever in Torsion 69
15.1 Problem Description . . . 69
15.2 Reference Solution . . . 69
15.3 Model and Results . . . 70
15.4 Conclusion . . . 71
15.5 Literature . . . 71

16 BE13: Buckling of a Bar with Hinged Ends I 73
16.1 Problem Description . . . 73
16.2 Reference Solution . . . 73
16.3 Model and Results . . . 74
16.4 Conclusion . . . 75
16.5 Literature . . . 75

17 BE14: Buckling of a Bar with Hinged Ends II 77
17.1 Problem Description . . . 77
17.2 Reference Solution . . . 77
17.3 Model and Results . . . 78
17.4 Conclusion . . . 78
17.5 Literature . . . 78

18 BE15: Flexural and Torsional Buckling 79
18.1 Problem Description . . . 79
18.2 Reference Solution . . . 79
18.3 Model and Results . . . 80
18.4 Conclusion . . . 81
18.5 Literature . . . 81

19 BE16: Torsion due to Biaxial Bending 83
19.1 Problem Description . . . 83
19.2 Reference Solution . . . 83
19.3 Model and Results . . . 83
19.4 Conclusion . . . 84
19.5 Literature . . . 84

20 BE17: Lateral Torsional Buckling 85
20.1 Problem Description . . . 85
20.2 Reference Solution . . . 85
20.3 Model and Results . . . 85
20.4 Conclusion . . . 86
20.5 Literature . . . 86

21 BE18: Three-storey Column under Large Compressive Force and Torsional Moment 87
21.1 Problem Description 87
21.2 Reference Solution 87
21.3 Model and Results 88
21.4 Conclusion 89
21.5 Literature 89

22 BE19: Two-span Beam with Warping Torsion and Compressive Force 91
22.1 Problem Description 91
22.2 Reference Solution 91
22.3 Model and Results 92
22.4 Conclusion 94
22.5 Literature 94

23 BE20: Passive Earth Pressure I 95
23.1 Problem Description 95
23.2 Reference Solution 95
23.3 Model and Results 96
23.4 Conclusion 98
23.5 Literature 98

24 BE21: Passive Earth Pressure II 99
24.1 Problem Description 99
24.2 Reference Solution 99
24.3 Model and Results 101
24.4 Conclusion 102
24.5 Literature 103

25 BE22: Tunneling - Ground Reaction Line 105
25.1 Problem Description 105
25.2 Reference Solution 105
25.3 Model and Results 107
25.4 Conclusion 108
25.5 Literature 108

26 BE23: Undamped Free Vibration of a SDOF System 109
26.1 Problem Description 109
26.2 Reference Solution 109
26.3 Model and Results 110
26.4 Conclusion 112
26.5 Literature 112

27 BE24: Free Vibration of a Under-critically Damped SDOF System 113
27.1 Problem Description 113
27.2 Reference Solution 113
27.3 Model and Results 115
27.4 Conclusion 116
27.5 Literature 116

28 BE25: Eigenvalue Analysis of a Beam Under Various End Constraints 117
28.1 Problem Description 117
28.2 Reference Solution 117
28.3 Model and Results 118
28.4 Conclusion 118

28.5 Literature 118

29 BE26: Response of a SDOF System to Harmonic Excitation 119
29.1 Problem Description 119
29.2 Reference Solution 119
29.3 Model and Results 121
29.4 Conclusion 122
29.5 Literature 122

30 BE27: Response of a SDOF System to Impulsive Loading 123
30.1 Problem Description 123
30.2 Reference Solution 123
30.3 Model and Results 125
30.4 Conclusion 126
30.5 Literature 126

31 BE28: Cylindrical Hole in an Infinite Elastic Medium 127
31.1 Problem Description 127
31.2 Reference Solution 127
31.3 Model and Results 128
31.4 Conclusion 130
31.5 Literature 130

32 BE29: Cylindrical Hole in an Infinite Mohr-Coulomb Medium 131
32.1 Problem Description 131
32.2 Reference Solution 131
32.3 Model and Results 132
32.4 Conclusion 134
32.5 Literature 134

33 BE30: Strip Loading on an Elastic Semi-Infinite Mass 135
33.1 Problem Description 135
33.2 Reference Solution 135
33.3 Model and Results 136
33.4 Conclusion 138
33.5 Literature 138

34 BE31: Snap-Through Behaviour of a Truss 139
34.1 Problem Description 139
34.2 Reference Solution 139
34.3 Model and Results 140
34.4 Conclusion 141
34.5 Literature 141

35 BE32: Thermal Extension of Structural Steel in case of Fire 143
35.1 Problem Description 143
35.2 Reference Solution 143
35.3 Model and Results 143
35.4 Conclusion 145
35.5 Literature 145

36 BE33: Work Laws in case of Fire for Concrete and Structural Steel 147
36.1 Problem Description 147
36.2 Reference Solution 147
36.3 Model and Results 147

36.4 Conclusion 151
36.5 Literature 151

37 BE34: Ultimate Bearing Capacity of Concrete and Steel under Fire 153
37.1 Problem Description 153
37.2 Reference Solution 153
37.3 Model and Results 153
37.4 Conclusion 155
37.5 Literature 155

38 BE35: Calculation of Restraining Forces in Steel Members in case of Fire 157
38.1 Problem Description 157
38.2 Reference Solution 157
38.3 Model and Results 157
38.4 Conclusion 159
38.5 Literature 159

39 BE36: Pushover Analysis: Performance Point Calculation by ATC-40 Procedure 161
39.1 Problem Description 161
39.2 Reference Solution 161
39.3 Model and Results 162
39.4 Conclusion 164
39.5 Literature 164

40 BE37: Beam Calculation of Varying Cross-Section according to Second Order Theory 165
40.1 Problem Description 165
40.2 Reference Solution 165
40.3 Model and Results 166
40.4 Conclusion 167
40.5 Literature 168

41 BE38: Calculation of Slope Stability by Phi-C Reduction 169
41.1 Problem Description 169
41.2 Reference Solution 169
41.3 Model and Results 170
41.4 Conclusion 172
41.5 Literature 172

42 BE39: Natural Frequencies of a Rectangular Plate 173
42.1 Problem Description 173
42.2 Reference Solution 173
42.3 Model and Results 174
42.4 Conclusion 175
42.5 Literature 175

43 BE40: Portal Frame 177
43.1 Problem Description 177
43.2 Reference Solution 177
43.3 Model and Results 178
43.4 Conclusion 179
43.5 Literature 179

44 BE41: Linear Pinched Cylinder 181
44.1 Problem Description 181

44.2 Reference Solution 181
44.3 Model and Results 181
44.4 Conclusion 183
44.5 Literature 184

45 BE42: Thick Circular Plate 185
45.1 Problem Description 185
45.2 Reference Solution 185
45.3 Model and Results 186
45.4 Conclusion 187
45.5 Literature 187

46 BE43: Panel with Circular Hole 189
46.1 Problem Description 189
46.2 Reference Solution 189
46.3 Model and Results 190
46.4 Conclusion 192
46.5 Literature 192

47 BE44: Undrained Elastic Soil Layer Subjected to Strip Loading 193
47.1 Problem Description 193
47.2 Reference Solution 193
47.3 Model and Results 193
47.4 Conclusion 195
47.5 Literature 195

48 BE45: One-Dimensional Soil Consolidation 197
48.1 Problem Description 197
48.2 Reference Solution 197
48.3 Model and Results 198
48.4 Conclusion 199
48.5 Literature 200

49 BE46: Material Nonlinear Analysis of Reinforced Concrete Beam 201
49.1 Problem Description 201
49.2 Reference Solution 201
49.3 Model and Results 201
49.4 Conclusion 204
49.5 Literature 204

50 BE47: Pushover Analysis: SAC LA9 Building 205
50.1 Problem Description 205
50.2 Reference Solution 205
50.3 Model and Results 205
50.4 Conclusion 209
50.5 Literature 209

51 BE48: Triaxial Consolidated Undrained (CU) Test 211
51.1 Problem Description 211
51.2 Reference Solution 211
51.3 Model and Results 213
  51.3.1 Hostun-RF Sand, $\sigma_c = 200\ kN/m^2$ 215
  51.3.2 Hostun-RF Sand, $\sigma_c = 300\ kN/m^2$ 216
51.4 Conclusion 218
51.5 Literature 218

52 BE49: Triaxial Drained Test 219
52.1 Problem Description 219
52.2 Reference Solution 219
52.3 Model and Results 219
52.3.1 Hostun-RF Sand, $\sigma_c = 100\ kN/m^2$ 221
52.3.2 Hostun-RF Sand, $\sigma_c = 300\ kN/m^2$ 222
52.4 Conclusion 224
52.5 Literature 224

53 BE50: A Circular Cavity Embedded in a Full-Plane Under Impulse Pressure 225
53.1 Problem Description 225
53.2 Reference Solution 225
53.3 Model and Results 226
53.4 Conclusion 227
53.5 Literature 228

54 BE51: Pushover Analysis: Performance Point Calculation by EC8 Procedure 229
54.1 Problem Description 229
54.2 Reference Solution 229
54.3 Model and Results 231
54.4 Conclusion 234
54.5 Literature 234

55 BE52: Verification of Wave Kinematics 235
55.1 Problem Description 235
55.2 Reference Solution 235
55.3 Model and Results 235
55.4 Conclusion 237
55.5 Literature 237

56 BE53: Verification of Wave Loading 239
56.1 Problem Description 239
56.2 Reference Solution 239
56.3 Model and Results 239
56.4 Conclusion 241
56.5 Literature 241

57 BE54: Equivalent Linear Temperature Load 243
57.1 Problem Description 243
57.2 Reference Solution 243
57.3 Model and Results 244
57.4 Conclusion 246
57.5 Literature 246

58 BE55: Design elements and SOFiSTiK T-beam Philosophy 247
58.1 Problem Description 247
58.2 Reference Solution 247
58.3 Model and Results 248
58.4 Conclusion 249
58.5 Literature 249

59 BE56: Interface element 251
59.1 Problem Description 251
59.2 Reference Solution 251
59.3 Model and Results 252

59.4 Conclusion 254
59.5 Literature 254

60 **BE57: Response Spectrum Analysis of a Simply Supported Beam** **255**
60.1 Problem Description 255
60.2 Reference Solution 256
60.3 Model and Results 257
60.4 Conclusion 258
60.5 Literature 258

61 **BE58: Automatic computation of spring constant values in BDK** **259**
61.1 Problem Description 259
61.2 Reference Solution 260
61.3 Model and Results 261
61.4 Conclusion 262
61.5 Literature 263

Introduction

1 About this Manual

The primary objective of this manual is to verify the capabilities of SOFiSTiK by means of nontrivial problems which are bound to reference solutions.

To this end, this manual contains a compilation of a number of selected computational benchmarks, each benchmark focusing on a specific (mechanical/design) topic. The obtained results from the SOFiSTiK analysis are contrasted with corresponding reference solutions[1].

The tasks covered by SOFiSTiK, address a broad scope of engineering applications and it is therefore not possible to validate all specific features with known reference solutions in terms of this Verification Manual. An attempt has been made though, to include most significant features of the software with respect to common problems of general static and dynamic analysis of structures.

1.1 Layout and Organization of a Benchmark

For the description of each Benchmark, a standard format is employed, where the following topics are always treated:

- Problem Description
- Reference Solution
- Model and Results
- Conclusion
- Literature

First, the problem description is given, where the target of the benchmark is stated, followed by the reference solution, where usually a closed-form analytical solution is presented, when available. The next section is the description of the model, where its properties, the loading configuration, the analysis method and assumptions, further information on the finite element model, are presented in detail. Finally, the results are discussed and evaluated with respect to the reference solution and a final conclusion for the response of the software to the specific problem is drawn. Last but not least, the textbooks and references used for the verification examples are listed, which are usually well known and come from widely acclaimed engineering literature sources.

1.2 Finding the Benchmark of interest

There are several ways of locating a Benchmark that is of interest for the user. For each example a description table is provided in the beginning of the document, where all corresponding categories, that are treated by the specific benchmark, are tabulated, as well as the name of the corresponding input file. Such a description table with some example entries, follows next.

Overview	
Element Type(s):	C2D
Analysis Type(s):	STAT, MNL
Procedure(s):	LSTP

---

[1] Where available, analytical solutions serve as reference. Where this is not feasible, numerical or empirical solutions are referred to. In any case, the origin of the reference solution is explicitly stated.

Topic(s):	SOIL
Module(s):	TALPA
Input file(s):	passive_earth_pressure.dat

As it can be seen, the available categories are the element type, the analysis type, the procedure, the topics and the modules. For each category that is provided in the description table, a hyperlink is created, linking each example to the global categories tables. In this manner, the user has a direct overview of the attributes involved in each problem, and at the same time is able to browse by category through the Verification Manual focusing only on the one of his interest. Table 1.1 provides an overview of all the categories options that are available.

Table 1.1: Categories Overview

Categories	Options
Element Type	Continuum 3D
	Continuum 2D (plane strain)
	Continuum axisymmetric
	Shell
	FE beam 3D
	Nonlinear FE beam 3D (AQB)
	Fiber beam 2D
	Fiber beam 3D
	Truss element
	Cable element
	Spring element
	Damping element
	Couplings
Analysis Type	Geometrically nonlinear
	Physically nonlinear
	Dynamic
	Static
	Potential problem
Procedure	Buckling analysis
	Eigenvalue/ Modal analysis
	Time stepping
	Load stepping
	Phi-C reduction
Topic	Soil related
	Seismic

Table 1.1: (continued)

Categories	Options
	Fire design
Module	AQB AQUA ASE BDK BEMESS CSM DYNA SOFiLOAD SOFiMSHC STAR2 TALPA TENDON

1.3 Symbols

For the purpose of this manual the following symbols and abbreviations apply.

SOF.	SOFiSTiK
Ref.	reference
Tol.	tolerance
cs	cross-section
sect.	section
temp.	temperature
homog.	homogeneous
Be.	benchmark
con.	construction
SDOF	single degree of freedom
e_r	relative error of the approximate number
$\lvert e_r \rvert$	absolute relative error of the approximate number
e	error of the approximate number
$\lvert e \rvert$	absolute error of the approximate number
$exp\,()$	same as $e^{()}$

2 Index by Categories

Subsequent tables show all Benchmarks included in this Verification Manual, indexed by category.

2.1 Mechanical Benchmarks

ELEMENT TYPE	**Keyword**	**Benchmark Examples**
Continuum 3D	C3D	BE41, BE42, BE43
Continuum 2D	C2D	BE20, BE21, BE22, BE28, BE29, BE30, BE38, BE44, BE45, BE50, BE56
Continuum axisymmetric	CAXI	BE48, BE49
Shell	SH3D	BE7, BE8, BE11, BE14, BE32, BE33, BE34, BE35, BE39, BE46, BE55
FE beam 3D	B3D	BE3, BE4, BE5, BE6, BE7, BE8, BE9, BE10, BE11, BE12, BE13, BE15, BE16, BE17, BE18, BE19, BE25, BE37, BE40, BE46, BE47, BE55, BE58
Fiber beam 2D	BF2D	BE11, BE32, BE33, BE34, BE35
Truss element	TRUS	BE1, BE31
Spring element	SPRI	BE23, BE24, BE26, BE27
Damper element	DAMP	BE24, BE26

ANALYSIS TYPE	**Keyword**	**Benchmark Examples**
Geometrically nonlinear	GNL	BE4, BE7, BE8, BE12, BE13, BE14, BE15, BE16, BE17, BE18, BE19, BE31, BE37, BE40
Physically nonlinear	MNL	BE11, BE20, BE21, BE22, BE29, BE32, BE33, BE34, BE35, BE38, BE46, BE47, BE48, BE49, BE56
Dynamic	DYN	BE23, BE24, BE25, BE26, BE27, BE39, BE50
Static	STAT	BE1, BE2, BE3, BE4, BE5, BE6, BE7, BE8, BE9, BE10, BE11, BE12, BE13, BE14, BE15, BE16, BE17, BE18, BE19, BE20, BE21, BE22, BE28, BE29, BE30, BE31, BE32, BE33, BE34, BE35, BE37, BE38, BE40, BE41, BE42, BE43, BE44, BE45, BE46

PROCEDURE	**Keyword**	**Benchmark Examples**
Buckling analysis	STAB	BE13, BE14, BE15, BE37
Eigenvalue / Modal analysis	EIGE	BE25, BE39, BE47
Time stepping	TSTP	BE23, BE24, BE26, BE27
Load stepping	LSTP	BE7, BE8, BE11, BE20, BE21, BE22, BE29, BE31, BE32, BE33, BE34, BE35, BE38, BE48, BE49
Phi-C reduction	PHIC	BE38

TOPIC	**Keyword**	**Benchmark Examples**
Soil related	SOIL	BE20, BE21, BE22, BE28, BE29, BE30, BE38, BE44, BE45, BE48, BE49, BE50
Seismic	EQKE	BE36, BE47, BE51, BE57
Fire design	FIRE	BE32, BE33, BE34, BE35
Wave	WAVE	BE52, BE53

MODULE	**Keyword**	**Benchmark Examples**
Design of Cross Sections and of Prestressed Concrete and Composite Cross Sections	AQB	BE5
Materials and Cross Sections	AQUA	BE9
General Static Analysis of Finite Element Structures	ASE	BE1, BE2, BE3, BE4, BE5, BE6, BE7, BE8, BE10, BE11, BE12, BE13, BE14, BE15, BE16, BE17, BE18, BE19, BE31, BE32, BE33, BE34, BE35, BE37, BE40, BE41, BE42, BE43, BE46, BE47, BE55
Dynamic Analysis	DYNA	BE18, BE19, BE23, BE24, BE25, BE26, BE27, BE37, BE39, BE50, BE57
Loadgenerator for Finite Elements and Frameworks	SOFiLOAD	BE36, BE47, BE51, BE52, BE53, BE54
Geometric Modelling	SOFiMSHC	BE2
Statics of Beam Structures 2nd Order Theory	STAR2	BE11, BE37, BE46
2D Finite Elements in Geotechnical Engineering	TALPA	BE11, BE20, BE21, BE22, BE28, BE29, BE30, BE32, BE33, BE34, BE35, BE38, BE44, BE45, BE48, BE49, BE56

Part I

SOFiSTiK Software Quality Assurance (*SQA*)

3 SOFiSTiK SQA Policy

3.1 Objectives

3.1.1 About SOFiSTiK

SOFiSTiK finite element software has been continuously developed since 1981. It is currently used by more than 10000 customers worldwide. SOFiSTiK is a multipurpose tool with extensive capabilities which fall into a wide spectrum of engineering analyses such as static and dynamic structural analysis, modal and buckling eigenvalue problems, nonlinearities and higher order effects, geotechnics and tunnel analysis, heat transfer and fire analysis, as well as numerous types of other applications.

3.1.2 Innovation and Reliability

As a provider of cutting-edge engineering software, confidence in robustness and reliability of the product is an issue of outstanding relevance for SOFiSTiK. To some degree, however, innovation and reliability are conflicting targets, since every change introduces new possible sources of uncertainty and error. To meet both demands on a sustainable basis, SOFiSTiK has installed a comprehensive quality assurance system. The involved organizational procedures and instruments are documented in the following Sections.

3.2 Organisation

3.2.1 Software Release Schedule

SOFiSTiK is now switching to a yearly release cycle for all SOFiSTiK products (incl. current OEMs) with a service period of 3 years. Meaning the next release 2023 will not only be a BIM App and compatibility release for SOFiCAD and SOFiPLUS, but also a release of the FEA products including latest OEM versions: e.g. SOFiSTiK — 2023.

The first customer shipment (FCS) of a SOFiSTiK major release is preceded by an extensive testing period. The major release cycle is supplemented by a two-month service pack cycle. Service packs are quality assured, which means they have passed both the continuous testing procedures and the functional tests. They are available for download via the SOFiSTiK update tool SOFiSTiK Application Manager (SAM).

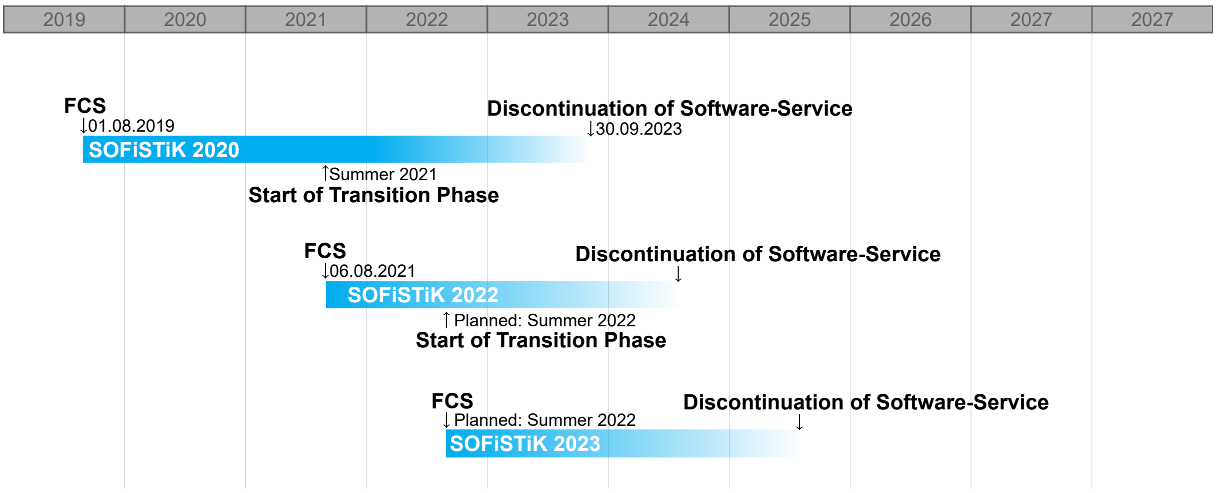

Figure 3.1: SOFiSTiK Release Schedule

Software updates for the current version (service packs) include bug-fixes and minor new features. Major new developments with increased potential regarding side- effects are reserved for major releases with an obligatory extensive testing period.

3.2.2 SQA Modules - Classification

Figure 3.2 depicts the ”three pillars” of the SOFiSTiK SQA procedure. Preventive and analytic provisions can be differentiated.

Preventive provisions essentially concern the organization of the *development process*. They aim at minimizing human errors by a high degree of automatism and by avoiding error-prone stress situations. These provisions comprise:

- A thoroughly planned feature map and release schedule.
- Strict phase differentiation: Prior to any software release (also for service packs), the *development phase* is followed up by a *consolidation phase* . This phase is characterized by extensive functional testing. No new features are implemented, only test feedback is incorporated. For major releases, an additional *BETA test phase* is scheduled.
- Fully automated build and publishing mechanisms.

Analytic provisions provide for the actual testing of the software products. *Continuous Testing* directly accompanies the development process: Automated and modular regression tests assure feedback at a very early stage of the development (Section 3.3.3: Continuous Testing). *Functional Testing* is carried out in particular during the consolidation phases. These tests essentially involve manual testing; they focus on comprehensive workflow tests and product oriented semantic tests.

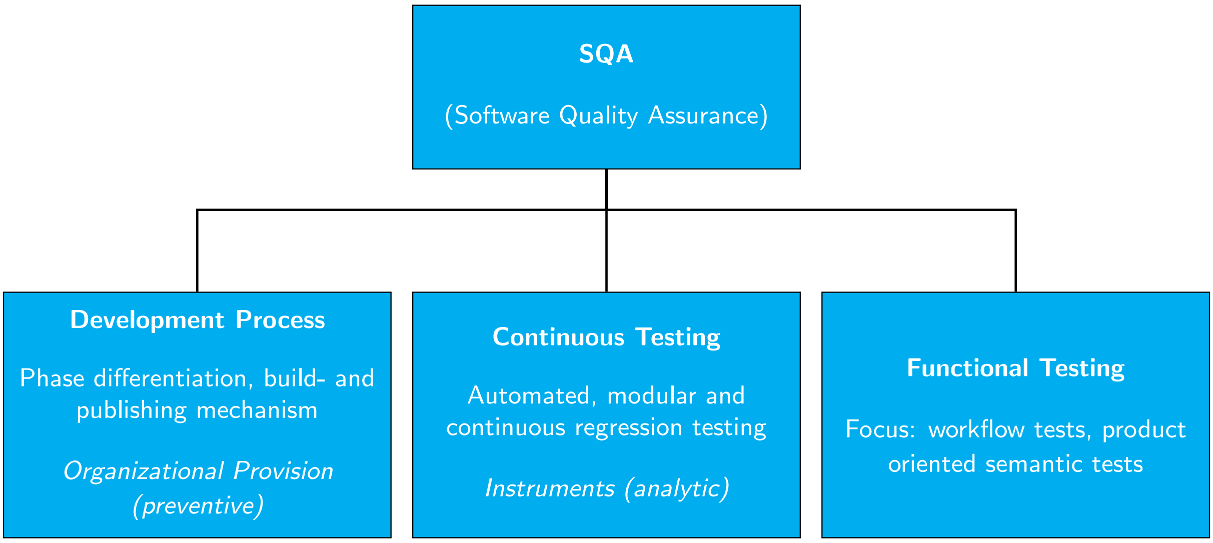
SQA
(Software Quality Assurance)
Development Process
Phase differentiation, build- and publishing mechanism
Organizational Provision (preventive)
Continuous Testing
Automated, modular and continuous regression testing
Instruments (analytic)
Functional Testing
Focus: workflow tests, product oriented semantic tests

Figure 3.2: SQA Modules

3.2.3 Responsibilities

The consistent implementation of quality assurance procedures is responsibly coordinated by the managing board executive for products.

The development divisions are in authority for:

- The establishment, maintenance and checking of continuous testing procedures.
- The implementation of corresponding feedback.

The product management is responsible for:

- The coordination and execution of functional testing.
- The integration of customer feedback into the QA process.

As a corporate activity is carried out:

- Continuous review of processes.
- The identification of supplemental objectives.
- Identification and implementation of possible optimizations.

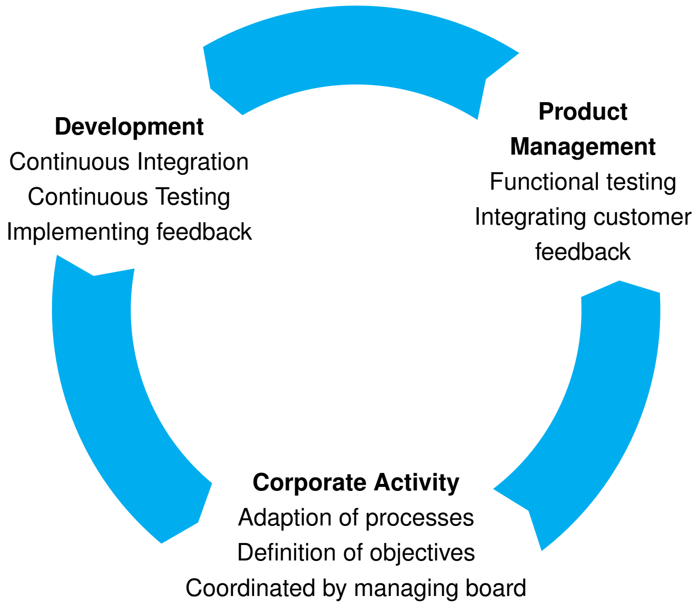
Development
Continuous Integration
Continuous Testing
Implementing feedback
Product Management
Functional testing
Integrating customer feedback
Corporate Activity
Adaption of processes
Definition of objectives
Coordinated by managing board

Figure 3.3: SQA Responsibilities

3.2.4 Software Release Procedure

The defined minimum requirements for software releases of type Hotfix, Service Pack and Major Release are illustrated by Figure 3.4. Approval of individual products is accomplished by the respective person in charge; the overall approval is in authority of the managing board executive for products.

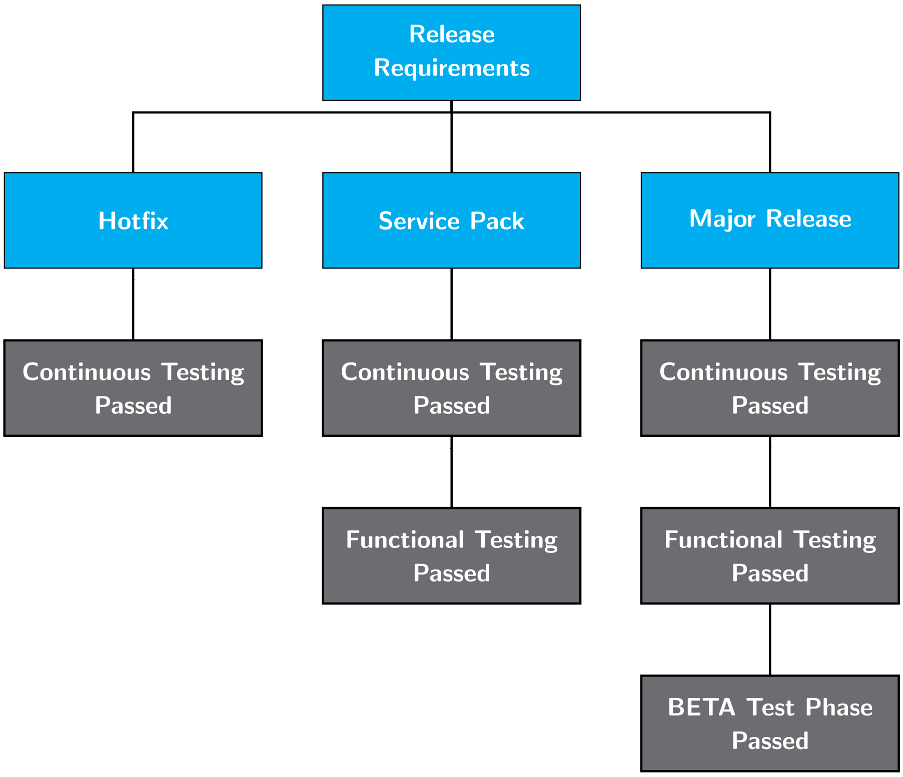
Release Requirements
Hotfix
Service Pack
Major Release
Continuous Testing Passed
Continuous Testing Passed
Continuous Testing Passed
Functional Testing Passed
Functional Testing Passed
BETA Test Phase Passed

Figure 3.4: Software Release Requirements

3.3 Instruments

3.3.1 CRM System

Each request from our customers is traced by means of a Customer Relation Management (CRM) System assuring that no case will be lost. Detailed feedback to the customer is provided via this system.

Possible bug fixes or enhancements of the software are documented with version number and date in corresponding log files. These log files are published via RSS-feed to our customers. In this way, announcement of available software updates (service-pack or hotfix) is featured proactively. Moreover, information is provided independent of and prior to the actual software update procedure.

Further sources of information are the electronic newsletter/ newsfeeds and the internet forum (www.sofistik.de / www.sofistik.com).

3.3.2 Tracking System (internal)

For SOFiSTiK-internal management and coordination of the software development process - both regarding implementation of features and the fixing of detected bugs - a web-based tracking system is adopted.

3.3.3 Continuous Integration – Continuous Testing

As mentioned above, the production chain is characterized by a high degree of automation. An important concern is the realization of prompt feedback cycles featuring an immediate response regarding quality of the current development state.

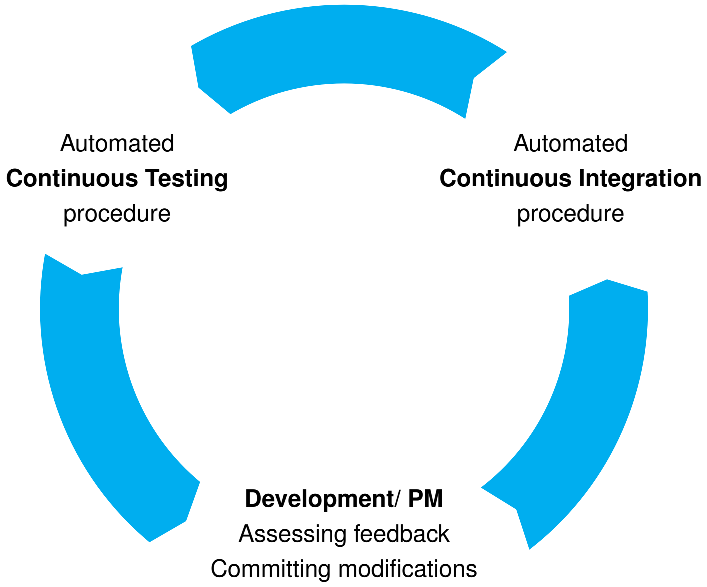

Figure 3.5: Feedback cycle: Continuous Integration – Continuous Testing

Continuous integration denotes the automated process, assuring that all executed and committed modifications of the program's code basis are directly integrated via rebuild into the internal testing environment.

Upon completion of the integration, the *continuous testing* procedure is triggered automatically. This procedure executes a standardized testing scenario using the newly updated software. Test results are prepared in form of compact test protocols allowing for quick assessment.

The executed tests are so-called regression tests. Regression tests examine by means of associated reference solutions wether the conducted modifications of the code basis cause undesired performance in other already tested parts of the program.

Together, continuous integration and continuous testing form the basis for a quality control that directly accompanies the development process. This way, possibly required corrections can be initiated promptly. SOFiSTiK has successfully implemented this procedure. Currently, the continuous test database comprises more than 3000 tests.

3.4 Additional Provisions

3.4.1 Training

As a special service to our customers, SOFiSTiK provides for comprehensive and individually tailored training to support a qualified and responsible use of the software. This is complemented by offering a variety of thematic workshops which are dedicated to specific engineering topics.

It is the credo of SOFiSTiK that a high-quality product can only be created and maintained by highly qualified personnel. Continuing education of the staff members is required by SOFiSTiK and it is supported by an education program which involves both in- house trainings and provisions of external trainings on a regular basis.

3.4.2 Academia Network

Arising questions are treated by an intense discussion with customers, authorities and scientists to find the best interpretation.

3.5 Disclaimer

Despite all efforts to achieve the highest possible degree of reliability, SOFiSTiK cannot assure that the provided software is bug-free or that it will solve a particular problem in a way which is implied with the opinion of the user in all details. Engineering skill is required when assessing the software results.

Part II

Mechanical Benchmarks

4 BE1: Joint Deflection of Plane Truss

Overview

Element Type(s):	TRUS
Analysis Type(s):	STAT
Procedure(s):	
Topic(s):	
Module(s):	ASE
Input file(s):	truss.dat

4.1 Problem Description

The problem consists of a plane truss structure, as shown in Fig. 4.1. Determine the vertical deflection at the free node 8.

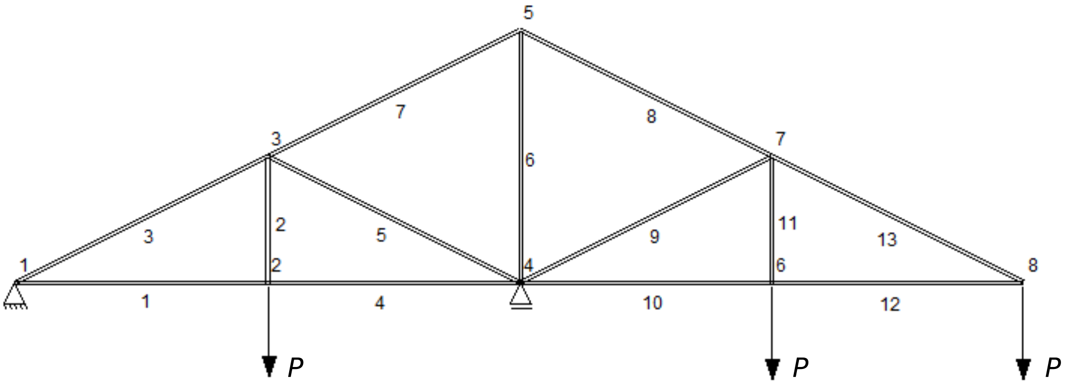

Figure 4.1: Problem Description

4.2 Reference Solution

The problem of determining the displacements of trusses can be treated in various ways. Popular among engineers, is to apply energy methods, e.g. the method of virtual work or Castigliano's theorem, to solve problems involving slope and deflection, that are based on the conservation of energy principle, and are more suitable for structures with complicated geometry such as trusses. Further information on this topic can be found in numerous engineering books, dealing with structural analysis [1].

4.3 Model and Results

The general properties of the model [2] are defined in Table 4.1. The total width of the truss is $60\ ft$, consisting of four spaces of $15\ ft$ each, and the total height is $15\ ft$. The load is applied equally at the three free nodes at the bottom of the truss. The results are presented in Table 4.2 and compared to the reference example [2]. Fig. 4.2 shows the deflections and the deformed shape of the structure.

Table 4.1: Model Properties

Material Properties	Geometric Properties	Loading
$E = 29\,10^3\,ksi$	$l_{total} = 60\,ft = 18.288\,m$	$P = 20\,kip = 89.0\,kN$
$= 206842.773\,MPa$	$h_{total} = 15\,ft = 4.572\,m$	
$\nu = 0.3$	$l_2 = l_{11} = 7.5\,ft = 2.286\,m$	
	$l_1 = l_4 = l_6 = l_{10} = l_{12} = 15\,ft = 4.572\,m$	
	$A_1 = A_4 = 2\,in^2 = 12.90\,cm^2$	
	$A_2 = A_{11} = A_{10} = A_{12} = 1\,in^2 = 6.45\,cm^2$	
	$A_5 = A_9 = 1.5\,in^2 = 9.68\,cm^2$	
	$A_3 = A_6 = 3\,in^2 = 19.35\,cm^2$	
	$A_7 = A_8 = 4\,in^2 = 25.81\,cm^2$	

Table 4.2: Results

	SOF.	Ref. [2]	$\lvert e_r \rvert$ [%]
$\delta_8\ [mm]$	69.11	69.09	0.036

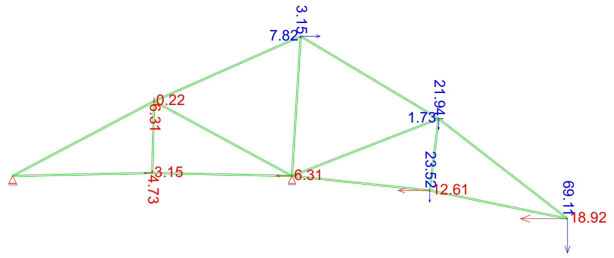

Figure 4.2: Problem Description

4.4 Conclusion

This example verifies the deflection of trusses. It has been shown that the behaviour of the truss is accurately captured. It should be noted that in the reference example [2] the deflection in inches was rounded to two decimal places, which leads to a higher relative error in Table 4.2. When comparing the SOFiSTIK result with an analytical solution rounded to four decimal places, the relative error decreases to 0.0004%.

4.5 Literature

[1] R. C. Hibbeler. *Structural Analysis*. 8th. Prentice Hall, 2012.
[2] J. C. McCormac. *Structural Analysis*. Wileys & Sons, 2007.

5 BE2: Kinematic Coupling Conditions

Overview

Element Type(s):	COUP
Analysis Type(s):	STAT
Procedure(s):	
Topic(s):	
Module(s):	SOFiMSHC, ASE
Input file(s):	coupling.dat

5.1 Problem Description

This problem verifies the kinematic coupling conditions for a structural point. Each coupling condition is tested on a pair of beams coupled with each other through structural points, as shown in Fig. 5.1. Four different cases are considered and the deflections of the beams are determined and compared to the analytical solution.

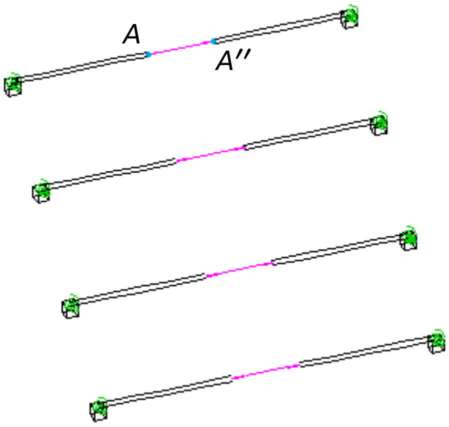

Figure 5.1: Problem Description

5.2 Reference Solution

In this example the problem of coupling structural points is treated. Through the definition of kinematic coupling conditions between structural points the constraint of one or multiple degrees of freedom is allowed. The displacement values of the given structural point A'' are defined according to the respective displacement values of the referenced (or master-) node A. Various cases are possible in SOFiSTiK for the coupling conditions. With the exception of the three conditions KPX, KPY and KPZ, which only couple the corresponding displacement. e.g. $u_x = u_{xo}$, all other coupling conditions satisfy the mechanical equilibrium conditions by taking the real distances between the two connected points into account, e.g. the conditions $KPPX$, $KPPY$, $KPPZ$ correspond to the following expressions respectively [3] [4]:

$$u_x = u_{xo} + \phi_{yo}(z - z_o) - \phi_{zo}(y - y_o) \tag{5.1}$$

$$u_y = u_{yo} + \phi_{zo}(x - x_o) - \phi_{xo}(z - z_o) \tag{5.2}$$

$$u_z = u_{zo} + \phi_{xo}(y - y_o) - \phi_{yo}(x - x_o) \tag{5.3}$$

Mechanically they act like infinitely stiff structural members. A number of additional literals are provided in SOFiSTiK which allow to define a combination of coupling relations. For example, a rigid connection with hinged conditions at the reference node is described by

$$KP = KPPX + KPPY + KPPZ \tag{5.4}$$

whereas

$$KF = KP + KMX + KMY + KMZ = KPPX + KPPY + KPPZ + KMX + KMY + KMZ \tag{5.5}$$

describes mechanically a rigid connection with clamped support at the reference node. Further information on the topic are provided in SOFiSTiK manual of module SOFiMSHC [3].

5.3 Model and Results

The general properties of the model are defined in Table 5.1. All beams are of 4 m length and consist of a standard rectangular cross-section and a standard concrete material. The structural points A and A'' have a distance of 2 m in the axial direction. Four coupling conditions are considered :

- $KPPX$, where only the displacement in the global x direction is connected
- LPX, where only the displacement in the structural point's local x direction is connected
- KP, where the displacements in x, y and z direction are connected
- KF, where the displacements and the rotations in x, y and z direction are connected

All cases are tested for four loadcases, i.e. a horizontal P_y, a longitudinal P_x, a vertical P_z and a rotational M_x.

Table 5.1: Model Properties

Material Properties	Geometric Properties	Loading
$C\,30/45$	$l_{beam} = 4\,m$	$P_y = 50.0\,kN$
	$h_A = 0.4\,m$, $b_A = 0.2\,m$	$P_x = -50.0\,kN$
	$h_{A''} = 0.3\,m$, $b_{A''} = 0.15\,m$	$P_z = 50.0\,kN$
	$(x_{A''} - x_A) = 2\,m$	$M_x = 10.0\,kN$
	$(y_{A''} - y_A) = 0\,m$	
	$(z_{A''} - z_A) = 0\,m$	

In the cases, where only a displacement is transferred in the vertical u_z or horizontal direction u_y , a rotation results in the other direction. If for example, we consider a coupling of only the displacement in the y direction, then a rotation of $\phi_z = 3u_y/(2l_{beam})$ will also result as the effect of a prescribed displacement of value u_y at the beam tip A''.

Table 5.2: Results for KPPX Coupling Condition

Load	u_x [mm]	
Case	SOF.	Ref.
P_x	-0.107	-0.107

Table 5.3: Results for LPX Coupling Condition

Load	u_y [mm]		ϕ_z [$mrad$]	
Case	SOF.	Ref.	SOF.	Ref.
P_y	165.284	165.284	-61.919	-61.982

Table 5.4: Results for KP and KF Coupling Condition

Coupling		KP			KF			
DOF / LC		P_y	P_x	P_z	P_y	P_x	P_z	M_x
u_x [mm]	SOF.	0.0	-0.107	0.0	0.0	-0.107	0.0	0.0
	Ref.	0.0	-0.107	0.0	0.0	-0.107	0.0	0.0
u_y [mm]	SOF.	165.284	0.0	0.0	49.325	0.0	0.0	0.0
	Ref.	165.284	0.0	0.0	49.325	0.0	0.0	0.0
u_z [mm]	SOF.	0.0	0.0	41.528	0.0	0.0	12.531	0.0
	Ref.	0.0	0.0	41.528	0.0	0.0	12.531	0.0
ϕ_x [$mrad$]	SOF.	0.0	0.0	0.0	0.0	0.0	0.0	6.671
	Ref.	0.0	0.0	0.0	0.0	0.0	0.0	6.671
ϕ_y [$mrad$]	SOF.	0.0	0.0	15.510	0.0	0.0	0.200	0.0
	Ref.	0.0	0.0	15.573	0.0	0.0	0.200	0.0
ϕ_z [$mrad$]	SOF.	-61.919	0.0	0.0	-0.725	0.0	0.0	0.0
	Ref.	-61.982	0.0	0.0	-0.725	0.0	0.0	0.0

The results are presented in Tables 5.2 - 5.4, where they are compared to the reference results calculated with the formulas provided in Section 5.2. Due to the extent of the results only non zero values will be presented in the result tables. Figures 5.2, 5.3 present the results for the *KF* coupling condition for the load cases 1 to 4 for both displacements and rotations, respectively.

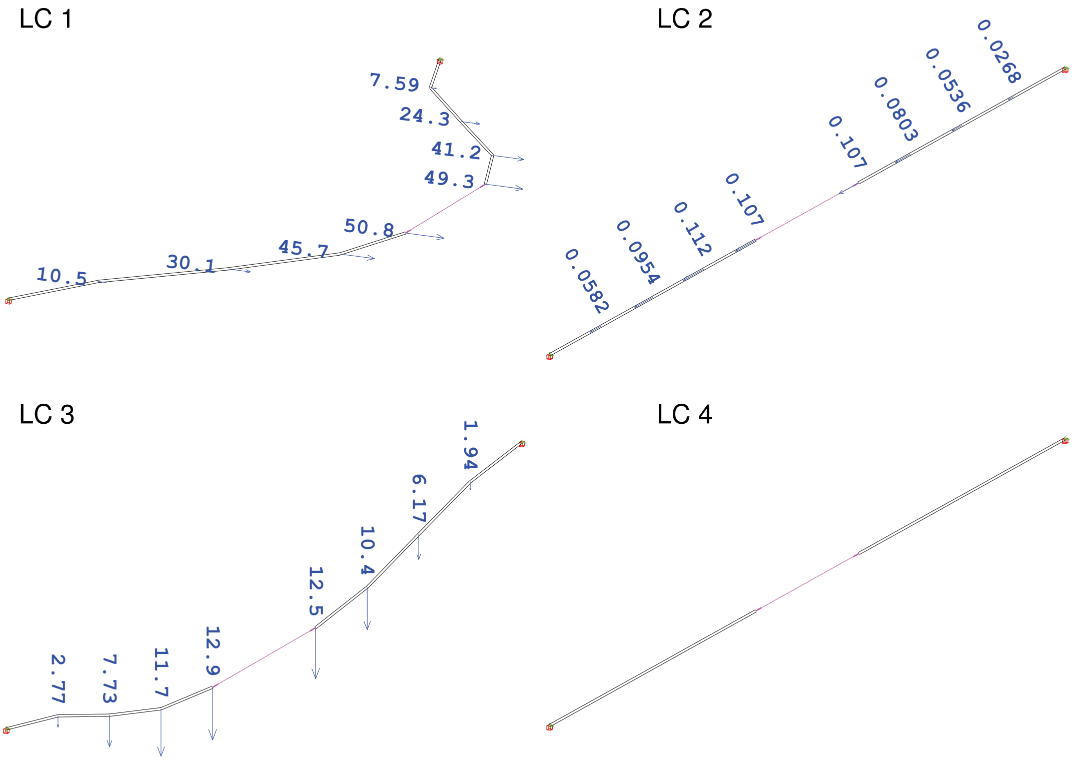

Figure 5.2: Displacement Results for KF coupling for LC 1-4

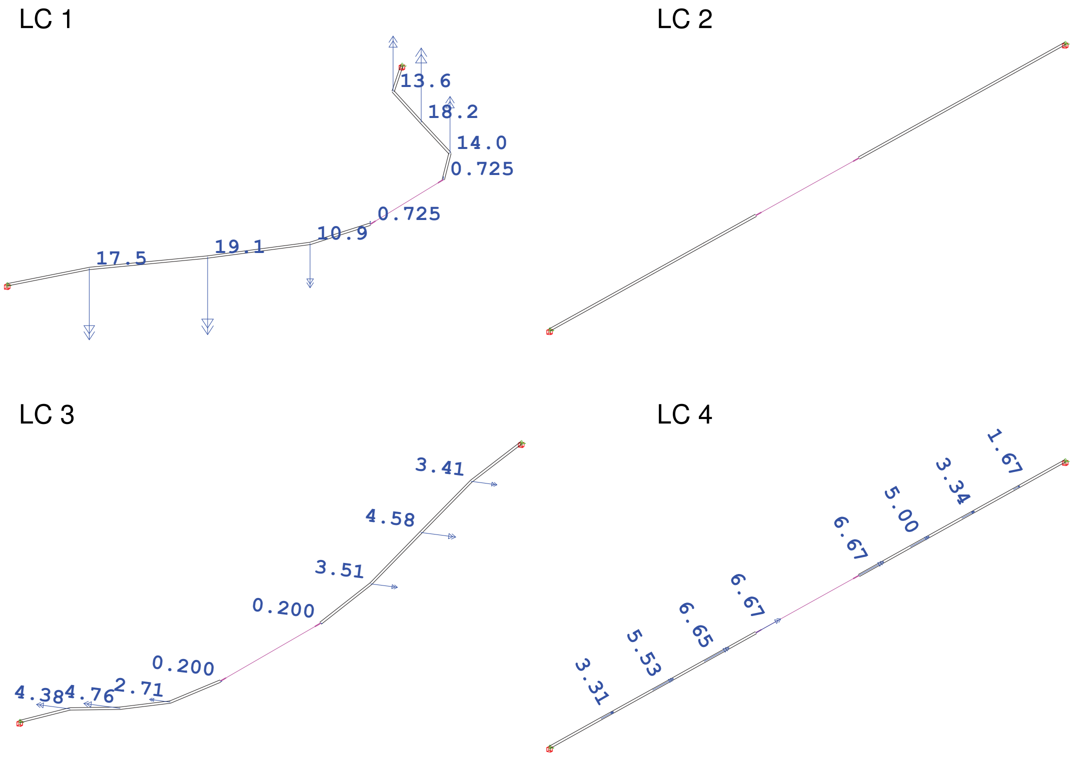

Figure 5.3: Rotation Results for KF coupling for LC 1-4

5.4 Conclusion

This example verifies the coupling of structural points. It has been shown that the behaviour is accurately captured.

5.5 Literature

[3] *SOFiMSHC Manual: Geometric Modelling*. Version 18-0. SOFiSTiK AG. Oberschleißheim, Germany, 2017.

[4] *SOFiMSHA Manual: Import and Export of Finite Elements and Beam Structures*. Version 18-0. SOFiSTiK AG. Oberschleißheim, Germany, 2017.

6 BE3: Beam Stresses and Deflections

Overview

Element Type(s): B3D
Analysis Type(s): STAT
Procedure(s):
Topic(s):
Module(s): ASE
Input file(s): rect_beam.dat, I_beam.dat

6.1 Problem Description

A rectangular beam is supported as shown in Fig. 6.1 and loaded on the overhangs by a uniformly distributed load q. Determine the maximum bending stress σ in the middle portion of the beam and the deflection δ at the middle of the beam.

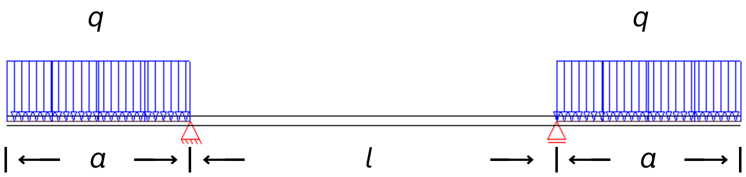

Figure 6.1: Beam structure

6.2 Reference Solution

The magnitude of the stresses at a cross-section is defined by the magnitude of the shearing force and bending moment at that cross-section. Under pure bending, the maximum tensile and compressive stresses occur in the outermost fibers. For any cross-section, which has its centroid at the middle of the depth h, and for a linear elastic material behaviour, the maximum stresses occur for $z = \pm h/2$ [5]:

$$\sigma_{max} = \frac{Mh}{2I} \qquad \text{and} \qquad \sigma_{min} = -\frac{Mh}{2I}, \tag{6.1}$$

in which I, is the moment of inertia of the cross-section with respect to the neutral axis and M the bending moment. For a beam overhanging equally at both supports with a uniformly distributed load applied at the overhangs (Fig. 6.1), assuming Bernoulli beam theory, the deflection at the middle of the beam is:

$$\delta = \frac{qa^2 l^2}{16EI} = \frac{Ml^2}{8EI}, \tag{6.2}$$

where q is the value of the uniformly distributed load, a the length of the overhangs, l the length of the middle span and M the bending moment at the middle of the beam.

6.3 Model and Results

The model is analysed for two different cross-sections, a rectangular and a general I-beam cross-section. The properties are defined in Table 6.1. The results are presented in Table 6.2. As to be expected, the analysis yields the same results for the maximum bending stress and deflection at the middle of the beam for the two models. Figure 6.2 shows the distribution of the stresses along the cross-sections for the two analysed examples. Figure 6.3 shows the deformed structure with the nodal displacements.

Table 6.1: Model Properties

Material Properties	Geometric Properties Rectangular	Geometric Properties I-beam	Loading
$E = 30000\, MPa$	$l = 200\, mm$	$l = 200\, mm$	$q = 10\, kN/m$
	$a = 100\, mm$	$b = 16\, mm$	
	$h = 30\, mm$	$t_{web} = 2.174\, mm$	
	$b = 7\, mm$	$t_{flange} = 2\, mm$	
	$I_y = 1.575\, cm^4$	$I_y = 1.575\, cm^4$	

Table 6.2: Results

	Rectangular	I-beam	Ref.
σ_{max} [MPa]	47.619	47.620	47.619
δ [mm]	0.529	0.529	0.529

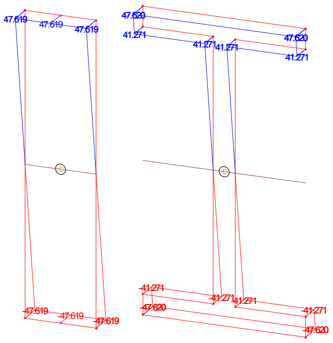
47.619
47.619
47.619
47.620
41.271
41.271
41.271
47.620
41.271
-41.271
-41.271
-41.271
-41.271
-47.620
-47.620
-47.619
-47.619
-47.619

Figure 6.2: Distribution of stresses

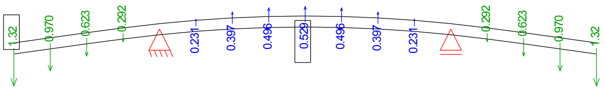
1.32
0.970
0.623
0.292
0.231
0.397
0.496
0.529
0.496
0.397
0.231
0.292
0.623
0.970
1.32

Figure 6.3: Deformed Structure

6.4 Conclusion

This example adresses the computation of beam stresses and deflections. It has been shown that the behaviour of the beam is captured with an excellent accuracy.

6.5 Literature

[5] S. Timoshenko. *Strength of Materials, Part I, Elementary Theory and Problems*. 2nd. D. Van Nostrand Co., Inc., 1940.

7 BE4: Tie Rod with Lateral Loading

Overview

Element Type(s):	B3D
Analysis Type(s):	STAT, GNL
Procedure(s):	
Topic(s):	
Module(s):	ASE
Input file(s):	tie_rod.dat

7.1 Problem Description

A tie rod is subjected to the action of a tensile force N and a lateral load P applied at the middle as shown in Fig. (7.1). Determine the maximum deflection δ_{max}, the slope θ at the left-hand end and the maximum bending moment M_{max}. In addition, compare these three quantities for the case of the unstiffned tie rod ($N = 0$).

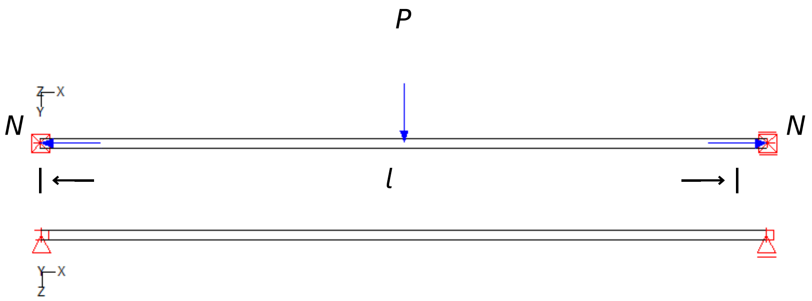

Figure 7.1: Tie Rod

7.2 Reference Solution

The combination of direct axial force and lateral load applied at a beam influences the reaction of the structure. Assuming that the lateral force acts in one of the principal planes of the beam and that the axial force is centrally applied by two equal and opposite forces, the expressions for the deflections can be derived from the differential equations of the deflection curve of the beam [6]. Under tension, the maximum deflections of a laterally loaded beam decrease whereas under compression they increase. The moments of the structure are influenced accordingly.

For the simple problem of a beam with hinged ends, loaded by a single force P at the middle, the maximum deflection at the middle is:

$$\delta_{max} = \frac{Pl^3}{48EI}, \tag{7.1}$$

where l is the lenght of the beam and EI its flexural rigidity. The slope θ at both ends is:

$$\theta = \pm \frac{Pl^2}{16EI}. \tag{7.2}$$

The maximum value of the bending moment at the middle is:

$$M_{max} = \frac{Pl}{4}. \tag{7.3}$$

When now the structure (Fig. 7.1) is submitted to the action of tensile forces N in addition to the initial lateral load P, the deflection at the middle becomes [6]:

$$\delta_{max} = \frac{Pl^3}{48EI} \cdot \frac{u - \tanh u}{\frac{1}{3}u^3}, \tag{7.4}$$

where $u^2 = Nl^2/4EI$. The first factor in Eq. (7.4) represents the deflection produced by the lateral load P acting alone. The second factor indicates in what proportion the deflection produced by P is magnified by the axial tensile force N, respectively. When N is small, it approaches unity, which indicates that under this condition the effect on the deflection of the axial force is negligible. The expressions for the moment and the slopes can be derived accordingly [6].

7.3 Model and Results

The properties of the model are defined in Table 7.1 and the results are presented in Table 7.2. Fig. 7.2 shows the deformed structure under tension and lateral loading.

Table 7.1: Model Properties

Material Properties	Geometric Properties	Loading
$E = 30000\ MPa$	$l = 2\ m$	$P = 0.1\ kN$
	$h = 30\ mm$	$N = 0.1\ kN$
	$b = 30\ mm$	
	$I = 6.75 \times 10^{-8}\ m^4$	

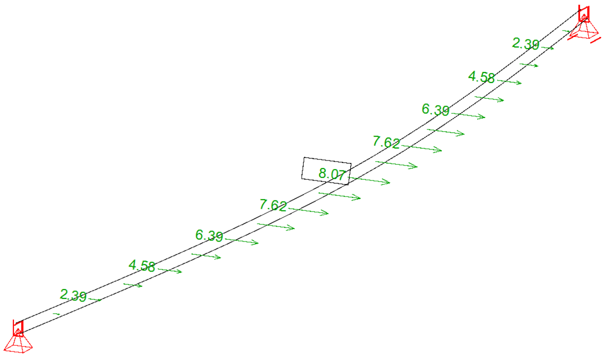

Figure 7.2: Deformed Structure [mm]: $N \neq 0$

Table 7.2: Results

	$N = 0$	Ref.	$N \neq 0$	Ref.
$\delta_{max}\,[m]$	0.00823	0.00823	0.00807	0.00807
$M_{max}\,[kNm]$	0.05000	0.05000	0.04919	0.04919
$\theta\,[rad]$	0.01235	0.01235	0.01210	0.01210

7.4 Conclusion

This example presents the influence of axial forces applied at a laterally loaded beam. The case of a tie rod is examined and the maximum deflections and moment are derived. It has been shown that the behaviour of a beam under the combination of direct axial force and lateral load can be adequately captured.

7.5 Literature

[6] S. Timoshenko. *Strength of Materials, Part II, Advanced Theory and Problems*. 2nd. D. Van Nostrand Co., Inc., 1940.

8 BE5: Bending of a T-beam

Overview	
Element Type(s):	B3D
Analysis Type(s):	STAT
Procedure(s):	
Topic(s):	
Module(s):	AQB, ASE
Input file(s):	t_beam.dat

8.1 Problem Description

An asymmetric T-beam is supported as shown in Fig. 8.1 and subjected to uniform bending M_z. Determine the maximum tensile and compressive bending stresses.

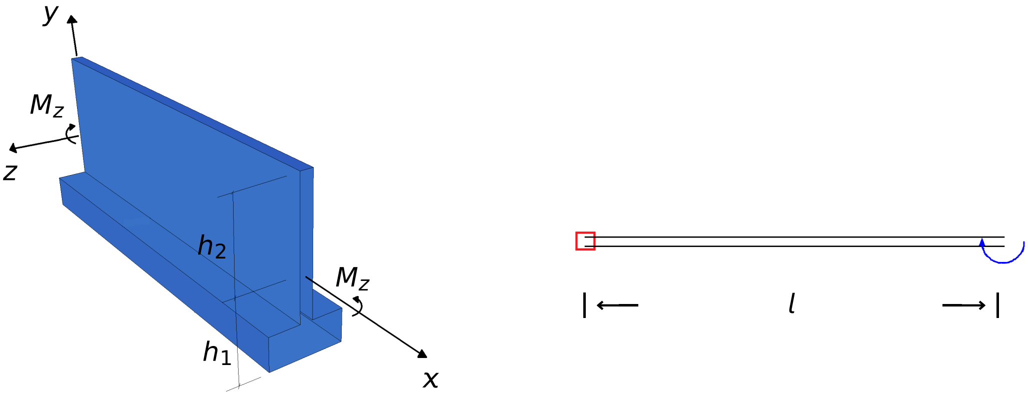

Figure 8.1: Model Properties

8.2 Reference Solution

According to the discussion in Benchmark Example no. 3, it follows that the maximum tensile and compressive stresses in a beam in pure bending are proportional to the distances of the most remote fibers from the neutral axis of the cross-section. When the centroid of the cross-section is not at the middle of the depth, as, for instance, in the case of a T-beam, let h_1 and h_2 denote the distances from the neutral axis to the outermost fibers in the downward and upward directions (Fig. 8.1) respectively. Then for a bending moment M_z, we obtain the maximum tensile and compressive stresses [5]:

$$\sigma_{max} = \frac{M_z h_1}{I_z} \quad \text{and} \quad \sigma_{min} = -\frac{M_z h_2}{I_z}. \tag{8.1}$$

8.3 Model and Results

The properties of the model are defined in Table 8.1. Distances from the centroid to the top and bottom of the beam are calculated as $14\ cm$ and $6\ cm$ respectively. The results are presented in Table 8.2. Figure 8.2 shows the distribution of the stresses along the cross-section.

Table 8.1: Model Properties

Material Properties	Geometric Properties	Loading
$E = 30000\, MPa$	$l = 1\, m$	$M_z = 100\, kNm$
	$h = 20\, cm$	
	$h_1 = 6\, cm$, $h_2 = 14\, cm$	
	$b = 9\, cm$	
	$t_{web} = 1.5\, cm$	
	$t_{flange} = 4\, cm$	
	$I_z = 2000\, cm^4$	

Table 8.2: Results

	SOF.	Ref.
σ_{max} [MPa]	300	300
σ_{min} [MPa]	-700	-700

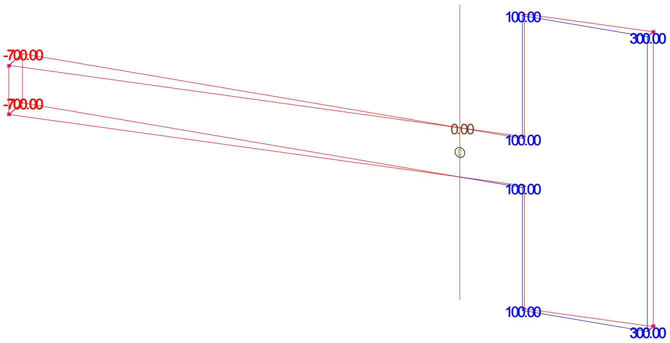

Figure 8.2: Distribution of Stresses

8.4 Conclusion

This example shows the derivation of stresses for beams with asymmetric cross-section in which the centroid of the cross-section is not at the middle of the depth. It has been shown that the behaviour of the beam is captured with an excellent accuracy.

8.5 Literature

[5] S. Timoshenko. *Strength of Materials, Part I, Elementary Theory and Problems*. 2nd. D. Van Nostrand Co., Inc., 1940.

9 BE6: Warping Torsion Bar

Overview

Element Type(s):	B3D
Analysis Type(s):	STAT
Procedure(s):	
Topic(s):	
Module(s):	ASE
Input file(s):	warping.dat

9.1 Problem Description

A cantilever I-bar is fixed at both ends, as shown in Fig. 9.1, and subjected to a uniformly distributed torque m_T [7]. Determine the angle of twist ϕ at the midspan.

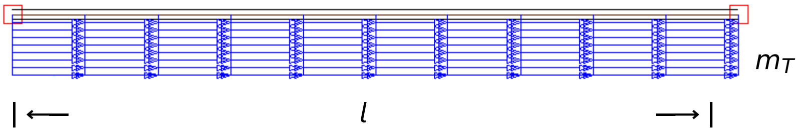

Figure 9.1: An I-bar with Uniformly Distributed Torque

9.2 Reference Solution

In mechanics, torsion is the twisting of a structure due to an applied torque. There are two types of torsion: St. Venant torsion and warping torsion. St. Venant torsion exists always when an element is twisted, whereas the warping torsion occurs additionally under specific conditions. The warping of a section depends on the section geometry which means that there exist warping-free, such as circular, and warping-restrained sections. St. Venant torsion is based on the assumption that either the cross-section is warping-free or that the warping is not constrained. If at least one of these conditions is not met then the warping torsion appears [6].

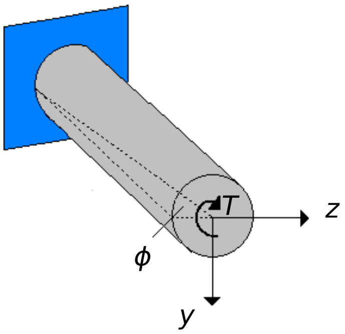

Figure 9.2: Circular Shaft

A member undergoing torsion will rotate about its shear center through an angle of ϕ. Consider a circular shaft that is attached to a fixed support at one end. If a torque T is applied to the other end, the shaft will twist, with its free end rotating through an angle ϕ called the angle of twist [8]:

$$\phi = \frac{TL}{GI_T}, \tag{9.1}$$

where G is the shear modulus and I_T the torsional moment of inertia. For a circular shaft subjected to torsion, each cross-section rotates along the shaft as a solid rigid slab (warping-free cross-section). The torsional moment resisted by the cross-section is:

$$T = GI_T \frac{d\phi}{dx}, \tag{9.2}$$

For most cross-sections, e.g. non-circular, this rotation of the cross-section is accompanied by warping. Then the total torsional moment resisted by the cross-section becomes the sum of the pure torsion and warping torsion [9]. The stresses induced on the member is then classified into three categories: torsional shear stress, warping shear stress and warping normal stress. For example, when a bar of an I-cross-section is subjected to torsion, then the flanges of the cross-section experience bending in the flange planes. This means that torsion induces bending about the strong axis of the flanges. When the tendency for the cross-section to warp freely is prevented or restrained, it causes stresses to develop. The torque that the cross-section carries by bending is:

$$T = EC_M \frac{d^3\phi}{dx^3} \tag{9.3}$$

where EC_M, is the warping torsion stiffness. Furthermore, in warping torsion theory the bimoment is defined as an auxiliary quantity. The objective is to introduce a degree of freedom for beam elements that represents the torque due to restrained warping. The bimoment M_ω is defined as:

$$M_\omega = EC_M \frac{d^2\phi}{dx^2} \tag{9.4}$$

It should be noted, that the bimoment itself is not measurable, however it serves as a convenient parameter to quantify this prevention of warping.

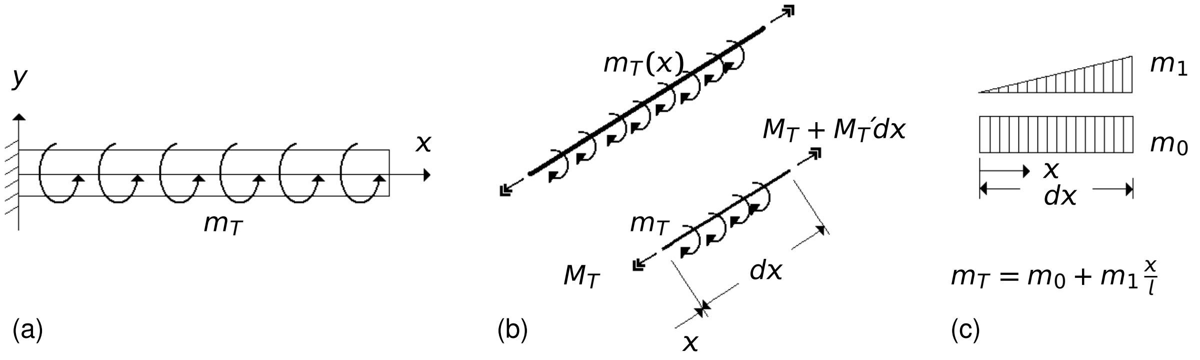

Figure 9.3: The Warping Torsion Problem

Fig. 9.3 (a) shows the warping torsion problem of a bar subjected to a distributed external torque. The differential equation governing the warping torsion problem, for a constant cross-section, becomes [10]:

$$EC_M \frac{d^4\phi}{dx^4} - GI_T \frac{d^2\phi}{dx^2} = m_T, \tag{9.5}$$

where m_T the distributed torque along the bar. The natural boundary conditions are:

$$M_\omega = EC_M \frac{d^2\phi}{dx^2}\ , \qquad \text{z = 0 or l} \tag{9.6}$$

and

$$-EC_M \frac{d^3\phi}{dx^3} + GI_T \frac{d\phi}{dx} = M_T\ , \qquad \text{z = 0 or l} \tag{9.7}$$

where M_T is the concentrated end torque and M_ω the bimoment. Introducing λ, the so called decay factor, in the above equation, and a simplified notation for the derivatives of ϕ, we obtain:

$$\phi^{''''} - \lambda^2 \phi^{''} = \frac{m_T}{EC_M}. \tag{9.8}$$

The solution of the warping torsion equation depends on the type of the torsional load and the kinematic boundary conditions, especially the amount of prevention of the warping. The complete solution system of Eq. 9.8, for the load type given in Fig. 9.3 (c), is thus:

$$\phi = \frac{C_1}{\lambda^2} sinh\, \lambda x + \frac{C_2}{\lambda^2} cosh\, \lambda x + C_3 x + C_4 - \frac{1}{2GI_T}(m_0 + \frac{1}{3} m_1 \frac{x}{l}) x^2 \tag{9.9}$$

$$\phi^{'} = \frac{C_1}{\lambda} cosh\, \lambda x + \frac{C_2}{\lambda} sinh\, \lambda x + C_3 - \frac{1}{2GI_T}(2m_0 + m_1 \frac{x}{l}) x \tag{9.10}$$

$$\phi^{''} = C_1 sinh\, \lambda x + C_2 cosh\, \lambda x - \frac{1}{GI_T}(m_0 + m_1 \frac{x}{l}) \tag{9.11}$$

$$\phi^{'''} = C_1 \lambda cosh\, \lambda x + C_2 \lambda sinh\, \lambda x - \frac{m_1}{GI_T l} \tag{9.12}$$

The values of the constants C_1 to C_4 can be derived with respect to the kinematic boundary conditions of the problem. For the case of warping-free sections, where $C_M = 0$, the differential equation is shortened, leading to the St. Venant torsion problem.

9.3 Model and Results

The properties of the analysed model, are defined in Table 9.1. The corresponding results are presented in Table 9.2. Figure 9.4 shows the deformed shape of the structure and the angle of twist.

Table 9.1: Model Properties

Material Properties	Cross-sectional Properties	Loading
$E = 217396.3331684\, N/mm^2$	$l = 1\, m$	$m_T = 1\, Nmm/mm$
$G = 81386.6878\, N/mm^2$	$h = 80\, mm$	
$\nu = 0.33557673$	$t = 2\, mm$	
	$b = 40\, mm$	
	$C_M = 0.323 \times 10^8\, mm^6$	
	$I_T = 431.979\, mm^4$	

Table 9.2: Results

	Twist in x-direction	Ref. [7]
ϕ_x $[mrad]$	0.329659	0.329262

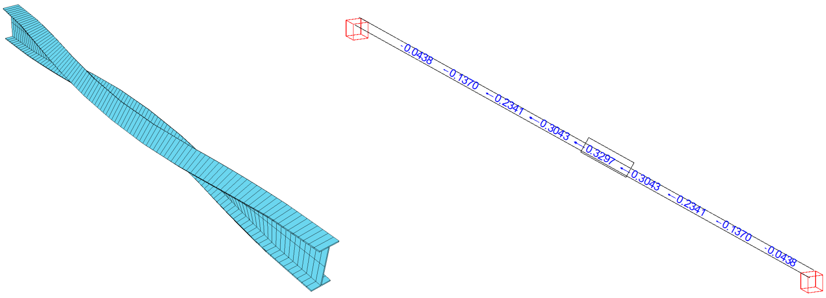

Figure 9.4: Deformed Stucture

9.4 Conclusion

This example presents the warping torsion problem. The total torsional moment resisted by the cross-section is the sum of that due to pure torsion, which is always present, and that due to warping. It has been shown that the behaviour of the beam for warping is captured correctly.

9.5 Literature

[6] S. Timoshenko. *Strength of Materials, Part II, Advanced Theory and Problems*. 2nd. D. Van Nostrand Co., Inc., 1940.

[7] C-N. Chen. “The Warping Torsion of a Bar Model of the Differential Quadrature Element Method”. In: *Computers and Structures* 66.2-3 (1998), pp. 249–257.

[8] F.P. Beer, E.R. Johnston, and J.T. DeWolf. *Mechanics of Materials*. 4th. McGraw-Hill, 2006.

[9] P. Seaburg and C.J. Carter. *Steel Design Guide Series 9: Torsional Analysis of Structural Steel Members*. AISC. 2003.

[10] C. Petersen. *Stahlbau*. 2nd. Vieweg, 1990.

10 BE7: Large Deflection of Cantilever Beams I

Overview

Element Type(s):	B3D, SH3D
Analysis Type(s):	STAT, GNL
Procedure(s):	LSTP
Topic(s):	
Module(s):	ASE
Input file(s):	beam_elem.dat, quad_elem.dat

10.1 Problem Description

A cantilever beam is supported as shown in Fig. 10.1. The beam is subjected to a total vertical load, applied at the tip of the cantilever, which should cause the tip to deflect significantly. The determination of the non-dimensional tip deflections ratios are determined.

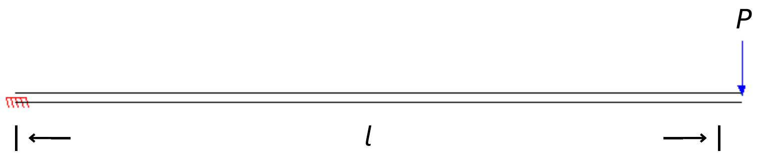

Figure 10.1: Model Properties

10.2 Reference Solution

The classical problem of deflection of a cantilever beam of linear elastic material, under the action of an external vertical concentrated load at the free end, is analysed (Fig. 10.2). The solution for large deflection of a cantilever beam cannot be obtained from elementary beam theory since basic assumptions are no longer valid. The elementary theory includes specific simplifications e.g. in the consideration of curvature derivatives, and provides no correction for the shortening of the moment arm as the loaded end of the beam deflects. For large finite loads, it gives deflections greater than the length of the beam [11].

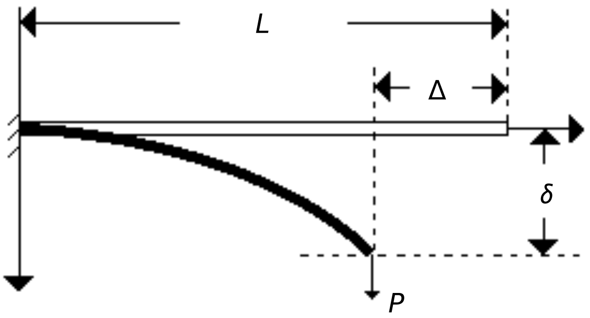

Figure 10.2: Problem Definition

The mathematical treatment of the equilibrium of cantilever beams does not involve great difficulty. Nevertheless, unless small deflections are considered, an analytical solution does not exist, since for large deflections a differential equation with nonlinear terms must be solved. The problem is said to involve geometrical nonlinearity [12]. Therefore in order to account for this nonlinear term, third order theory is performed, where the equilibrium is established at the deformed configuration (geometrically nonlinear analysis).

10.3 Model and Results

A circular pipe with cross-section of outer diameter $0.2\,m$ and wall thickness $0.01\,m$ is used, so that the beam is moderately slender. This type of problem becomes considerably more difficult numerically as the slenderness ratio increases [13]. The finite element model consists of twenty elements. The properties of the model are defined in Table 10.1.

Table 10.1: Model Properties

Material Properties	Geometric Properties	Loading
$E = 100\,MPa$	$l = 10\,m$	$P = 269.35\,N$
	$D = 0.2\,m$	
	$t = 0.01\,m$	

As an alternative, the structure is analysed with quad plane elements with a cross-section of the same stiffness as the circular, in order to achieve the same results and compare the behaviour of the two types of elements. The quad cross-section has a width of $0.3\,m$ and a thickness of $0.10261\,m$, and therefore the same moment of inertia $I = 2.701\ m^{-5}$ as the one of the circular cross-section. Results for both models are presented in Table 10.2. Figure 10.3 shows the deflection of the beam for the two analysed models. Figure 10.4 presents the results, in terms of the motion of the tip of the cantilever, where they are compared to the exact solution for the inextensible beam, as given by Bisshopp and Drucker [11].

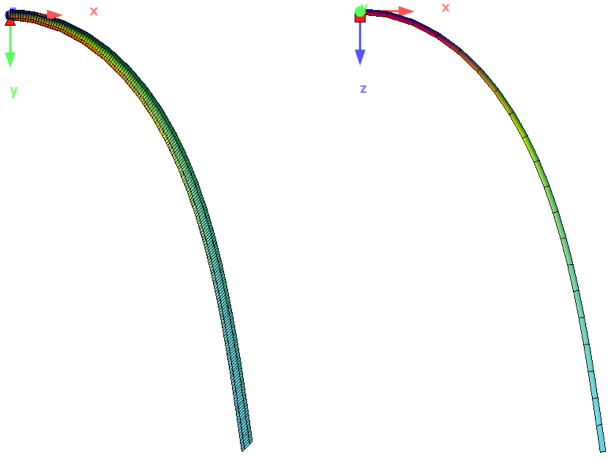

Figure 10.3: Deformed structure: a) Beam elements b) Quad elements

Table 10.2: Results

	Beam	Quad
$\delta[m]$	8.113	8.102
$\Delta[m]$	5.545	5.539

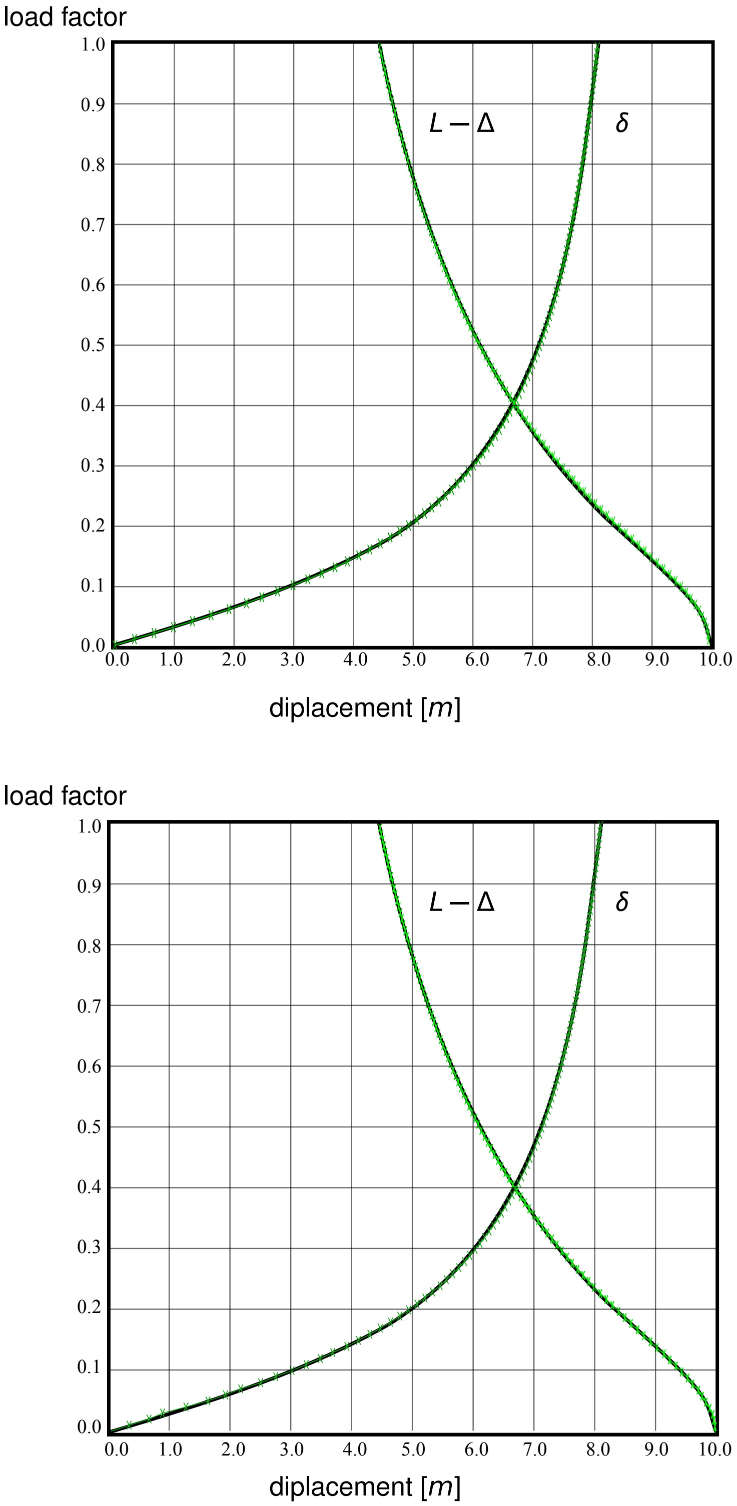

Figure 10.4: Load - Deflection: (a). Beam elements (b). Quad elements

10.4 Conclusion

This benchmark shows the classical problem of a cantilever beam undergoing large deformations under the action of a vertical load at the tip. Results are presented in terms of the motion of the tip of the cantilever where the accuracy of the solution is apparent.

10.5 Literature

[11] K. E. Bisshopp and D. C. Drucker. “Large Deflection of Cantilever Beams”. In: *Quarterly of Applied Mathematics* 3 (1945), pp. 272–275.
[12] T. Beléndez, C. Neipp, and A. Beléndez. “Large and Small Deflections of a Cantilever Beam”. In: *European Journal of Physics* 23.3 (2002), pp. 371–379.
[13] *Abaqus Benchmarks Manual 6.10*. Dassault Systémes Simulia Corp. 2010.

11 BE8: Large Deflection of Cantilever Beams II

Overview

Element Type(s):	B3D, SH3D
Analysis Type(s):	STAT, GNL
Procedure(s):	LSTP
Topic(s):	
Module(s):	ASE
Input file(s):	moment_beam.dat, moment_quad.dat

11.1 Problem Description

The cantilever beam of Benchmark Example No. 7 is analysed here for a moment load, as shown in Fig. 11.1, with both beam and quad plane elements. The accuracy of the elements is evaluated through the deformed shape of the beam retrieved by limit load iteration procedure.

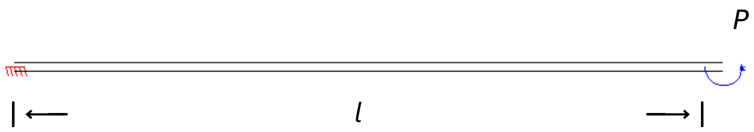

Figure 11.1: Model Properties

11.2 Reference Solution

The classical problem of deflection of a cantilever beam of linear elastic material, is here extended for the case of a moment applied at the beam tip. The concentrated moment causes the beam to wind around itself, i.e. deflect upwards and bend towards the built-in end. The analytical solution can be derived from the fundamental Bernoulli-Euler theory, which states that the curvature of the beam at any point is proportional to the bending moment at that point [14]. For the case of pure bending, the beam will bend into a circular arc of curvature R

$$R = \frac{EI}{M}, \tag{11.1}$$

and will wind n times around itself [13]

$$\frac{ML}{EI} = 2\pi n, \tag{11.2}$$

where I is the moment of inertia, E the Elasticity modulus and M the concentrated moment applied at the tip.

11.3 Model and Results

The properties of the two models analysed are defined in Table 11.1. For the moment load, the deformed shape of the structure for quad elements at various increments throughout the steps, are shown in Fig.

11.2. According to the analytical solution and the moment load applied, the cantilever is expected to wind around itself $n = 2$.

Table 11.1: Model Properties

Material Properties	Geometric Properties Beam elements	Geometric Properties Quad elements	Loading
$E = 100\,MPa$	$l = 10\,m$	$l = 10\,m$	$M = 3.38478\,kNm$
	$D = 0.2\,m$	$B = 0.3\,m$	
	$t = 0.01\,m$	$t = 0.10261\,m$	

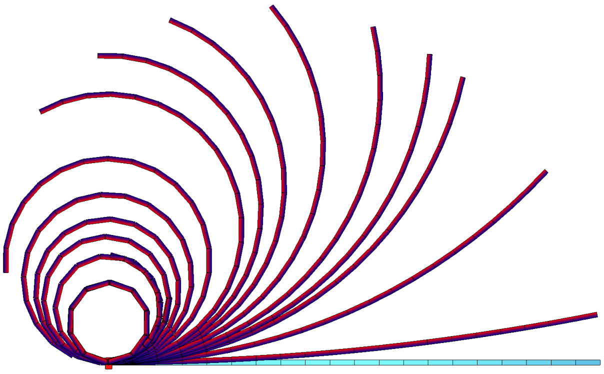

Figure 11.2: Deformed Structure - Quad Elements

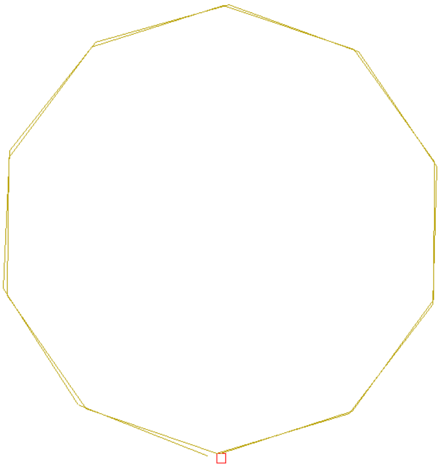

Figure 11.3: Final Deformed Shape of Cantilever with Quad Elements

Figure 11.4 presents the load - deflection curve for the horizontal and vertical direction for the two cases. From the final deformed shape of the beam (Fig. 11.3), it is evident that the cantilever achieves $n \approx 2$, which can also be observed at the second load-deflection curve where the vertical displacement becomes zero twice.

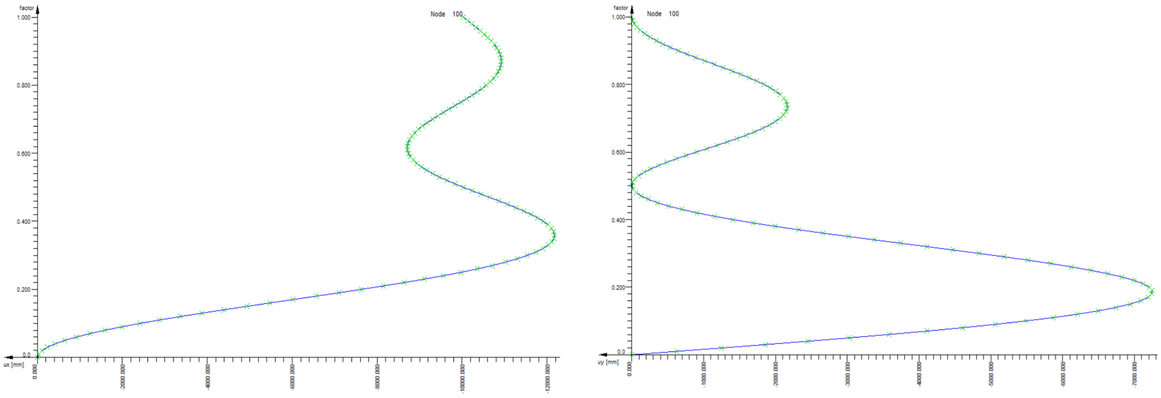

Beam Elements

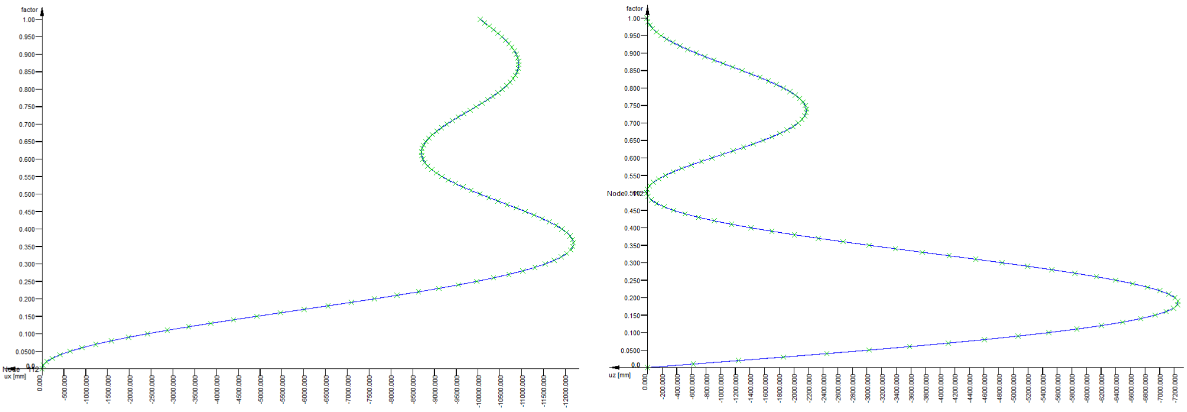

Quad Elements

Figure 11.4: Load - Deflection Curve

11.4 Conclusion

This benchmark shows the classical problem of a cantilever beam undergoing large deformations under the action of a moment load applied at the tip. The accuracy of the deformation solution for the quad and beam elements is evident.

11.5 Literature

[13] *Abaqus Benchmarks Manual 6.10*. Dassault Systémes Simulia Corp. 2010.
[14] A. A. Becker. *Background to Finite Element Analysis of Geometric Non-linearity Benchmarks*. Tech. rep. NAFEMS, 1998.

12 BE9: Verification of Beam and Section Types I

Overview

Element Type(s): B3D
Analysis Type(s): STAT
Procedure(s):
Topic(s):
Module(s): AQUA
Input file(s): cross_sections_FEM.dat,cross_sections_BEM.dat

12.1 Problem Description

In this Benchmark different cross-section types are investigated, in order to test the properties of each cross-section associated with their definition in AQUA module. The analysed non-tabulated and tabulated cross sections are shown in Figures 12.1 and 12.2, respectively.

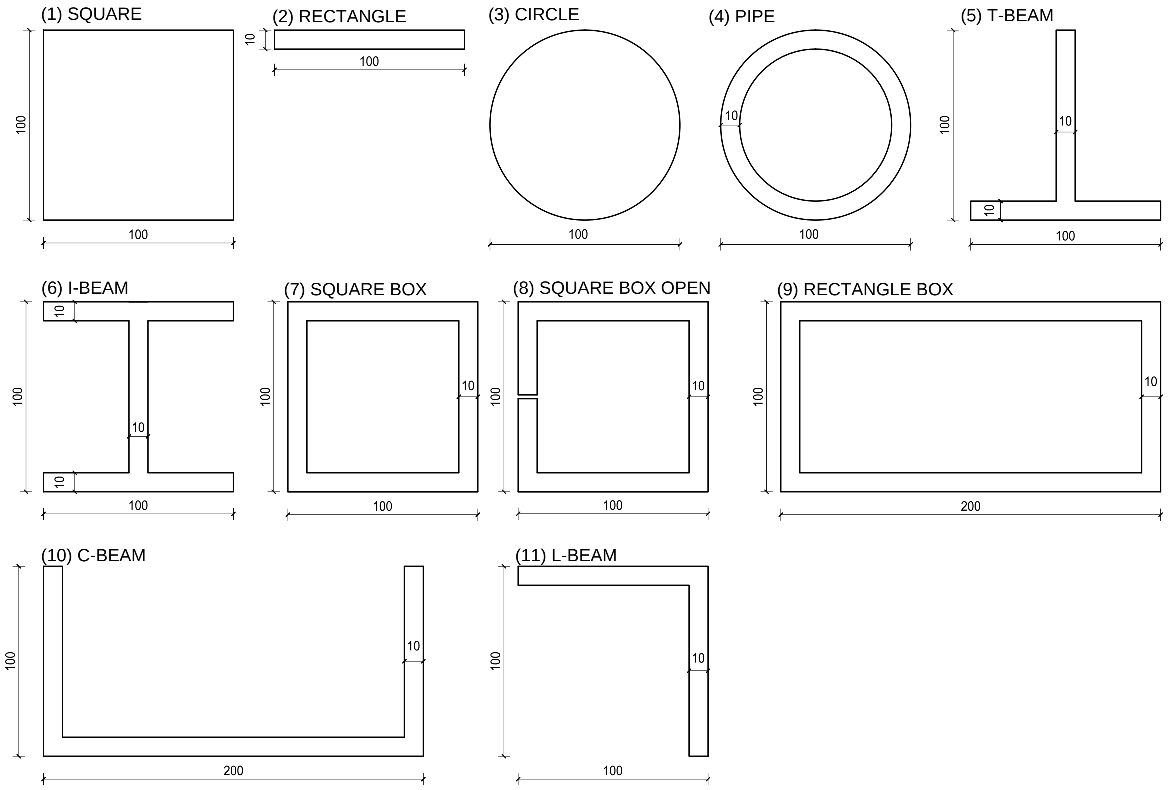
(1) SQUARE
100
100
(2) RECTANGLE
10
100
(3) CIRCLE
100
(4) PIPE
10
100
(5) T-BEAM
100
10
10
100
(6) I-BEAM
10
100
10
10
100
(7) SQUARE BOX
100
10
100
(8) SQUARE BOX OPEN
100
10
100
(9) RECTANGLE BOX
100
10
200
(10) C-BEAM
100
10
200
(11) L-BEAM
100
10
100

Figure 12.1: Non-tabulated Cross Sections

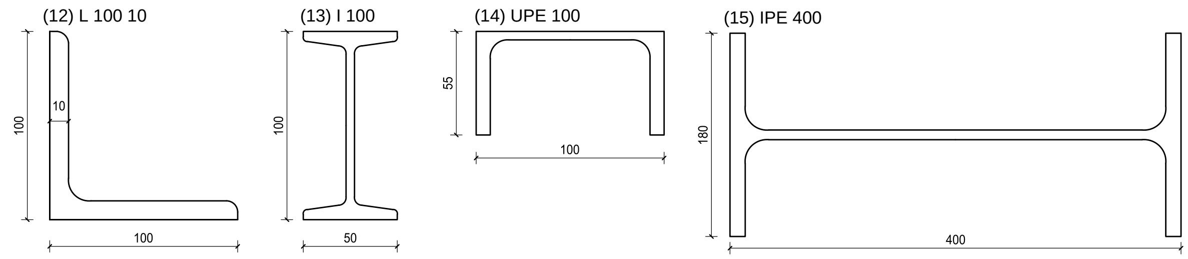

Figure 12.2: Tabulated Cross Sections

12.2 Reference Solution

The important values of a cross-section for the simple cases of bending and torsion are the moment of inertia and the torsional moment, respectively. The analytical solution for the moment of inertia I_y with respect to y axis is [5]:

$$I_y = \int_A z^2 dA, \tag{12.1}$$

in which each element of area dA is multiplied by the square of its distance from the z-axis and the integration is extended over the cross-sectional area A of the beam (Fig. 12.3). The torsional moment I_T is more complicated to compute and depends on the cross-sections geometry. For circular cross-sections is:

$$I_T = \int_A r^2 dA, \tag{12.2}$$

For thick-walled non-circular cross-sections, it depends on the warping function. Tabulated formulas are given in all relevant handbooks for the most common geometries [15]. For closed thin-walled non-circular cross-sections I_T is [10]:

$$I_T = \frac{4A_m^2}{\sum_{i=1}^{n} \frac{s_i}{t_i}}, \tag{12.3}$$

and for open thin-walled non-circular cross-sections is:

$$I_T = \frac{1}{3} \sum_{i=1}^{n} s_i t_i^3, \tag{12.4}$$

where A_m is the area enclosed from the center line of the wall (Fig. 12.3), and t_i, s_i the dimensions of the parts from which the cross-section consists of. For the specific case of an I-cross-section, another approximate formula can be utilised, as defined by Petersen [10]:

$$I_T = 2\frac{1}{3}\, b\, t^3 \left(1 - 0.630\, \frac{t}{b}\right) + \frac{1}{3}\,(h - 2t)\, s^3 + 2\, \alpha\, D^4, \tag{12.5}$$

where s, t and D are described in Fig. 12.3 and α is extracted from the corresponding diagram, given in [10], w.r.t. the cross-section properties. For the same cross-section but according to Gensichen, I_T is accordingly computed as:

$$I_T = 2\frac{1}{3}\, b\, t^3 \left(1 - 0.630\,\frac{t}{b}\right) + \frac{1}{3}\,(h - 2t)\, s^3 + 0.29\,\frac{s}{t}\left[\frac{\left(\frac{s}{2}\right)^2 + t^2}{t}\right]^4 \tag{12.6}$$

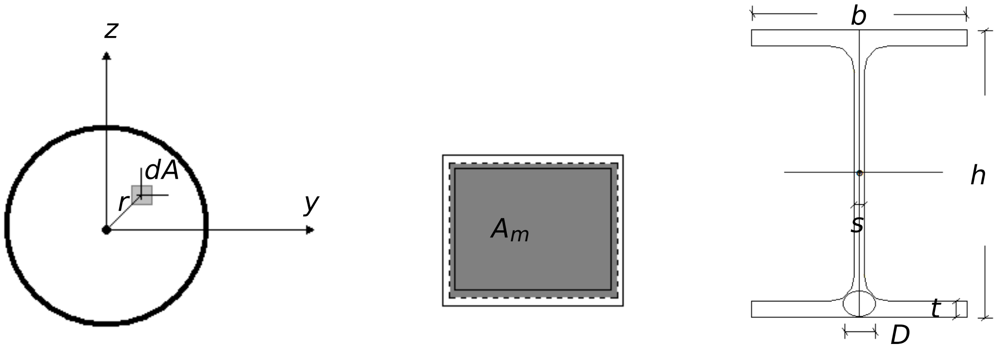

Figure 12.3: Cross-Sectional Properties

12.3 Model and Results

The properties of different cross-sections, analysed in this example, are defined in Table 12.1. The cross-sections types are modelled in various ways in AQUA and compared. For differentiation between them, the modelling type is specified next to the name of each cross-section. The cross-sectional properties of the thick walled sections are computed by implementing the finite element method (FEM).

Table 12.1: Cross-Sections Properties

Material Properties	Cross-sectional Properties
$E = 30\,MPa$	$b = 100\,mm$
$\nu = 0.3$	$h = 100\,mm$
	$t = 10\,mm$
	$D = 100\,mm$

Table 12.2: Results

		$I_y\ [cm^4]$	$\lvert e_r \rvert$		$I_T\ [cm^4]$	$\lvert e_r \rvert$
Type	SOF.	Ref.	[%]	SOF.	Ref.	[%]
(1) Square -srec	833.33	833.33	0.00	1405.78	1400.00 (12.4)	0.41
(2) Rectangle -srec	0.83	0.83	0.00	3.12	3.13 (12.4)	0.22
(3) Circle -scit	490.87	490.87	0.00	981.75	981.75 (12.4)	0.00
(3) Circle -tube	490.87	490.87	0.00	981.75	981.75 (12.4)	0.00

Table 12.2: (continued)

	I_y $[cm^4]$		$\lvert e_r \rvert$	I_T $[cm^4]$		$\lvert e_r \rvert$
Type	SOF.	Ref.	[%]	SOF.	Ref.	[%]
(4) Pipe -scit	289.81	289.81	0.00	579.62	579.62 (12.4)	0.00
(4) Pipe -tube	289.81	289.81	0.00	579.62	579.62 (12.4)	0.00
(5) T-beam -poly	180.00	180.00	0.00	6.37	6.33 (12.4)	0.63
(5) T-beam -plat	181.37	182.82	0.79	6.50	6.50 (12.4)	0.00
(6) I-beam -poly	449.33	449.33	0.00	9.67	9.33 (12.4)	3.64
					9.62 (12.6)	0.52
					9.21 (12.5)	4.99
(6) I-beam -plat	465.75	467.42	0.36	9.67	9.33 (12.4)	3.64
(6) I-beam -weld	447.67	449.33	0.37	9.33	9.33 (12.4)	0.00
(7) Square box -poly	492.00	492.00	0.00	796.78	729.00 (12.4)	9.30
				772.34[1]	729.00 (12.4)	5.95
(7) Square box -plat	486.00	487.50	0.31	741.00	729.00 (12.4)	1.65
(8) Square box open -plat	486.00	487.50	0.31	11.98	12.00 (12.4)	0.17
(9) Rectang. box -poly	898.67	898.67	0.00	2221.56	2088.64 (12.4)	6.36
				2168.44[1]	2088.64 (12.4)	3.82
(9) Rectang. box -plat	891.00	889.17	0.21	2107.31	2088.64 (12.4)	0.89
(10) C-beam -poly	2292.67	2292.67	0.00	12.76	12.67 (12.4)	0.73
(10) C-beam -plat	2286.33	2287.92	0.07	12.67	12.67 (12.4)	0.0
(11) L-beam -poly	180.00	180.00	0.00	6.26	6.33 (12.4)	1.22
(11) L-beam -weld	179.25	180.00	0.42	6.33	6.33 (12.4)	0.0
(11) L-beam -plat	178.62	179.40	0.44	6.33	6.33 (12.4)	0.0
(12) L 100 10 (tabulated)	176.66	177.0 [16]	0.19	6.85	6.33 [17]	8.19
(13) I 100 (tabulated)	170.38	171.0 [16]	0.36	1.52	1.60 [16]	4.93
		170.3 [17]	0.05		1.511 [17]	0.67
(14) UPE 100 (tabulated)	206.90	207.0 [16]	0.05	2.02	1.99 [16]	1.56
		206.9 [17]	0.00		2.01 [17]	0.55
(15) IPE 400 (tabulated)	23129.58	23130 [16]	0.00	50.50	51.40 [16]	1.75

Table 12.2: (continued)

Type	I_y $[cm^4]$ SOF.	Ref.	$\lvert e_r \rvert$ [%]	I_T $[cm^4]$ SOF.	Ref.	$\lvert e_r \rvert$ [%]
		23128 [17]	0.01		50.41 [17]	0.18

1	Calculated with a finer mesh: HDIV 2[mm]

From the results in Table 12.2 we can see that for the definition of general cross-sections the use of -POLY option gives the exact values for I_y. When evaluating the results of the torsional moment of inertia I_T, it has to be taken into consideration, that the presented reference solutions in Sect. 12.2, for all non-circular cross-sections, are approximate and various assumptions are taken according to the adopted theory. For the case of the I-beam, it is observed in Table 12.2, that the relative error ranges between 4.99 % and 0.52 %.

For the definition of thin-walled cross-sections the use of -PLAT gives very good results for I_T whereas for the determination of I_y some deviations appear. This is due to the fact that in order for the cross-section to be connected for shear, some parts of the plates overlap at the connections giving an additional moment of inertia around the y-axis. This can be seen at Fig. 12.4 for the I beam. It can be avoided if the -PLAT option is used without overlapping of parts but in combination with -WELD in order to ensure the proper connection of the plates. This can be seen from the results for the I- and L-beam which are analysed for the three options -POLY, -PLAT, -PLAT and -WELD.

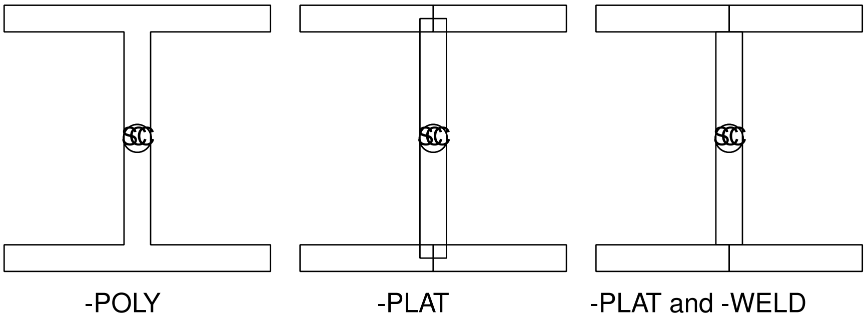

Figure 12.4: Definition types of I-beam

12.3.1 Comparison of numerical approaches for thick walled cross sections

The torsional moment of inertia is additionally calculated for the thick walled non-circular cross sections by using the boundary element method (BEM). The computed values are compared with the results obtained from the FEM method and with the reference values in Table 12.3.

Table 12.3: Torsional moment of inertia calculated by using the boundary element method (BEM) and the finite element method (FEM)

Type	I_t $[cm^4]$ SOF. BEM	SOF. FEM	Ref.	$\lvert e_r \rvert$ BEM/FEM [%]
(5) T-beam -poly	6.45	6.37	6.33 (12.4)	1.89/0.63

Table 12.3: (continued)

	I_t $[cm^4]$			$\lvert e_r \rvert$ BEM/FEM
Type	SOF. BEM	SOF. FEM	Ref.	[%]
(6) I-beam -poly	9.52	9.67	9.33 (12.4)	2.00/3.64
			9.62 (12.6)	1.04/0.52
			9.21 (12.5)	3.36/4.99
(7) Square box -poly	771.96	772.34[1]	729.00 (12.4)	5.89/5.94
(9) Rectang. box -poly	2171.77	2168.44[1]	2088.64 (12.4)	3.98/3.82
(10) C-beam -poly	13.29	12.76	12.67 (12.4)	4.90/0.73
(11) L-beam -poly	6.35	6.26	6.33 (12.4)	0.21/1.22
(12) L 100 10 (tabulated)	6.95	6.85	6.33 [17]	9.81/8.19
(13) I 100 (tabulated)	1.51	1.52	1.60 [16]	5.55/4.93
			1.511 [17]	0.01/0.67
(14) UPE 100 (tabulated)	2.04	2.02	1.99 [16]	2.76/1.56
			2.01 [17]	1.74/0.55
(15) IPE 400 (tabulated)	51.04	50.50	51.40 [16]	0.71/1.75
			50.41 [17]	1.24/0.18

[1] Calculated with a finer mesh: HDIV 2[mm]

12.3.2 Convergence of the thick walled sections (FEM-BEM) in regard to the thin-walled theory

The reference values for the open sections I, L, C, T-beam are computed with respect to the thin-walled theory reference solution (Eq. 12.4). Therefore for the calculated values with -POLY (FEM and BEM), which do not correspond to the thin-walled theory, deviations appear. If we now make a convergence study, for the case of the I-beam, decreasing the thickness of the cross-section and comparing it to the thin-walled reference solution, we will observe that the deviation is vanishing as we approach even thinner members. This is presented in Fig. 12.5 for an I-beam, where the absolute difference of the calculated from the reference value is depicted for the decreasing thickness values. The results obtained with -POLY (FEM) are presented in Fig. 12.5 with three different mesh sizes: default mesh, 25% and 50%finer mesh.

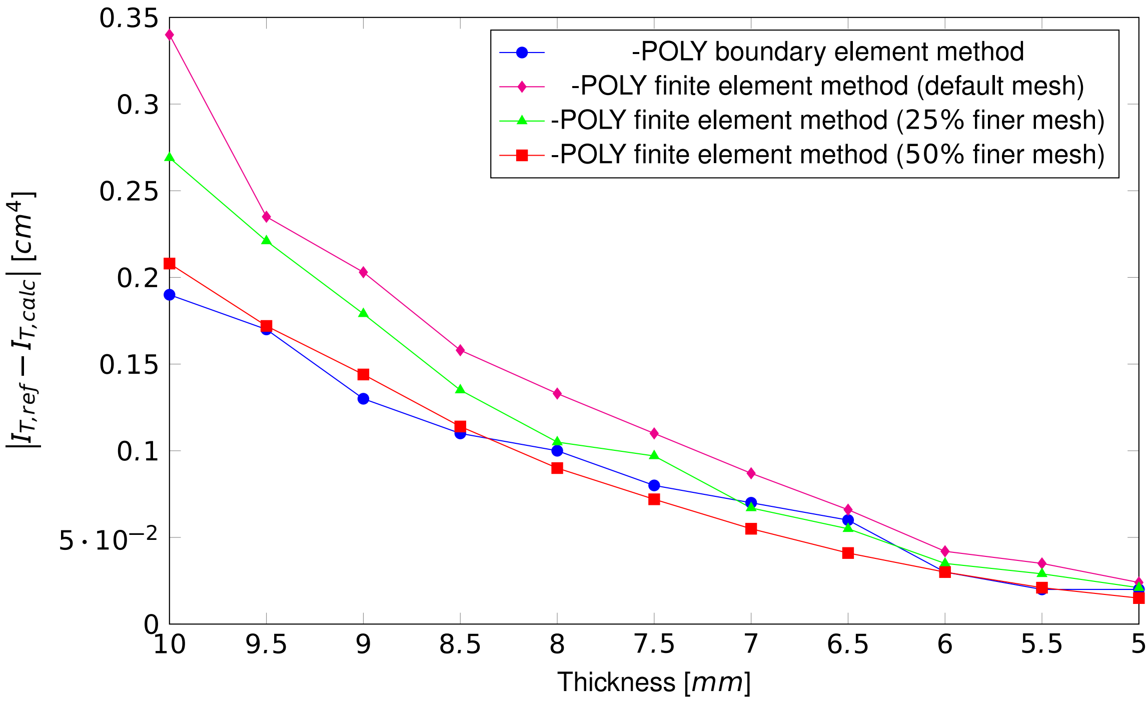

Figure 12.5: Convergence of I-beam

For the case of open thin-walled non-circular cross-sections, modelled with -PLAT, we can observe that I_T matches exactly the reference solution. For closed thin-walled non-circular cross-sections though, some deviations arise. If we take a closer look at the case of the square box, at first glance it appears to be not accurate enough, since the calculated value is $741.00\ cm^4$ and the reference is $729.00\ cm^4$ (Table 12.2). The difference between them is 741.00 - 729.00 = $12\ cm^4$, which corresponds to the reference value of the open square box. This is due to the fact, that the reference solution for this type of sections given by Eq. 12.3, corresponds to the thin-walled theory and assumes a constant distribution of shear stresses over the thickness of the cross-section. However, SOFiSTiK assumes a generalised thin-walled theory, where the shear stresses due to torsion, are distributed linearly across the thickness, as shown in Fig. 12.6, and thus holds:

$$I_{T_{generalised\,thin-walled\,theory}} = I_{T_{closed,SOFiSTiK}} = I_{T_{closed,thin-walled\,theory}} + I_{T_{open,thin-walled\,theory}} \tag{12.7}$$

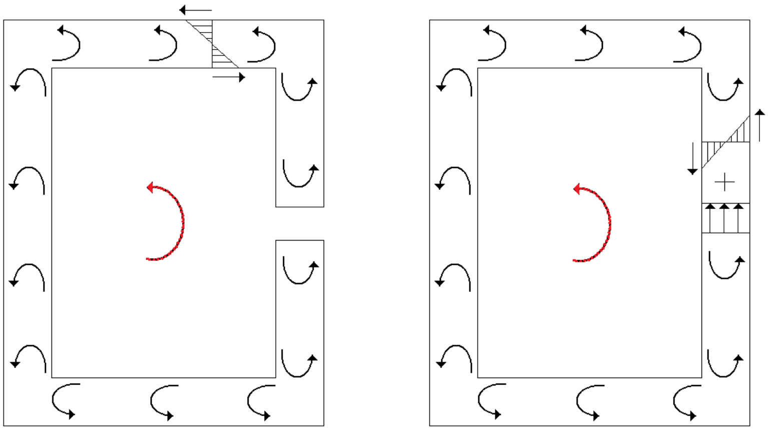

Open Closed

Figure 12.6: Distribution of Stresses

Eq. 12.7 is satisfied exactly for the square box cross-section and it can be visualised in Fig. 12.7 by the purple line for decreasing thicknesses, whereas the blue line denotes the deviation of the calculated values with respect to the $I_{T_{closed,thin-walled\,theory}}$.

For the same cross-section, but now modelled with -POLY, it is evident that the difference from the reference solution is larger, reaching the value of 5.89 %, as presented by the green line. This is due to the fact that except from the difference in the stresses consideration, as explained above, the thin-walled assumption is also engaged. If we do a convergence study for this cross-section, and compared it to the one modelled with -PLAT, represented by the red line, we will observe that as the thickness decreases the deviation curves gradually coincide.

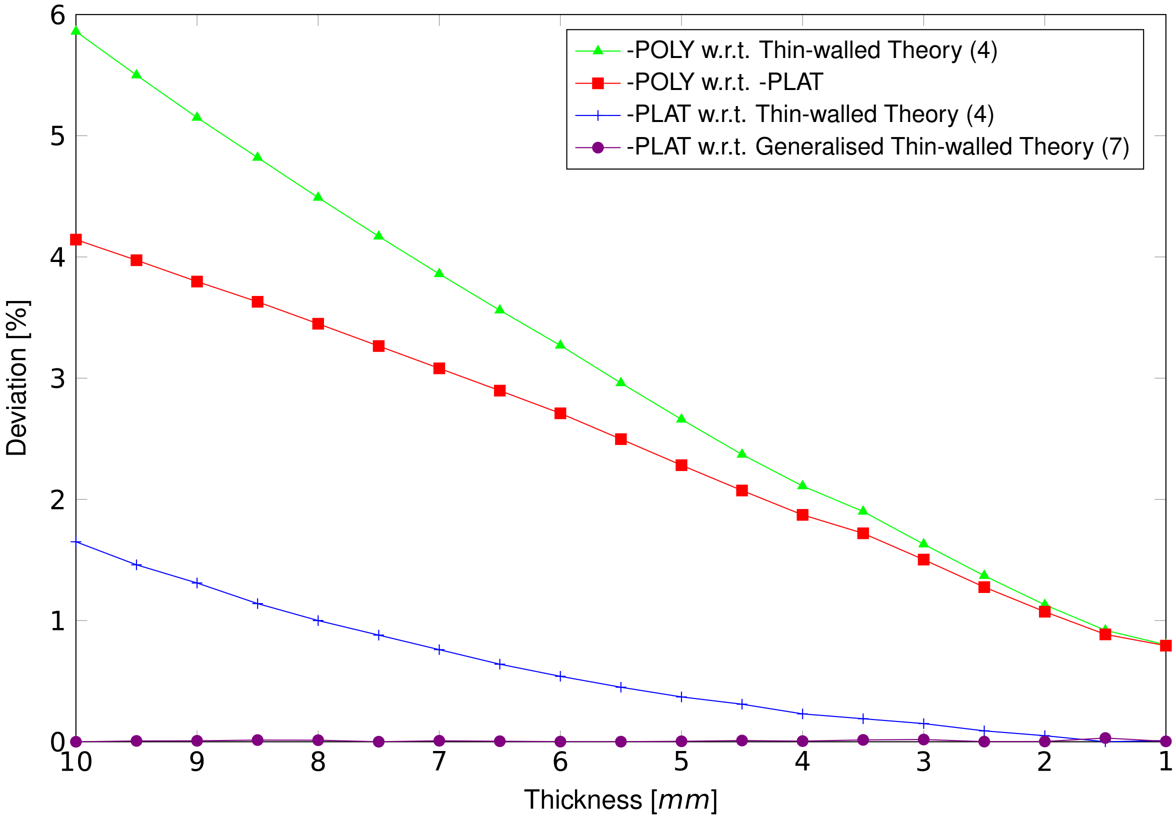

Figure 12.7: Convergence of Square Box

12.4 Conclusion

This example presents the different cross-sections and their properties according to their definition in AQUA. It has been shown that the properties of the cross-sections can be adequately captured irrelevantly of their definition with small deviations from the exact solution.

12.5 Literature

[5] S. Timoshenko. *Strength of Materials, Part I, Elementary Theory and Problems*. 2nd. D. Van Nostrand Co., Inc., 1940.
[10] C. Petersen. *Stahlbau*. 2nd. Vieweg, 1990.
[15] K. Holschemacher. *Entwurfs- und Berechnungstafeln für Bauingenieure*. 3rd. Bauwerk, 2007.
[16] M. Schneider-Bürger. *Stahlbau-Profile*. 24th. Verlag Stahleisen, 2004.
[17] R. Kindmann, M. Kraus, and H. J. Niebuhr. *Stahlbau Kompakt, Bemessungshilfen, Profiltabellen*. Verlag Stahleisen, 2006.

13 BE10: Verification of Beam and Section Types II

Overview

Element Type(s):	B3D
Analysis Type(s):	STAT
Procedure(s):	
Topic(s):	
Module(s):	ASE
Input file(s):	cross_sections_ii_FEM.dat, cross_sections_ii_BEM.dat

13.1 Problem Description

The problem consists of a cantilever beam as shown in Fig. 13.1. For the first case analysed, a transverse load is applied at the end of the beam. For the second case, a moment is applied around the x axis. The various cross-section types analysed in Benchmark Example 9 are used, in order to test the behaviour of the beam associated with each of the section definitions.

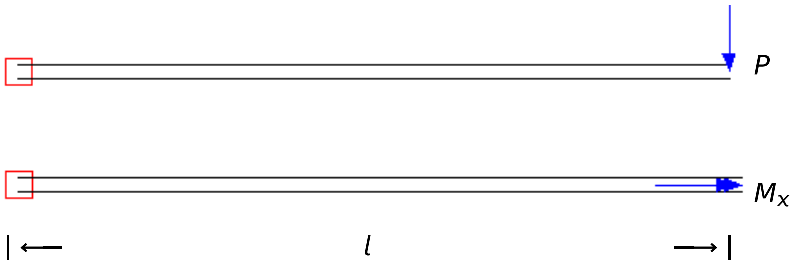

Figure 13.1: Problem Description

13.2 Reference Solution

For a Bernoulli beam and a linear elastic material behaviour, the maximum deflection δ_{max} of the cantilever, under the action of a transverse load P, occurs at the tip and is [15]:

$$\delta_{max} = \frac{PL^3}{3EI}, \tag{13.1}$$

and the rotation ϕ_z

$$\phi_z = \frac{PL^2}{2EI}. \tag{13.2}$$

For the case of the moment M, applied at the x-axis the angle of twist ϕ_x is [10]:

$$\phi_x = \frac{ML}{GI_T}, \tag{13.3}$$

where G is the shear modulus, EI the flexural rigidity and I_T the torsional moment.

13.3 Model and Results

The properties of the model and the cross-sections analysed, are defined in Table 13.1. For all cross-sections the shear deformation areas A_y and A_z are given equal to zero, in order to consider a Bernoulli beam formulation which doesn't account for shear deformations.

Table 13.1: Model Properties

Material Properties	Cross-sectional Properties	Loading
$E = 30\,MPa$	$L = 1\,m$	$P = 1\,kN$
$\nu = 0.3$	$h = 100\,mm$	$M = 1\,kNm$
	$t = 10\,mm$	
	$b = 100\,mm$	
	$D = 100\,mm$	

Table 13.2: Results Case 1

		$u_y\ [m]$	$\lvert e_r \rvert$		$\phi_z\ [mrad]$	$\lvert e_r \rvert$
Type	SOF.	Ref.	[%]	SOF.	Ref.	[%]
square -srec	1.333	1.333	0.00	2.000	2.000	0.00
rectangular -srec	1333.333	1333.333	0.00	2000.000	2000.000	0.00
circul -scit	2.264	2.264	0.00	3.395	3.395	0.00
circul -tube	2.264	2.264	0.00	3.395	3.395	0.00
pipe -scit	3.834	3.834	0.00	5.751	5.751	0.00
pipe -tube	3.834	3.834	0.00	5.751	5.751	0.00
Tbeam -poly	6.173	6.173	0.00	9.259	9.259	0.00
Tbeam -plat	6.126	6.078	0.80	9.189	9.116	0.80
Ibeam -poly	2.473	2.473	0.00	3.709	3.709	0.00
Ibeam -plat	2.386	2.377	0.36	3.578	3.566	0.36
Ibeam -weld	2.482	2.473	0.37	3.723	3.709	0.37
square box -poly	2.258	2.258	0.00	3.388	3.388	0.00
square box -plat	2.286	2.279	0.31	3.429	3.419	0.31
square box open -plat	2.286	2.279	0.31	3.429	3.419	0.31
rectang. box -poly	1.236	1.236	0.00	1.855	1.855	0.00
rectang. box -plat	1.247	1.250	0.21	1.871	1.874	0.21
C-beam -poly	0.485	0.485	0.00	0.727	0.727	0.00

Table 13.2: (continued)

		$u_y\ [m]$	$\lvert e_r \rvert$		$\phi_z\ [mrad]$	$\lvert e_r \rvert$
Type	SOF.	Ref.	[%]	SOF.	Ref.	[%]
C-beam -plat	0.486	0.486	0.07	0.729	0.728	0.07
L-beam -poly	6.173	6.173	0.00	9.259	9.259	0.00
L-beam -weld	6.199	6.173	0.42	9.298	9.259	0.42
L-beam -plat	6.221	6.193	0.44	9.331	9.290	0.44

The cross-sections types are modelled in various ways in AQUA as shown in Benchmark Example 9. The results are presented in Table 13.2 for the case of the transverse load P and in Table 13.3 for the case of the moment M. For the non-circular cross sections modelled with -POLY, both the results calculated with the boundary element method (BEM) and the finite element method (FEM) are presented in Table 13.3. It should be noted, that the calculated angle of twist for the square and rectangular box cross section modelled with -POLY (FEM), denoted with a star in Table 13.3, corresponds to a relatively coarse default finite element mesh. For the investigated box sections with relatively thin walls, a better approximation in regard to the reference values can be obtained by implementing a finer element mesh.

Table 13.3: Results Case 2

		$\phi_x\ [mrad]$	$\lvert e_r \rvert$
Type	SOF.	Ref.	[%]
square -srec	6.165	6.190	0.41
rectangular -srec	2774.886	2768.903	0.22
circul -scit	8.828	8.828	0.00
circul -tube	8.828	8.828	0.00
pipe -scit	14.952	14.952	0.00
pipe -tube	14.952	14.952	0.00
Tbeam -poly (BEM)	1343.070	1368.421	1.85
Tbeam -poly (FEM)	1359.899		0.62
Tbeam -plat	1333.333	1333.333	0.00
Ibeam -poly (BEM)	910.375	928.571	1.96
Ibeam -poly (FEM)	895.95		3.51
Ibeam -plat	896.552	896.552	0.00
Ibeam -weld	928.571	928.571	0.00
square box -poly (BEM)	11.227	11.888	5.56
square box -poly (FEM - default mesh)	10.886$\star$		8.43
square box -poly (FEM - finer mesh: HDIV 2 [mm])	11.221		5.61

Table 13.3: (continued)

	ϕ_x $[mrad]$		$\lvert e_r \rvert$
Type	SOF.	Ref.	$[\%]$
square box -plat	11.696	11.888	1.62
square box open -plat	723.428	722.222	0.17
rectang. box -poly (BEM)	3.991	4.149	3.83
rectang. box -poly (FEM - default mesh)	3.914⋆		5.67
rectang. box -poly (FEM - finer mesh: HDIV 2 [mm])	3.998		3.64
rectang. box -plat	4.113	4.149	0.89
C-beam -poly (BEM)	652.274	684.211	4.67
C-beam -poly (FEM)	679.255		0.72
C-beam -plat	684.210	684.211	0.00
L-beam -poly (BEM)	1365.51	1368.421	0.21
L-beam -poly (FEM)	1385.289	1368.421	1.23
L-beam -weld	1368.421	1368.421	0.00
L-beam -plat	1368.421	1368.421	0.00

From the above results, and with respect to the results of Benchmark Example 9, we can see that the differences are a direct influence of the calculations of the properties of the cross-sections according to their definition in AQUA, and are not associated to the beam formulation. This can also be verified, if instead of, e.g. the reference value for $I_{y_{REF}}$, the calculated value is used $I_{y_{CALC}}$ in Eq. 13.1 . Then the error is eliminated for all the cross-sections types.

13.4 Conclusion

This example presents the influence of the cross-sections types, for the case of a simple cantilever beam. It has been shown that the behaviour of the beam is accurately captured.

13.5 Literature

[10] C. Petersen. *Stahlbau*. 2nd. Vieweg, 1990.
[15] K. Holschemacher. *Entwurfs- und Berechnungstafeln für Bauingenieure*. 3rd. Bauwerk, 2007.

14 BE11: Plastification of a Rectangular Beam

Overview

Element Type(s):	B3D, BF2D, SH3D
Analysis Type(s):	STAT, MNL
Procedure(s):	LSTP
Topic(s):	
Module(s):	ASE, STAR2, TALPA
Input file(s):	beam_star2.dat, fiber_beam.dat, quad.dat

14.1 Problem Description

The problem consists of a rectangular cantilever beam, loaded in pure bending as shown in Fig. 14.1. The model [18] is analysed for different load levels, including the capacity limit load, where the cross-section fully plastifies. The beam is modelled and analysed with different elements and modules.

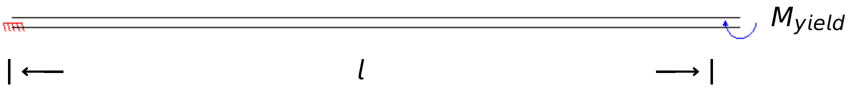

Figure 14.1: Problem Description

14.2 Reference Solution

The model follows an elastic-perfectly-plastic stress-strain behaviour as shown in Fig. 14.2. Under this assumption, the beam remains elastic until the outermost fibers reach the yield stress. The corresponding limit load can be calculated as:

$$M_{yield} = \frac{\sigma_{yield}\, bh^2}{6}, \tag{14.1}$$

where σ_{yield} is the yield stress, b and h the dimensions of the beam. The cross-section fully plastifies when the load reaches $M = M_{ult} = 1.5 \times M_{yield}$, where all fibers of the beam are in condition of yielding [6].

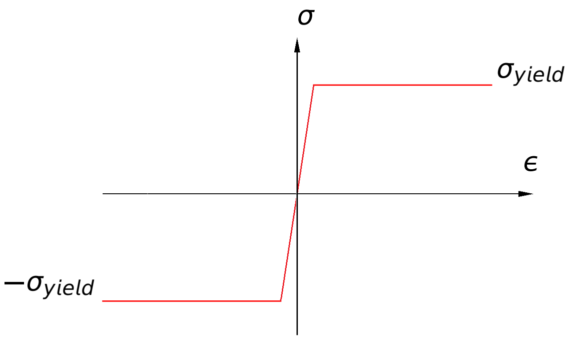

Figure 14.2: Stress-Strain Curve

14.3 Model and Results

The properties of the model are defined in Table 14.1. A standard steel material is used and modified accordingly to account for the intended elastic-perfectly-plastic material behaviour.

Table 14.1: Model Properties

Material Properties	Geometric Properties	Loading
$E = 210000\,MPa$	$L = 1\,m$	$M_{yield} = 280\,Nm$
$\nu = 0.3$	$h = 20\,mm$	
$\sigma_{yield} = 420\,MPa$	$b = 10\,mm$	

The structure is modelled and analysed in various ways. For the first case the fiber beam is used (TALPA), where the cross-section is discretised into single fibers and directly integrates the continuum mechanical material reaction into beam theory, and physically nonlinear analysis is performed. For the second case the standard beam elements are used and the model is analysed with STAR2 where a nonlinear stress and strain evaluation determination is performed. For the third case, the quad elements are used and a nonlinear analysis is done with ASE. The results are presented in Table 14.2 for the three cases.

Table 14.2: Results

M/M_{yield}	Fiber Beam	Standard Beam	Quad		Ref.
	σ $[MPa]$	σ $[MPa]$	σ	σ_{eff}	
0.99	415.80	415.80	415.80	415.80	$\sigma < 420.00$ Fully Elastic
1.00	≤ 420	≤ 420	≤ 420	≤ 420	$\sigma \leq 420.00$ First Yield
1.48	≤ 420	≤ 420	≤ 431.0	≤ 420	$\sigma \leq 420.00$ Elastic-Plastic
1.50	Fully-Plastic	Fully-Plastic No Convergence	Fully-Plastic No Convergence		$\sigma = 420.00$ Fully-Plastic
1.51	Fully-Plastic No Convergence	Fully-Plastic No Convergence	Fully-Plastic No Convergence		Fully-Plastic No Convergence

This benchmark is designed to test elastic-plastic material behaviour under uniaxial loading conditions. From the above results, it is evident that both beam element formulations adequately reproduce the intended behaviour. Fig. 14.3 shows the distribution of stresses for the case of the fiber beam with $M/M_{yield} = 0.99$, 1.0 and 1.5. For the quad element, the stress appears to exceed the limit value of $420\,MPa$. This is due to the fact that, as the plasticity involves at the cross-section, plastic strains also appear in the lateral direction. This causes a biaxial stress state, which is not neglected by the quad formulation, as shown in Fig. 14.4 for $M/M_{yield} = 1.0$ and 1.48. A closer look at the list of results though, reveals that the `effective stresses` do not exceed the σ_{yield}.

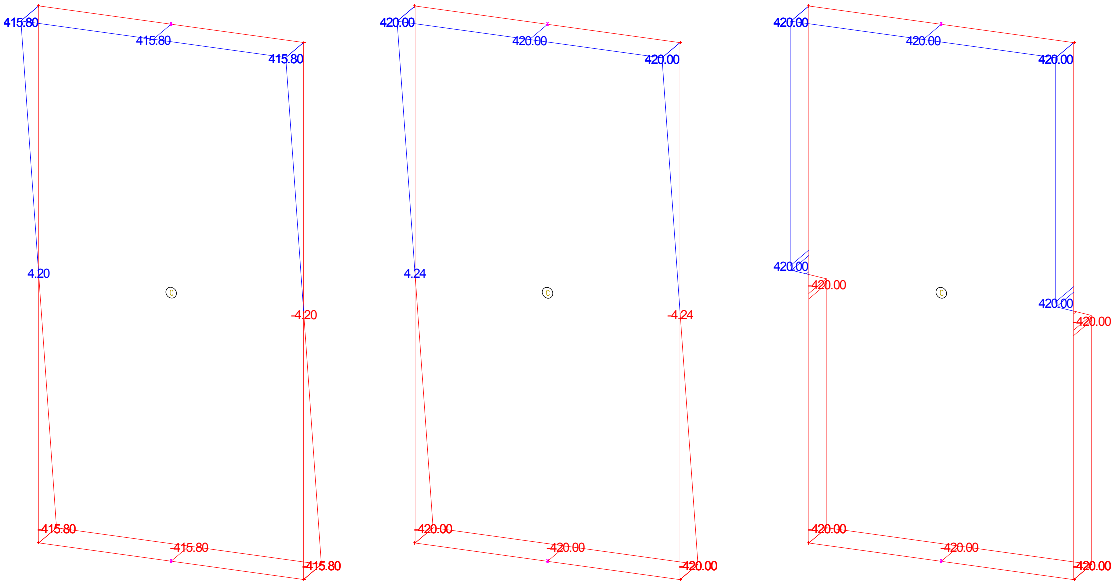
415.80
415.80
415.80
4.20
-4.20
-415.80
-415.80
-415.80
420.00
420.00
420.00
4.24
-4.24
-420.00
-420.00
-420.00
420.00
420.00
420.00
420.00
-420.00
420.00
-420.00
-420.00
-420.00
-420.00

Figure 14.3: Fiber Beam Stress State

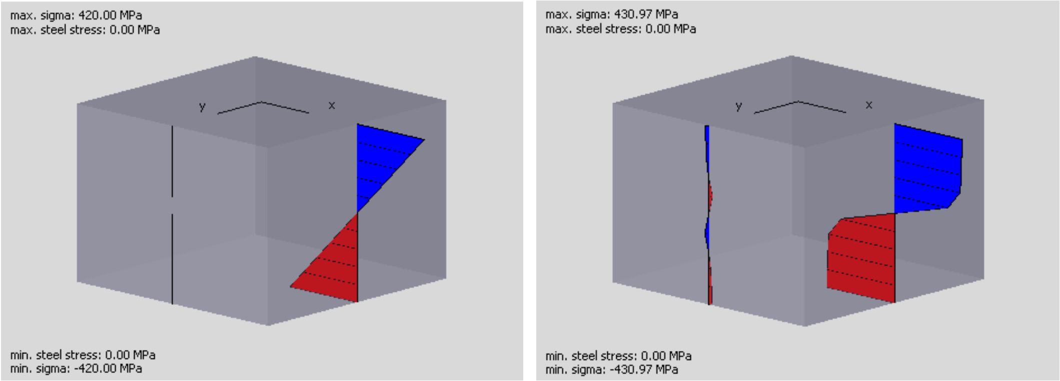
max. sigma: 420.00 MPa
max. steel stress: 0.00 MPa
min. steel stress: 0.00 MPa
min. sigma: -420.00 MPa

max. sigma: 430.97 MPa
max. steel stress: 0.00 MPa
min. steel stress: 0.00 MPa
min. sigma: -430.97 MPa

Figure 14.4: Quad Stress State

14.4 Conclusion

This example presents the pure bending of beams beyond their elastic limit for a non elastic material. It has been shown that the behaviour of the beam is accurately captured for all three modelling options.

14.5 Literature

[6] S. Timoshenko. *Strength of Materials, Part II, Advanced Theory and Problems*. 2nd. D. Van Nostrand Co., Inc., 1940.
[18] *Verification Manual for the Mechanical APLD Application, Release 12.0*. Ansys, Inc. 2009.

15 BE12: Cantilever in Torsion

Overview

Element Type(s):	B3D
Analysis Type(s):	STAT, GNL
Procedure(s):	
Topic(s):	
Module(s):	ASE
Input file(s):	torsion.dat

15.1 Problem Description

The problem consists of a cantilever beam as shown in Fig. 15.1. The tip of the cantilever is offsetted in y-direction by $\Delta_y = l/200 = 2.5\ cm$, creating a geometrical imperfection. The beam is loaded with a transverse force P_z and an axial force P_x. The imperfection acts as a lever arm for the loading, causing a torsional moment. The torsional moment at the support with respect to the local and global coordinate system is determined.

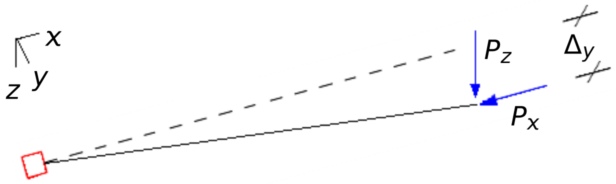

Figure 15.1: Problem Description

15.2 Reference Solution

In order to account for the effect of the geometrical imperfection on the structure, second-order theory should be used, where the equilibrium is established at the deformed system. According to the equilibrium of moments at the deformed system, with respect to the global x-axis, the torsional moment at the support $M_{x_{global}}$ is:

$$M_{x_{global}} = P_z\ (u_y + \Delta_y) - P_y\ u_z\ , \tag{15.1}$$

whereas by the local x-axis the torsional moment $M_{x_{local}}$ is:

$$M_{x_{local}} = P_z\ u_y + P_x\ (\frac{\Delta_y}{l})\ u_z\ , \tag{15.2}$$

where l is the length of the beam, Δ_y the initial geometrical imperfection and P_x is negative for compression.

15.3 Model and Results

The properties of the model [19] [20] are defined in Table 15.1. A standard steel material is used as well as a standard hot formed hollow section with properties according to DIN 59410, DIN EN 10210-2. A safety factor $\gamma_M = 1.1$ is used, which according to DIN 18800-2 it is applied both to the yield strength and the stiffness. Furthermore, the self weight, the shear deformations and the warping modulus C_M are neglected. At the support the warping is not constrained.

Table 15.1: Model Properties

Material Properties	Geometric Properties	Loading
$S\,355$	$l = 5\,m$	$P_z = 10\,kN$
$\gamma_M = 1.1$	$RRo/SH\ 200 \times 100 \times 10$ [15]	$P_x = 100\,kN$
$C_M = 0$	$\Delta_y = 2.5\,cm$	

Table 15.2: Results

	u_y $[cm]$	u_z $[cm]$	$M_{x_{global}}$ $[kNcm]$	$M_{x_{local}}$ $[kNcm]$	P_{buck} $[kN]$
SOF.	3.209	10.204	57.08	26.98	163.7
Ref.[21]	3.20	10.2	57.0	26.9	164

The corresponding results are presented in Table 15.2. Figure 15.2 shows the deformed shape of the structure and the nodal displacements for the z and y direction. From the presented results, we can observe that the values of the moments are correctly computed. Here has to be noted that the reference results are according to [19], where they are computed with another finite element software, and not with respect to an analytical solution.

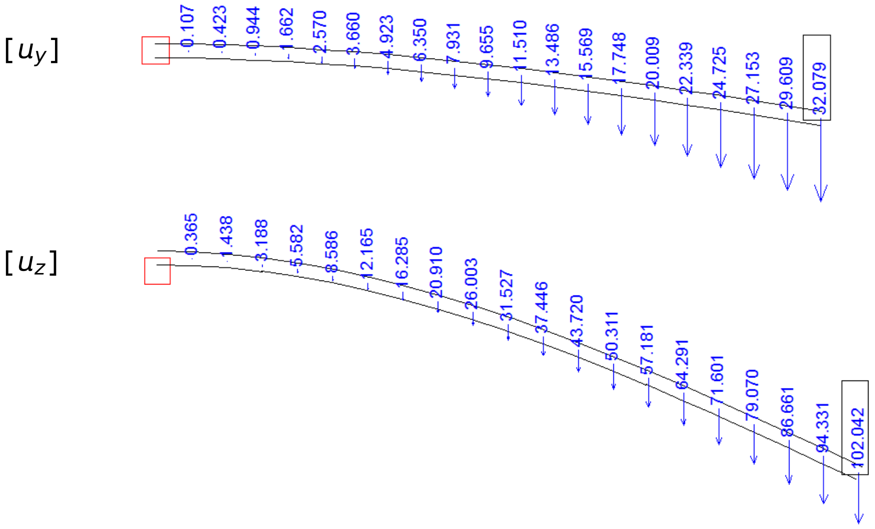

Figure 15.2: Deformations $[mm]$

15.4 Conclusion

This example presents a case where torsion is induced to the system because of an initial geometrical imperfection. It has been shown that the behaviour of the beam is captured accurately.

15.5 Literature

[15] K. Holschemacher. *Entwurfs- und Berechnungstafeln für Bauingenieure*. 3rd. Bauwerk, 2007.

[19] V. Gensichen and G. Lumpe. *Zur Leistungsfähigkeit, korrekten Anwendung und Kontrolle räumlicher Stabwerksprogramme*. Stahlbau Seminar 07.

[20] V. Gensichen. *Zur Leistungsfähigkeit räumlicher Stabwerksprogramme, Feldstudie in Zusammenarbeit mit maßgebenden Programmherstellern*. Stahlbau Seminar 07/08.

[21] V. Gensichen and G. Lumpe. "Zur Leistungsfähigkeit, korrekten Anwendung und Kontrolle von EDV-Programmen für die Berechnung räumlicher Stabwerke im Stahlbau". In: *Stahlbau 77 (Teil 2)* (2008).

16 BE13: Buckling of a Bar with Hinged Ends I

Overview	
Element Type(s):	B3D
Analysis Type(s):	STAT, GNL
Procedure(s):	STAB
Topic(s):	
Module(s):	ASE
Input file(s):	buckling_bar.dat

16.1 Problem Description

The problem consists of an axially loaded long slender bar of length l with hinged ends, as shown in Fig. 16.1. Determine the critical buckling load. [18]

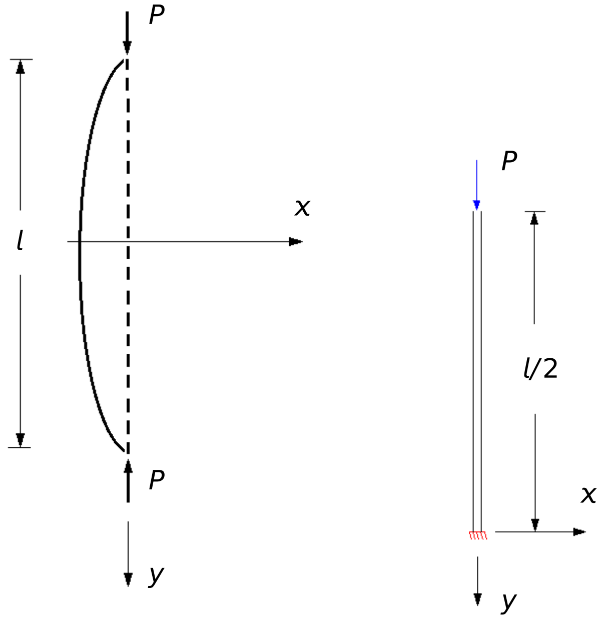

Figure 16.1: Problem Description

16.2 Reference Solution

The problem of lateral buckling of bars is examined here. The case of a bar with hinged ends is very often encountered in practical applications and is called the $fundamental$ case of buckling of a prismatic bar. For the case of an axially compressed bar there is a certain critical value of the compressive force at which large lateral deflection may be produced by the slightest lateral load. For a prismatical bar with hinged ends (Fig. 16.1) this critical compressive force is [6]:

$$P_{cr} = \frac{\pi^2 EI}{(\beta l)^2} = \frac{\pi^2 EI}{l^2}, \tag{16.1}$$

where l is the full length of the bar, EI its flexural rigidity and β the effective length coefficient, whose value depends on the conditions of end support of the bar. For the fundamental case, $\beta = 1$. If the load P is less than its critical value the bar remains straight and undergoes only axial compression. This straight form of elastic equilibrium is stable, i.e., if a lateral force is applied and a small deflection is produced this deflection disappears when the lateral load is removed and the bar becomes straight again. By increasing P up to the critical load causes the column to be in a state of unstable equilibrium, which means, that the introduction of the slightest lateral force will cause the column to undergo large lateral deflection and eventually fail by buckling.

16.3 Model and Results

Only the upper half of the bar is modelled because of symmetry (Fig. 16.1). The boundary conditions thus become free-fixed for the half symmetry model. A total of 20 elements are used to capture the buckling mode. The properties of the model are defined in Table 16.1.

Table 16.1: Model Properties

Material Properties	Geometric Properties	Loading
$E = 300\, MPa$	$l = 20\, m$	$P_y = 1\, kN$
	$h = 0.5\, m$	$P_x << 1\, kN$
	$A = 0.25\, m^2$	
	$I = 5.20833 \times 10^{-3}\, m^4$	
	$\beta = 2$, free-fixed ends	

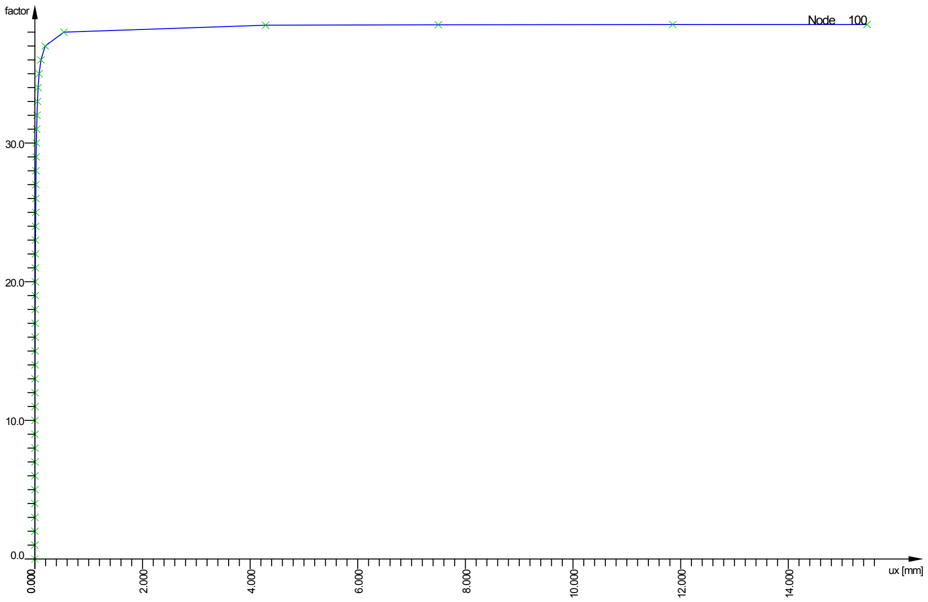

Figure 16.2: Load-Deflection curve

A small horizontal load at the top is necessary in order to induce an initial horizontal displacement. It should be sufficiently large to cause a nonlinear iteration, but it should not affect the result unintentionally. A buckling eigenvalue determination is performed where the critical load factor is calculated. The results are presented in Table 16.2. Moreover, an ultimate limit load iteration is done and the produced Load-Deflection curve is shown in Fig. 16.2, as well as a part of the iteration summary.

Table 16.2: Results

	SOF.	Ref.
P_{cr} $[kN]$	38.553	38.553

16.4 Conclusion

This example presents the buckling of slender bars. It has been shown that the buckling properties of the bar are accurately captured.

16.5 Literature

[6] S. Timoshenko. *Strength of Materials, Part II, Advanced Theory and Problems*. 2nd. D. Van Nostrand Co., Inc., 1940.

[18] *Verification Manual for the Mechanical APLD Application, Release 12.0*. Ansys, Inc. 2009.

17 BE14: Buckling of a Bar with Hinged Ends II

Overview

Element Type(s): SH3D
Analysis Type(s): STAT, GNL
Procedure(s): STAB
Topic(s):
Module(s): ASE
Input file(s): buckling_bar_quad.dat

17.1 Problem Description

Benchmark Example 13 is tested here for QUAD plane elements. The problem consists of an axially loaded long slender bar of length l with hinged ends, as shown in Fig. 17.1. Determine the critical buckling load [18].

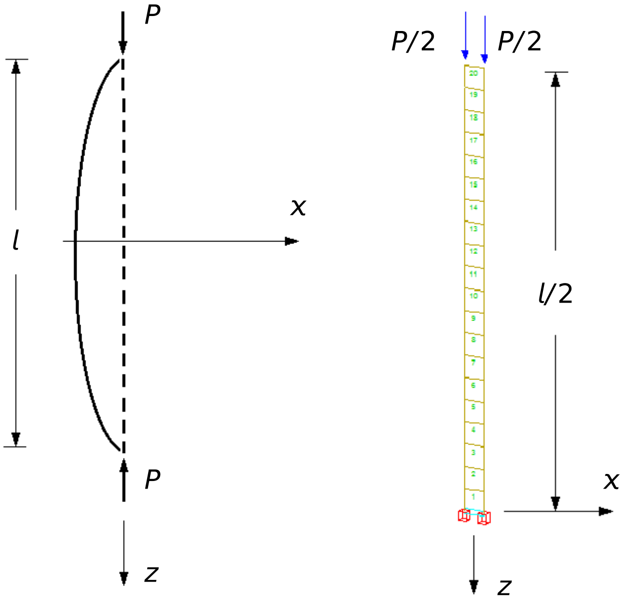

Figure 17.1: Problem Description

17.2 Reference Solution

The problem of lateral buckling of bars is presented at Benchmark Example 13. For a prismatic bar, the critical load is [6]:

$$P_{cr} = \frac{\pi^2 EI}{(\beta l)^2}. \tag{17.1}$$

From the above equation it is evident, that the critical load does not depend upon the strength of the material but only upon the dimensions of the structure and the modulus of elasticity of the material. Two equal slender axially compressed bars, will buckle at the same compressive force, if they consist of the same flexural rigidity and material with the same Young's modulus.

17.3 Model and Results

Only the upper half of the bar is modelled because of symmetry (Fig. 17.1). The boundary conditions thus become free-fixed for the half symmetry model. A total of 20 elements are used to capture the buckling mode. The properties of the model are defined in Table 17.1.

Table 17.1: Model Properties

Material Properties	Geometric Properties	Loading
$E = 300\,MPa$	$l = 20\,m$, $h = 0.5\,m$	$P = 1\,kN$
	$A = 0.25\,m^2$	$P_x << 1\,kN$
	$t = 0.5\,m$	
	$I = 5.20833 \times 10^{-3}\,m^4$	
	$\beta = 2$, free-fixed ends	

A buckling eigenvalue determination is performed where the critical load factor is calculated. Result of the eigenvalue calculation are presented in Table 17.2. The reference value of the critical load for Benchmark Example 13 and 14 is calculated the same, since the properties of the two models are equivalent, as explained in Section 17.2.

Table 17.2: Results

Solver	P_{cr} [kN]	Ref.	$\lvert e_r \rvert$ [%]
BUCK - Simultaneous vector iteration	38.539	38.553	0.0379

17.4 Conclusion

This example presents the buckling of slender bars. It has been shown that the buckling properties of the bar are accurately captured also with QUAD elements.

17.5 Literature

[6] S. Timoshenko. *Strength of Materials, Part II, Advanced Theory and Problems*. 2nd. D. Van Nostrand Co., Inc., 1940.

[18] *Verification Manual for the Mechanical APLD Application, Release 12.0*. Ansys, Inc. 2009.

18 BE15: Flexural and Torsional Buckling

Overview	
Element Type(s):	B3D
Analysis Type(s):	STAT, GNL
Procedure(s):	STAB
Topic(s):	
Module(s):	ASE
Input file(s):	flex_tors_buckling.dat

18.1 Problem Description

The problem consists of a standard I-beam, subjected to a compressive load P and supported as shown in Fig. 18.1. The flexural and torsional buckling load is determined.

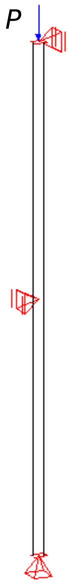

Figure 18.1: Problem Description

18.2 Reference Solution

For the rolled steel profiles, such as $IPE\ 300$, the torsional buckling is generally only decisive, when the buckling length for torsional buckling s_θ is significantly larger than the one for the flexural buckling s_z, and at the same time the slenderness ratio is low [19]. The analysed model fulfils the above prerequisites. The flexural buckling load is:

$$P_{buck_z} = \frac{\pi^2\, EI_z}{s_z^2\, \gamma_M}, \tag{18.1}$$

whereas the torsional buckling load is:

$$P_{buck_\theta} = \frac{1}{i_m^2\, \gamma_M} \left(GI_T + \frac{\pi^2\, EC_M}{s_\theta^2} \right), \tag{18.2}$$

where EI_z the flexural rigidity, C_M the warping modulus, γ_M a safety factor, G the shear modulus, I_T the torsional moment and i_M is the polar radius of gyration calculated as following:

$$i_M = \frac{I_y + I_z}{A}. \tag{18.3}$$

18.3 Model and Results

The properties of the model [19] are defined in Table 18.1. A standard steel material is used, as well as a standard rolled steel profile with properties according to DIN 1025-5. A safety factor $\gamma_M = 1.1$ is used, which according to DIN 18800-2 it is applied both to the yield strength and the stiffness. Furthermore, the self weight and the shear deformations are neglected. At all the supports the warping is not constrained.

Table 18.1: Model Properties

Material Properties	Geometric Properties	Loading
$S\,355$	$s_\theta = 5$ or $6\,m$	$P = 600\,kN$
$\gamma_M = 1.1$	$s_z = 2.5$ or $3\,m$	
$C_M = 125900\,cm^6$	$IPE\ 300$ [15]	
	$I_y = 8360\,cm^4$	
	$I_z = 604\,cm^4$	
	$A = 53.81\,cm^2$	

The corresponding results are presented in Table 18.2. Figure 18.2 shows the deformed shape of the structure for the first and second buckling eigenvalues. It is obvious that the first one corresponds to the torsional buckling while the second one to the flexural.

Table 18.2: Results

	$s_\theta = 5.0\ [m]$ / $s_z = 2.5\ [m]$		$s_\theta = 6.0\ [m]$ / $s_z = 3.0\ [m]$	
	$P_{buck_z}\ [kN]$	$P_{buck_\theta}\ [kN]$	$P_{buck_z}\ [kN]$	$P_{buck_\theta}\ [kN]$
SOF.	1820.92	1462.87	1264.53	1288.78
Exact	1820.89	1462.87	1264.51	1288.78
Ref. [21]	1818	1459	1264	1285

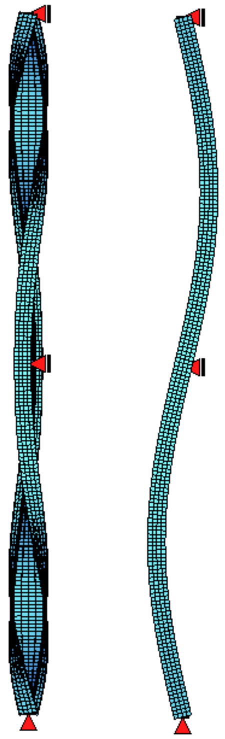

Figure 18.2: Buckling Eigenvalues

18.4 Conclusion

This example presents the determination of torsional and flexural buckling loads. It has been shown that the behaviour of the beam is captured accurately.

18.5 Literature

[15] K. Holschemacher. *Entwurfs- und Berechnungstafeln für Bauingenieure*. 3rd. Bauwerk, 2007.

[19] V. Gensichen and G. Lumpe. *Zur Leistungsfähigkeit, korrekten Anwendung und Kontrolle räumlicher Stabwerksprogramme*. Stahlbau Seminar 07.

[21] V. Gensichen and G. Lumpe. “Zur Leistungsfähigkeit, korrekten Anwendung und Kontrolle von EDV-Programmen für die Berechnung räumlicher Stabwerke im Stahlbau”. In: *Stahlbau 77 (Teil 2)* (2008).

19 BE16: Torsion due to Biaxial Bending

Overview

Element Type(s):	B3D
Analysis Type(s):	STAT, GNL
Procedure(s):	
Topic(s):	
Module(s):	ASE
Input file(s):	torsion_bending.dat

19.1 Problem Description

The problem consists of a beam subjected to transverse load P_z and a lateral load P_y, as shown in Fig. 19.1. The effect of torsion due to biaxial bending is examined.

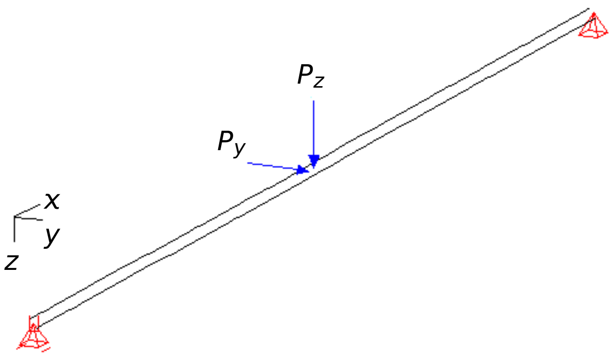

Figure 19.1: Problem Description

19.2 Reference Solution

For an I-beam subjected to biaxial bending, without the action of a normal force, it follows directly from the beam theory that a torsional moment will inevitably appear, even if the cross-section is double symmetric, the load is centrically applied, and the beam is statically determined. In order to account for this effect, third order theory has to be utilised.

19.3 Model and Results

The properties of the model [19] are defined in Table 19.1. A standard steel material is used as well as a cross-section with a standard rolled steel shape. A safety factor $\gamma_M = 1.1$ is used, which according to DIN 18800-2 it is applied both to the yield strength and the stiffness. Furthermore, the self weight and the shear deformations are neglected. At the supports the warping is not constrained.

Table 19.1: Model Properties

Material Properties	Geometric Properties	Loading
$S\,355$	$l = 5\,m$	$P_z = 20\,kN$
$\gamma_M = 1.1$	$IPE\ 300$ [17] [22]	$P_y = 4\,kN$
$C_M = 125900\,cm^6$		

The results are presented in Table 19.2. It has to be noted that the reference results are according to [19] and [21], where they are computed with another finite element software, and not with respect to an analytical solution.

Table 19.2: Results

max | |	$C_M = 125900\ [cm^6]$	Ref. [19]	$C_M = 0$	Ref. [19]
$\phi_x\ [rad]$	0.0316	0.0315	0.0321	0.0321
$M_x\ [kN\,m]$	0.183	0.185	0.185	0.189
$M_y\ [kN\,m]$	24.88	24.9	24.85	24.9
$M_z\ [kN\,m]$	5.57	5.6	5.71	5.7

19.4 Conclusion

This example presents a case where torsion is induced to the system because of biaxial bending. It has been shown that the behaviour of the beam is captured accurately.

19.5 Literature

[17] R. Kindmann, M. Kraus, and H. J. Niebuhr. *Stahlbau Kompakt, Bemessungshilfen, Profiltabellen*. Verlag Stahleisen, 2006.

[19] V. Gensichen and G. Lumpe. *Zur Leistungsfähigkeit, korrekten Anwendung und Kontrolle räumlicher Stabwerksprogramme*. Stahlbau Seminar 07.

[21] V. Gensichen and G. Lumpe. “Zur Leistungsfähigkeit, korrekten Anwendung und Kontrolle von EDV-Programmen für die Berechnung räumlicher Stabwerke im Stahlbau”. In: *Stahlbau 77 (Teil 2)* (2008).

[22] R. Kindmann. “Neue Berechnungsformel für das IT von Walzprofilen und Berechnung der Schubspannungen”. In: *Stahlbau 75* (2006).

20 BE17: Lateral Torsional Buckling

Overview

Element Type(s): B3D
Analysis Type(s): STAT, GNL
Procedure(s):
Topic(s):
Module(s): ASE
Input file(s): lateral_torsional_buckling.dat

20.1 Problem Description

The problem consists of a single span beam with an initial geometrical imperfection at the middle, subjected to a uniformly distributed load q_z, as shown in Fig. 20.1. The structure is examined for lateral torsional buckling.

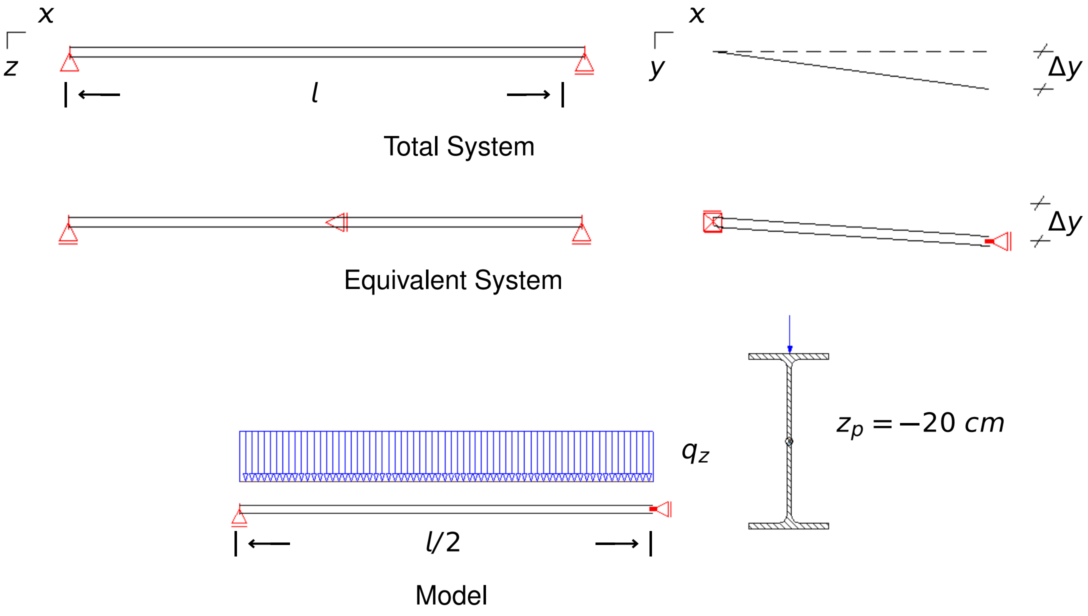

Figure 20.1: Problem Description

20.2 Reference Solution

The I-beam of Fig. 20.1 has an initial geometrical imperfection in the y-direction $\Delta y = l/200 = 3.0\ cm$. Using the symmetry of the equivalent system the model can be reduced to half as shown at Fig. 20.1. Due to the bending moments, the load application on the upper flange of the beam (z_p) and the imperfection, the beam is at risk for lateral torsional buckling. In order to account for this effect, third order theory has to be utilised.

20.3 Model and Results

The properties of the model [19] are defined in Table 20.1. A standard steel material is used as well as a standard rolled steel profile with properties according to DIN 1025-5. A safety factor $\gamma_M = 1.1$

is used, which according to DIN 18800-2 it is applied both to the yield strength and the stiffness. The loading is applied at the upper flange as shown in Fig. 20.1. Furthermore, the self weight and the shear deformations are neglected. At the supports the warping is not constrained.

Table 20.1: Model Properties

Material Properties	Geometric Properties	Loading
$S\,355$, $\gamma_M = 1.1$	$l = 6\,m$, $\Delta y = 3\,cm$	$q_z = 10\,kN/m$
$C_M = 490000\,cm^6$	IPE 400 [15]	$z_p = -20\,cm$

The results are presented in Table 20.2. It is observed that second-order theory (TH. II) fails to capture the moments with respect to the z-axis, therefore third-order theory (TH. III) has to be used. It has to be noted that the reference results are according to [19], where they are computed with another finite element software, and not with respect to an analytical solution.

Table 20.2: Results

	C_M = 490000 [cm^6]		Ref. [19]	C_M = 0		Ref. [19]
	TH. II	TH. III		TH. II	TH. III	
u_y [cm]	0.094	0.082	0.089	0.184	0.158	0.172
u_z [cm]	0.422	0.425	0.424	0.470	0.479	0.475
phi_x [rad]	0.0167	0.0166	0.0167	0.0367	0.0363	0.0365
M_x [$kN\,m$]	0.439	0.437	0.438	0.510	0.504	0.508
M_y [$kN\,m$]	45.0	45.0	45.0	45.0	45.0	45.0
M_z [$kN\,m$]	0.001	0.747	0.752	0.001	1.627	1.641
M_ω [$kN\,m$]	0.606	0.604	0.607	0.0	0.0	0.0

20.4 Conclusion

This example examines the lateral torsional buckling of beams. It has been shown that the behaviour of the beam is captured accurately.

20.5 Literature

[15] K. Holschemacher. *Entwurfs- und Berechnungstafeln für Bauingenieure*. 3rd. Bauwerk, 2007.

[19] V. Gensichen and G. Lumpe. *Zur Leistungsfähigkeit, korrekten Anwendung und Kontrolle räumlicher Stabwerksprogramme*. Stahlbau Seminar 07.

21 BE18: Three-storey Column under Large Compressive Force and Torsional Moment

Overview

Element Type(s):	B3D
Analysis Type(s):	STAT, GNL
Procedure(s):	
Topic(s):	
Module(s):	ASE, DYNA
Input file(s):	three_storey_column.dat

21.1 Problem Description

The problem consists of a three-storey column, subjected to a large compressive axial force N and a torsional moment M_t at the middle, as shown in Fig. 21.1. The rotation and twisting as well as the torsional moments of the structure are determined.

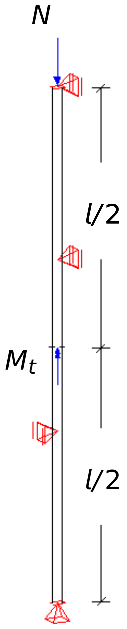

Figure 21.1: Problem Description

21.2 Reference Solution

A large axial compressive force is applied to the column of Fig. 21.1, in combination with a torsional moment at the middle, which can cause warping and potentially buckling of the structure. In order to account for this effect, second order theory has to be utilised. The total torsional moment M_T is given as a sum of the different torsional parts, the primary, secondary and third respectively:

$$\sum M_x = M_T = M_{T1} + M_{T2} + M_{T3}, \tag{21.1}$$

where

$$M_{T1} = G\,I_T\,\phi^{'}, \tag{21.2}$$

$$M_{T2} = -\,E\,C_M\,\phi^{'''}, \tag{21.3}$$

$$M_{T3} = N\,i_p^2\,\phi^{'}, \tag{21.4}$$

and the warping moment

$$M_{\omega} = -\,E\,C_M\,\phi^{''}. \tag{21.5}$$

where G is the shear modulus, I_T the torsional moment of inertia, i_p the polar radius of gyration and EC_M the warping torsion stiffness. Introducing the above into Eq. 21.1 we have:

$$\left(G\,I_T\, +\, N\,i_p^2\right)\,\phi^{'} -\,E\,C_M\,\phi^{'''}\, =\, M_T\, = \sum M_x. \tag{21.6}$$

21.3 Model and Results

The properties of the model [23] are defined in Table 21.1. A standard steel material is used and an I-beam profile for the cross-section. A safety factor $\gamma_M = 1.1$ is used, which according to DIN 18800-2 it is applied both to the yield strength and the stiffness. At the supports the warping is not constrained. The cross-sectional properties given in Table 21.1 are the values calculated by SOFiSTiK, matching the analytical solution, except from the torsional moment I_T and the warping modulus C_M which are modified to match the values of the reference example. This modification is done only for the sake of comparison and it has to be noted that the reference results [23] are computed with another finite element software, and not with respect to an analytical solution.

Table 21.1: Model Properties

Material Properties	Geometric Properties	Loading
$\gamma_M = 1.1$	$b = 180\,mm$	$N = 1712\,kN$
$l = 6\,m$	$h = 400\,mm$	$M_t = 272\,kN\,cm$
$S\,355$	$t_{web} = 10\,mm$	
	$t_{flange} = 14\,mm$	
	$C_M = 506884\,cm^6$	
	$I_y = 23071.6\,cm^4$	
	$I_z = 1363.9\,cm^4$	
	$I_T = 44.18\,cm^4$	

The results are presented in Table 21.2 and Fig 21.2. The value of M_{T3} is not given in the Reference

[23], but according to Eq. 21.4 is computed as $-721\ kNcm$, which matches the calculated value by SOFiSTiK. If we now sum the torsional moment parts, it is observed that Eq. 21.1 is satisfied and that the total torsional moment at $x = 0$ is $136\ kNcm$.

Table 21.2: Results

	SOF.	Ref.[23]
ϕ $[mrad]$ $(x = l/2)$	294.4	294
ϕ' $[mrad/cm]$ $(x = 0; x = l)$	1.5096	1.50965
M_{T1} $[kN\,cm]$ $(x = 0)$	491	491
M_{T2} $[kN\,cm]$ $(x = 0)$	366	366
M_{T3} $[kN\,cm]$ $(x = 0)$	-721	-
M_T $[kN\,cm]$ $(x = 0)$	136	136
M_ω $[kN\,cm]$	85583	85620

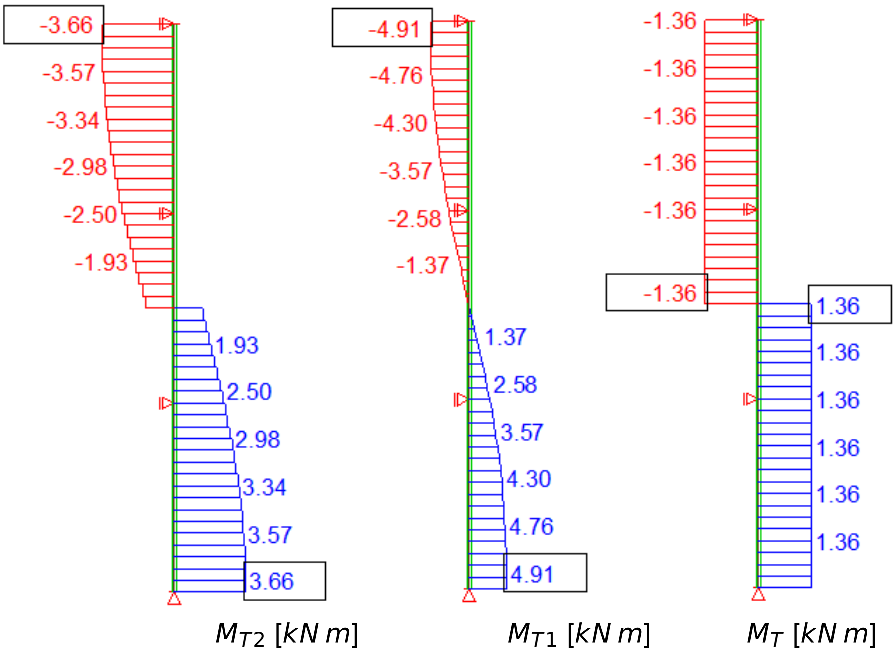

Figure 21.2: Results $[kN\,m]$

21.4 Conclusion

This example examines the torsional behaviour of the beam and the different parts involved in the calculation of the total torsional moment. The results are reproduced accurately.

21.5 Literature

[23] V. Gensichen and G. Lumpe. *Anmerkungen zur linearen und nichtlinearen Torsionstheorie im Stahlbau*. Stahlbau Seminar 2012.

22 BE19: Two-span Beam with Warping Torsion and Compressive Force

Overview	
Element Type(s):	B3D
Analysis Type(s):	STAT, GNL
Procedure(s):	
Topic(s):	
Module(s):	ASE, DYNA
Input file(s):	two_span_beam.dat

22.1 Problem Description

The problem consists of a two-span beam, subjected to a large compressive axial force N_2 at its right end node, as well as a torsional moment M_t at the middle and an additional axial force N_1 in the middle of the right span, as shown in Fig. 22.1. The structure is examined for its torsional and warping behaviour.

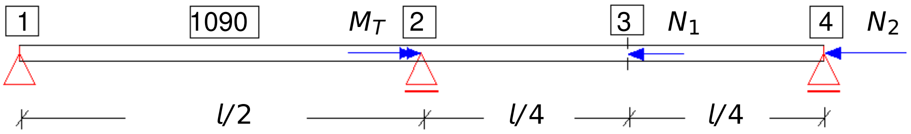

Figure 22.1: Problem Description

22.2 Reference Solution

While in first order theory, the axial force has no effect in the torsional deformations and moments, in second order torsional theory, the influence of the axial force in the rotation and twisting is considered. From the formulation of the equilibrium conditions at the twisted element, the torsional moment part M_{T3} results, which covers the contribution of the axial force in the total torsional moment. Therefore second order theory is utilised here, in order to account for the torsional effect of the axial force, as well as the warping torsion arising from the application of the torsional moment and the axial force at the intermediary nodes of the beam. The total torsional moment M_T is given as a sum of the different torsional parts, the primary, secondary and third respectively:

$$\sum M_x = M_T = M_{T1} + M_{T2} + M_{T3}, \tag{22.1}$$

where

$$M_{T1} = G\, I_T\, \phi', \tag{22.2}$$

$$M_{T2} = -E\, C_M\, \phi''', \tag{22.3}$$

$$M_{T3} = N\, i_p^2\, \phi', \tag{22.4}$$

and the warping moment

$$M_\omega = -\, E\, C_M\, \phi''. \tag{22.5}$$

where G is the shear modulus, I_T the torsional moment of inertia, i_p the polar radius of gyration and EC_M the warping torsion stiffness. Introducing the above into Eq. 22.1 we have:

$$\left(G\, I_T \,+\, N\, i_p^2\right)\phi' - E\, C_M\, \phi''' \,=\, M_T \,= \sum M_x. \tag{22.6}$$

22.3 Model and Results

The properties of the model [23] are defined in Table 22.1. A standard steel material is used and an I-beam profile for the cross-section. A safety factor $\gamma_M = 1.1$ is used, which according to DIN 18800-2 it is applied both to the yield strength and the stiffness. At the supports the warping is not constrained. The cross-sectional properties, given in Table 22.1, are the values calculated by SOFiSTiK, matching the reference solution, except from the torsional moment I_T and the warping modulus C_M, which are modified to match the values of the reference example. This modification is done only for the sake of comparison and it has to be noted that the reference results [23] are computed with another finite element software, and not with respect to an analytical solution. The results are presented in Table 22.2, 22.3 and Fig 22.2. The double result values given for some nodes, e.g. 309/308, indicate the value left and right of the node respectively, and the exact result lies in between. When '—' is used, it indicates a change in the moment diagram.

Table 22.1: Model Properties

Material Properties	Geometric Properties	Loading
$\gamma_M = 1.1$	$b = 180\,mm$, $h = 400\,mm$	$N_1 = 200\,kN$
$l = 6\,m$	$t_{web} = 10\,mm$, $t_{flange} = 14\,mm$	$N_2 = 1600\,kN$
$S\,355$	$I_y = 23071.6\,cm^4$, $I_z = 1363.9\,cm^4$	$M_t = 280\,kN\,cm$
	$C_M = 506900\,cm^6$	
	$I_T = 45.00\,cm^4$	

Table 22.2: Torsional Deformation Results

	Node 1		Node 2	
	SOF.	Ref.[23]	SOF.	Ref.[23]
$\phi\ [mrad]$	-	-	294	294
$\phi'\ [rad/cm]$	1.525	1.52	-	-

Table 22.3: Torsional Moment Results

Node		M_T $[kNcm]$	M_{T1} $[kNcm]$	M_{T2} $[kNcm]$	M_{T3} $[kNcm]$	M_ω $[kNm^2]$
1	SOF.	121	505	382	-766	0
	Ref. [23]	121	505	382	-766	0
1090	SOF.	121	363	309/308	$-550/-550$	5.35
	Ref. [23]	121	363	308	-550	5.35
2	SOF.	$121\|-159$	-9	$118\|-165$	13/13	8.65
	Ref. [23]	$121\|-159$	-9	$117\|-163$	14	8.65
3	SOF.	-159	-364	$-345\|-285$	551|490	4.70
	Ref. [23]	-159	-363	$-346\|-285$	551|490	4.70
4	SOF.	-159	-487	-328	656	0
	Ref. [23]	-159	-487	-328	656	0

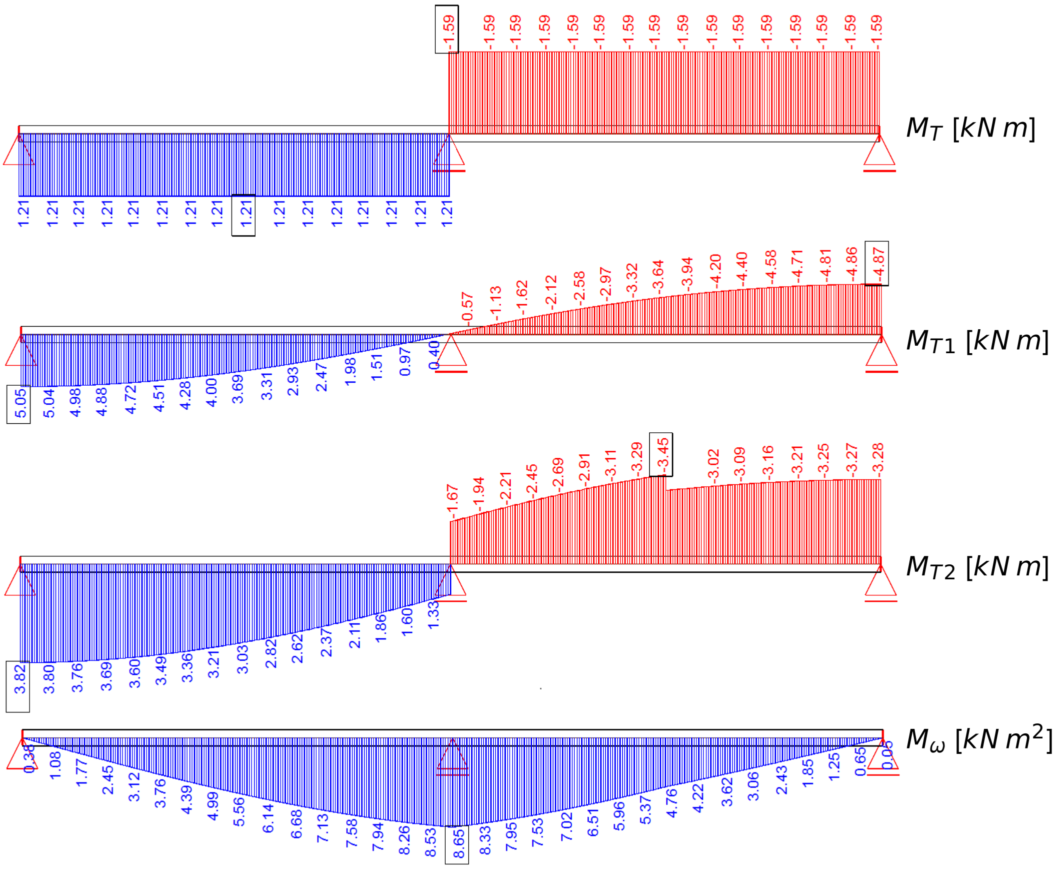

Figure 22.2: Results

In reference [23], except from the second order theory, the example is also analysed with respect to geometrically nonlinear torsional theory which accounts additionally for the large torsional deformations. This is done by introducing an additional torsional moment part, the helix torsional moment M_{TH}. The results of both analysis are compared, leading to the conclusion that second order theory lies almost always to the safe side.

22.4 Conclusion

This example examines the torsional behaviour of the beam and the different parts involved in the calculation of the total torsional moment. The results are reproduced accurately.

22.5 Literature

[23] V. Gensichen and G. Lumpe. *Anmerkungen zur linearen und nichtlinearen Torsionstheorie im Stahlbau*. Stahlbau Seminar 2012.

23 BE20: Passive Earth Pressure I

Overview

Element Type(s):	C2D
Analysis Type(s):	STAT, MNL
Procedure(s):	LSTP
Topic(s):	SOIL
Module(s):	TALPA
Input file(s):	passive_earth_pressure.dat

23.1 Problem Description

The problem consists of a soil mass retained by a wall as shown in Fig. 23.1. The horizontal passive earth pressure is determined and is compared to the value obtained for the case of the soil mass externally forced to its limiting strength.

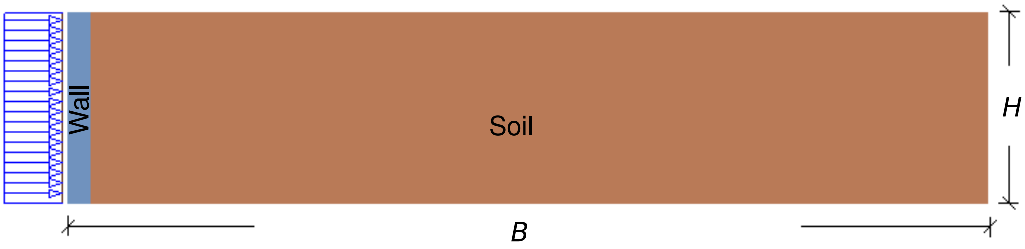

Figure 23.1: Problem Description

23.2 Reference Solution

When a retaining wall is forced against a soil mass, lateral passive earth pressure is exerted from the soil to the wall. In order to describe the horizontal component of the pressure the soil will exert, an earth pressure coefficient K_{ph} according to Coulomb theory is used:

$$K_{ph} = \frac{cos^2\left(\phi - \alpha\right)}{\left(1 - \sqrt{\frac{sin\left(\phi + \delta_p\right) \cdot sin(\phi + \beta)}{cos\left(\alpha + \delta_p\right) \cdot cos(\alpha + \beta)}}\right)^2 cos^2\alpha}, \tag{23.1}$$

where the parameters α, ϕ, δ_p and β are defined in Fig. 23.2. The wall friction angle is denoted by δ_p and the soil friction angle by ϕ. The horizontal passive earth pressure resultant is [15]:

$$E_{ph} = \frac{1}{2}\,\gamma\,H^2\,K_{ph}. \tag{23.2}$$

In order to account for the development of irreversible strains in the soil, under the action of the passive load, a plasticity model has to be utilised. Whether plasticity occurs in a calculation, can be evaluated with a yield function f, where the condition $f = 0$ stands for the plastic yielding. This condition can be represented as a surface in principal stress space. In this Benchmark, the Mohr-Coulomb model is adopted, which represents an elastic perfectly-plastic behaviour. A perfectly-plastic model corresponds to a fixed yield surface, i.e. a yield surface that is fully defined by model parameters and is not affected by plastic straining. Moreover, for stress state within the yield surface, the behaviour is purely elastic and all strains are reversible. Hence, the Mohr-Coulomb model requires the input of a total of five parameters, the Young's modulus E and Poisson's ratio ν for the definition of the elasticity, and three for the plasticity, the friction angle ϕ, the cohesion c and the dilatancy angle ψ. The dilatancy angle is involved in the plastic potential function and controls the evolution of plastic volumetric strain increments [24].

$$f = \sigma_1 - \frac{1 - sin\phi}{1 + sin\phi} \cdot \sigma_3 - \frac{2c\, cos\phi}{1 + sin\phi}, \tag{23.3}$$

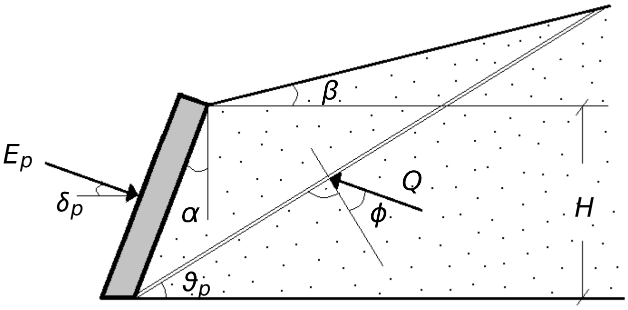

Figure 23.2: Passive Earth Pressure by Coulomb

The yield function for the Mohr-Coulomb model [24] is defined by Eq. 23.3, where σ_1 and σ_3 are the principal stresses, and its yield surface is shown in Fig. 23.3.

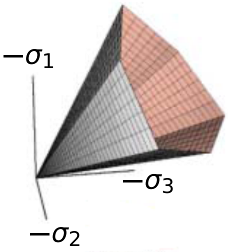

Figure 23.3: Mohr-Coulomb Yield Surface in Principal Stress Space

23.3 Model and Results

The properties of the model are defined in Table 23.1. The Mohr-Coulomb plasticity model is used for the modelling of the soil behaviour. The load is defined as a unit support displacement in the x-direction and is increased gradually until a limit value. It is applied at node 405, which is kinematically coupled with the wall nodes as shown in Fig. 23.4, and therefore corresponds to a uniformly applied load at the wall nodes. Maximum displacement is recorded for each loading increment, and the curve of horizontal passive earth pressure-displacement (Fig. 23.5) is plotted against the reference solution according to Coulomb theory.

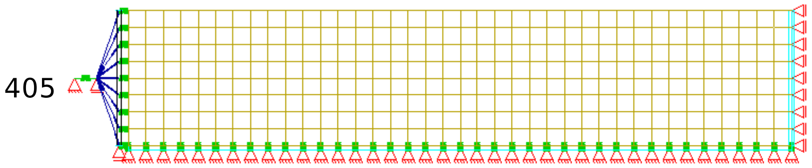

Figure 23.4: Finite Element Model

Table 23.1: Model Properties

Material Properties		Geometric Properties		Loading
Wall	Soil	Wall	Soil	
$E = 30000\,MPa$	$E = 300\,MPa$	$B = 0.1\,m$	$B = 30\,m$	$W_x = 1\,mm$
$\nu = 0.18$	$\nu = 0.20$	$H = 0.8\,m$	$H = 6\,m$	
$\gamma = 24\,kN/m^3$	$\gamma = 19\,kN/m^3$			
	$c = 1\,kN/m^2$			
	$\phi = 38°$			
	$\psi = 6°$			
$\delta_p = \phi/3$				

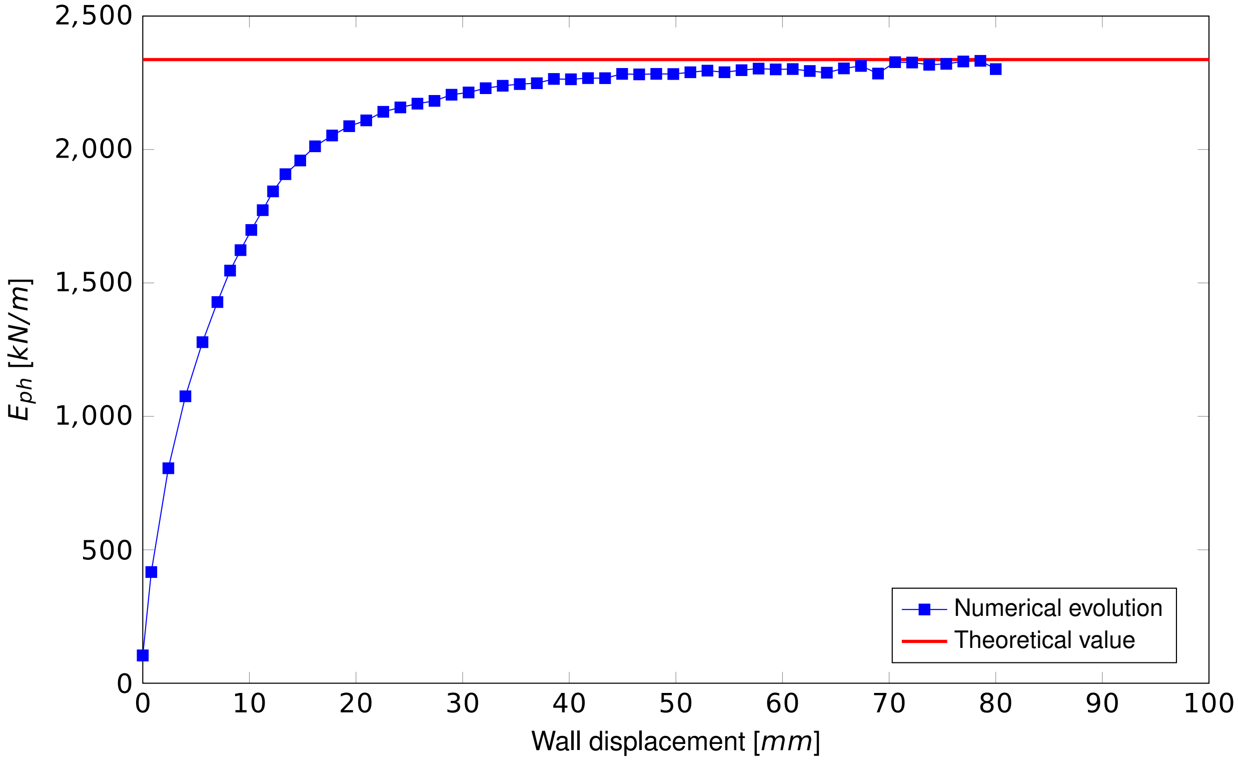

Figure 23.5: Horizontal Passive Earth Pressure-Displacement Curve

23.4 Conclusion

This example examines the horizontal passive earth pressure determination for a soil mass retained by a wall. The Mohr-Coulomb model for the definition of the soil material behaviour is adopted. It has been shown that the behaviour of the soil is captured accurately.

23.5 Literature

[15] K. Holschemacher. *Entwurfs- und Berechnungstafeln für Bauingenieure*. 3rd. Bauwerk, 2007.

[24] *AQUA Manual: Materials and Cross Sections*. Version 18-0. SOFiSTiK AG. Oberschleißheim, Germany, 2017.

24 BE21: Passive Earth Pressure II

Overview	
Element Type(s):	C2D
Analysis Type(s):	STAT, MNL
Procedure(s):	LSTP
Topic(s):	SOIL
Module(s):	TALPA
Input file(s):	passive_earth_pressure_harden.dat

24.1 Problem Description

The model of Benchmark 20 is here extended for the case of a soil material described by the hardening plasticity soil model. The problem consists of a soil mass retained by a wall as shown in Fig. 24.1. The horizontal passive earth pressure is determined and is compared to the value obtained for the case of the soil mass externally forced to its limiting strength.

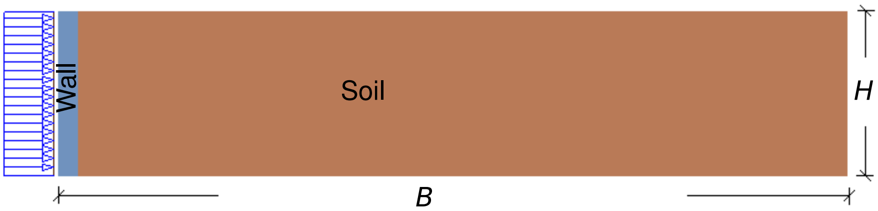

Figure 24.1: Problem Description

24.2 Reference Solution

When a retaining wall is forced against a soil mass, lateral passive earth pressure is exerted from the soil to the wall. In order to describe the horizontal component of the pressure the soil will exert, an earth pressure coefficient K_{ph} according to Coulomb theory is used:

$$K_{ph} = \frac{cos^2\,(\phi - \alpha)}{\left(1 - \sqrt{\frac{sin(\phi + \delta_p)\cdot sin(\phi + \beta)}{cos(\alpha + \delta_p)\cdot cos(\alpha + \beta)}}\right)^2 cos^2\alpha}, \tag{24.1}$$

where the parameters α, ϕ, δ_p and β are defined in Fig. 24.2. The wall friction angle is denoted by δ_p and the soil friction angle by ϕ. The horizontal passive earth pressure resultant is [15]:

$$E_{ph} = \frac{1}{2}\,\gamma\,H^2\,K_{ph}. \tag{24.2}$$

In order to account for the development of irreversible strains in the soil, under the action of the passive load, a plasticity model has to be used. In this Benchmark the hardening plasticity soil model is adopted, which is an extended elastoplastic material with an optimized hardening rule [24]. In contrast to the Mohr-Coulomb model (Be. 20), which is an elastic-perfectly-plastic model, the yield surface of a hardening plasticity model is not fixed but it can expand due to plastic straining. Its hardening rule is based on a hyperbolic stress-strain relationship, derived from triaxial testing. Hardening is limited by the material 's strength, represented by the classic Mohr-Coulomb failure criterion. Additionally, the model accounts for the stress dependent stiffness, it captures the loading state and can therefore account for the different stiffness in primary loading and un-/reloading paths. The important features of the model are [24]:

- the deviatoric hardening based on hyperbolic stress-strain relationship: input parameter $E_{50,ref}$, R_f
- the Mohr-Coulomb failure criterion: input parameter ϕ, c, ψ
- the stress dependent stiffness: input parameter m, P_{ref}
- the loading dependent stiffness: input parameter μ, E_{ur}
- the optional limitation of tensile stress: input parameter f_t
- the modelling of the contractant behaviour and stiffness during primary compression (oedometric testing): input parameter $E_{s,ref}$
- the preservation of a realistic stress ratio: input parameter k_0

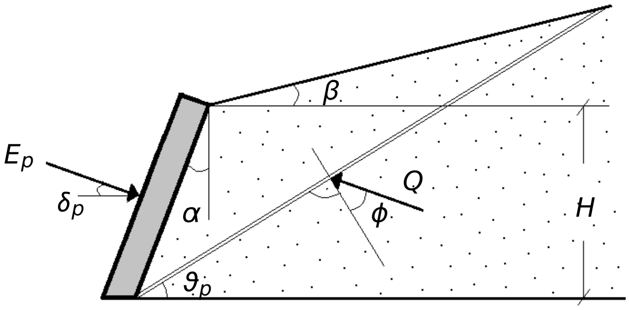

Figure 24.2: Passive Earth Pressure by Coulomb

The yield surface (Fig. 24.3) for the hardening plasticity model is bounded by the Mohr-Coulomb failure criterion, while the oedometric properties create a cap yield surface, closing the elastic region in the direction of the p-axis.

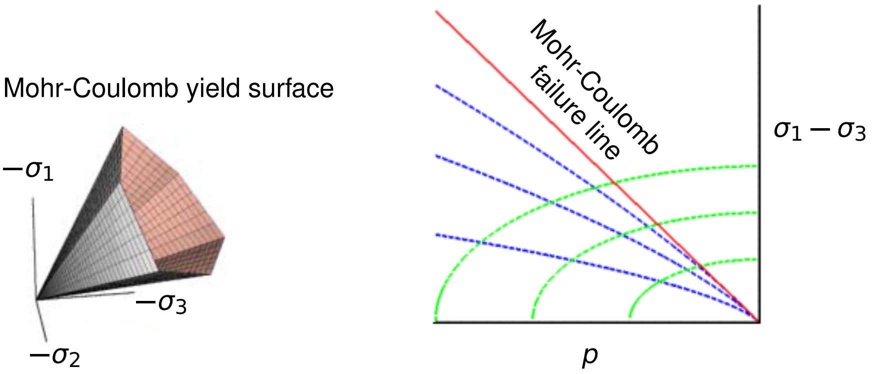

Figure 24.3: Yield Surface Properties

24.3 Model and Results

The properties of the model are defined in Table 24.1. The hardening plasticity model (GRAN) is used for the modelling of the soil behaviour in order for a more realistic representation in comparison to the elastic-perfectly-plastic Mohr-Coulomb model (Benchmark 20). The load is defined as a unit support displacement in the x-direction and is increased gradually until a limit value. It is applied at node 405, which is kinematically coupled with the wall nodes as shown in Fig. 24.4, and therefore corresponds to a uniformly applied load at the wall nodes. Maximum displacement is recorded for each loading increment, and the curve of horizontal passive earth pressure-displacement (Fig. 24.5) is plotted against the reference solution according to Coulomb theory.

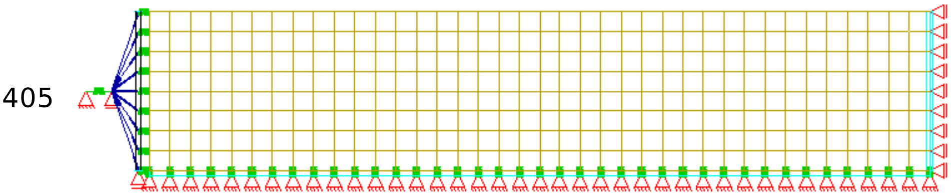

Figure 24.4: Finite Element Model

Table 24.1: Model Properties

Material Properties		Geometric Properties		Loading
Wall	Soil	Wall	Soil	
$E = 30000\,MPa$	$E = 300\,MPa$	$B = 0.1\,m$	$B = 30\,m$	$W_x = 1\,mm$
$\nu = 0.18$	$\mu = 0.20$	$H = 0.8\,m$	$H = 6\,m$	
$\gamma = 24\,kN/m^3$	$\gamma = 19\,kN/m^3$			
	$c = 1\,kN/m^2$			
	$\phi = 38°$			
	$\psi = 6°$			
	$E_{s,ref} = 75\,MPa$			
	$E_{50,ref} = 75\,MPa$			
	$m = 0.55$			
	$R_f = 0.9$			
	$P_{ref} = 0.1\,MPa$			
$\delta_p = \phi/3,\ \gamma_{buoyancy} = 9\,kN/m^3$				

From the comparison of the curves with respect to the two different plasticity models and the reference solution, it can be observed that both approach the limit value accurately. Their basic difference lies on the accounting of the hardening effect, a more realistic approach, which corresponds to higher deformations for the limit value, as it can be observed by the hardening plasticity curve in Fig. 24.5.

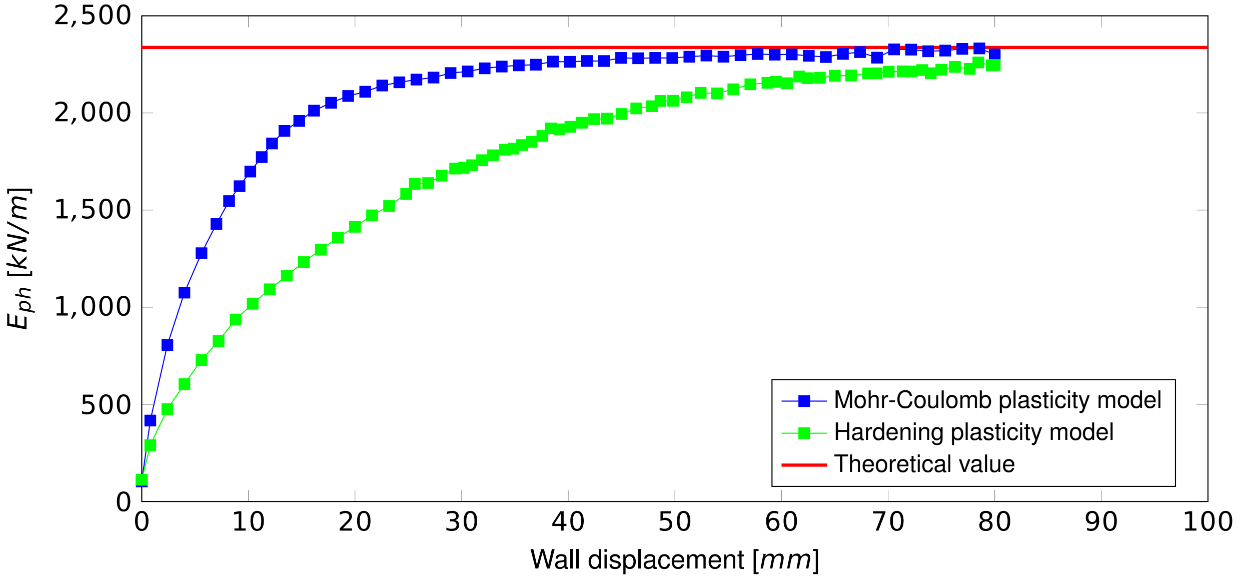

Figure 24.5: Horizontal Passive Earth Pressure-Displacement Curve

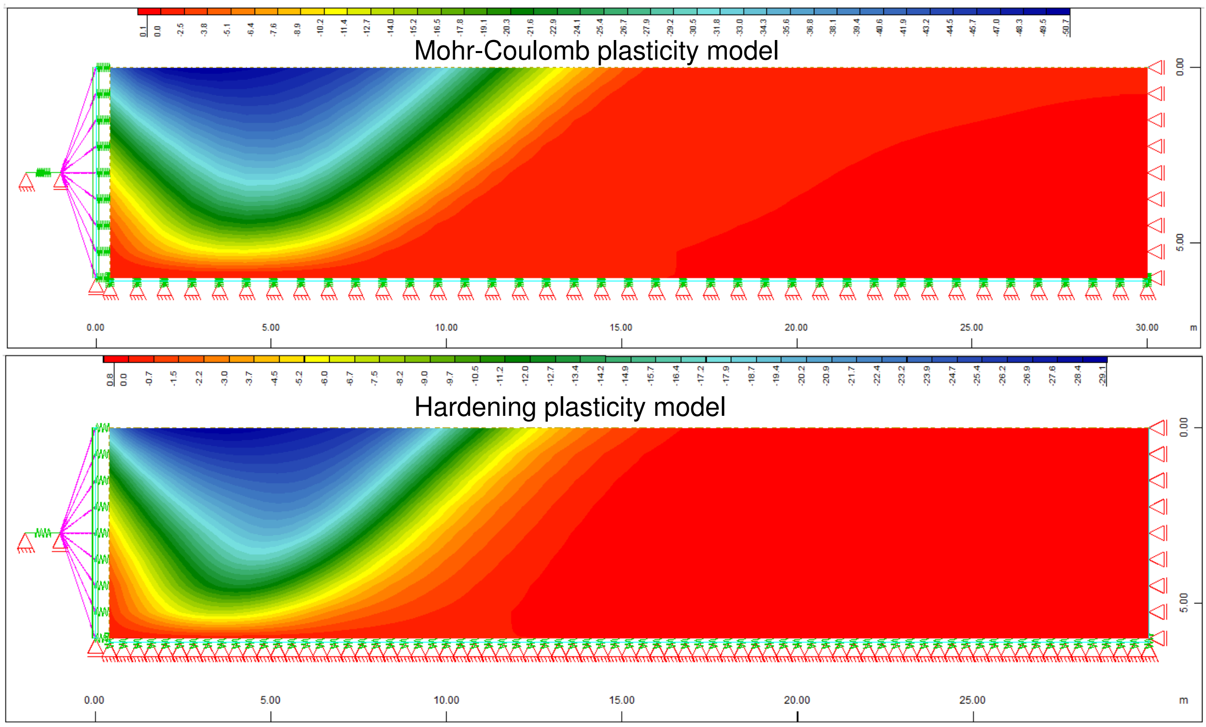
Mohr-Coulomb plasticity model
Hardening plasticity model
0.00
5.00
10.00
15.00
20.00
25.00
30.00
m

Figure 24.6: Nodal Displacement for End Load in y-direction

24.4 Conclusion

This example examines the horizontal passive earth pressure determination for a soil mass retained by a wall. The hardening plasticity model for the definition of the soil material behaviour is adopted and compared to the Mohr-Coulomb model. It has been shown that the behaviour of the soil is captured accurately.

24.5 Literature

[15] K. Holschemacher. *Entwurfs- und Berechnungstafeln für Bauingenieure*. 3rd. Bauwerk, 2007.

[24] *AQUA Manual: Materials and Cross Sections*. Version 18-0. SOFiSTiK AG. Oberschleißheim, Germany, 2017.

25 BE22: Tunneling - Ground Reaction Line

Overview

Element Type(s):	C2D
Analysis Type(s):	STAT, MNL
Procedure(s):	LSTP
Topic(s):	SOIL
Module(s):	TALPA
Input file(s):	groundline_hoek.dat

25.1 Problem Description

This problem consists of a cylindrical hole in an infinite medium, subjected to a hydrostatic in-situ state, as shown in Fig. 25.1. The material is assumed to be linearly elastic-perfectly plastic with a failure surface defined by the Mohr-Coulomb criterion and with zero volume change during plastic flow. The calculation of the ground reaction line is performed and compared to the analytical solution according to Hoek [25] [26].

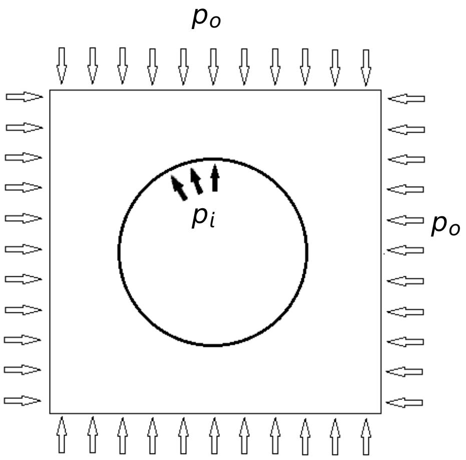

Figure 25.1: Problem Description

25.2 Reference Solution

The stability of deep underground excavations depends upon the strength of the rock mass surrounding the excavations and upon the stresses induced in this rock. These induced stresses are a function of the shape of the excavations and the in-situ stresses which existed before the creation of the excavations [25]. When tunnelling in rock, it should be examined how the rock mass, surrounding the tunnel, deforms and how the support system acts to control this deformation. In order to explore this effect, an analytical solution for a circular tunnel will be utilised, which is based on the assumption of a hydrostatic in-situ state. Furthermore, the surrounding rock mass is assumed to follow an elastic-perfectly-plastic material behaviour with zero volume change during plastic flow. Therefore the Mohr-Coulomb failure criterion is adopted, in order to model the progressive plastic failure of the rock mass surrounding the tunnel. The onset of plastic failure, is thus expressed as:

$$\sigma_1 = \sigma_{cm} + k\sigma_3, \tag{25.1}$$

where σ_1 is the axial stress where failure occurs, σ_3 the confining stress and σ_{cm} the uniaxial compressive strength of the rock mass defined by:

$$\sigma_{cm} = \frac{2c\,cos\phi}{1 - sin\phi}. \tag{25.2}$$

The parameters c and ϕ correspond to the cohesion and angle of friction of the rock mass, respectively. The tunnel behaviour on the other hand, is evaluated in terms of the internal support pressure. A circular tunnel of radius r_o subjected to hydrostatic stresses p_o and a uniform internal support pressure p_i, as shown in Fig. 25.2, is assumed.

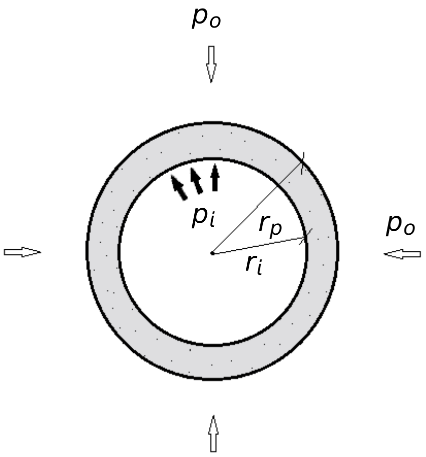

Figure 25.2: Plastic zone surrounding a circular tunnel

As a measure of failure, the critical support pressure p_{cr} is defined:

$$p_{cr} = \frac{2p_o - \sigma_{cm}}{1 + k}, \tag{25.3}$$

where k is the coefficient of passive earth pressure defined by:

$$k = \frac{1 + sin\phi}{1 - sin\phi}. \tag{25.4}$$

If the internal support pressure p_i is greater than p_{cr}, the behaviour of the surrounding rock mass remains elastic and the inward elastic displacement of the tunnel wall is:

$$u_{ie} = \frac{r_o\,(1 + \nu)}{E}\,(p_o - p_i), \tag{25.5}$$

where E is the Young's modulus and ν the Poisson's ratio. If p_i is less than p_{cr}, failure occurs and the total inward radial displacement of the walls of the tunnel becomes:

$$u_{ip} = \frac{r_o\,(1 + \nu)}{E}\left[2\,(1 + \nu)\,(p_o - p_{cr})\left(\frac{r_p}{r_o}\right)^2 - (1 - 2\nu)\,(p_o - p_i)\right], \tag{25.6}$$

and the plastic zone around the tunnel forms with a radius r_p defined by:

$$r_p = r_o \left[\frac{2\,(p_o\,(k-1) + \sigma_{cm})}{(1+k)\,((k-1)\,p_i + \sigma_{cm})} \right]^{\frac{1}{(k-1)}} \tag{25.7}$$

25.3 Model and Results

The properties of the model are defined in Table 25.1. The Mohr-Coulomb plasticity model is used for the modelling of the rock behaviour. The load is defined as a unit supporting pressure, uniform along the whole line of the circular hole, following the real curved geometry. The ground reaction line is calculated, which depicts the inward oriented deformation along the circumference of the opening that is to be expected in dependence of the acting support pressure.

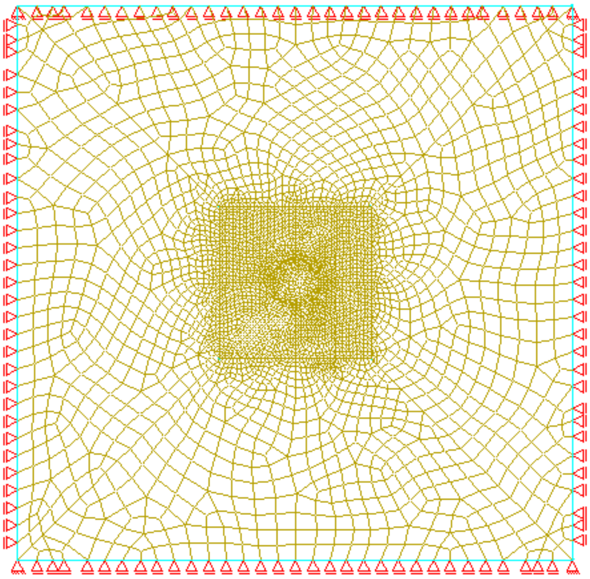

Figure 25.3: Finite Element Model

Table 25.1: Model Properties

Material Properties	Geometric Properties	Pressure Properties
$E = 5000000\,kN/m^2$	$r_o = 3.3\,m$	$P_o = 29700\,kN/m^2$
$\nu = 0.2$		$P_{i_{max}} = 7000\,kN/m^2$
$\gamma = 27\,kN/m^3$		$P_{cr} = 8133.744\,kN/m^2$
$\gamma_{buoyancy} = 17\,kN/m^3$		
$\phi = 39°$, $\psi = 0°$		
$c = 3700\,kN/m^2$		
$k = 4.395$		

The uniaxial compressive stress of the rock mass σ_{cm} is calculated at $15514.423\ kN/m^2$ and the critical pressure p_{c_r} is $8133.744\ kN/m^2$. The ground reaction line is presented in Fig. 25.4, as the curve of the inward radial displacement over the acting support pressure. It can be observed that the calculated values are in agreement with the analytical solution according to Hoek.

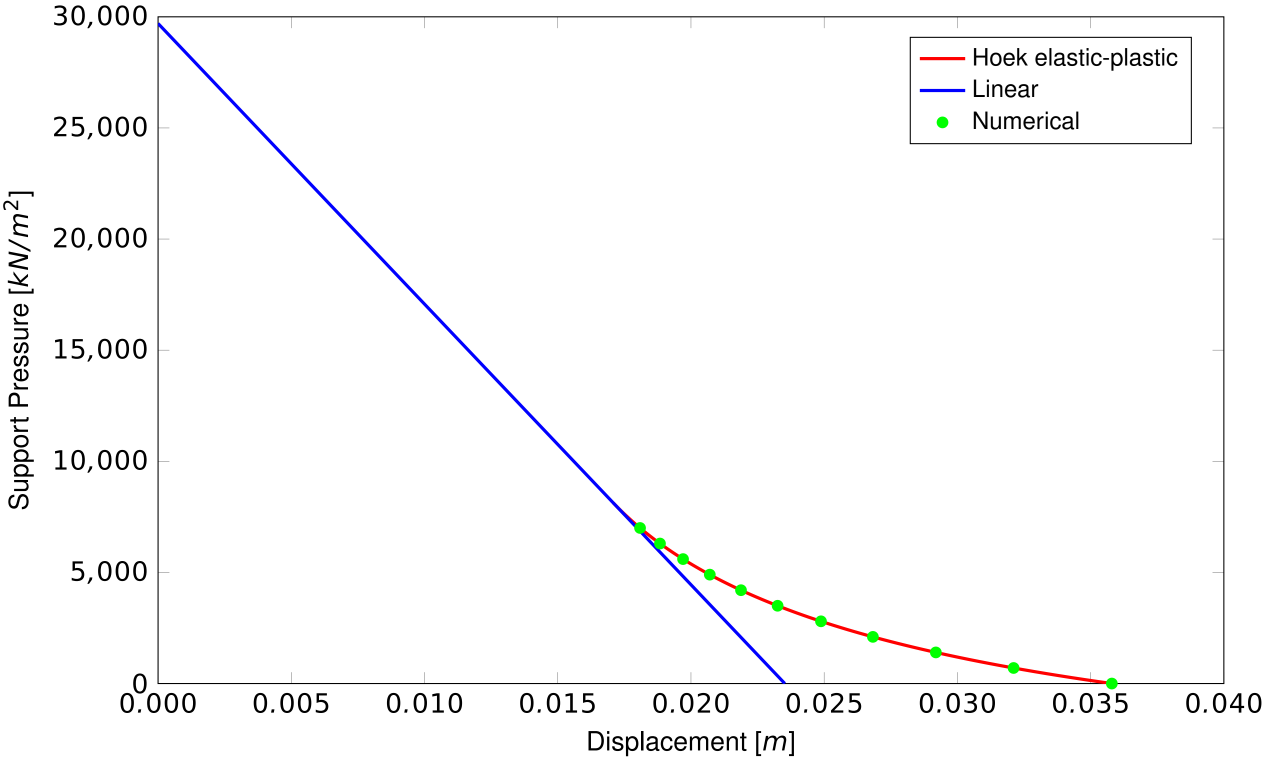

Figure 25.4: Ground Reaction Line

25.4 Conclusion

This example examines the tunnel deformation behaviour with respect to the acting support pressure. It has been shown that the behaviour of the tunnel in rock is captured accurately.

25.5 Literature

[25] E. Hoek. *Practical Rock Engineering*. 2006.
[26] E. Hoek, P.K. Kaiser, and W.F. Bawden. *Support of Underground Excavations in Hard Rock*. 1993.

26 BE23: Undamped Free Vibration of a SDOF System

Overview

Element Type(s):	SPRI
Analysis Type(s):	DYN
Procedure(s):	TSTP
Topic(s):	
Module(s):	DYNA
Input file(s):	undamped_sdof.dat

26.1 Problem Description

This problem consists of an undamped linearly elastic SDOF system undergoing free vibrations, as shown in Fig. 26.1. The response of the system is determined and compared to the exact reference solution.

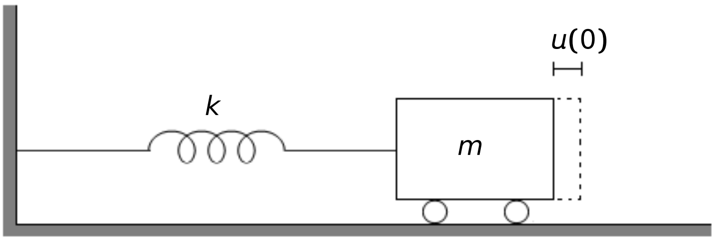

Figure 26.1: Problem Description

26.2 Reference Solution

The essential physical properties of a linearly elastic structural system subjected to an external excitation or dynamic loading are its mass, stiffness and damping. In the simplest model of a SDOF system, as shown in Fig. 26.2 in its idealized form, these properties are concentrated in a single physical element. For this system the elastic resistance to displacement is provided by the spring of stiffness k, while the energy-loss mechanism by the damper c. The mass m is included in the rigid body, which is is able to move only in simple translation, and thus the single displacement coordinate $u(t)$ completely describes its position [27].

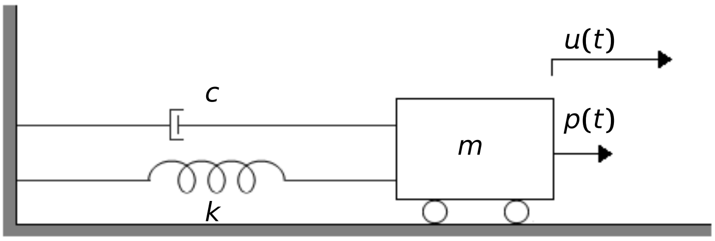

Figure 26.2: Problem Description

The motion of a linear SDOF system, subjected to an external force $p(t)$ is governed by [27] [28]:

$$m\ddot{u} + c\dot{u} + ku = p(t) \tag{26.1}$$

Setting $p(t) = 0$, gives the differential equation governing the free vibration of the system

$$m\ddot{u} + c\dot{u} + ku = 0 \tag{26.2}$$

For a system without damping (c =0), Eq. 26.2 specialises to

$$m\ddot{u} + ku = 0 \tag{26.3}$$

Free vibration is initiated by disturbing the system from its static equilibrium position by imparting the mass some displacement $u(0)$ and/or velocity $u(\dot{0})$ at time zero. Subjected to these initial conditions, the solution to the homogeneous differential equation of motion is:

$$u(t) = u(0)\,cos(\omega_n t) + \frac{\dot{u}(0)}{\omega_n} sin(\omega_n t) \tag{26.4}$$

where

$$\omega_n = \sqrt{\frac{k}{m}} \tag{26.5}$$

represents the natural circular frequency of vibration and f the natural cyclic frequency of vibration

$$f_n = \frac{\omega_n}{2\pi} \tag{26.6}$$

The period T represents the time required for the undamped system to complete one cycle of free vibration and is given by

$$T_n = \frac{2\pi}{\omega_n} = \frac{1}{f_n} \tag{26.7}$$

26.3 Model and Results

The properties of the model are defined in Table 26.1. The system is initially disturbed from its static equilibrium position by a displacement of $20\ mm$ and is then let to vibrate freely. Eq. 26.4 is plotted in Fig. 26.4, presenting that the system undergoes vibration motion about its undeformed (u = 0) position, and that this motion repeats itself every $2\pi/\omega_n$ seconds. The exact solution is compared to the calculated time history of the displacement of the SDOF system for different time integration methods. The time step is taken equal to $0.02\ sec$ corresponding to a dt/T ratio of $1/50$.

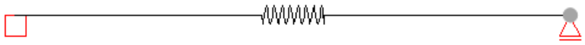

Figure 26.3: Finite Element Model

Table 26.1: Model Properties

Model Properties	Excitation Properties
$m = 1\,t$	$u(0) = 20\,mm$
$k = 4\pi^2\,kN/m$	$\dot{u}(0) = 0$
$T = 1\,sec$	

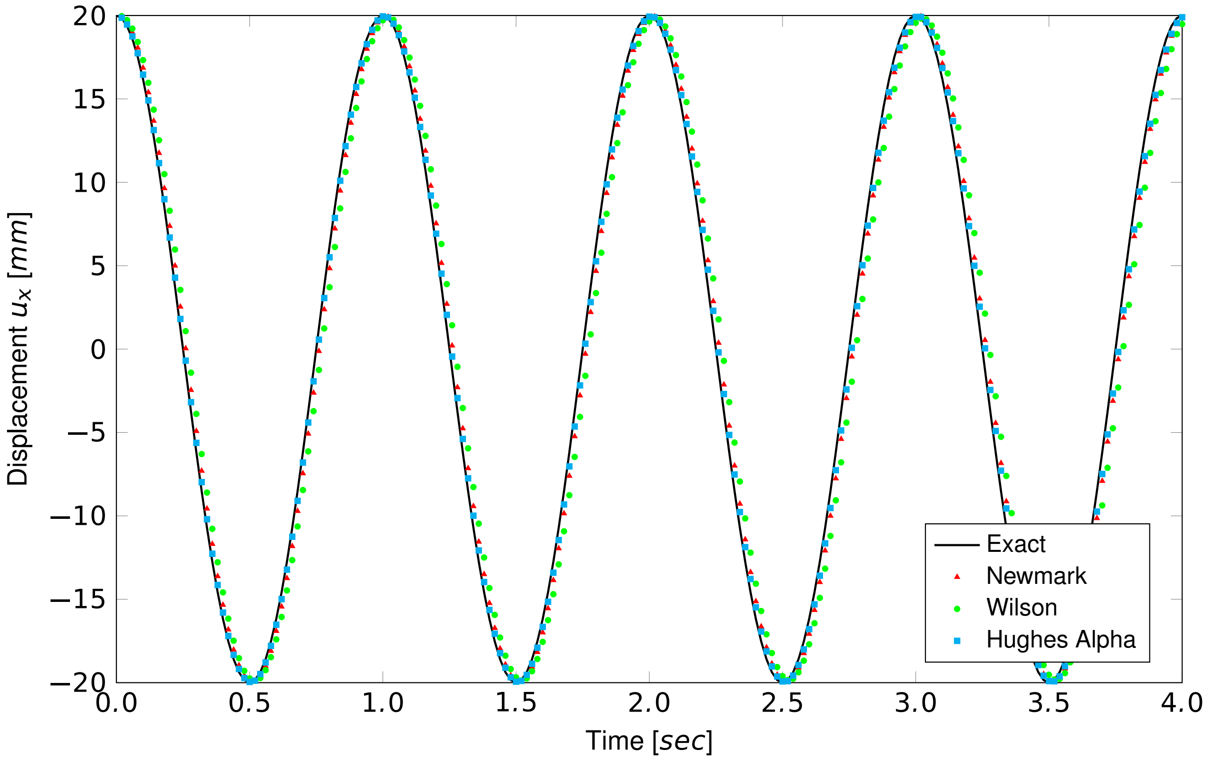

Figure 26.4: Undamped Free Vibration Response

From the results presented in Table 26.2, we observe that the response computed by the examined integration schemes is in a good agreement with the exact solution.

Table 26.2: Results

	Integration method	Newmark	Wilson	Hughes Alpha	Ref.
u_{max} [mm]		19.949	19.963	19.956	20.000

26.4 Conclusion

This example examines the response of a linear elastic undamped SDOF system undergoing free vibration. It has been shown that the behaviour of the system is captured adequately.

26.5 Literature

[27] R. W. Clough and J. Penzien. *Dynamics of Structures*. 3rd. Computers & Structures, Inc., 2003.
[28] A. K. Chopra. *Dynamics of Structures: Theory and Applications to Earthquake Engineering*. Prentice Hall, 1995.

27 BE24: Free Vibration of a Under-critically Damped SDOF System

Overview

Element Type(s):	SPRI, DAMP
Analysis Type(s):	DYN
Procedure(s):	TSTP
Topic(s):	
Module(s):	DYNA
Input file(s):	damped_sdof.dat

27.1 Problem Description

This problem consists of an under-critically damped linearly elastic SDOF system undergoing free vibrations, as shown in Fig. 27.1. The response of the system is determined and compared to the exact reference solution.

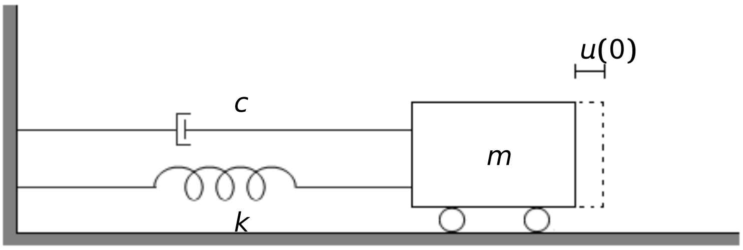

Figure 27.1: Problem Description

27.2 Reference Solution

The differential equation governing the free vibration of a linear elastic damped SDOF system, as shown in Fig. 27.1 is given by [27] [28]:

$$m\,\ddot{u} + c\,\dot{u} + k\,u = 0 \tag{27.1}$$

where c is the linear viscous damping, k the linear spring stiffness and m the mass of the system. Dividing Eq. 27.1 by m gives

$$\ddot{u} + 2\,\xi\,\omega_n\,\dot{u} + \omega_n^2\,u = 0 \tag{27.2}$$

where $\omega_n = \sqrt{k/m}$ as defined in Benchmark 23 and ξ represents the damping ratio

$$\xi = \frac{c}{2\,m\,\omega_n} = \frac{c}{c_{cr}} \tag{27.3}$$

The parameter c_{cr} is called the critical damping coefficient (Eq. 27.4), because it is the smallest value of c that inhibits oscillation completely. If c ¡ c_{cr} or ξ ¡ 1 the system is said to be under-critically damped and thus oscillates about its equilibrium position with a progressively decreasing amplitude [28].

$$c_{cr} = 2\, m\, \omega_n = 2\sqrt{k\, m} = \frac{2k}{\omega_n} \tag{27.4}$$

Free vibration is initiated by disturbing the system from its static equilibrium position by imparting the mass some displacement $u(0)$ and/or velocity $u(\dot{0})$ at time 0. Subjected to these initial conditions, the solution to the homogeneous differential equation of motion is:

$$u(t) = e^{-\xi\, \omega_n\, t}\left[u(0)\, cos\,(\omega_D\, t) + \left(\frac{\dot{u}(0) + \xi\, \omega_n\, u(0)}{\omega_D}\right) sin\,(\omega_D\, t)\right] \tag{27.5}$$

where ω_n represents the natural frequency of damped vibration and T_D the natural period of damped vibration given by

$$\omega_n = \omega_n \sqrt{1-\xi^2} \tag{27.6}$$

$$T_d = \frac{2\pi}{\omega_D} = \frac{T_n}{\sqrt{1-\xi^2}} \tag{27.7}$$

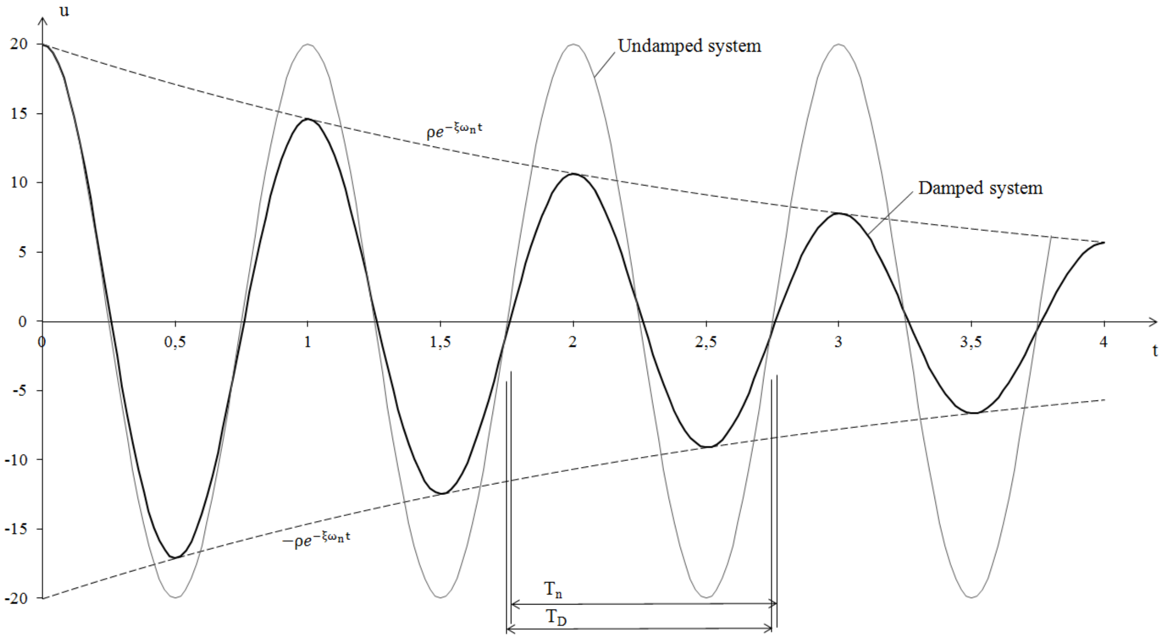

Figure 27.2: Effects of Damping on Free Vibration

The damped system oscillates with a displacement amplitude decaying exponentially with every cycle of vibration, as shown in Fig. 27.2. The envelope curves $\pm\rho e^{-\xi\, \omega_n\, t}$ touch the displacement curve at points slightly to the right of its peak values, where

$$\rho = \sqrt{u(0)^2 + \left(\frac{\dot{u}(0) + \xi\,\omega_n\,u(0)}{\omega_D}\right)^2} \tag{27.8}$$

27.3 Model and Results

The properties of the model are defined in Table 27.1. The system is initially disturbed from its static equilibrium position by a displacement of $20\ mm$ and is then let to vibrate freely. Eq. 27.5 is plotted in Fig. 27.3 and is compared to the calculated time history of the displacement of the SDOF system for different time integration methods. The time step is taken equal to $0.02\ sec$ corresponding to a dt/T ratio of $1/50$. From the curves, it is obvious that the examined integration schemes are in a good agreement with the exact solution. The damping of the SDOF system is represented in two ways, either by the spring element with a damping value in axial direction or with the damping element. The results obtained are exactly the same for both case. This can be visualised in the result files for the case of the Newmark integration scheme.

Table 27.1: Model Properties

Model Properties	Excitation Properties
$m = 1\,t$	$u(0) = 20\,mm$
$k = 4\pi^2\ kN/m$	$u(\dot{0}) = 0$
$T = 1\,sec$	
$\xi = 5\ \%$	

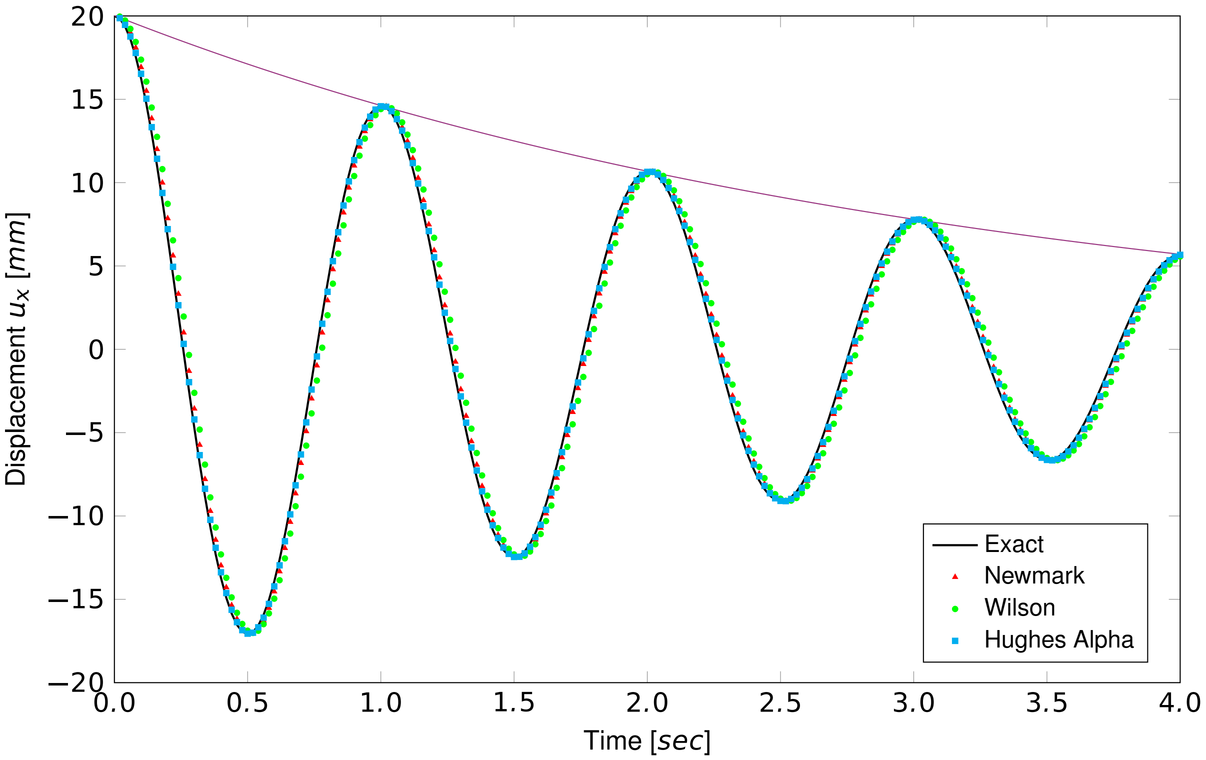

Figure 27.3: Damped Free Vibration Response

27.4 Conclusion

This example examines the response of a linear elastic under-critically damped SDOF system undergoing free vibration. It has been shown that the behaviour of the system is captured adequately.

27.5 Literature

[27] R. W. Clough and J. Penzien. *Dynamics of Structures*. 3rd. Computers & Structures, Inc., 2003.

[28] A. K. Chopra. *Dynamics of Structures: Theory and Applications to Earthquake Engineering*. Prentice Hall, 1995.

28 BE25: Eigenvalue Analysis of a Beam Under Various End Constraints

Overview

Element Type(s):	B3D
Analysis Type(s):	DYN
Procedure(s):	EIGE
Topic(s):	
Module(s):	DYNA
Input file(s):	eigenvalue_analysis.dat

28.1 Problem Description

This problem consists of a beam with various end constraints, as shown in Fig. 28.1. The eigenfrequencies of the the system are determined and compared to the exact reference solution for each case.

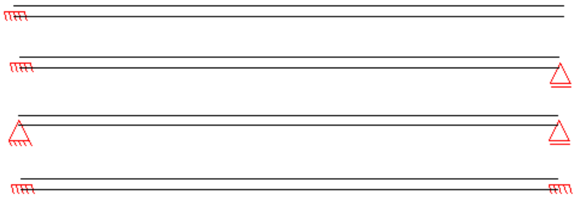

Figure 28.1: Problem Description

28.2 Reference Solution

The general formula to determine the eigenfrequency of a standard Bernoulli beam for a linear elastic material is given by [15] [29]

$$f = \frac{\lambda^2}{2\pi}\sqrt{\frac{EI}{\mu l^4}} \tag{28.1}$$

where EI the flexural rigidity of the beam, l the length, $\mu = \gamma * A/g$ the mass allocation and λ a factor depending on the end constraints. The values of λ for various cases are given in Table 28.1. In this example, we analyse four different cases of a beam structure:

1. simple cantilever
2. cantilever with simply supported end
3. simply supported
4. both ends fixed

Table 28.1: Constraints Factor

End Constraints	λ
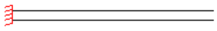	$\lambda = 1.875$
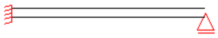	$\lambda = 3.926$
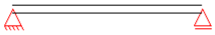	$\lambda = \pi$
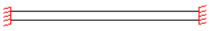	$\lambda = 4.73$

28.3 Model and Results

The properties of the model are defined in Table 28.2 and the resulted eigenfrequencies are given in Table 28.3. For the eigenvalue analysis a consistent mass matrix formulation is used as well as a Bernoulli beam. The finite element model for all examined cases consists of ten beam elements.

Table 28.2: Model Properties

Material Properties	Geometric Properties
$E = 200\,MPa$	$h = 1\,cm$, $b = 1\,cm$, $l = 1\,m$
$\gamma = 25\,kN/m^3$	$A = 1\,cm^2$, $I = 0.1\,cm^4$, $\mu = 0.025\,t/m$

Table 28.3: Results

Eigenfrequency	SOF. [Hz]	Ref. [Hz]
simple cantilever	0.457	0.457
cantilever with simply supported end	2.004	2.003
simply supported	1.283	1.283
both ends fixed	2.907	2.907

28.4 Conclusion

The purpose of this example is to test the eigenvalue capability of the program w.r.t. different options. It has been shown that the eigenfrequencies for all beam systems are calculated accurately.

28.5 Literature

[15] K. Holschemacher. *Entwurfs- und Berechnungstafeln für Bauingenieure*. 3rd. Bauwerk, 2007.
[29] S. Timoshenko. *Vibration Problems in Engineering*. 2nd. D. Van Nostrand Co., Inc., 1937.

29 BE26: Response of a SDOF System to Harmonic Excitation

Overview

Element Type(s):	SPRI, DAMP
Analysis Type(s):	DYN
Procedure(s):	TSTP
Topic(s):	
Module(s):	DYNA
Input file(s):	harmonic_damped.dat, harmonic_undamped.dat

29.1 Problem Description

This problem consists of an elastic SDOF system undergoing forced vibration, as shown in Fig. 29.1. The response of an undamped and damped system is determined and compared to the reference solution.

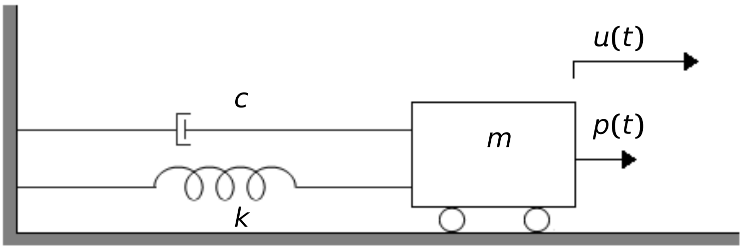

Figure 29.1: Problem Description

29.2 Reference Solution

A harmonic force is $p(t) = p_o \sin \omega_p t$, where p_o is the amplitude value of the force and its frequency ω_p is called the exciting frequency. The differential equation governing the forced harmonic vibration of a damped system is given by [27] [28]:

$$m\,\ddot{u} + c\,\dot{u} + k\,u = p_o \sin \omega_p t \tag{29.1}$$

$$m\,\ddot{u} + k\,u = p_o \sin \omega_p t \tag{29.2}$$

For undamped systems it simplifies to Eq. 29.2. Subjected also to initial conditions, $u(0)$ and $u(\dot{0})$, the total solution to Eq. 29.2 is:

$$u(t) = \underbrace{u(0) \cos \omega_n t + \left[\frac{\dot{u}(0)}{\omega_n} - \frac{p_o}{k}\,\frac{\omega_p/\omega_n}{1-(\omega_p/\omega_n)^2}\right] \sin \omega_n t}_{transient} + \underbrace{\frac{p_o}{k}\,\frac{1}{1-(\omega_p/\omega_n)^2} \sin \omega_p t}_{steadystate} \tag{29.3}$$

Eq. 29.3 shows, that u(t) contains two distinct vibration components, first the term $sin\,\omega_p t$ gives a vibration at the exciting frequency and second the terms $sin\,\omega_n t$ and $cos\,\omega_n t$ give a vibration at the natural frequency of the system. The first term is the steady state vibration, corresponding to the applied force and the latter is the transient vibration, depending on the initial conditions. It exists even if the initial conditions vanish, in which case it becomes

$$u(t) = \frac{p_o}{k} \frac{1}{1-(\omega_p/\omega_n)^2} \left[sin\,\omega_p t - \frac{\omega_p}{\omega_n} sin\,\omega_n t \right] \tag{29.4}$$

For the case of a damped SDOF system, the total solution is given by

$$u(t) = \underbrace{e^{-\xi\omega_n t}\left[A\,cos\,\omega_D t + B\,sin\,\omega_D t\right]}_{transient} + \underbrace{C\,sin\,\omega_p t + D\,cos\,\omega_p t}_{steadystate} \tag{29.5}$$

The coefficients C and D are determined from the particular solution of the differential equation of motion (Eq. 29.1), whereas A and B are determined in terms of the initial conditions. For the special case of zero initial conditions, the coefficients are given by

$$C = \frac{p_o}{k} \frac{1-(\omega_p/\omega_n)^2}{[1-(\omega_p/\omega_n)^2]^2 + [2\xi(\omega_p/\omega_n)]^2} \tag{29.6}$$

$$D = \frac{p_o}{k} \frac{-2\xi(\omega_p/\omega_n)}{[1-(\omega_p/\omega_n)^2]^2 + [2\xi(\omega_p/\omega_n)]^2} \tag{29.7}$$

$$A = -D \tag{29.8}$$

$$B = \frac{A\,\xi - C\,(\omega_p/\omega_n)}{\sqrt{1-\xi^2}} \tag{29.9}$$

For the special case where the exciting frequency equals the natural frequency of the SDOF system, we observe the resonant response. For the undamped system, the steady state response amplitude tends towards infinity as we approach unity and the peak values build up linearly, as shown in Fig. 29.2. For the damped case though, they build up in accordance to $(u_{st}/2\xi)e^{-\xi\omega_n t}$ and towards a steady state level, as shown in Fig. 29.2. The static deformation u_{st} = p_o/k, corresponds to the displacement which would be produced by the load p_o if applied statically, and serves as a measure of amplitude.

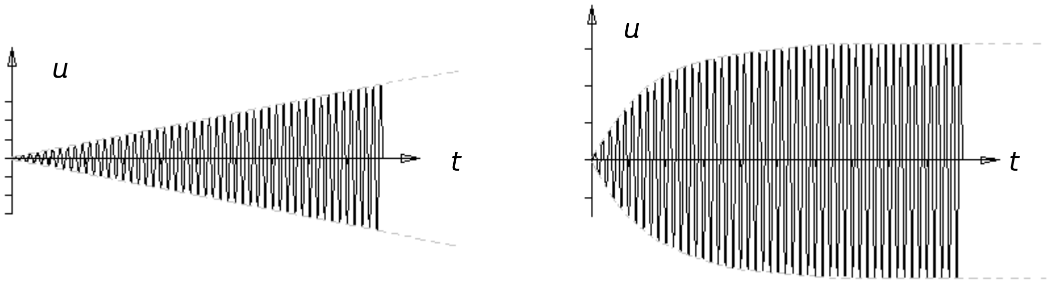

Undamped system

Damped system

Figure 29.2: Response to Resonant Loading for at-rest initial conditions

29.3 Model and Results

The properties of the model are defined in Table 29.1. The system is excited by a harmonic sinusoidal force and undergoes a forced vibration with zero initial conditions. The cases of the elastic damped and undamped SDOF system with a frequency ratio $\omega_p/\omega_n = 2$ are examined and their responses are compared to the exact solutions presented in Section 29.2. The resonance response is also examined for both systems, as shown in Fig. 29.4.

Table 29.1: Model Properties

Model Properties	Excitation Properties
$m = 1\,t$	$u(0) = 0$
$k = 4\pi^2\,kN/m$	$u(\dot{0}) = 0$
$T = 1\,sec$	$p_0 = 10\,kN$
$\xi = 2\,\%$	$\omega_p = 2\,\omega_n$

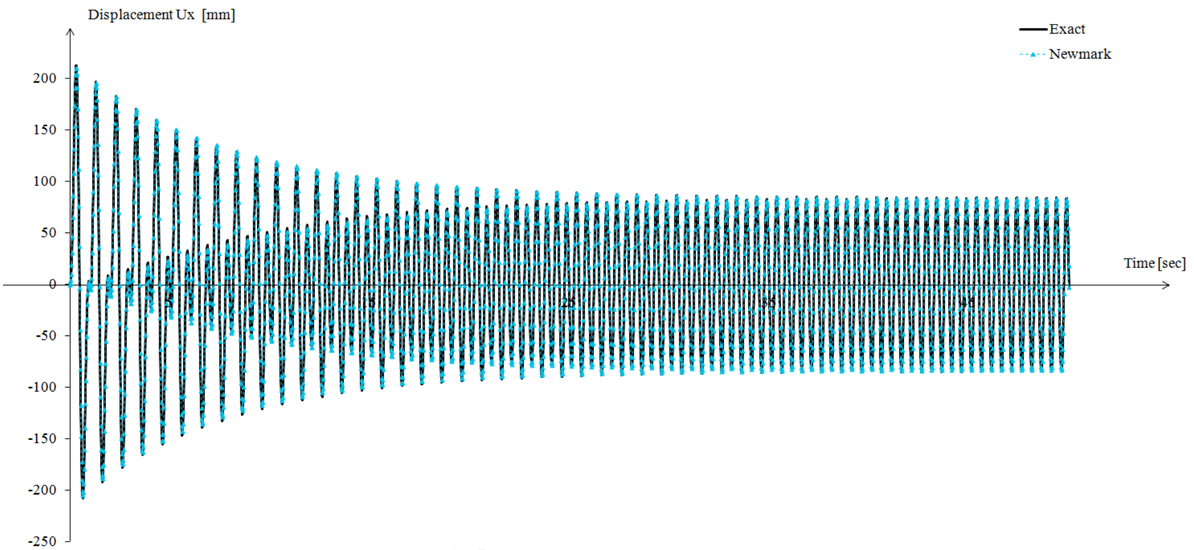

(a) Damped system

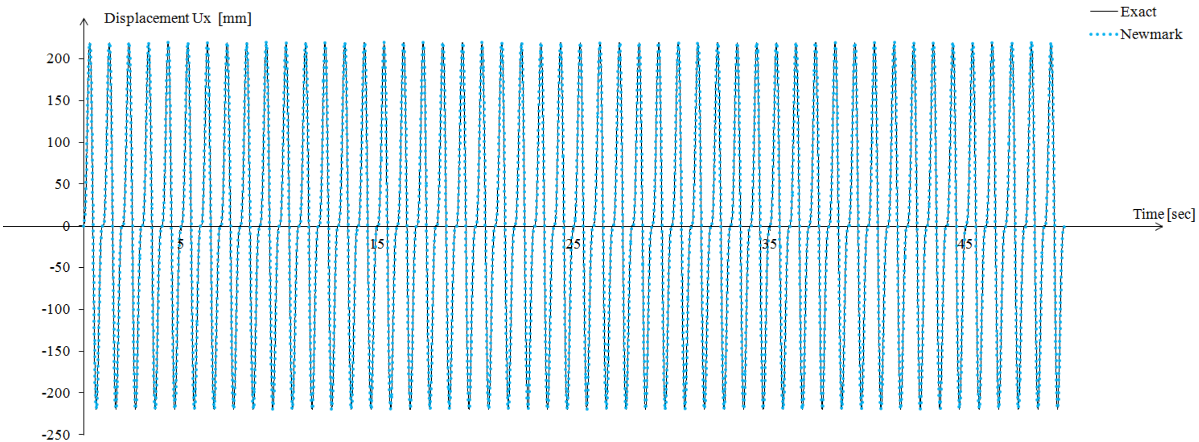

(b) Undamped system

Figure 29.3: Response to Harmonic Loading for at-rest initial conditions and ratio $\omega_p/\omega_n = 2$: (a) $\xi = 2\%$, (b) $\xi = 0$

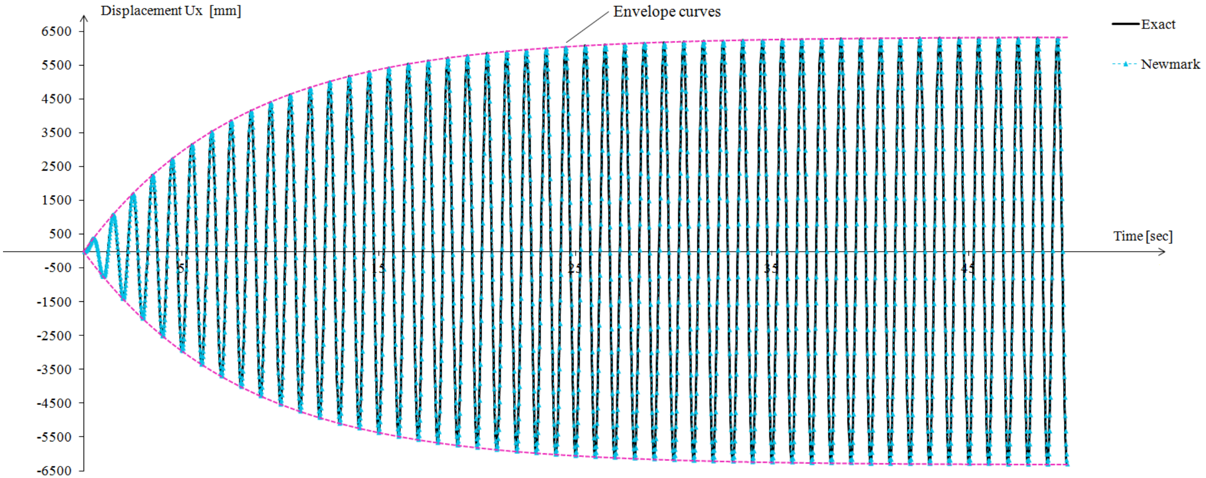

(a) Damped system

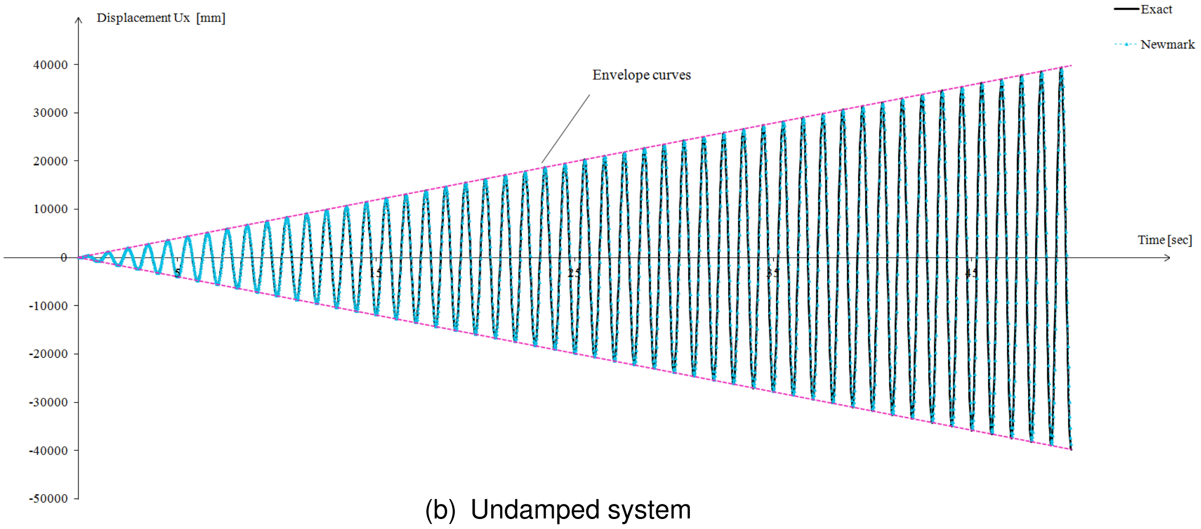

(b) Undamped system

Figure 29.4: Response to Resonant Loading ($\omega_p/\omega_n = 1$) for at-rest initial conditions: (a) $\xi = 2\%$, (b) $\xi = 0$

29.4 Conclusion

The purpose of this example is to test the calculation of the response of a dynamic system in terms of a harmonic loading function. It has been shown that the behaviour of the system is captured adequately.

29.5 Literature

[27] R. W. Clough and J. Penzien. *Dynamics of Structures*. 3rd. Computers & Structures, Inc., 2003.
[28] A. K. Chopra. *Dynamics of Structures: Theory and Applications to Earthquake Engineering*. Prentice Hall, 1995.

30 BE27: Response of a SDOF System to Impulsive Loading

Overview	
Element Type(s):	SPRI
Analysis Type(s):	DYN
Procedure(s):	TSTP
Topic(s):	
Module(s):	DYNA
Input file(s):	impulse_sine_wave.dat, impulse_rectangular.dat

30.1 Problem Description

This problem consists of an elastic undamped SDOF system undergoing forced vibration (Fig. 30.1) due to an impulsive loading as the one shown in Fig. 30.2. The response of the system is determined and compared to the exact reference solution.

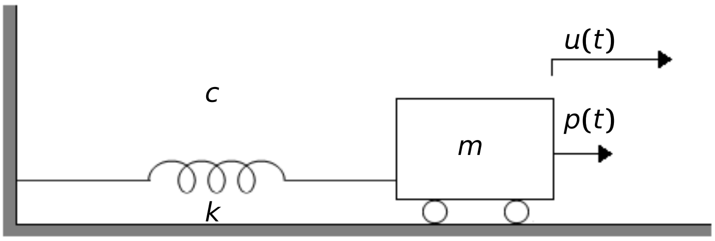

Figure 30.1: Problem Description

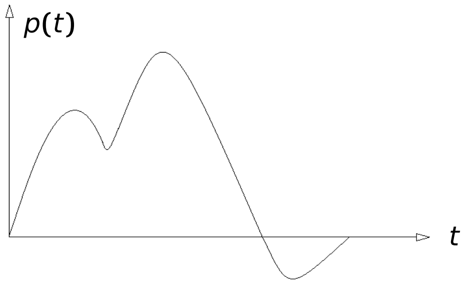

Figure 30.2: Arbitrary Impulsive Loading

30.2 Reference Solution

Another special case of dynamic loading of the SDOF system is the impulsive load. Such a load consists of a single principal impulse of arbitrary form, as illustrated in Fig. 30.2, and generally is of relatively short duration. Damping has much less importance in controlling the maximum response of a structure to impulsive loads than for periodic or harmonic loads because the maximum response to a particular impulsive load will be reached in a very short time, before the damping forces can absorb much energy from the structure [27]. Therefore the undamped response to impulsive loads will be considered in this Benchmark.

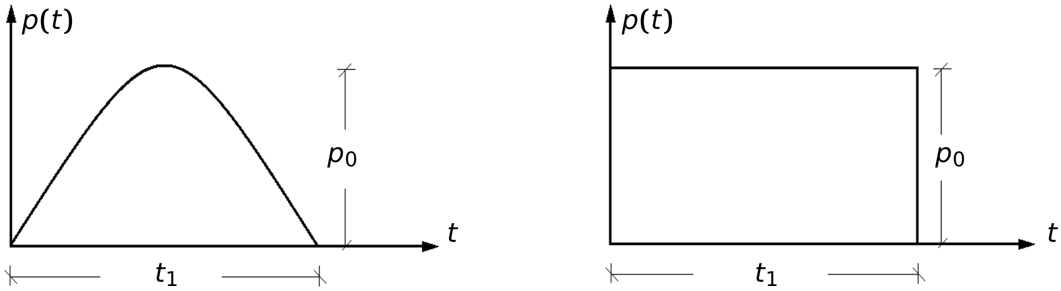

(a) Half sine wave (b) Rectangular

Figure 30.3: Examined Impulse Loading

The response to an impulse loading is always divided into two phases, the first corresponds to the forced vibration phase in the interval during which the load acts and the second corresponds to the free vibration phase which follows. Let us consider the case, where the structure is subjected to a single half sine wave loading as shown in Fig. 30.3(a). Assuming that the system starts from rest, the undamped response ratio time history $R(t) = u(t)/(p_0/k)$, is given by the simple harmonic load expression

$$R(t) = \frac{1}{1-\beta^2}\left[sin\;\omega_p t - \beta\;sin\;\omega_n t\right] \tag{30.1}$$

where $\beta = \omega_p/\omega_n$, p_o is the amplitude value of the force and ω_p its frequency. Introducing the non dimensional time parameter $\alpha = t/t_1$ so that $\omega_p t = \pi\alpha$ and $\omega_n t = \pi\alpha/\beta$, we can rewrite the equation accordingly

$$R(\alpha) = \frac{1}{1-\beta^2}\left[sin\;\pi\alpha - \beta\;sin\;\frac{\pi\alpha}{\beta}\right] \qquad 0 \leq \alpha \leq 1 \tag{30.2}$$

where t_1 the duration of the impulse and $\beta \equiv T/2t_1$. This equation is valid only for phase I corresponding to $0 \leq \alpha \leq 1$. While it is very important to understand the complete time history behaviour as shown in Fig. 30.4, the engineer is usually only interested in the maximum value of response as represented by Points a, b, c, d, and e. If a maximum value occurs in Phase I, the value of α at which it occurs can be determined by differentiating Eq. 30.2 with respect to α and equating to zero

$$\frac{d\,R(\alpha)}{d\,\alpha} = 0 \tag{30.3}$$

solving for α yields the α values for the maxima

$$\alpha = \frac{2\beta n}{\beta + 1} \qquad n = 0, 1, 2, \ldots \qquad 0 \leq \alpha \leq 1 \tag{30.4}$$

For phase II where $t \geq t_1$ and the free vibration occurs, the value of α is not necessary and the maximum response is given by

$$R_{max} = \left[\frac{-2\beta}{1-\beta^2}\right] cos\,\frac{\pi}{2\beta} \qquad \alpha \geq 1 \tag{30.5}$$

Accordingly for the case of a rectangular impulse loading Fig. 30.3(b), the general response ratio solution for at rest initial conditions and for phase I is given by

$$R\,(\alpha) = 1 - cos\,2\pi\,\frac{t_1}{T}\,\alpha \qquad 0 \leq \alpha \leq 1 \tag{30.6}$$

The maximum response ratio R_{max} is given again in terms of α and can be determined in the same manner by differentiating Eq. 30.6 with respect to α and equating to zero, yielding

$$\alpha = \beta n \qquad n = 0, 1, 2, \ldots \qquad 0 \leq \alpha \leq 1 \tag{30.7}$$

For phase II, the maximum response of the free vibrating system is given by

$$R_{max} = 2\,sin\,\pi\,\frac{t_1}{T} \qquad \alpha \geq 1 \tag{30.8}$$

Special attention has to be given in the case of β = 1 where the expression of the response ratio becomes indeterminate and the L' Hospital's rule has to be utilised.

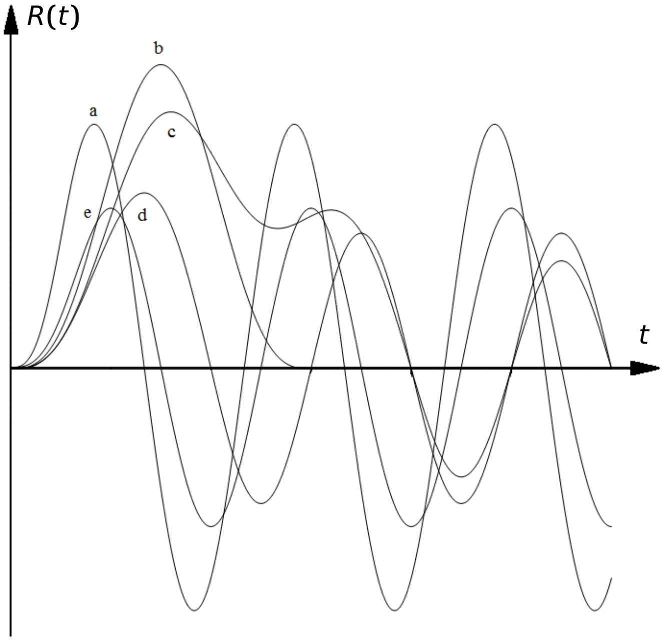

Figure 30.4: Response Ratios due to Half Sine Pulse

30.3 Model and Results

In the expressions derived before, the maximum response produced in an undamped SDOF structure by each type of impulsive loading depends only on the ratio of the impulse duration to the natural period of the structure t_1/T. Thus, it is useful to plot the maximum value of response ratio $Rmax$ as a function of t_1/T for various forms of impulsive loading. Such plots are commonly known as displacement-response spectra and are derived here, for two forms of loading, a rectangular and a half sine wave impulse.

Generally plots like these can be used to predict with adequate accuracy the maximum effect to be expected from a given type of impulsive loading acting on a simple structure. The properties of the model are defined in Table 30.1. The resulting figures are presented in Fig. 30.5.

Table 30.1: Model Properties

Model Properties	Excitation Properties
$m = 1\,t$	$u(0) = 0$
$k = 4\pi^2\,kN/m$	$u(\dot{0}) = 0$
$T = 1\,sec$	$p_0 = 10\,kN$

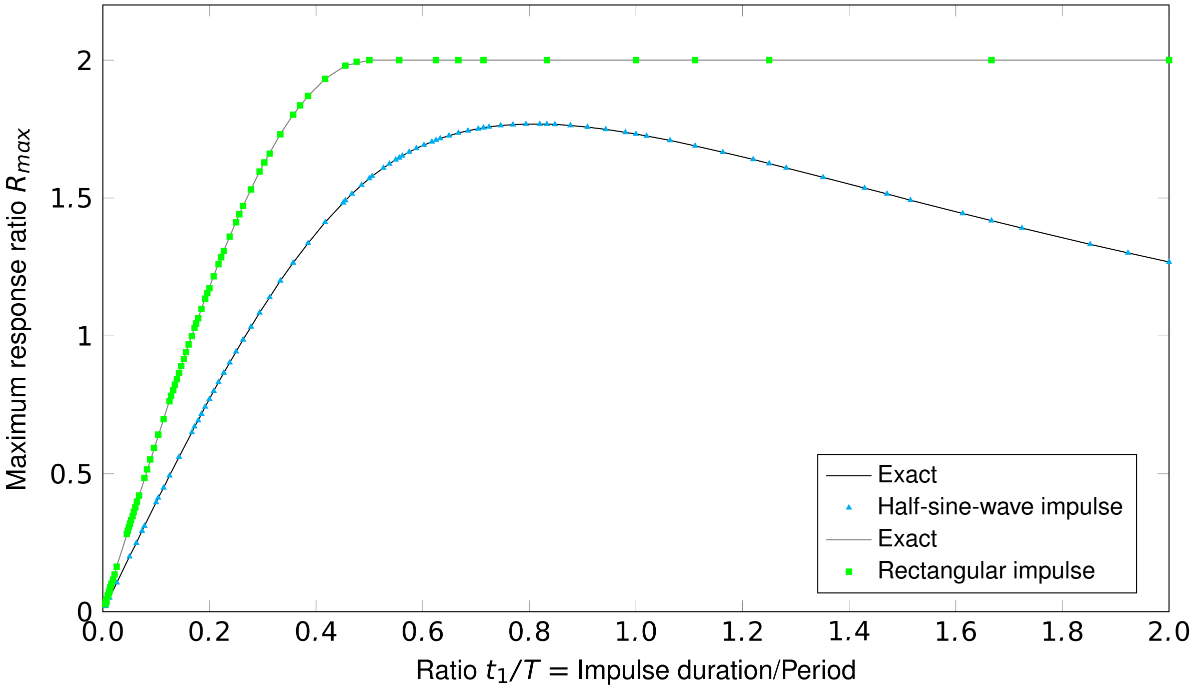

Figure 30.5: Displacement - Response Spectra for Two Types of Impulse

30.4 Conclusion

The purpose of this example is to test the calculation of the response of a dynamic system in terms of an impulsive loading. It has been shown that the behaviour of the system is captured adequately.

30.5 Literature

[27] R. W. Clough and J. Penzien. *Dynamics of Structures*. 3rd. Computers & Structures, Inc., 2003.

31 BE28: Cylindrical Hole in an Infinite Elastic Medium

Overview	
Element Type(s):	C2D
Analysis Type(s):	STAT
Procedure(s):	
Topic(s):	SOIL
Module(s):	TALPA
Input file(s):	hole_elastic.dat

31.1 Problem Description

This problem consists of a cylindrical hole in an infinite elastic medium subjected to a constant in-situ state, as shown in Fig. 31.1. The material is assumed to be isotropic and elastic. The stresses and the displacements are verified.

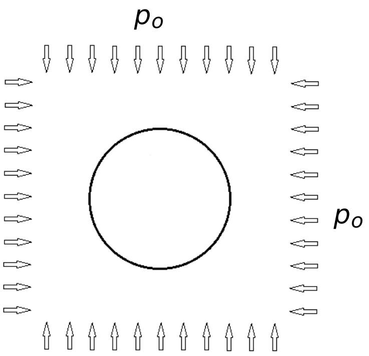

Figure 31.1: Problem Description

31.2 Reference Solution

The problem of calculating the displacements and stresses outside a circular hole in an infinite elastic medium, with a uniform stress state far from the hole, was first solved by the German engineer Kirsch in 1898. It is a rather important topic due to the fact that most of the holes drilled through rock are of circular section.

The classical Kirsch solution can be used to find the radial and tangential displacement fields and stress distributions, for a cylindrical hole in an infinite isotropic elastic medium under plane strain conditions. The stresses σ_r and σ_θ for a point at polar coordinates (r, θ) outside the cylindrical opening of radius α are given by [30]:

$$\sigma_r = \frac{p_1 + p_2}{2}\left(1 - \frac{\alpha^2}{r^2}\right) + \frac{p_1 - p_2}{2}\left[1 - \frac{4\alpha^2}{r^2} + \frac{3\alpha^4}{r^4}\right] cos\,2\theta \tag{31.1}$$

$$\sigma_\theta = \frac{p_1 + p_2}{2}\left(1 + \frac{\alpha^2}{r^2}\right) - \frac{p_1 - p_2}{2}\left(1 + \frac{3\alpha^4}{r^4}\right) cos\,2\theta \tag{31.2}$$

The radial outward displacement u_r, assuming conditions of plane strain, is given by:

$$u_r = \frac{p_1 + p_2}{4G} \frac{\alpha^2}{r} + \frac{p_1 - p_2}{4G} \frac{\alpha^2}{r} \left[4\,(1-\nu) - \frac{\alpha^2}{r^2} \right] cos\, 2\theta \tag{31.3}$$

where G is the shear modulus, ν the Poisson ratio and p_1, p_2, θ, r are defined in Fig. 31.2

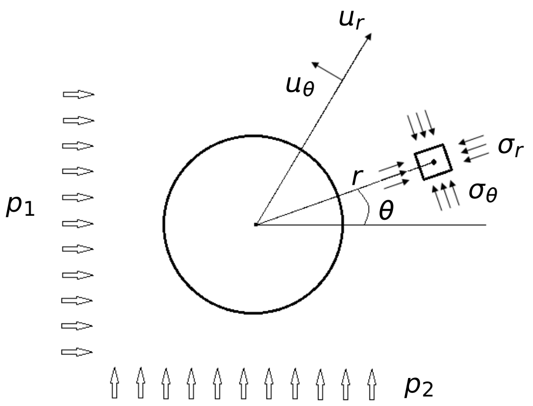

Figure 31.2: Cyllindrical Hole in an Infinite Elastic Medium

31.3 Model and Results

The properties of the model are defined in Table 31.1. The radius of the hole is $1\ m$ and is assumed to be small compared to the length of the cylinder, therefore $2D$ plane strain conditions are in effect. A fixed external boundary is located $29.7\ m$ from the hole center. The model is presented in Fig. 31.3. The stresses and displacements are calculated and verified with respect to the formulas provided in Section 31.2.

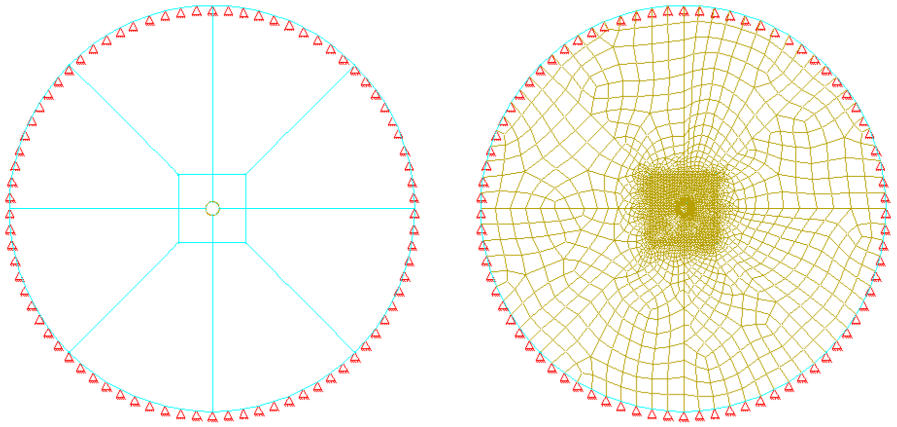

Figure 31.3: Finite Element Model

Table 31.1: Model Properties

Material Properties	Geometric Properties	Pressure Properties
$E = 6777.9\ MPa$	$\alpha = 1\ m$	$P_o = 30\ MPa$
$\nu = 0.21$	$r_{boundary} = 29.7\ m$	

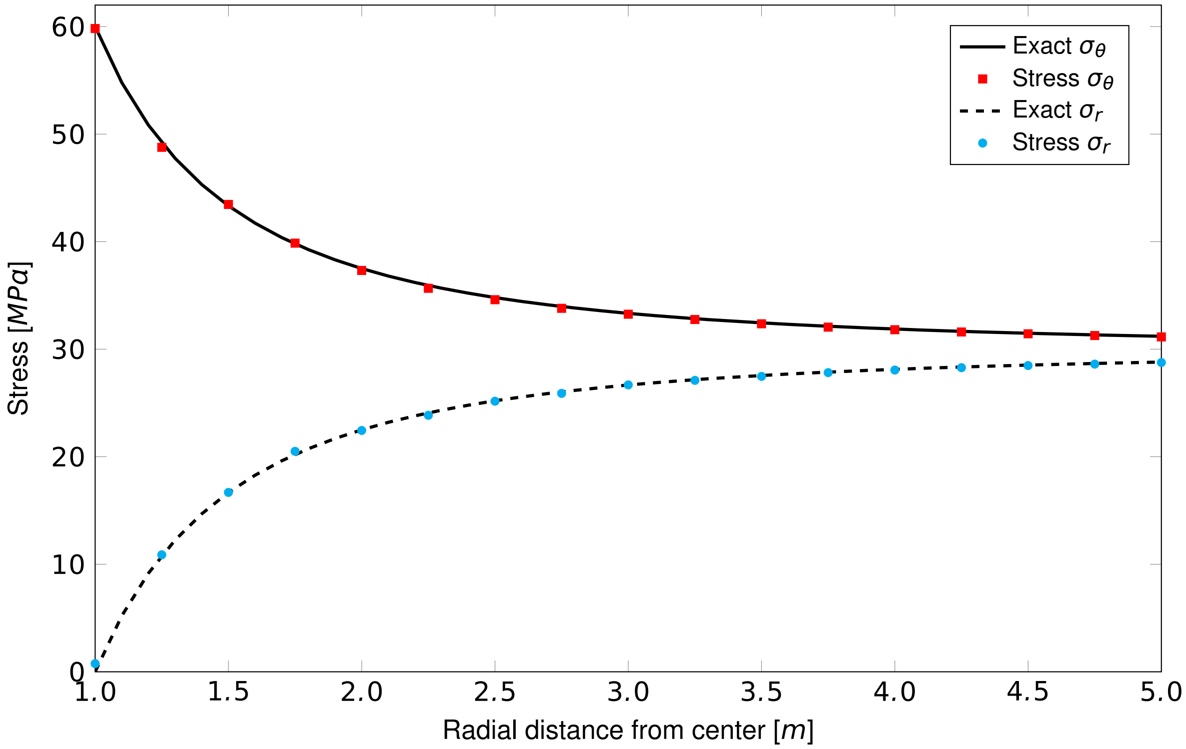

Figure 31.4: Radial and Tangential Stresses for Cylindrical Hole in Infinite Elastic Medium

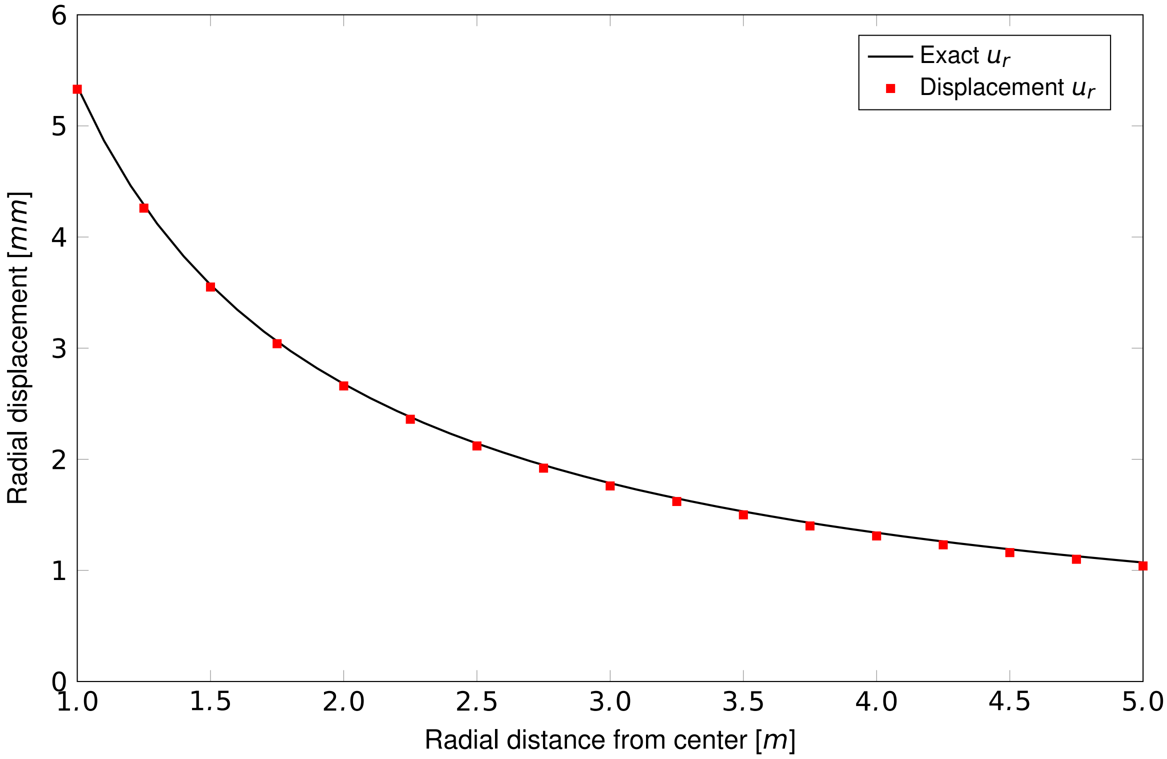

Figure 31.5: Radial Displacement for Cylindrical Hole in Infinite Elastic Medium

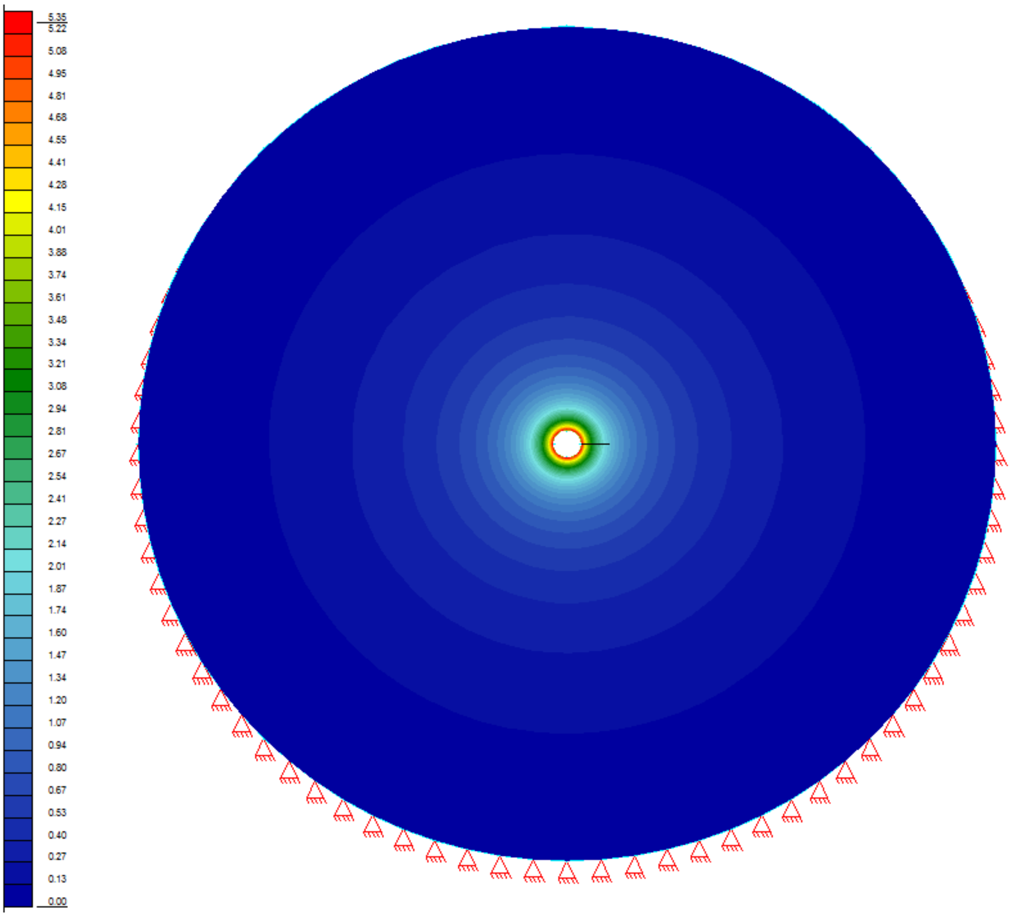

Figure 31.6: Total Displacement Distribution

Figures 31.4 and 31.5 show the radial and tangential stress and the radial displacement respectively, along a line, lying on the *X*-axis. This line (cut) can be visualised in Fig. 31.6, where the radial displacement distribution is illustrated. The results are in very good agreement with the reference solution.

31.4 Conclusion

This example verifies the deformation and stresses behaviour of a cylindrical hole in an infinite elastic medium. It has been shown that the behaviour of the model is captured accurately.

31.5 Literature

[30] J. C. Jaeger, N. G. W. Cook, and R. W. Zimmerman. *Fundamentals of Rock Mechanics*. 4th. Blackwell Publishing, 2007.

32 BE29: Cylindrical Hole in an Infinite Mohr-Coulomb Medium

Overview

Element Type(s):	C2D
Analysis Type(s):	STAT, MNL
Procedure(s):	LSTP
Topic(s):	SOIL
Module(s):	TALPA
Input file(s):	hole_mohr.dat

32.1 Problem Description

This problem verifies stresses for the case of a cylindrical hole in an infinite elastic-plastic medium subjected to a constant in-situ state, as shown in Fig. 32.1. The material is assumed to be linearly elastic and perfectly plastic with a failure surface defined by the Mohr-Coulomb criterion. The stresses and the displacements are verified.

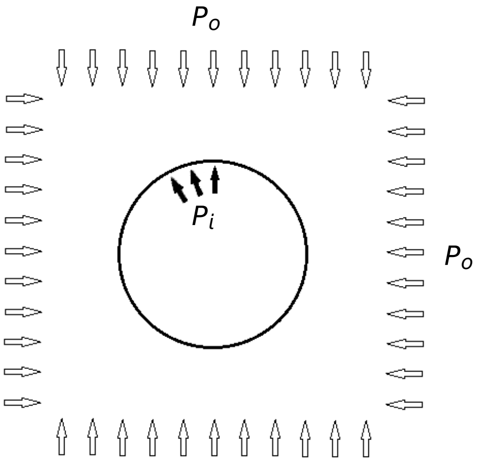

Figure 32.1: Problem Description

32.2 Reference Solution

Consider a hollow cylinder with inner radius a and outer radius r, under plane strain conditions, with a uniform pressure applied to its outer surface. If this pressure is slowly increased from 0 to some value P_o, at first the cylinder will everywhere be in the elastic zone. As Po increases further, the yielding will start, the yielded zone will grow radially outward, and the cylinder will consist of an inner annular region that has yielded and an outer annulus that is still in its elastic state [30]. A specialised problem is now the calculation of the stresses outside a cylindrical hole in an infinite elastic-perfectly-plastic medium, here with a failure surface defined by the Mohr-Coulomb criterion. Assume that the rock mass is initially under hydrostatic stress P_o and then a circular hole of radius a is drilled into the rock, so that the stress at $r = a$ is reduced to some value P_i. The yield zone radius R_o is given analytically by the theoretical model based on the solution of Salencon [31]

$$R_o = \alpha \left(\frac{2}{K_p + 1} \frac{P_o + \frac{q}{K_p - 1}}{P_i + \frac{q}{K_p - 1}} \right)^{\frac{1}{K_p - 1}} \tag{32.1}$$

where α is the radius of the hole, P_o the initial in-situ stress, P_i the internal pressure and K_p, q are given by

$$K_p = \frac{1 + sin\,\phi}{1 - sin\,\phi} \tag{32.2}$$

$$q = 2c\,tan\,(45 + \phi/2) \tag{32.3}$$

The parameters c and ϕ correspond to the cohesion and angle of friction of the medium respectively. For sufficiently small values of P_o, where P_o ¡ P_i holds, the medium will be in its elastic state, and the stresses will be given by [30] [32]

$$\sigma_r = P_o - (P_o - \sigma_{re}) \left(\frac{R_o}{r} \right)^2 \tag{32.4}$$

$$\sigma_\theta = P_o + (P_o - \sigma_{re}) \left(\frac{R_o}{r} \right)^2 \tag{32.5}$$

where r is the distance from the field point to the center of the hole and σ_{re} is the radial stress at the elastic-plastic interface

$$\sigma_{re} = \frac{1}{K_p + 1} (2P_o - q) \tag{32.6}$$

For $P_o > P_i$, the rock will fail within some annular region surrounding the borehole. The stresses in the yielded zone will be given by

$$\sigma_r = -\frac{q}{K_p - 1} + \left(P_i + \frac{q}{K_p - 1} \right) \left(\frac{r}{\alpha} \right)^{K_p - 1} \tag{32.7}$$

$$\sigma_r = -\frac{q}{K_p - 1} + K_p \left(P_i + \frac{q}{K_p - 1} \right) \left(\frac{r}{\alpha} \right)^{K_p - 1} \tag{32.8}$$

32.3 Model and Results

The properties of the model are defined in Table 32.1. The radius of the hole is $1\ m$ and is assumed to be small compared to the length of the cylinder, therefore $2D$ plane strain conditions are in effect. A fixed external boundary is located $29.7\ m$ from the hole center. The model is presented in Fig. 32.2. The stresses are calculated and verified with respect to the formulas provided in Section 32.2.

Table 32.1: Model Properties

Material Properties	Geometric Properties	Pressure Properties
$E = 6777.9\ MPa$	$\alpha = 1\ m$	$P_o = 30\ MPa$
$\nu = 0.21$	$r_{boundary} = 29.7\ m$	$P_i = 0$ or $1\ MPa$

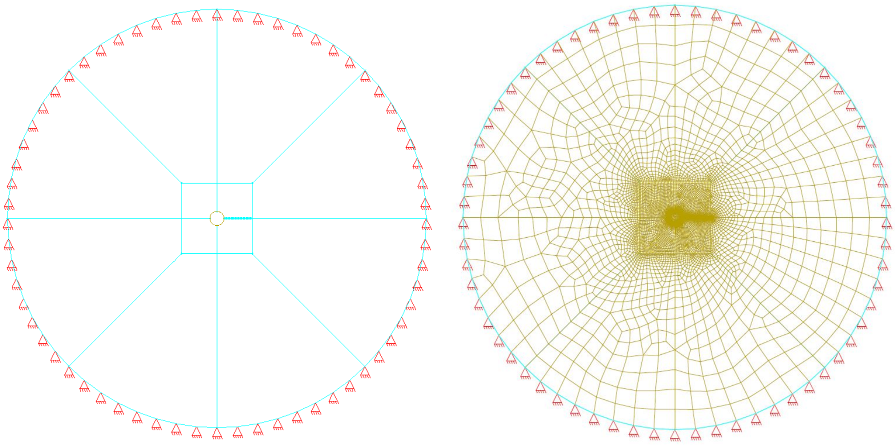

Figure 32.2: Finite Element Model

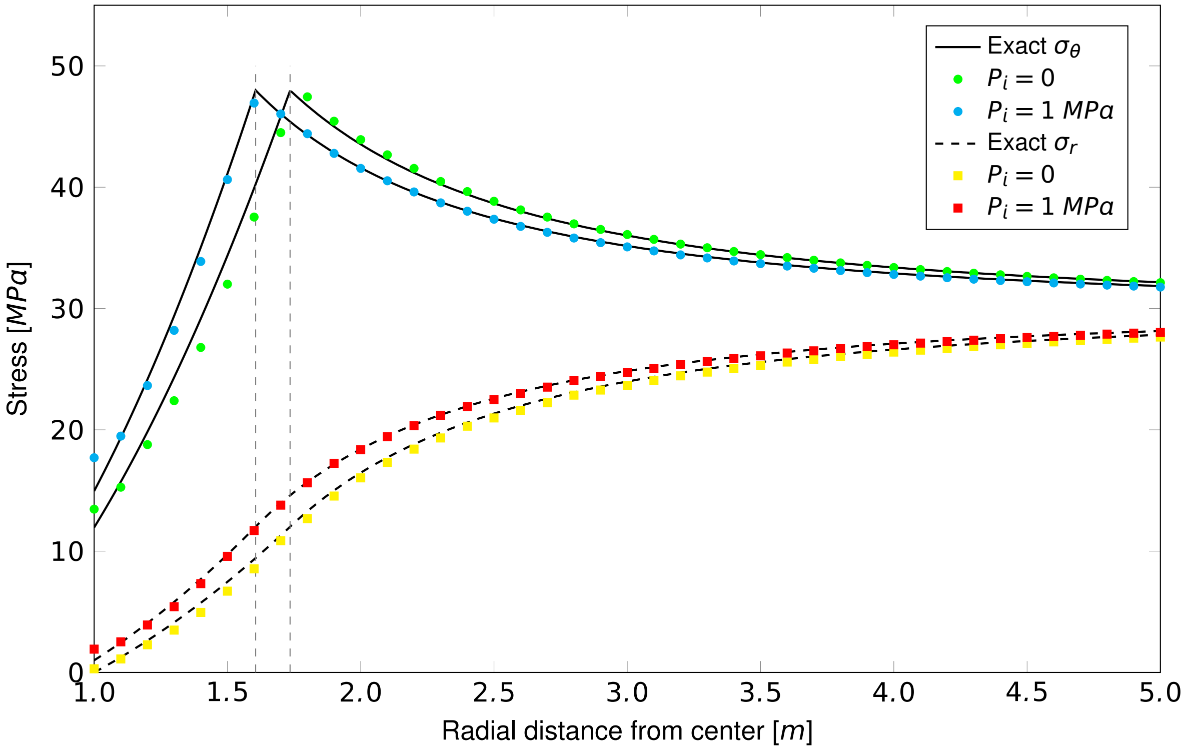

Figure 32.3: Radial and Tangential Stresses for Cylindrical Hole in Infinite Mohr-Coulomb Medium

Figure 32.3 show the radial and tangential stress, along a line, lying on the X-axis. Results are presented for two cases, first with no internal pressure and second with $P_i = 1\ MPa$. The results in both cases are in very good agreement with the reference solution.

32.4 Conclusion

This example verifies the stresses of a cylindrical hole in an infinite elastic-perfectly-plastic medium. It has been shown that the behaviour of the model is captured accurately.

32.5 Literature

[30] J. C. Jaeger, N. G. W. Cook, and R. W. Zimmerman. *Fundamentals of Rock Mechanics*. 4th. Blackwell Publishing, 2007.
[31] J. Salencon. “Contraction Quasi-Statique D’ une Cavite a Symetrie Spherique Ou Cylindrique Dans Un Milieu Elasto-Plastique”. In: *Annales Des Ports Et Chaussees* 4 (1969).
[32] *Phase 2 Stress Analysis Verification Manual Part I*. Rocscience Inc. 2009.

33 BE30: Strip Loading on an Elastic Semi-Infinite Mass

Overview

Element Type(s):	C2D
Analysis Type(s):	STAT
Procedure(s):	
Topic(s):	SOIL
Module(s):	TALPA
Input file(s):	strip_load.dat

33.1 Problem Description

This problem concerns the analysis of a strip loading on an elastic semi-infinite mass, as shown in Fig. 33.1. The material is assumed to be isotropic and elastic. The stresses are verified.

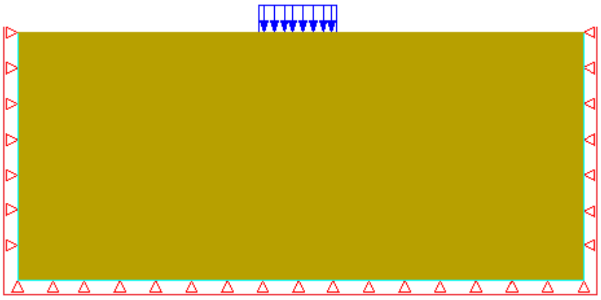

Figure 33.1: Problem Description

33.2 Reference Solution

The problem focuses on the calculation of the stresses due to a strip loading on an semi-infinite mass. The stresses under the surface are given by [33]:

$$\sigma_y = \frac{p}{\pi}\left[\alpha + sin\,\alpha\,cos\,(\alpha + 2\delta)\right] \tag{33.1}$$

$$\sigma_x = \frac{p}{\pi}\left[\alpha - sin\,\alpha\,cos\,(\alpha + 2\delta)\right] \tag{33.2}$$

and the principal stresses are

$$\sigma_1 = \frac{p}{\pi}\left[\alpha + sin\,\alpha\right] \tag{33.3}$$

$$\sigma_3 = \frac{p}{\pi}\left[\alpha - sin\,\alpha\right] \tag{33.4}$$

where p, α, δ are described in Fig. 33.2

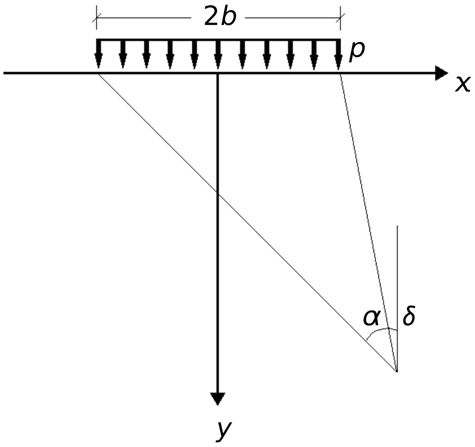

Figure 33.2: Vertical Strip Loading on a Semi-Infinite Mass

33.3 Model and Results

The properties of the model are defined in Table 33.1. The strip footing has a width of 2 m. The material is considered to be isotropic and elastic and plane strain conditions are in effect. For the analysis, boundary conditions are applied as shown in Fig. 33.3. The model is analysed with various dimensions in order to record the influence of the boundary in the results. The stresses are calculated and verified with respect to the formulas provided in Section 33.2. The results are printed for the case of a vertical line (cut) for $x = 0$ where the stresses in x and y coincide with the principal stresses.

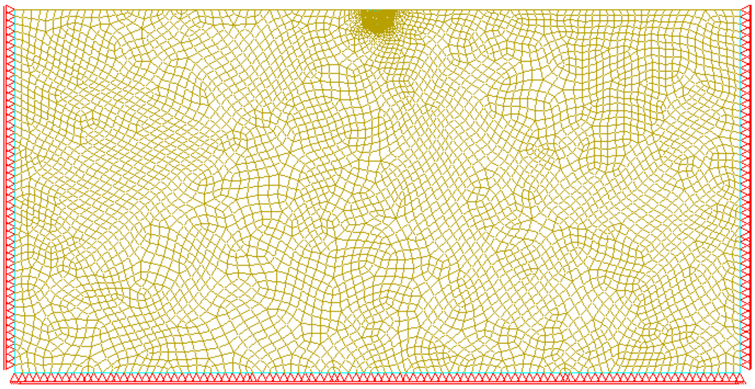

Figure 33.3: Finite Element Model

Table 33.1: Model Properties

Material Properties	Geometric Properties	Pressure Properties
$E = 20000\,MPa$	$H = 25, 50, 100\,m$	$P = 1\,MPa/area$
$\nu = 0.2$	$B = 2\,H$	

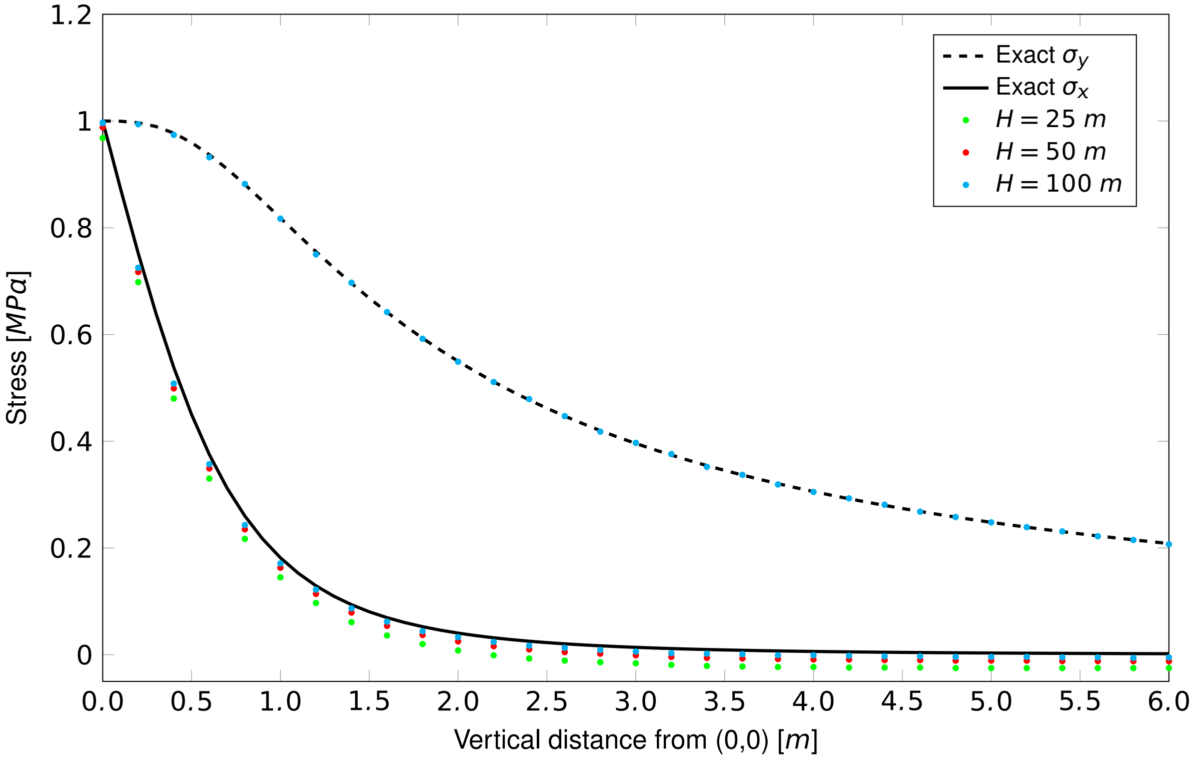

Figure 33.4: Comparison of Horizontal and Vertical Stresses Under the Strip Loading

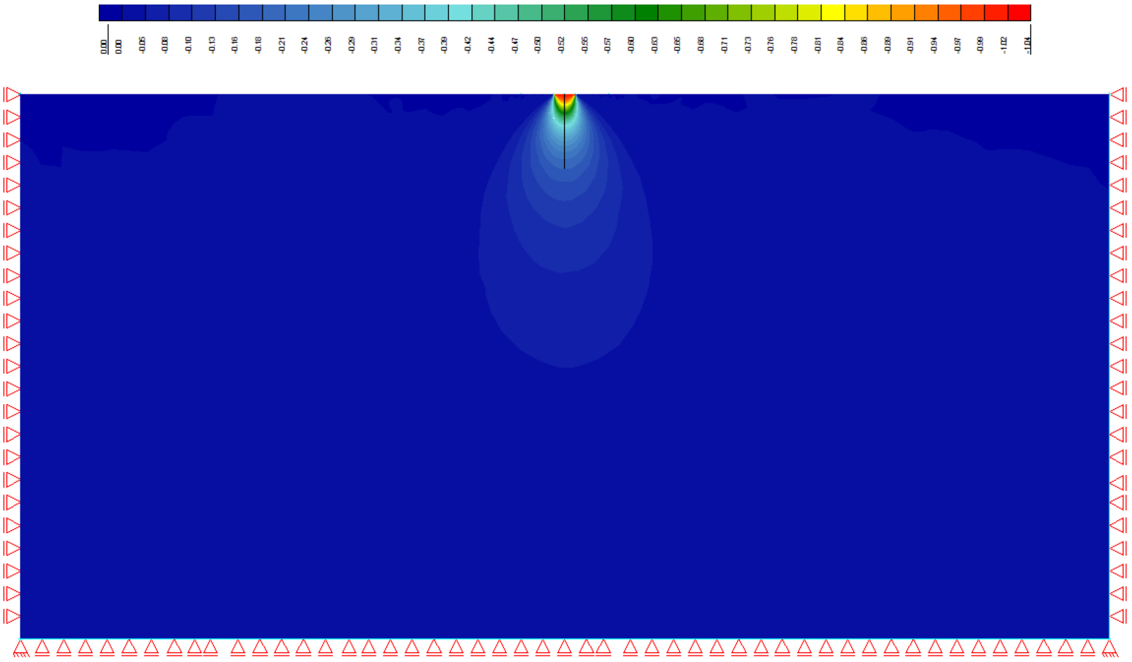
0.00
0.00
-0.05
-0.08
-0.10
-0.13
-0.16
-0.18
-0.21
-0.24
-0.26
-0.29
-0.31
-0.34
-0.37
-0.39
-0.42
-0.44
-0.47
-0.50
-0.52
-0.55
-0.57
-0.60
-0.63
-0.65
-0.68
-0.71
-0.73
-0.76
-0.78
-0.81
-0.84
-0.86
-0.89
-0.91
-0.94
-0.97
-0.99
-1.02
-1.04

Figure 33.5: Vertical Stress Distribution for a Strip Loading on a Semi-Infinite Mass

Fig. 33.4 shows the horizontal and vertical stress along the cutting line, for the analysed models with various dimensions. This line (cut) can be visualised in Fig. 33.5, where the contours of the vertical stress for the case of $H = 50\ m$ are illustrated. From the results of the stresses, it is evident that the vertical stresses are not influenced significantly from the dimensions of the model. On the contrary, for the horizontal stresses it is obvious, that as the boundary moves further away, its influence vanishes and the results are in very good agreement with the reference solution.

33.4 Conclusion

This example verifies the distribution of stresses of a semi-infinite mass under strip loading. It has been shown that the behaviour of the model is captured accurately.

33.5 Literature

[33] H.G. Poulos and E.H. Davis. *Elastic Solutions for Soil and Rock Mechanics*. Centre for Geotechnical Research, University of Sydney, 1991.

34 BE31: Snap-Through Behaviour of a Truss

Overview

Element Type(s): TRUS
Analysis Type(s): STAT, GNL
Procedure(s): LSTP
Topic(s):
Module(s): ASE
Input file(s): snap_through.dat

34.1 Problem Description

This problem is concerned with one of the fundamental geometric non-linearity (GNL) tests. A simple two-node truss, as shown in Fig. 34.1, is examined in terms of the limit load and snap-through behaviour.

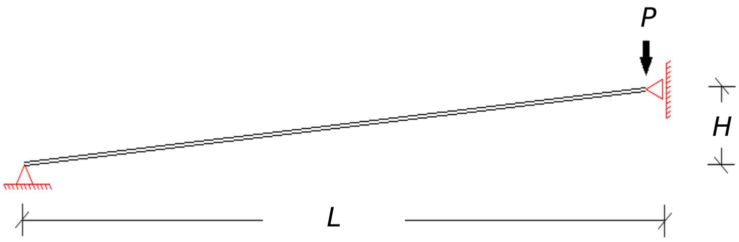

Figure 34.1: Problem Description

34.2 Reference Solution

In this problem a truss is pin-jointed to a rigid surface at one end and subjected to a transverse vertical point force at the other end as shown in Fig. 34.1. The loaded end is restrained to move only vertically and the truss in inclined with respect to the horizontal. This problem is effectively a symmetrical half of a two-bar structure and is utilised here in order to demonstrate the snap-through behaviour and limit points. The analytical solution assuming a shallow strut is given by [34] [14]

$$P = \frac{EAH^3}{2L^3}\left(\frac{2u}{H} + \frac{3u^2}{H^2} + \frac{u^3}{H^3}\right) \tag{34.1}$$

where the parameters H and L are shown in Fig. 34.1. The reference solution is plotted in Fig. 34.2.The load-displacement curve rises until it reaches a limit point A. If we continue further, the next point will be B, where the bar is horizontal and the vertical load reduces to zero. Further increments cause the bar to deflect below the horizontal axis until the second limit point is reached at point C. Note that after point B, the load reverses its sign and acts upwards. After point C, the bar continues its motion downwards until it reaches point D, where the vertical load is zero.

Note that under load-control approach, snap-through behaviour occurs after the first limit point A, where the bar suddenly jumps from point A to point E without any increase in the load. By switching from load-control to displacement-control, i.e. the displacement rather than the load is applied in small increments, the solution is able to progress beyond the limit point A, where further displacements cause the load to reduce as the bar reaches a horizontal position at B.

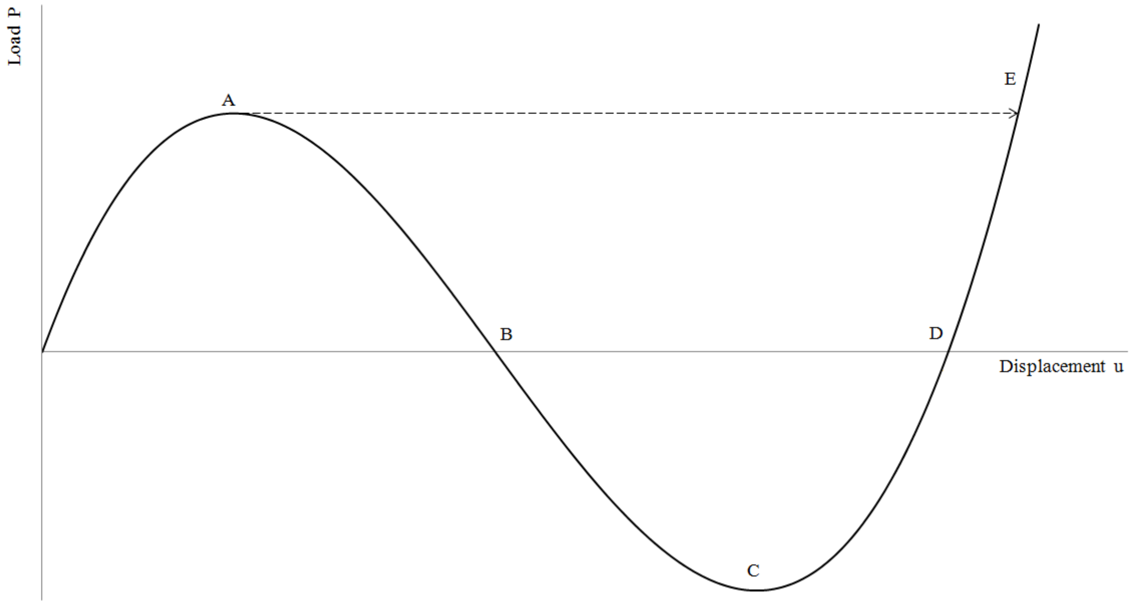

Figure 34.2: Analytical Load-Displacement Curve

34.3 Model and Results

The properties of the model are defined in Table 34.1. In the load-control approach, the load is applied in significantly small increments in order to be able to capture point A. In the displacement-control, the displacement increments are of $1\ mm$. The load-displacement curve for both approaches is presented in Fig. 34.3 and compared to the analytical solution. If we solve Eq. 34.1 with respect to the limit points, we observe that at point A the displacement is $10.57\ mm$ and the corresponding critical loading is P_{cr} = $9.6225\ N$.

Table 34.1: Model Properties

Material Properties	Geometric Properties	Loading
$E = 500 \times 10^3\ N/mm^2$	$H = 25\ mm$	$P = 10\ N$
$\nu = 0.4999 \approx 0.5$	$L = 2500\ mm$	$\Delta u = 1\ mm$
	$A = 100\ mm^2$	

Fig. 34.3 shows that the load-control approach reaches the first limit point and suddenly snaps to the new equilibrium state, corresponding to point E in Fig. 34.2. The value of the load obtained before the snap-through occurs, corresponding to point A, is P = $9.62\ N$, with a displacement of $10.415\ mm$, which is in very good agreement with the theoretical critical value P_{cr}. Furthermore, we can observe that the more suitable solution strategy, for such a simple system, for obtaining the load-deflection response is to adopt the displacement control approach, which clearly as shown in Fig. 34.3, has no difficulty with the local limit point at A and traces the complete equilibrium path.

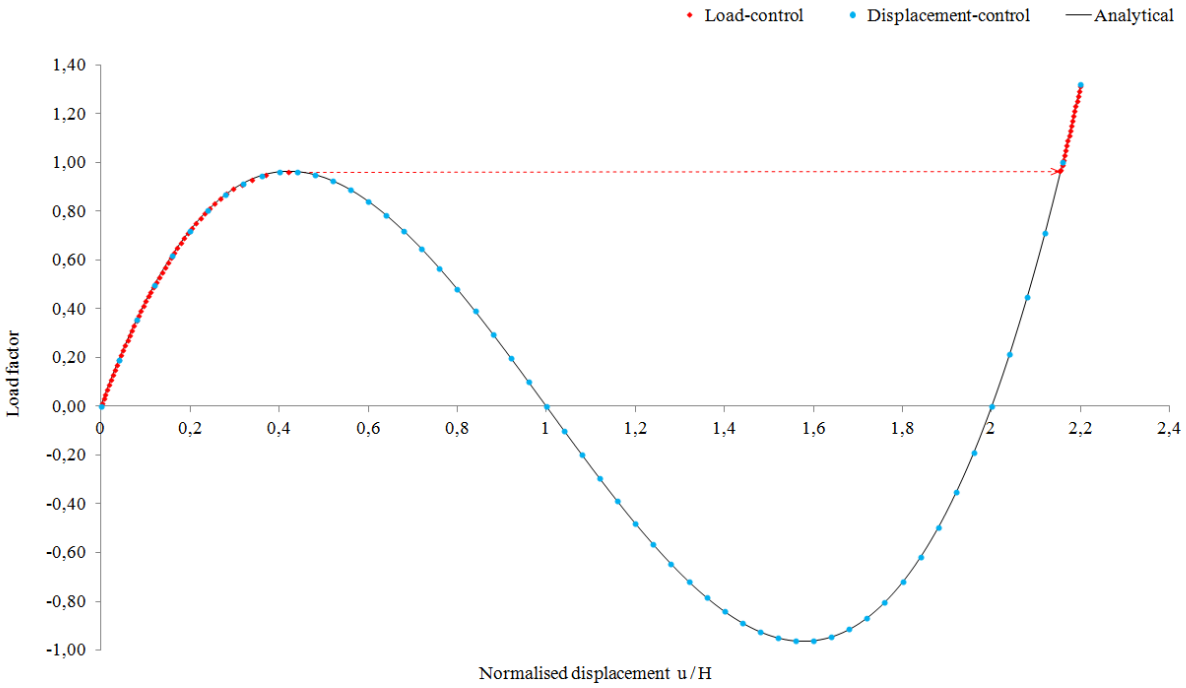

Figure 34.3: Calculated Load-Displacement Curve

34.4 Conclusion

This example verifies the determination of the limit load and snap-through behaviour of a simple truss. It has been shown that the geometric non-linear behaviour of the model is captured accurately.

34.5 Literature

[14] A. A. Becker. *Background to Finite Element Analysis of Geometric Non-linearity Benchmarks*. Tech. rep. NAFEMS, 1998.

[34] M. A. Crisfield. *Non-linear Finite Element Analysis of Solids and Structures - Volume 1*. John Wiley, 1991.

35 BE32: Thermal Extension of Structural Steel in case of Fire

Overview	
Element Type(s):	BF2D, SH3D
Analysis Type(s):	STAT, MNL
Procedure(s):	LSTP
Topic(s):	FIRE
Module(s):	TALPA, ASE
Input file(s):	thermal_extension, quad_32.dat

35.1 Problem Description

This benchmark is concerned with the validation of the structural analysis in case of fire with respect to the general calculation method according to DIN EN 1992-1-2. Therefore test case 4 is employed as presented in Annex CC of the standard DIN EN 1992-1-2/NA:2010-03 [35]. In this example the validation of the extension of structural steel, for the model of Fig. 35.1, at different constant temperature exposures is examined.

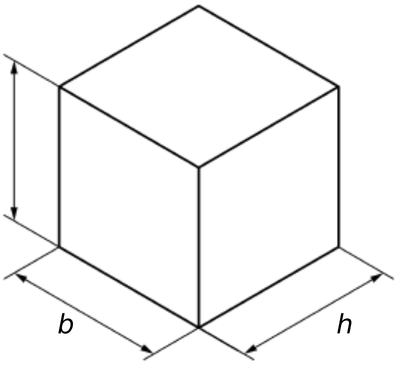

Figure 35.1: Problem Description

35.2 Reference Solution

The physical, mechanical and mathematical basics of engineering-based fire design programs, should be validated in terms of thermal, cross-sectional and system analysis. The aim of Annex CC [35] is, through a collection of test cases, to check their applicability for fire proof evaluation on real structures. For every example a parameter-dependent test matrix, for the relevant assessment criteria, is provided, where the computational accuracy of the program is examined. Results of existing analytical solutions or of approved programs are also provided, as well as the acceptable specified tolerances.

35.3 Model and Results

The properties of the model are defined in Table 35.1. A fictional beam, as depicted in Fig. 35.1, with cross-sectional dimensions b / h = $100/100$ mm and the length of 100 mm is examined. Different temperatures are assigned to the material S 355 of the cross-section. The analysis is performed with

TALPA, where the FIBER beam element is utilised, as well as with ASE, where the QUAD element is tested. The computed and the reference results are presented in Table 35.2, Fig. 35.2 and Table 35.3 for the FIBER beam and QUAD element, respectively.

Table 35.1: Model Properties

Material Properties	Geometric Properties	Test Properties
$S\ 355$	$l = 100\ mm$	Initial Conditions:
$f_{yk(20°C)} = 355\ N/mm^2$	$h = 100\ mm$	$\Theta = 20°C$
Stress-strain curve according to DIN EN 1993-1-2	$b = 100\ mm$	Homogeneous temperature component: $\Theta = 100, 300, 500, 600, 700, 900°C$

Table 35.2: Results for Thermal Elongation of Steel - FIBER

Θ [° C]	Ref. [35]	SOF.	$\|e_r\|$ [%]	Tol.
	Δl [mm]	$\Delta l'$ [mm]	or e [mm]	
100	0.09984	0.09984	0.000 mm	for $\Theta \leq 300$ ° C
300	0.37184	0.37184	0.000 mm	± 0.05 mm
500	0.67584	0.67584	0.000 %	
600	0.83984	0.83984	0.000 %	for $\Theta > 300$ ° C
700	1.01184	1.01184	0.000 %	± 1 %
900	1.18000	1.18000	0.000 %	

Table 35.3: Results for Thermal Elongation of Steel - QUAD

Θ [° C]	Ref. [35]	SOF.	$\|e_r\|$ [%]	Tol.
	Δl [mm]	$\Delta l'$ [mm]	or e [mm]	
100	0.09984	0.09984	0.000 mm	for $\Theta \leq 300$ ° C
300	0.37184	0.37184	0.000 mm	± 0.05 mm
500	0.67584	0.67584	0.000 %	
600	0.83984	0.83984	0.000 %	for $\Theta > 300$ ° C
700	1.01184	1.01184	0.000 %	± 1 %
900	1.18000	1.18000	0.000 %	

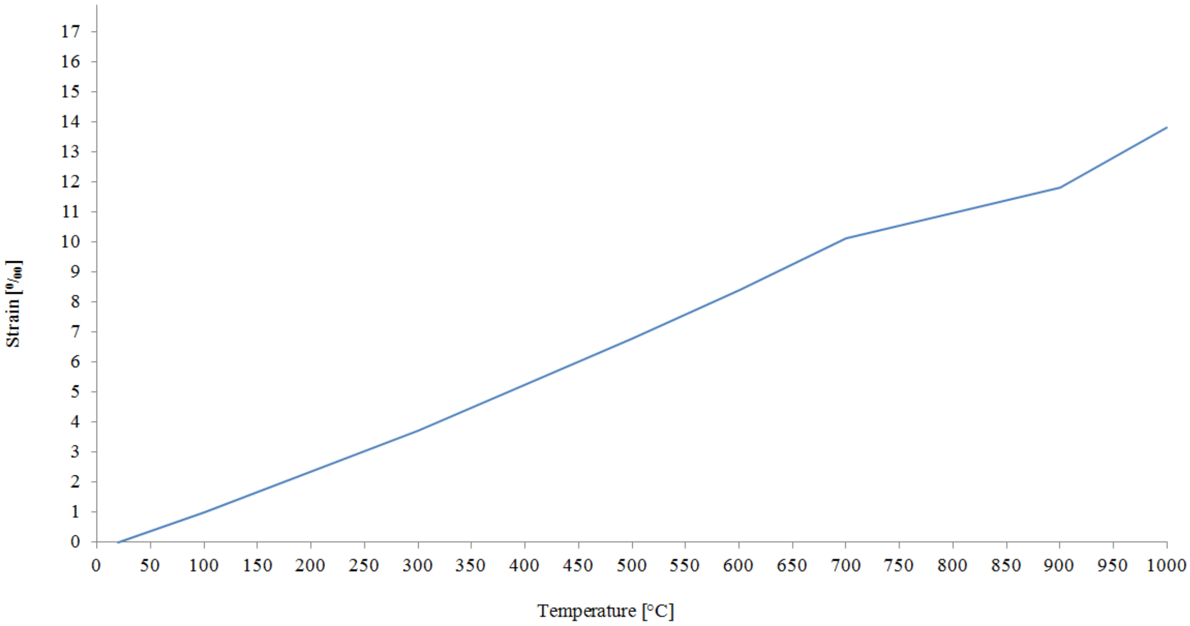

Figure 35.2: Temperature Strains

35.4 Conclusion

This example verifies the extension of structural steel at different constant temperature exposures. It has been shown that the calculation results are in excellent agreement with the reference results.

35.5 Literature

[35] *DIN EN 1991-1-2/NA: Eurocode 1: Actions on structures, Part 1-2/NA: Actions on structures exposed to fire*. CEN. 2010.

36 BE33: Work Laws in case of Fire for Concrete and Structural Steel

Overview

Element Type(s):	BF2D, SH3D
Analysis Type(s):	STAT, MNL
Procedure(s):	LSTP
Topic(s):	FIRE
Module(s):	TALPA, ASE
Input file(s):	temperature_compression.dat, quad_33.dat

36.1 Problem Description

This benchmark is concerned with the validation of the structural analysis in case of fire with respect to the general calculation method according to DIN EN 1992-1-2. Therefore test case 5 is employed as presented in Annex CC of the standard DIN EN 1992-1-2/NA:2010-03 [35]. In this example the validation of the change in length of structural steel and concrete in compression, for the model of Fig. 36.1, at varying temperature and load capacity levels, is investigated.

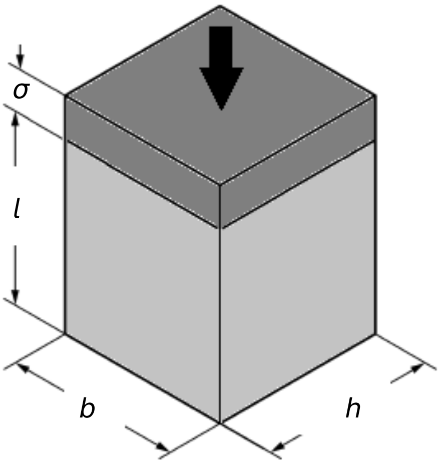

Figure 36.1: Problem Description

36.2 Reference Solution

The aim of Annex CC [35] is to check the applicability of the programs for engineering-based fire design on real structures. In this case the influence of the combination of increasing temperature and compressive loading with respect to the loading capacity of the structure is examined.

36.3 Model and Results

The properties of the model are defined in Table 36.1. A fictional beam as depicted in Fig. 36.1 is examined here, for the case of structural steel S 355 and of concrete C 20/25, with cross-sectional dimensions b / h = 10 / 10 mm, l = 100 mm and b / h = 31.6 / 31.6 mm, l = 100 mm, respectively.

Different temperatures and load levels are investigated. The boundary conditions are set such that stability failure is ruled out. The analysis is performed with TALPA, where the FIBER beam element is utilised. The computed and the reference results are presented in Table 36.2 for structural steel and in Table 36.3 for concrete. Fig. 36.2 presents stress-strain curves for structural steel for different temperature levels.

Table 36.1: Model Properties

Material Properties		Geometric Properties		Test Properties
Steel	Concrete	Steel	Concrete	
S 355	C 20/25	$l = 100\,mm$	$l = 100\,mm$	Initial Conditions:
$f_{yk} = 355\,MPa$	$f_{ck} = 20\,MPa$	$h = 100\,mm$	$h = 31.6\,mm$	$\Theta = 20°C$
Stress-strain:	Stress-strain:	$b = 10\,mm$	$b = 31.6\,mm$	Homog. temp.:
DIN EN 1993-1-2	DIN EN 1992-1-2			20, 200, 400,
				600, 800°C
				Loading:
				$\sigma_{s(\Theta)}$ / $f_{yk(\Theta)}$
				or
				$\sigma_{c(\Theta)}$ / $f_{ck(\Theta)}$ = 0.2, 0.6, 0.9

Table 36.2: Results for Structural Steel - FIBER

Θ [° C]		Ref. [35]	SOF.	e_r [%]	Tol.
	$\sigma_{s(\Theta)}$ / $f_{yk(\Theta)}$	Δl [mm]	$\Delta l'$ [mm]		[%]
20	0.2	0.034	0.034	0.560	± 3 %
	0.6	0.101	0.101	−0.424	
	0.9	0.152	0.152	−0.094	
200	0.2	−0.194	−0.194	−0.141	
	0.6	−0.119	−0.119	−0.119	
	0.9	0.159	0.156	1.794	
400	0.2	−0.472	−0.472	0.097	
	0.6	−0.293	−0.294	−0.305	
	0.9	0.451	0.449	0.525	
600	0.2	−0.789	−0.789	0.053	
	0.6	−0.581	−0.581	−0.054	
	0.9	0.162	0.160	1.245	
800	0.2	−1.059	−1.059	0.030	

Table 36.2: (continued)

Θ [° C]		Ref. [35]	SOF.	e_r [%]	Tol.
	$\sigma_{s(\Theta)}$ / $f_{yk(\Theta)}$	Δl [mm]	$\Delta l'$ [mm]		[%]
	0.6	−0.914	−0.914	−0.028	
	0.9	−0.170	−0.172	−1.164	

Table 36.3: Results for Concrete - FIBER

Θ [° C]		Ref. [35]	SOF.	e_r [%]	Tolerance
	$\sigma_{s(\Theta)}$ / $f_{yk(\Theta)}$	Δl [mm]	$\Delta l'$ [mm]		[%]
20	0.2	0.0334	0.0334	0.074	± 3 %
	0.6	0.104	0.1036	0.428	
	0.9	0.176	0.1763	−0.173	
200	0.2	−0.107	−0.1070	0.024	
	0.6	0.0474	0.0474	−0.035	
	0.9	0.2075	0.2075	0.014	
400	0.2	−0.356	−0.3557	0.085	
	0.6	−0.075	−0.0750	0.016	
	0.9	0.216	0.2160	−0.009	
600	0.2	−0.685	−0.6850	−0.007	
	0.6	0.0167	0.0167	−0.182	
	0.9	0.744	0.7442	−0.033	
800	0.2	−1.066	−1.0662	−0.023	
	0.6	−0.365	−0.3645	0.145	
	0.9	0.363	0.363	−0.010	

Next step is the analysis of the same example with ASE where the QUAD element is now tested. The results are presented in Table 36.4 for structural steel and in Table 36.5 for concrete.

Table 36.4: Results for Structural Steel - QUAD

Θ [° C]		Ref. [35]	SOF.	e_r [%]	Tolerance
	$\sigma_{s(\Theta)}$ / $f_{yk(\Theta)}$	Δl [mm]	$\Delta l'$ [mm]		[%]
20	0.2	0.034	0.034	0.560	
	0.6	0.101	0.101	−0.424	
	0.9	0.152	0.152	−0.094	

Table 36.4: (continued)

Θ [° C]	$\sigma_{s(\Theta)}$ / $f_{yk(\Theta)}$	Ref. [35] Δl [mm]	SOF. $\Delta l'$ [mm]	e_r [%]	Tolerance [%]
200	0.2	−0.194	−0.194	−0.208	± 3 %
	0.6	−0.119	−0.120	−0.448	
	0.9	0.159	0.151	5.341	
400	0.2	−0.472	−0.472	0.010	
	0.6	−0.293	−0.297	−1.447	
	0.9	0.451	0.422	6.396	
600	0.2	−0.789	−0.790	−0.103	
	0.6	−0.581	−0.589	−1.302	
	0.9	0.162	0.130	19.626	
800	0.2	−1.059	−1.060	−0.093	
	0.6	−0.914	−0.920	−0.657	
	0.9	−0.170	−0.202	−18.540	

Table 36.5: Results for Concrete - QUAD

Θ [° C]	$\sigma_{s(\Theta)}$ / $f_{yk(\Theta)}$	Ref. [35] Δl [mm]	SOF. $\Delta l'$ [mm]	e_r [%]	Tolerance [%]
20	0.2	0.0334	0.0334	0.081	± 3 %
	0.6	0.1040	0.1036	0.429	
	0.9	0.1760	0.1763	−0.173	
200	0.2	−0.1070	−0.1070	0.019	
	0.6	0.0474	0.0474	−0.037	
	0.9	0.2075	0.2075	0.015	
400	0.2	−0.3560	−0.3557	0.082	
	0.6	−0.0750	−0.0750	0.014	
	0.9	0.2160	0.2160	−0.008	
600	0.2	−0.6850	−0.6851	−0.010	
	0.6	0.0167	0.0167	−0.207	
	0.9	0.7440	0.7442	−0.033	
800	0.2	−1.0660	−1.0663	−0.025	
	0.6	−0.3650	−0.3645	0.147	
	0.9	0.3631	0.3630	−0.014	

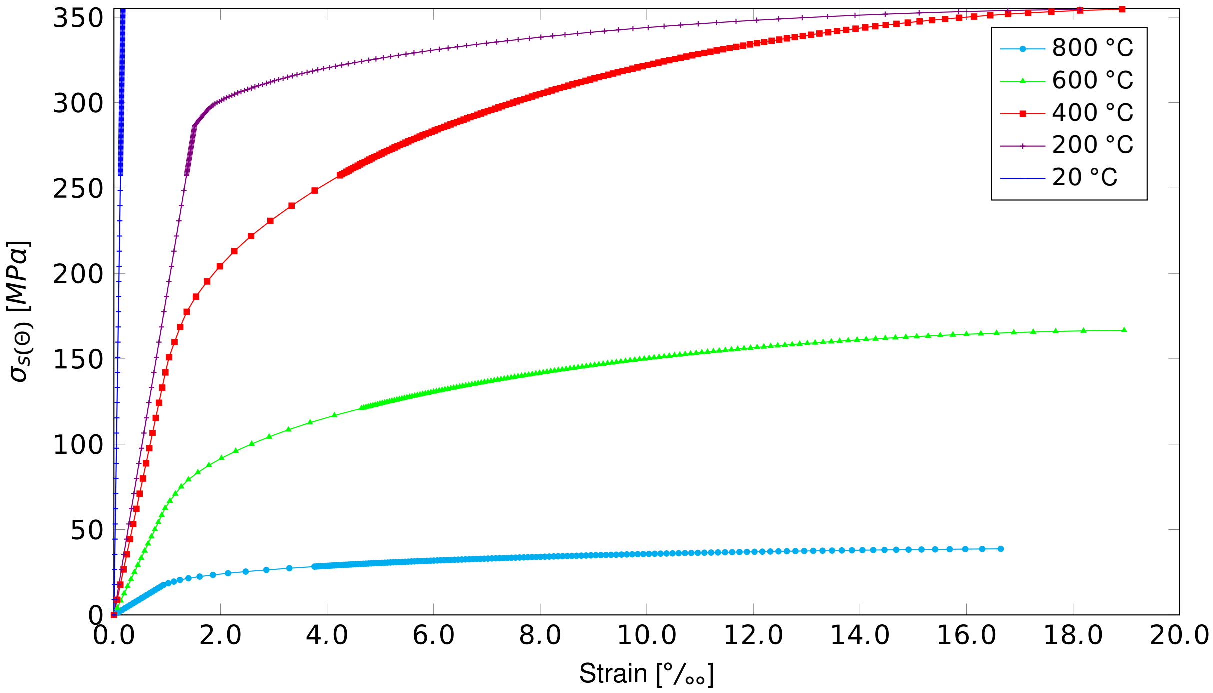

Figure 36.2: Steel Loading Strains

36.4 Conclusion

This example verifies the change in length of structural steel and concrete at different temperature and load levels. It has been shown that the calculation results with TALPA and the FIBER beam element are in very good agreement with the reference results. For the case of the QUAD layer element the results present some deviation only for the structural steel and specifically for the case of a high stress level, reaching the 90% of the steel strength.

36.5 Literature

[35] *DIN EN 1991-1-2/NA: Eurocode 1: Actions on structures, Part 1-2/NA: Actions on structures exposed to fire*. CEN. 2010.

37 BE34: Ultimate Bearing Capacity of Concrete and Steel under Fire

Overview

Element Type(s): BF2D, SH3D
Analysis Type(s): STAT, MNL
Procedure(s): LSTP
Topic(s): FIRE
Module(s): TALPA, ASE
Input file(s): capacity.dat, quad_34.dat

37.1 Problem Description

This benchmark is concerned with the validation of the structural analysis in case of fire with respect to the general calculation method according to DIN EN 1992-1-2. Therefore test case 6 is employed as presented in Annex CC of the standard DIN EN 1992-1-2/NA:2010-03 [35]. In this example the ultimate bearing capacity of structural steel and concrete in compression, for the model of Fig. 37.1, at varying temperature levels, is investigated.

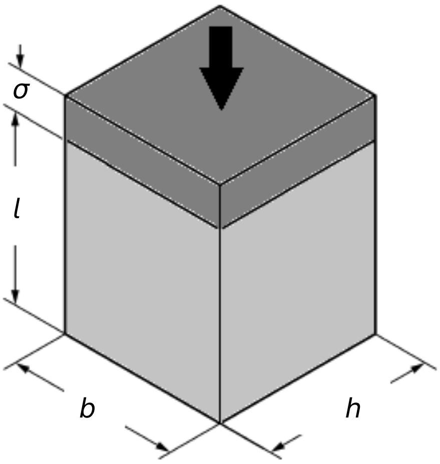

Figure 37.1: Problem Description

37.2 Reference Solution

The aim of Annex CC [35] is to check the applicability of the programs for engineering-based fire design on real structures. In this case the influence of the combination of temperature and compressive loading, on the ultimate bearing capacity is examined.

37.3 Model and Results

The properties of the model are defined in Table 37.1. A fictional beam as depicted in Fig. 37.1 is examined here, for the case of structural steel S 355 and of concrete C 20/25, with cross-sectional dimensions b / h = 10 / 10 mm, l = 100 mm and b / h = 31.6 / 31.6 mm, l = 100 mm, respectively. The boundary conditions are set such that stability failure is ruled out. The analysis is performed with TALPA, where the FIBER beam element is utilised. The computed and the reference results are presented in Table 37.2 for structural steel and in Table 37.3 for concrete.

Table 37.1: Model Properties

Material Properties		Geometric Properties		Test Properties
Steel	Concrete	Steel	Concrete	
S 355	C 20/25	$l = 100\,mm$	$l = 100\,mm$	Initial Conditions:
$f_{yk} = 355\,MPa$	$f_{ck} = 20\,MPa$	$h = 100\,mm$	$h = 31.6\,mm$	$\Theta = 20°C$
Stress-strain:	Stress-strain:	$b = 10\,mm$	$b = 31.6\,mm$	Homog. temp.:
DIN EN 1993-1-2	DIN EN 1992-1-2			$20, 200, 400,$
				$600, 800°C$

Table 37.2: Results for Structural Steel - FIBER beam

Θ [° C]	Ref. [35] $N_{R,fi,k}$ [kN]	SOF. $N_{R,fi,k}$' [kN]	e [kN]	e_r [%]	Tol.
20	−35.5	−35.5	0.000	0.000	
200	−35.5	−35.5	0.000	0.000	± 3 %
400	−35.5	−35.5	0.000	0.000	and
600	−16.7	−16.7	−0.015	0.090	± 0.5 [kN]
800	−3.9	−3.9	0.005	−0.128	

Table 37.3: Results for Concrete - FIBER beam

Θ [° C]	Ref. [35] $N_{R,fi,k}$ [kN]	SOF. $N_{R,fi,k}$' [kN]	e [kN]	e_r [%]	Tol.
20	−20.0	−20.0	−0.029	0.144	
200	−19.0	−19.0	−0.027	0.144	± 3 %
400	−15.0	−15.0	−0.022	0.144	and
600	−9.0	−9.0	−0.013	0.144	± 0.5 [kN]
800	−3.0	−3.0	−0.004	0.144	

Next step is the analysis of the same example with ASE where the QUAD element is now tested. The results are presented in Table 4 for structural steel and in Table 5 for concrete.

Table 37.4: Results for Structural Steel - QUAD

Θ [° C]	Ref. [35] $N_{R,fi,k}$ [kN]	SOF. $N_{R,fi,k}$' [kN]	e [kN]	e_r [%]	Tol.
20	−35.5	−35.5	0.000	0.000	
200	−35.5	−35.5	0.000	0.000	± 3 %
400	−35.5	−35.5	0.000	0.000	and
600	−16.7	−16.7	−0.015	0.090	± 0.5 [kN]
800	−3.9	−3.9	0.005	−0.128	

Table 37.5: Results for Concrete - QUAD

Θ [° C]	Ref. [35] $N_{R,fi,k}$ [kN]	SOF. $N_{R,fi,k}$' [kN]	e [kN]	e_r [%]	Tol.
20	−20.0	−20.0	−0.029	0.144	
200	−19.0	−19.0	−0.037	0.193	± 3 %
400	−15.0	−15.0	−0.023	0.156	and
600	−9.0	−9.0	−0.013	0.150	± 0.5 [kN]
800	−3.0	−3.0	−0.015	0.489	

37.4 Conclusion

This example verifies the influence of compressive loading on the ultimate bearing capacity under different temperature levels. It has been shown that the calculation results are in very good agreement with the reference results for both the QUAD layer element and the FIBER beam element.

37.5 Literature

[35] *DIN EN 1991-1-2/NA: Eurocode 1: Actions on structures, Part 1-2/NA: Actions on structures exposed to fire*. CEN. 2010.

38 BE35: Calculation of Restraining Forces in Steel Members in case of Fire

Overview

Element Type(s):	BF2D, SH3D
Analysis Type(s):	STAT, MNL
Procedure(s):	LSTP
Topic(s):	FIRE
Module(s):	TALPA, ASE
Input file(s):	restraining_forces.dat, quad_35.dat

38.1 Problem Description

This benchmark is concerned with the validation of the structural analysis in case of fire with respect to the general calculation method according to DIN EN 1992-1-2. Therefore test case 7 is employed as presented in Annex CC of the standard DIN EN 1992-1-2/NA:2010-03 [35]. In this example the restraining forces developed in an immovable steel member due to temperature exposure are investigated for the model of Fig. 38.1.

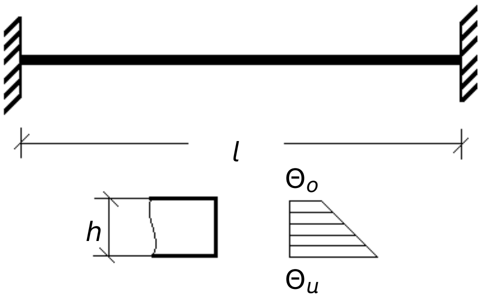

Figure 38.1: Problem Description

38.2 Reference Solution

The aim of Annex CC [35] is to check the applicability of the programs for engineering-based fire design on real structures. In this case the influence of temperature exposure on the development of restraining forces in steel is investigated. To illustrate the development of the restraining forces, consider a steel bar fixed at both ends and exposed to fire. As the bar is heated it tries to expand. However, the fixture prevents expansion in the longitudinal direction. Thus, the fixture exerts restraining forces on the bar. Since the bar is prevented from longitudinal expansion, it is possible to expand in the other directions.

38.3 Model and Results

The properties of the model are defined in Table 38.1. A beam with cross-sectional dimensions $b/h = 100/100\ mm$, $l = 1000\ mm$ and fixed at both ends, as depicted in Fig. 38.1, is examined here. The material of the cross-section is structural steel with a fictive yield strength of $f_{yk(20°C)} = 650\ N/mm^2$ and thermo-mechanical properties according to EN 1993-1-2. The model is exposed to different temperatures. In the first case the same temperature is assigned across the cross-section height, whereas in the second case, the temperature difference of the upper and lower fiber is $200°C$. The analysis is performed with TALPA, where the FIBER beam element is utilised. The computed and the reference results are presented in Table 38.2.

Table 38.1: Model Properties

Material Properties	Geometric Properties	Test Properties
$f_{yk(20°C)} = 650\,N/mm^2$	$l = 1000\,mm$	Case 1
$E_{a(20°C)} = 210000\,N/mm^2$	$h = 100\,mm$	$\Theta_o = 120°, C\ \Theta_u = 120°C$
Stress-strain curve	$b = 100\,mm$	Case 2
according to DIN EN 1993-1-2		$\Theta_o = 20°, C\ \Theta_u = 220°C$

Table 38.2: Results for Structural Steel - FIBER beam

Temperature Load Θ [° C]		Ref. [35] X	SOF. X'	$\lvert e_r \rvert$ [%]	Tol. [%]
120/120	N_{Zw} [kN]	−2585.0	−2584.8	0.006	± 1
	M_{Zw} [kNm]	0.0	0.0	0.000	± 1
	σ_{Zw} [N/mm^2]	−258.5	−258.5	0.006	± 5
20/220	N_{Zw} [kN]	−2511.0	−2503.9	0.282	± 1
	M_{Zw} [kNm]	−40.3	−40.2	0.249	± 1
	σ_{Zw} [N/mm^2]	−479.0	−479.0	0.000	± 5

Next step is the analysis of the same example with ASE where the QUAD element is now tested. The results are presented in Table 38.3 for both temperature loads.

Table 38.3: Results for Structural Steel - QUAD

Temperature Load Θ [° C]		Ref. [35] X	SOF. X'	$\lvert e_r \rvert$ [%]	Tol. [%]
120/120	N_{Zw} [kN]	−2585.0	−2595.7	0.414	± 1
	M_{Zw} [kNm]	0.0	0.0	0.000	± 1
	σ_{Zw} [N/mm^2]	−258.5	−258.98	0.186	± 5
20/220	N_{Zw} [kN]	−2511.0	−2539.7	1.14	± 1
	M_{Zw} [kNm]	−40.3	−41.23	2.31	± 1
	σ_{Zw} [N/mm^2]	−479.0	−484.65	1.180	± 5

For the quad element, the results appear to deviate from the reference solution. This is due to the fact that, as the plasticity involves at the cross-section, plastic strains appear also in the lateral direction[1]. This causes a biaxial stress state ($\sigma_x \neq 0$), which is not neglected by the quad formulation, as shown in Fig. 38.2, and has an effect on both the stresses and moments in the y direction.

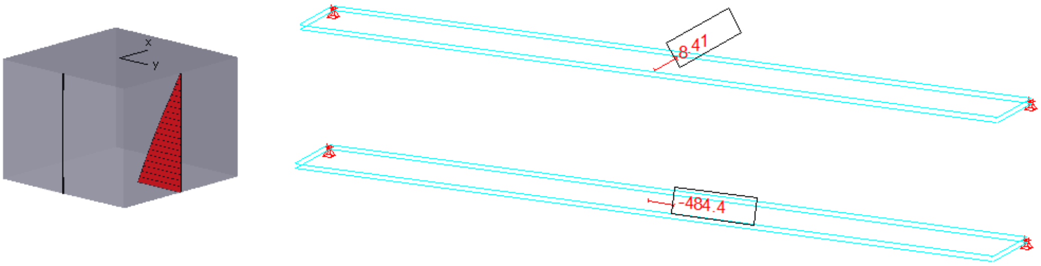

Figure 38.2: Nonlinear Stresses for Temperature 220 °C at Bottom Quad Layer

38.4 Conclusion

This example verifies the development of restraining forces in steel due to temperature exposure. It has been shown that the calculation results are in very good agreement with the reference results for both the QUAD layer element and the FIBER beam element.

38.5 Literature

[35] *DIN EN 1991-1-2/NA: Eurocode 1: Actions on structures, Part 1-2/NA: Actions on structures exposed to fire*. CEN. 2010.

---

[1] In the case of quad elements, μ is set to 0 for the better representation of the boundary conditions and the results.

39 BE36: Pushover Analysis: Performance Point Calculation by ATC-40 Procedure

Overview

Element Type(s):	
Analysis Type(s):	
Procedure(s):	
Topic(s):	EQKE
Module(s):	SOFiLOAD
Input file(s):	pushover-pp-atc.dat

39.1 Problem Description

The following example is intended to verify the ATC-40 procedure for the calculation of the performance point (illustrated schematically in Fig. 39.1), as implemented in SOFiSTiK. The elastic demand and capacity diagrams are assumed to be know.

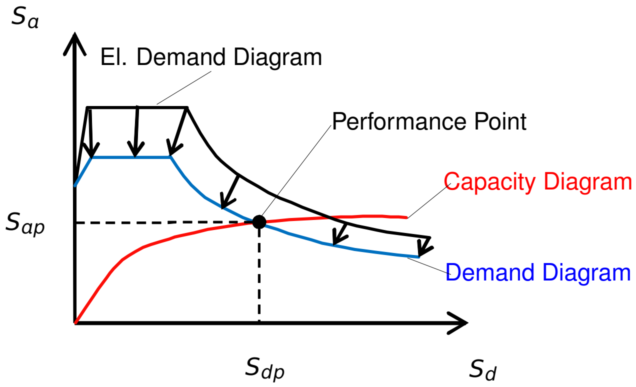

Figure 39.1: Determination of the performance point PP (S_{dp}, S_{ap})

39.2 Reference Solution

The reference solution is provided in [36], 8.3.3.3 ”Performance Point Calculation by Capacity Spectrum Method - Procedure A”.

Assuming that the elastic demand diagram (5% elastic response spectrum in ADRS format[1]) and the capacity diagram are known, it is possible to determine the performance point PP (S_{dp}, S_{ap}) (Fig. 39.1). The procedure comprises of a series of trial calculations (trial performance points PP_t $(S_{dp,t}, S_{ap,t})$), in which the equivalent *inelastic* single degree of freedom system (SDOF), represented by the capacity diagram, is transformed to an equivalent *elastic* SDOF system whose response in form of the performance point PP is then calculated from the reduced elastic response spectrum (demand diagram). The computation stops when the performance point PP is within a tolerance of a trial performance point PP_t. The ATC-40 Procedure A is a semi-analytical procedure since it involves graphical bilinear idealization of the capacity diagram. Detailed description of this step-by-step procedure can be found in [36].

---

[1] ADRS = Spectral Acceleration S_a - Spectral Displacement S_d format

39.3 Model and Results

In order to verify the analysis procedure for the determination of the performance point, a test case has been set up in such a way that it comprises of a SDOF with a unit mass and a non-linear spring element. It is obvious that for such an element the quantities governing the transformation from the original system to the equivalent inelastic SDOF system must be equal to one, i.e.

$$\phi_{cnod} = 1 \quad ; \quad \Gamma = 1 \quad ; \quad m = 1 \, , \tag{39.1}$$

where ϕ_{cnod} is the eigenvector value at control node, Γ is the modal participation factor and m is the generalized modal mass. Writing now the equations which govern the conversion of the pushover curve to capacity diagram, we obtain [37]

$$S_d = \frac{u_{cnod}}{\phi_{cnod} \cdot \Gamma} = u_{cnod} \, , \tag{39.2a}$$

$$S_a = \frac{V_b}{\Gamma^2 \cdot m} = V_b \, , \tag{39.2b}$$

where V_b is the base shear and u_{cnod} is the control node displacement.

Since the original system is a SDOF system, V_b and u_{cnod} are nothing else but the force in spring P and the displacement of the unit mass u, respectively. It follows further that the force-displacement work law assigned to the spring element corresponds to the capacity diagram in ADRS format, with the force P and displacement u equal to S_a and S_d, respectively.

The capacity diagram used in the reference example is defined by four points, whose coordinates are listed in the Table 39.1. According to the analysis above, these points can be used to define the force-displacement work law $P - u$ of the non-linear spring element (Fig.39.2).

Table 39.1: Model Properties [36]

Capacity Diagram		Elastic Demand
Point	$(S_d[mm],\ S_a[m/s^2])$	UBC 5% Elastic Response Spectrum.
A	$(48.77,\ 2.49)$	Seismic Zone 4, ZEN = 0.40.
B	$(71.37,\ 3.03)$	No near-fault effects.
C	$(96.01,\ 3.39)$	Soil Profile:
D	$(199.14,\ 3.73)$	- Type S_B: $C_A = 0.40, C_V = 0.40$
		- Type S_D: $C_A = 0.44, C_V = 0.64$

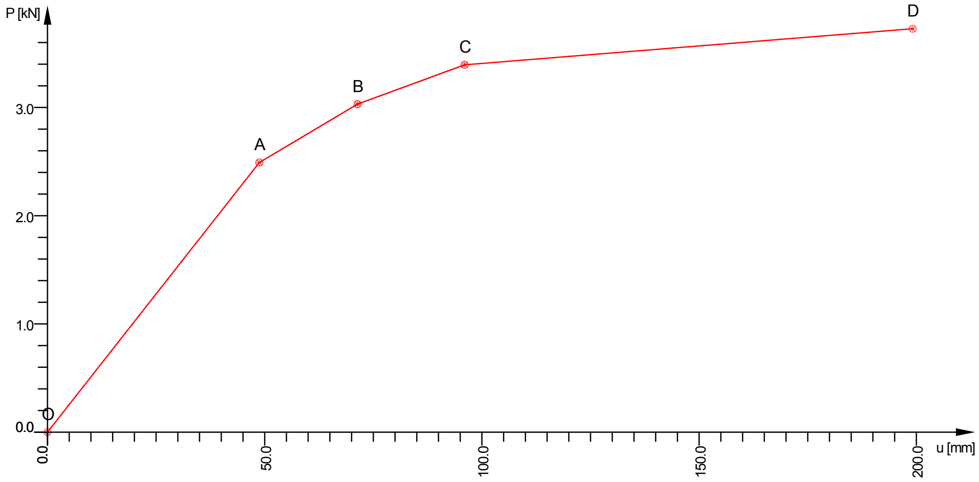

Figure 39.2: Force-displacement work law of the non-linear spring

The elastic demand is an UBC 5% damped elastic response spectrum, whose properties are summarized in Table 39.1. Two soil profile types are considered - soil profile type S_B and S_D.

The outcome of the analysis is shown in Figures 39.3 and 39.4.

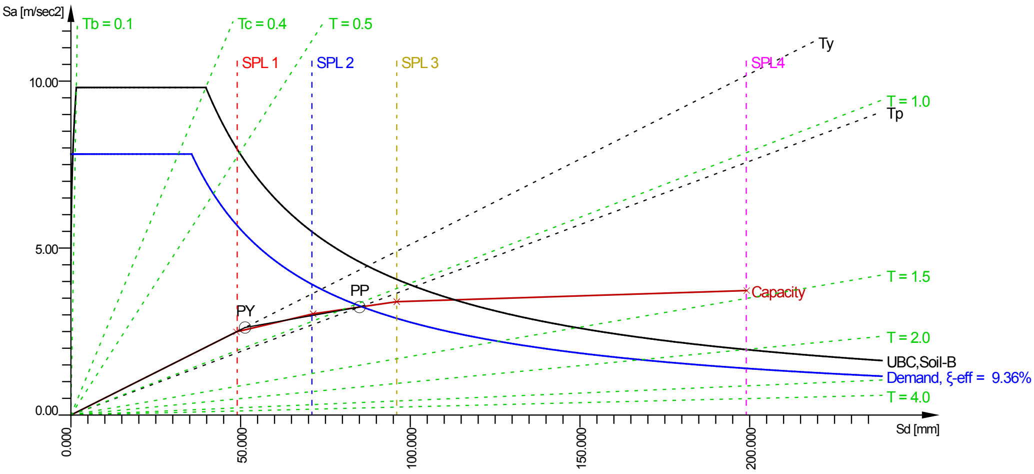

Figure 39.3: Capacity-Demand-Diagram (Soil Profile Type S_B)

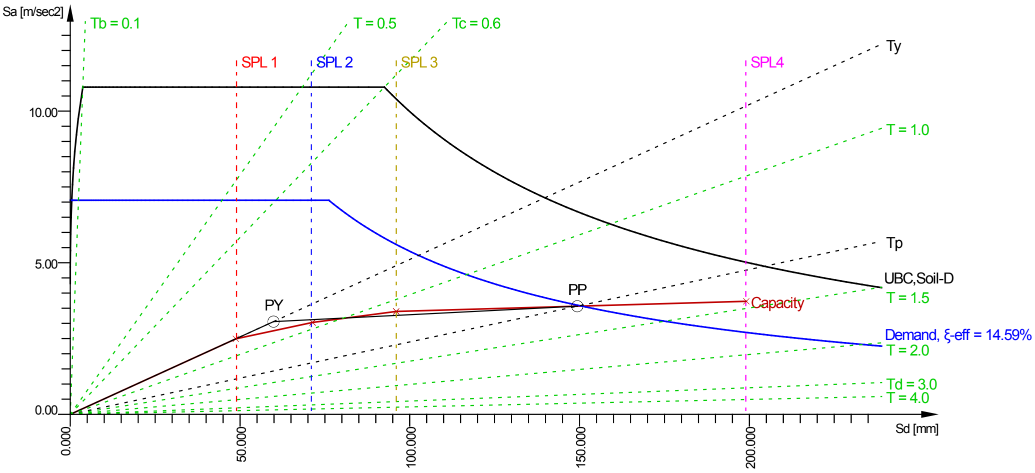

Figure 39.4: Capacity-Demand-Diagram (Soil Profile Type S_D)

The results of the SOFiSTiK calculation and the comparison with the reference solution are summarized in Table 39.2.

Table 39.2: Results

Soil type		ξ_{eff} $[\%]$	SR_a $[-]$	SR_v $[-]$	S_{dy} $[mm]$	S_{ay} $[m/s^2]$	S_{dp} $[mm]$	S_{ap} $[m/s^2]$
S_B	SOF.	9.4	0.80	0.84	51.30	2.62	85.04	3.23
	Ref. [36]	9.2	0.80	0.85	53.34	2.65	83.36	3.24
	$\lvert e \rvert$ $[\%]$	2.2	0.0	1.2	3.8	1.1	2.0	0.3
S_D	SOF.	14.6	0.65	0.73	59.86	3.06	149.34	3.57
	Ref. [36]	14.2	0.66	0.74	58.42	3.04	149.86	3.63
	$\lvert e \rvert$ $[\%]$	2.8	1.5	1.4	2.5	0.7	0.3	1.7

ξ_{eff}	effective viscous damping of the equivalent linear SDOF system
SR_a, SR_v	spectral reduction factors in constant acceleration and constant velocity range of spectrum
S_{dy}, S_{ay}	spectral displacement and spectral acceleration at yielding point
S_{dp}, S_{ap}	spectral displacement and spectral acceleration at performance point

The results are in excellent agreement with the reference solution. Small differences can mainly be attributed to the approximate nature of the graphical procedure for the bilinear idealization of the capacity used in the reference solution, while the procedure implemented in SOFiLOAD is refrained from such approximation and computes the hysteretic energy directly from the area underneath the capacity curve and the coordinates of the performance point [37]. Apart from that, the performance point displacement tolerance used in SOFiLOAD is lower than the one used in the reference solution (1% compared to 5%).

39.4 Conclusion

Excellent agreement between the reference and the results computed by SOFiSTiK verifies that the procedure for the calculation of the performance point according to ATC-40 is adequately implemented.

39.5 Literature

[36] ATC-40. *Seismic Evaluation and Retrofit of Concrete Buildings*. Applied Technology Council. Redwood City, CA, 1996.

[37] *SOFiLOAD Manual: Loads and Load Functions*. Version 2018-0. SOFiSTiK AG. Oberschleißheim, Germany, 2017.

40 BE37: Beam Calculation of Varying Cross-Section according to Second Order Theory

Overview

Element Type(s):	B3D
Analysis Type(s):	STAT, GNL
Procedure(s):	STAB
Topic(s):	
Module(s):	ASE, STAR2, DYNA
Input file(s):	beam_th2.dat

40.1 Problem Description

The problem consists of a column of continuously varying cross-section, subjected to a large compressive force in combination with imperfections as well as horizontal and temperature loads, as shown in Fig. 40.1. The forces and deflections of the structure, calculated according to second order theory, are determined.

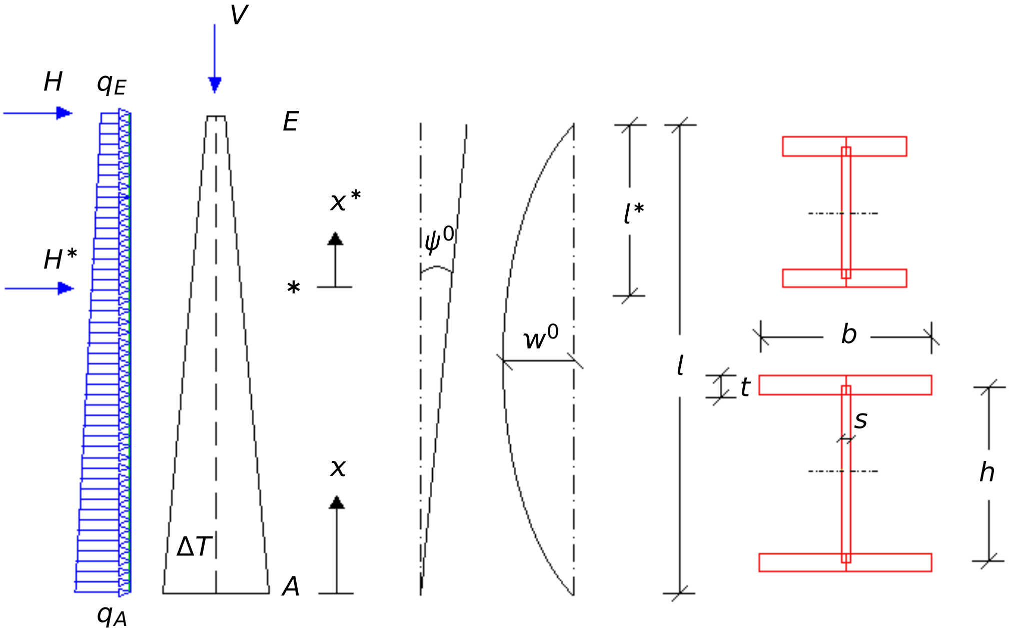

Figure 40.1: Problem Description

40.2 Reference Solution

This example attempts to give a complete description of the forces and the deflections of a beam with varying cross-section calculated with second order theory. As a reference solution, a general formulation concept is adopted, where through the application of series functions, uniform formulas can be derived to describe the beam behaviour of varying cross-section. In this concept, the cross-section properties can vary according to a polynomial of arbitrary degree, the normal force, with respect to second order theory, is assumed constant, the imperfections or predeformations as well as the temperature loads are taken into account and the deformations due to moments and normal forces are treated. Further information on the reference solution can be found in Rubin (1991) [38].

40.3 Model and Results

The general properties of the model [38] are defined in Table 40.1 and the cross-sections in Table 40.2. A general linear material is used and a linearly varying, thin-walled I-beam profile for the cross-section. The shear deformations are neglected. A safety factor of 1.35 is used for the dead weight, giving a total normal force of $N = -0.5 - 0.0203 = -0.5203\ MN$. An imperfection of linear distribution with maximum value of $60\ mm$ at node E is applied, as well as one of quadratic distribution with maximum value of $-48\ mm$ at the middle. The temperature load is given as a difference of temperature of $25°C$, between the left and the right side of the beam. The height of the cross-section is taken as the height of the web only. Second order theory is utilised and the structure is analysed both with ASE and STAR2.

Table 40.1: Model Properties

Model Properties	Loading
$E = 21\ MN/cm^2$, $\gamma_g = 1.35$	$V = 500\ kN$
$\psi^0 = 1/200$, $w^0 = -48\ mm$	$q_E = 6\ kN/m$, $q_A = 10\ kN/m$
$\alpha_T = 1.2 \times 10^{-5}\ 1/°K$	$\Delta T = T_{right} - T_{left} = -25\ °C$
$l = 12\ m$, $l^* = 4\ m$	$H = 20\ kN$, $H^* = 10\ kN$

Table 40.2: Cross-sectional Properties

Position	Web $[mm]$		Flange $[mm]$		Area $[cm^2]$	$I_y\ [cm^4]$
	h	s	b	t		
E	200	12	194	20	101.6	8560
$*$	300	12	260.7	20	140.27	26160.3
A	500	12	394	20	217.6	111000

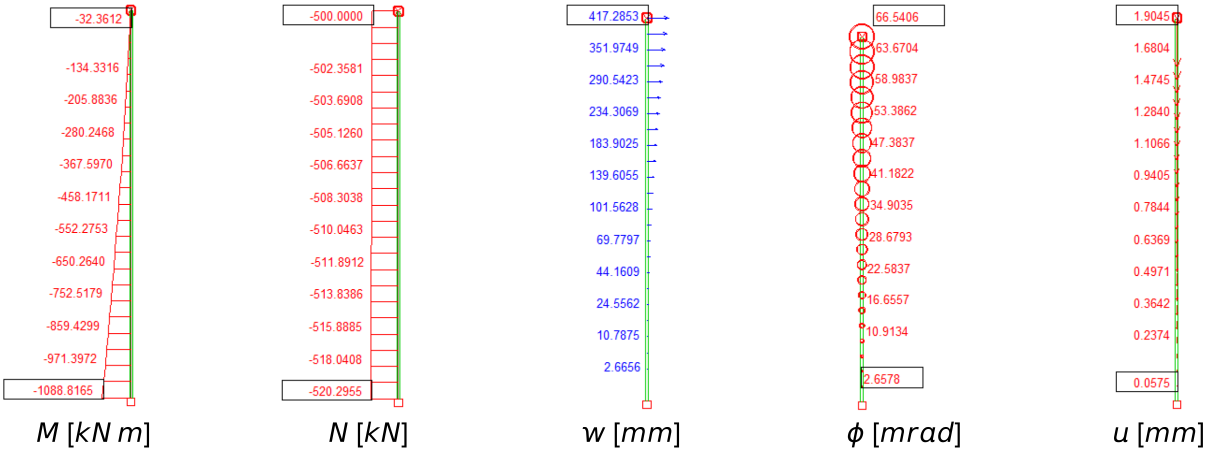

Figure 40.2: Results with Twenty Four Beam Elements calculated by ASE

The results are presented in Table 40.3, where they are compared to the reference solution according to Rubin (1991) [38]. Fig. 40.2 shows the forces and deflections of the structure as they have been calculated by ASE with twenty four beam elements.

Table 40.3: Results

Number of Elements		ϕ_E [$mrad$]	w_E [mm]	u_E [mm]	M_A [$MN\,m$]	N_A [MN]	N_E [MN]	N_{Ki} [MN]
-	Ref. [38]	67.70	423.50	-1.9050	-1.10	-0.5203	-0.50	-1.882
3	ASE	63.8819	402.8733	-1.8937	-1.0816	-0.5202	-0.50	-1.9556
	STAR2	82.1398	508.5219	-1.9288	-1.1352	-0.5203	-0.50	-
6	ASE	65.8787	413.7793	-1.9018	-1.0871	-0.5203	-0.50	-1.8993
	STAR2	70.0395	437.2366	-1.9108	-1.0990	-0.5203	-0.50	-
24	ASE	66.5406	417.2853	-1.9045	-1.0888	-0.5203	-0.50	-1.8827
	STAR2	66.7933	418.7001	-1.9050	-1.0895	-0.5203	-0.50	-

40.4 Conclusion

This example examines the behaviour of a tapered beam, treated with second order theory. The results, calculated both with ASE and STAR2, converge to the same solution as the number of elements increases. Their deviation arises from the fact that ASE uses an exponential interpolation based on area and inertia as well as numerical integration of the stiffness, while STAR2 uses the geometric mean value of the stiffness. The first is slightly too stiff, the latter is too soft and therefore resulting on the safe side. With a total of twenty four beam elements, the results are reproduced adequately. However, the obtained solution deviates from the reference. The reason for that is the fact, that for second order effects, Rubin has taken an unfavourable constant normal force of $-520.3\ kN$ for the whole column. If that effect is accounted for, the results obtained with twenty four elements are:

Table 40.4: Results with Constant Normal Force

Number of Elements		ϕ_E [$mrad$]	w_E [mm]	M_A [$MN\,m$]
-	Ref. [38]	67.70	423.50	-1.100
24	ASE	67.657	423.27	-1.0995
	STAR2	67.918	424.73	-1.1002

In the case where the example is calculated with DYNA, where a constant normal force of $-520.3kN$ is considered as a primary load case, leading to linearised second order theory and therefore satisfying Rubin's assumption, the results converge to the reference solution. The results, calculated with DYNA and twenty four elements, are presented in Table 40.5. Furthermore, different single loadings are examined and the results are given in Table 40.6.

Table 40.5: Results with DYNA

Number of Elements		ϕ_E $[mrad]$	w_E $[mm]$	u_E $[mm]$	M_A $[MN\,m]$	N_A $[MN]$	N_E $[MN]$
-	Ref. [38]	67.70	423.50	−1.9050	−1.10	−0.5203	−0.50
24	DYNA	67.6569	423.2766	−1.9045	−1.0994	−0.5203	−0.50

Table 40.6: Results with DYNA for Combination of Constant Normal Force and Single Loadings

Load Case	ϕ_E $[mrad]$	w_E $[mm]$	M_A $[MN\,m]$
H^*, H	23.6779	148.3151	−0.3972
q	22.5896	163.3797	−0.6130
ΔT	14.8218	77.1333	−0.0401
ψ^0	2.6481	15.9532	−0.0395
w^0	3.9194	18.4953	−0.0096
$\sum$	67.6569	423.2766	−1.0994

40.5 Literature

[38] H. Rubin. “Ein einheitliches, geschlossenes Konzept zur Berechnung von Stäben mit stetig verändlichem Querschnitt nach Theorie I. und II. Ordnung”. In: *Bauingenieur 66* (1991), pp. 465–477.

41 BE38: Calculation of Slope Stability by Phi-C Reduction

Overview	
Element Type(s):	C2D
Analysis Type(s):	STAT, MNL
Procedure(s):	LSTP, PHIC
Topic(s):	SOIL
Module(s):	TALPA
Input file(s):	slope_stability.dat

41.1 Problem Description

In this benchmark the stability of an embankment, as shown in Fig. 41.1, is calculated by means of a $phi - c$ reduction. The factor of safety and its corresponding slip surface are verified.

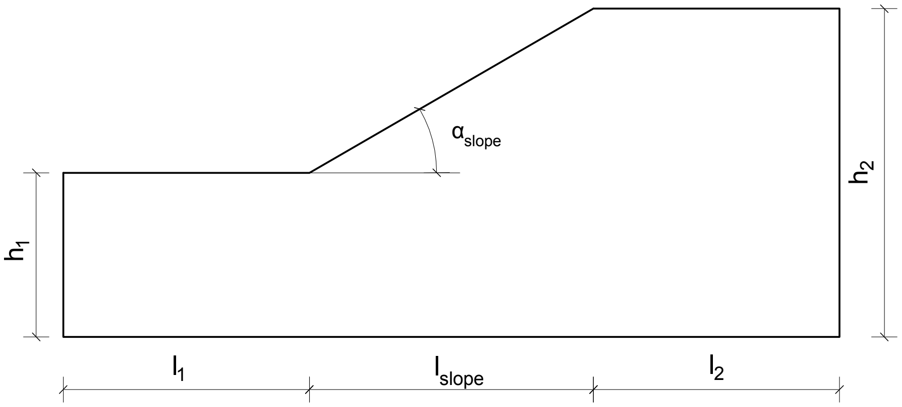

Figure 41.1: Problem Description

41.2 Reference Solution

The classical problem of slope stability analysis involves the investigation of the equilibrium of a mass of soil bounded below by an assumed potential slip surface and above by the surface of the slope. Forces and moments, tending to cause instability of the mass, are compared to those tending to resist instability. Most procedures assume a two-dimensional cross-section and plane strain conditions for analysis. Successive assumptions are made regarding the potential slip surface until the most critical surface, i.e. lowest factor of safety, is found. If the shear resistance of the soil along the slip surface exceeds that necessary to provide equilibrium, the mass is stable. If the shear resistance is insufficient, the mass is unstable. The stability of the mass depends on its weight, the external forces acting on it, the shear strengths and pore water pressures along the slip surface, and the strength of any internal reinforcement crossing potential slip surfaces. The factor of safety is defined with respect to the shear strength of the soil as the ratio of the available shear strength to the shear strength required for equilibrium [39]:

$$FS = \frac{available\,shear\,strength}{equilibrium\,shear\,stress} \tag{41.1}$$

The safety definition according to FELLENIUS is based on the investigation of the material's shear strength in the limit state of the system, i.e. the shear strength that leads to failure of the system.

Following this notion, in SOFiSTiK, the safety factors according to $phi-c$ reduction are defined as the ratio between available shear strength and the mobilized shear strength in the limit state of the system [40]:

$$\eta_{\phi} = \frac{tan\, \phi_{inp}}{tan\, \phi_{lim}} \tag{41.2}$$

$$\eta_c = \frac{c_{inp}}{c_{lim}} \tag{41.3}$$

where c is the cohesion and ϕ the friction angle. The $phi-c$ reduction stability analysis is based on an incremental reduction of the shear strength adopting a synchronized increase of the safety factors $\eta = \eta_{phi} = \eta_c$. The reached safety η at system failure represents the computational safety against stability failure.

The reference solution [41] is based on the finite element formulation of the upper- and lower-bound theorems of plasticity. Thus, the finite-element limit analysis (FELA) provides a good reference for the strength reduction method as it establishes upper and lower-bound estimates for the true stability limit.

41.3 Model and Results

The properties of the model [41] are presented in Table 41.1. The embankment has a slope height of $10\ m$ and a slope angle of $30°$. The initial stresses are generated using gravity loading. Then the embankment is subjected to the $phi-c$ reduction. Plane strain conditions are assumed.

Table 41.1: Model Properties

Material Properties	Geometric Properties
$E = 20000\, kN/m^2$, $\nu = 0.3$	$h_1 = 20.0\, m$
$\gamma = 19\, kN/m^3$	$h_2 = 10.0\, m$
$\phi = 25°$, $\psi = 25°$	$l_1 = l_2 = 15.0\, m$
$c = 20\, kN/m^2$	$\alpha_{slope} = 30°$, $l_{slope} = 17.321\, m$

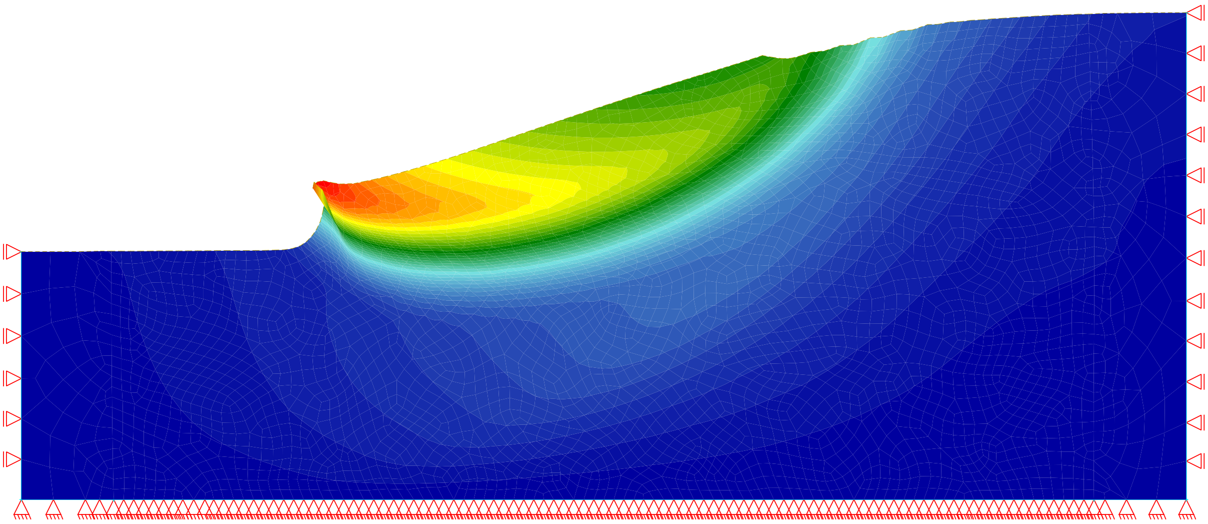

Figure 41.2: Nodal displacements for the factor of saftey obtained with the $phi-c$ reduction analysis

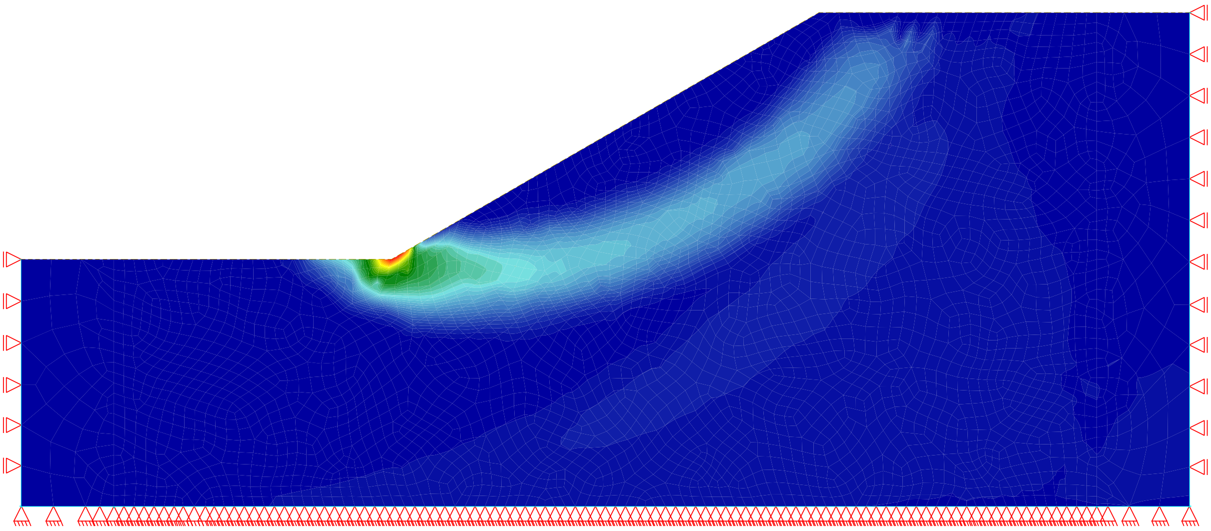

Figure 41.3: Deviatoric strain for the factor of saftey obtained with the $phi-c$ reduction analysis

Figure 41.2 presents the nodal displacement as a vector distribution for the factor of safety obtained with the $phi-c$ reduction analysis. Furthermore, the corresponding plastic deviatoric strain is shown in Figure 41.3. The calculated factor of safety is compared with the reference solution [41] in Table 41.2, i.e. with the results from the lower-bound and upper-bound *finite element limit analysis* (FELA). Additionally, the calculated factor of safety from $phi-c$ reduction analysis is plotted in Figure 41.4 as a function of the nodal displacement in x direction for the node at the top of the embankment slope.

Table 41.2: Factor of saftey - calculated and reference values according to [41]

SOFiSTiK FEM	FELA$_{lower\ bound}$	FELA$_{upper\ bound}$
2.00	1.97	2.01

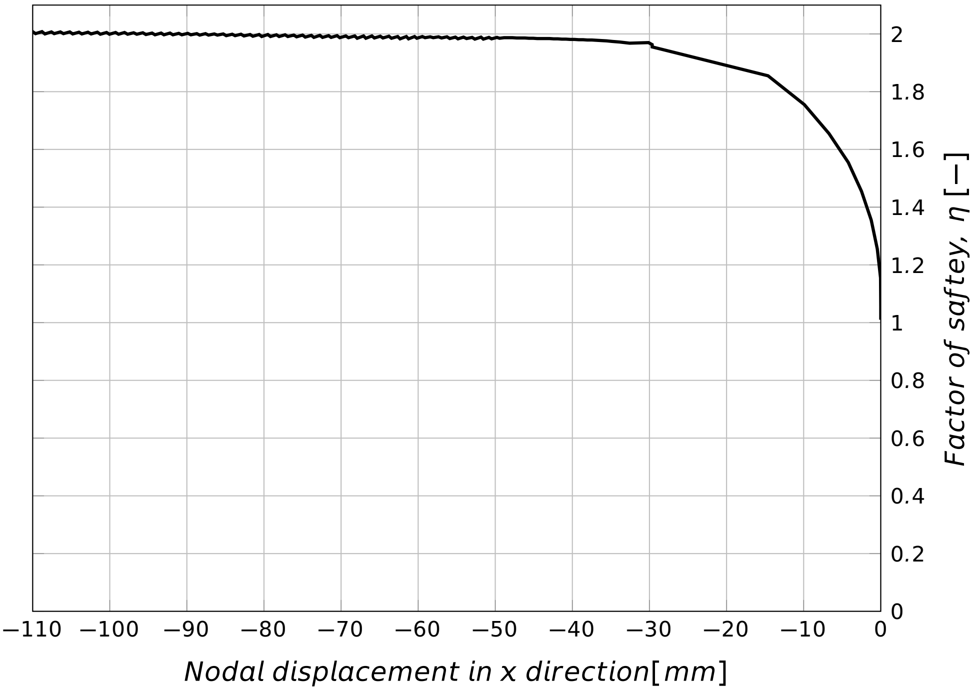

Figure 41.4: Factor of safety as a function of displacement in x direction for the node at the top of the embankment slope

41.4 Conclusion

This example verifies the stability of a soil mass and the determination of the factor of safety. The calculated factor of safety, which is obtained with the $phi-c$ reduction method, is compared to the finite element limit analysis results and it is shown that the behavior of the model is captured accurately.

41.5 Literature

[39] *USACE Engineering and Design: Slope Stability*. USACE. 2003.
[40] *TALPA Manual: 2D Finite Elements in Geotechnical Engineering*. 2018-0. SOFiSTiK AG. Oberschleißheim, Germany, 2017.
[41] F. Tschuchnigg et al. “Comparison of finite-element limit analysis and strength reduction techniques”. In: *Geotechnique* 65(4) (2015), pp. 249–257.

42 BE39: Natural Frequencies of a Rectangular Plate

Overview

Element Type(s):	SH3D
Analysis Type(s):	DYN
Procedure(s):	EIGE
Topic(s):	
Module(s):	DYNA
Input file(s):	freq_plate.dat

42.1 Problem Description

This problem consists of a rectangular plate which is simply supported on all four sides, as shown in Fig. 42.1. The eigenfrequencies of the system are determined and compared to the exact reference solution for each case.

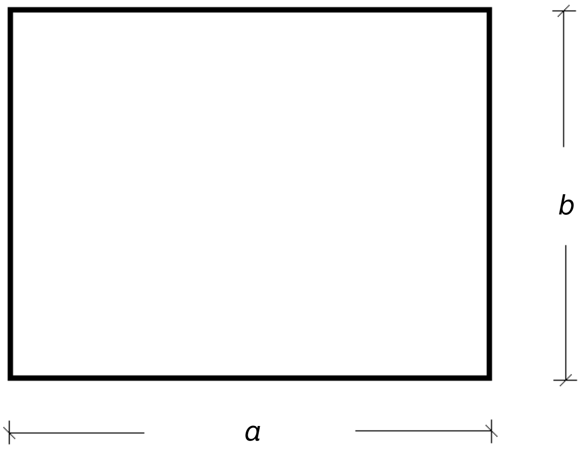

Figure 42.1: Problem Description

42.2 Reference Solution

The general formula to determine the eigenfrequencies of a simply-supported thin plate, consisting of a linear elastic homogeneous and isotropic material is given by [29], [42]

$$f_{m,n} = \frac{{\lambda_{m,n}}^2}{2\pi}\sqrt{\frac{gD}{\gamma h}} \tag{42.1}$$

where

$${\lambda_{m,n}}^2 = \pi^2\left(\frac{m^2}{a^2}+\frac{n^2}{b^2}\right) \tag{42.2}$$

and D is the flexural rigidity of the plate

$$D = \frac{Eh^3}{12(1-\nu^2)} \tag{42.3}$$

Combining the above equations gives

$$f_{m,n} = \frac{\pi}{2a^2}\left(m^2 + n^2\frac{a^2}{b^2}\right)\sqrt{\frac{g}{\gamma h}\frac{Eh^3}{12(1-\nu^2)}} \tag{42.4}$$

where a, b the dimensions of the plate, h the thickness and $\gamma h/g$ the mass of the plate per unit area. The values of ${\lambda_{m,n}}^2$ for the first five combinations of m, n are given in Table 42.1 for a simply-supported plate.

Table 42.1: Dimensionless parameter ${\lambda_{m,n}}^2$

m	n	${\lambda_{m,n}}^2$	Mode number
1	1	32.08	1
2	1	61.69	2
1	2	98.70	3
3	1	111.03	4
2	2	128.30	5

42.3 Model and Results

The properties of the model are defined in Table 42.2 and the resulted eigenfrequencies are given in Table 42.3. The corresponding eigenforms are presented in Fig. 42.2.

Table 42.2: Model Properties

Material Properties	Geometric Properties
$E = 30000\,MPa$	$a = 4.5\,m$
$\gamma = 80\,kN/m^3$	$b = 3.0\,m$
$\nu = 0.3$	$h = 0.02\,m$

Table 42.3: Results

Eigenfrequency Number	SOF. [Hz]	Ref. [Hz]	$\lvert e_r \rvert$ [%]
1	2.941	2.955	0.476
2	5.623	5.682	1.047
3	9.200	9.091	1.197
4	10.206	10.228	0.214

Table 42.3: (continued)

Eigenfrequency Number	SOF. $[Hz]$	Ref. $[Hz]$	$\lvert e_r \rvert$ [%]
5	11.706	11.819	0.954

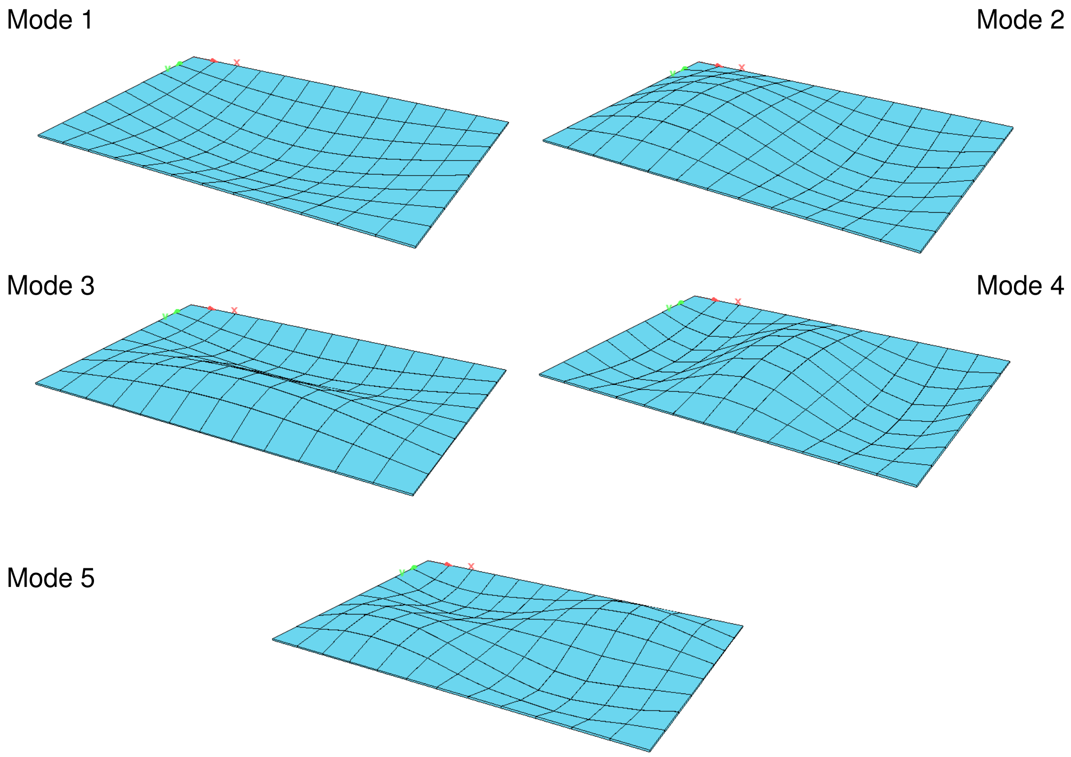
Mode 1
Mode 2
Mode 3
Mode 4
Mode 5

Figure 42.2: Eigenforms

42.4 Conclusion

The purpose of this example is to verify the eigenvalue determination of plate structures modelled with plane elements. It has been shown that the eigenfrequencies for a simply-supported thin rectangular plate are calculated accurately.

42.5 Literature

[29] S. Timoshenko. *Vibration Problems in Engineering*. 2nd. D. Van Nostrand Co., Inc., 1937.
[42] Schneider. *Bautabellen für Ingenieure*. 19th. Werner Verlag, 2010.

43 BE40: Portal Frame

Overview

Element Type(s):	B3D
Analysis Type(s):	STAT, GNL
Procedure(s):	
Topic(s):	
Module(s):	ASE
Input file(s):	frame.dat

43.1 Problem Description

The problem consists of a rigid rectangular frame, with an imperfection at the columns, subjected to a uniform distributed load q across the span and to various single loads, as shown in Fig. 43.1. For the linear case, the structure is subjected to the uniform load only, whereas for the nonlinear case, all defined loads including the imperfection are considered. The response of the structure is determined and compared to the analytical solution.

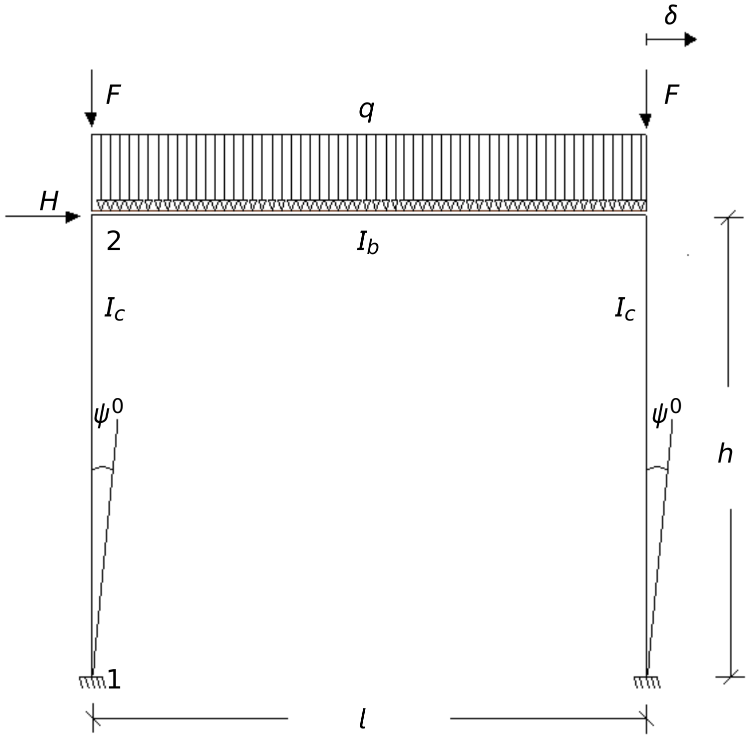

Figure 43.1: Problem Description

43.2 Reference Solution

For the linear case, where only the distributed load is considered, the moments M are determined in terms of the shear force H as follows:

$$H_1 = H_2 = \frac{ql^2}{4h(k+2)} \tag{43.1}$$

$$M_1 = M_2 = \frac{Hh}{3} \tag{43.2}$$

$$M_3 = M_4 = M_1 - H_1 h \tag{43.3}$$

where $k = I_b h \,/\, I_c l$. For the nonlinear case, in order to account for the effect of the normal force and the imperfections on the determination of the resulting forces and moments, second order theory has to be used. The moments at nodes $1-4$ are determined in dependency of the column characteristic ratio $\epsilon = l_c\sqrt{N/EI_c}$, giving the influence of the normal force $N = F + ql/2$ with respect to the column properties, length l_c and bending stiffness EI_c. Further information on the analytical formulas can be found in Schneider [42].

43.3 Model and Results

The properties of the model are defined in Table 43.1. The frame has an initial geometrical imperfection at the columns of linear distribution $\psi_0 = 1/200$, with a maximum value of $25\ mm$ at nodes 3 and 4. The normal force N, used to determine ϵ, is calculated to be $430\ kN$ at the columns and the ratio $\epsilon = 1.639$. For the linear case the results are presented in Table 43.3 and they are compared to the analytical solution calculated from the formulas presented in Section 43.2. For the nonlinear case, the results are presented in Table 43.2 and they are compared to the reference example provided in Schneider [42].

Table 43.1: Model Properties

Material Properties	Geometric Properties	Loading
$EI_c = 6000\ kNm^2$	$l = 6\ m$	$q = 10\ kN/m$
$EI_b = 4000\ kNm^2$	$h = 5\ m$	$H = 20\ kN$
	$\psi_0 = 1/200$	$F = 400\ kN$

Table 43.2: Nonlinear Case Results

	Ref. [42]	SOF.
$M_1\ [kN\,m]$	38.2	38.62
$M_2\ [kN\,m]$	22.5	22.52
$M_3\ [kN\,m]$	58.1	58.02
$M_4\ [kN\,m]$	58.8	58.79
$\delta\ [mm]$	65.3	65.44

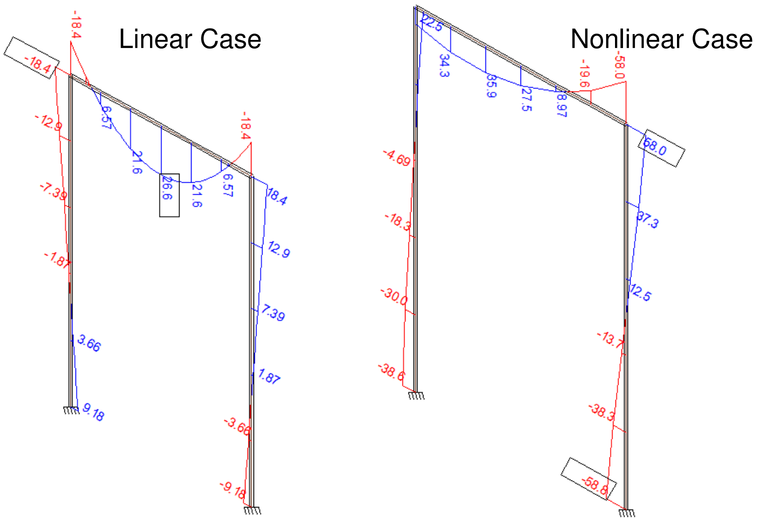
Linear Case
-18.4
-18.4
-12.9
-7.39
-1.87
3.66
9.18
6.57
21.6
26.6
21.6
6.57
-18.4
18.4
12.9
7.39
1.87
-3.66
-9.18
Nonlinear Case
22.5
34.3
35.9
27.5
8.97
-19.6
-58.0
68.0
-4.69
-18.3
-30.0
-38.6
37.3
12.5
-13.7
-38.3
-58.8

Figure 43.2: Bending Moments

Table 43.3: Linear Case Results

	Ref. $[Sect. 43.2]$	SOF.
$H_1 = H_2$ $[kN]$	5.54	5.52
$M_1 = M_2$ $[kN\,m]$	9.23	9.18
$M_3 = M_4$ $[kN\,m]$	18.46	18.43

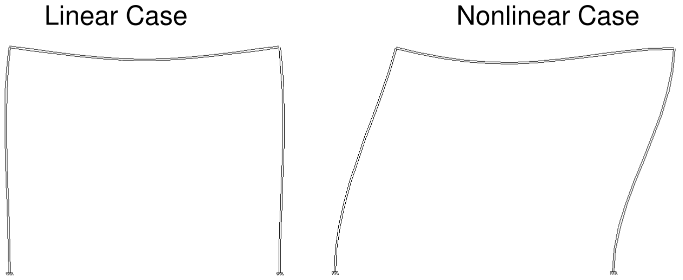
Linear Case
Nonlinear Case

Figure 43.3: Deformed Shape

43.4 Conclusion

This example examines a rigid frame under different loading conditions. It has been shown that the behaviour of the structure is captured accurately for both the linear and the nonlinear analysis.

43.5 Literature

[42] Schneider. *Bautabellen für Ingenieure*. 19th. Werner Verlag, 2010.

44 BE41: Linear Pinched Cylinder

Overview	
Element Type(s):	C3D
Analysis Type(s):	STAT
Procedure(s):	
Topic(s):	
Module(s):	ASE
Input file(s):	cylinder.dat

44.1 Problem Description

The problem consists of a thin cylinder shell with rigid end diaphragms, which is loaded in its middle by two oppositely directed radially point loads, as shown in Fig 44.1. The maximum deflection at the center of the cylinder, under the point loads, is determined and verified for refined meshes [43].

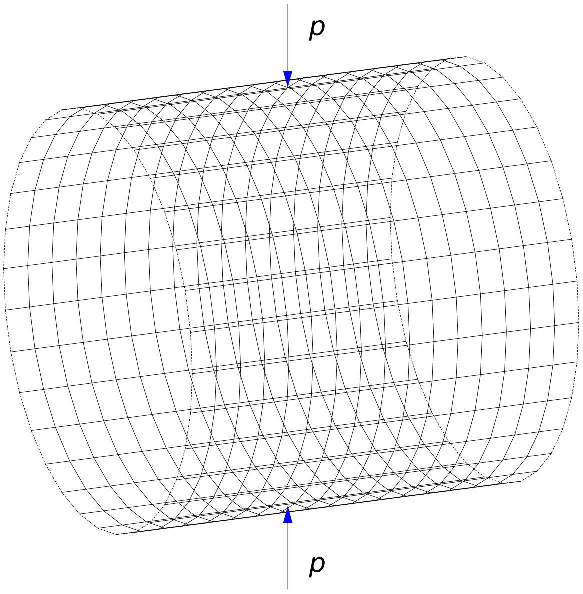

Figure 44.1: Problem Description

44.2 Reference Solution

There is a convergent numerical solution of $w = 1.8248 \cdot 10^{-5}$ for the radial displacement at the loaded points, as given by Belytschko [44]. This problem is one of the most severe tests for both inextensional bending and complex membrane states of stress [45] .

44.3 Model and Results

The properties of the model are defined in Table 44.1. The geometric parameters and the material are all dimensionless. The compressive point load $p = 1.0$ is applied radially and in opposite directions at the middle nodes of the cylinder, as shown in Fig. 44.1. Using symmetry, only one-eighth of the cylinder needs to be modeled, as shown in Fig. 44.2. For the simplified model only one fourth of the load $p*$ is applied at the the upper middle node, as it can be visualised in Fig. 44.2. The end of the cylinder is supported by a rigid diaphragm [46], while at the two edges of the cylinder, parallel to the x- and y- axis, symmetry support conditions are employed. In the plane of middle of the cylinder, the displacements in the longitudial direction, as well as the rotations around x- and y- axis are fixed. The example allows the verification of the calculation of thin shells with increasingly refined regular meshes.

Table 44.1: Model Properties

Material Properties	Geometric Properties	Loading
$E = 3.0 \cdot 10^6\ MPa$	$L = 600$, $l = 300$	$p = 1.0$
$\mu = 0.30$	$r = 300$	$p* = 0.25$
	$t = 3$	

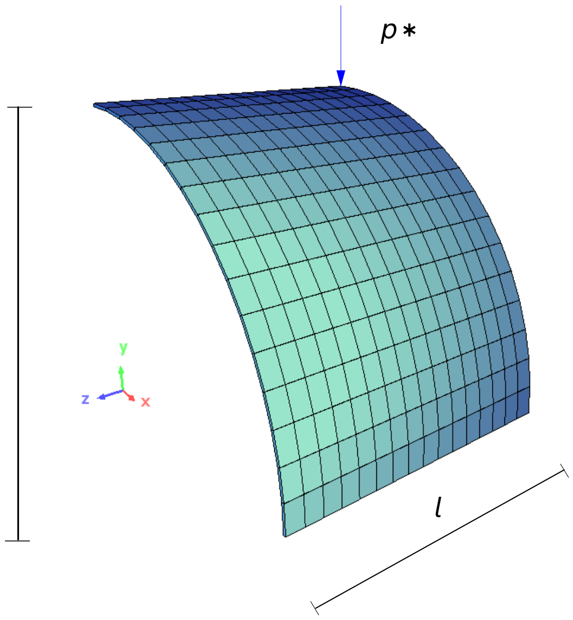

Figure 44.2: FEM model

Table 44.2: Normalised Point-Load Displacement w/w_a with Mesh Refinement

Element/Side	Conforming Element	Non-Conforming Element
4	0.4525	0.5917
8	0.8214	0.9057
16	0.9701	1.0082

The results are presented in Fig 44.3 and Table 44.2, where they are compared to the analytical solution as presented in Section 44.2. Two element formulations are considered. The first one, represented by the red curve, corresponds to the 4-node regular conforming element whereas the second, represented by the purple curve corresponds to the non-conforming element with six functions, offering a substantial improvement of the results.

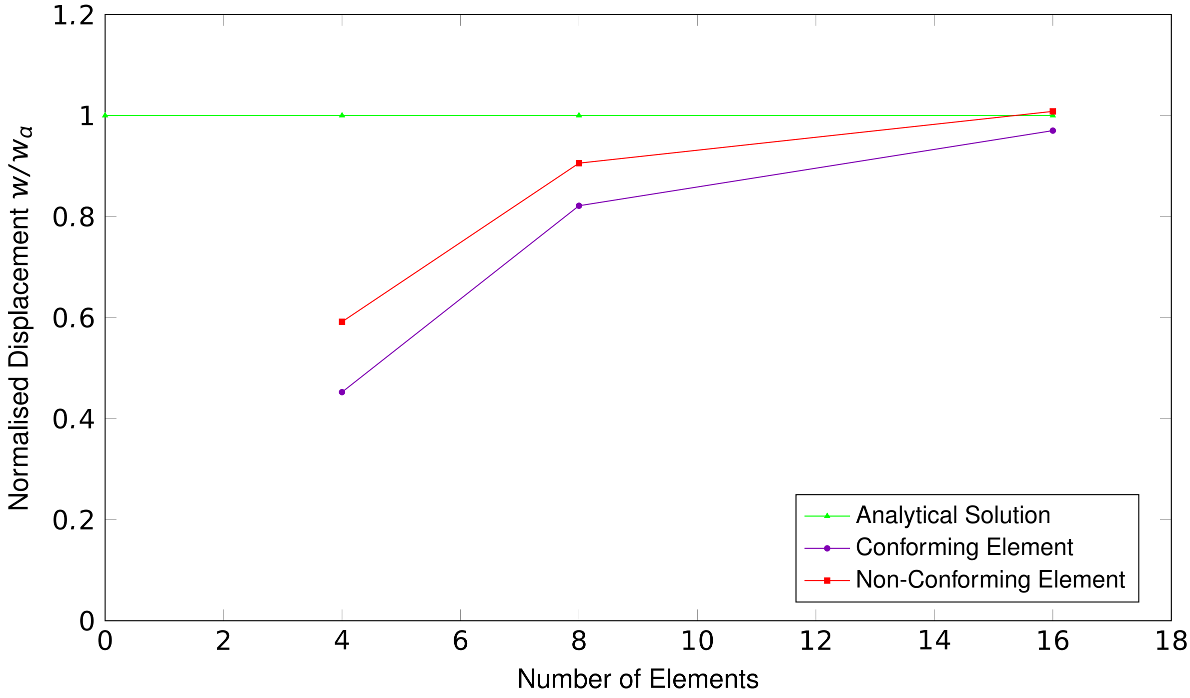

Figure 44.3: Convergence Diagram

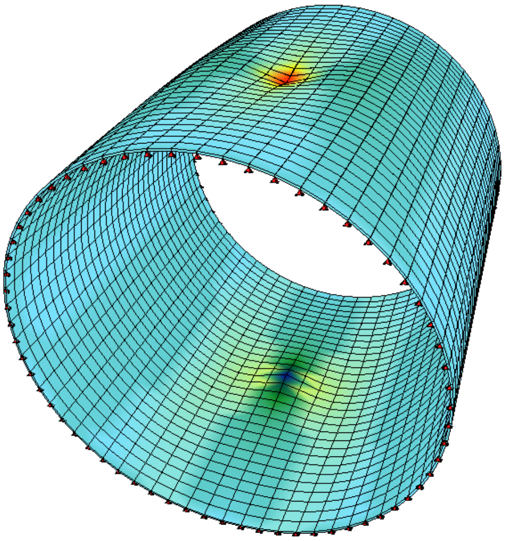

Figure 44.4: Deformed Shape

44.4 Conclusion

The example allows the verification of the calculation of thin shells. For increasing refined meshes, the calculated result for both types of elements convergence fast to the predetermined analytical solution. The advantage of the utilisation of the non-conforming element is evident, since it is in excellent agreement with the analytical solution for a refined mesh.

44.5 Literature

[43] *VDI 6201 Beispiel: Softwaregestütze Tragwerksberechnung - Beispiel Zylinderschale mit starren Endscheiben, Kategorie 1: Mechanische Grundlagen*. Verein Deutscher Ingenieure e. V.

[44] T. Belytschko et al. “Stress Projection for Membrane and Shear Locking in Shell Finite Elements”. In: *Computer Methods in Applied Mechanics and Engineering* 53(1-3) (1985), pp. 221–258.

[45] T. Rabczuk, P. M. A. Areias, and T. Belytschko. “A meshfree thin shell method for non-linear dynamic fracture”. In: *International Journal for Numerical Methods in Engineering* 72(5) (2007), pp. 524–548.

[46] P. Krysl and T. Belytschko. “Analysis of thin shells by the element-free Galerkin method”. In: *International Journal for Solids and Structures* 33(20-22) (1996), pp. 3057–3080.

45 BE42: Thick Circular Plate

Overview

Element Type(s):	C3D
Analysis Type(s):	STAT
Procedure(s):	
Topic(s):	
Module(s):	ASE
Input file(s):	thick_plate.dat

45.1 Problem Description

The problem consists of a circular plate with a constant area load, as shown in Fig. 45.1. The system is modelled as a plane problem and the deflection in the middle of the plate is determined for various thicknesses [47].

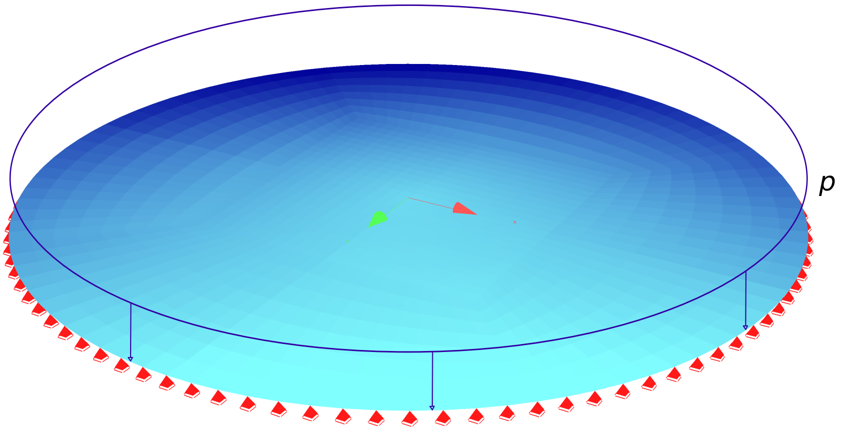

Figure 45.1: Problem Description

45.2 Reference Solution

Depending on the various thicknesses of the plate, the maximum deflection w in the middle of the plate can be obtained as $w = w_B + w_S$, where w_B is the dislacement due to bending and w_S is the displacement due to shear strains, determined as follows [48]:

$$w_B = \frac{p \cdot r^4}{64 \cdot K} \frac{(5+\mu)}{(5+\mu)} \tag{45.1}$$

$$K = \frac{E \cdot h^3}{12(1-\mu^2)} \tag{45.2}$$

$$w_S = \frac{1.2 \cdot p \cdot r^2}{4 \cdot G \cdot h} \tag{45.3}$$

where p is the load ordinate, r the radius, E the elasticity modulus, h the plate thickness, μ the Poissons ratio and G the shear modulus.

The maximum bending moment at the middle of the plate is independent of the plate thickness and corresponds for the specific load case to

$$M_x = M_y = \frac{p \cdot r^2}{16} \cdot (3 + \mu) = 4928.125 \qquad [kNm/m] \tag{45.4}$$

45.3 Model and Results

The properties of the model are defined in Table 45.1. The plate is modelled as a plane system with three degrees of freedom, u_z, ϕ_x, ϕ_y, per node and u_z hinged at the edge, as shown in Fig. 45.1. The weight of the system is not considered. A constant area load $p = 1000\ kN/m^2$ is applied, as shown in Fig. 45.1. The system is modelled with 1680 quadrilateral elements, as presented in Fig. 45.2, and a linear analysis is performed for increasing thicknesses. The results are presented in Table 45.2 where they are compared to the analytical solution calculated from the formulas presented in Section 45.2 and the influence of the varying thickness is assesed.

Table 45.1: Model Properties

Material Properties	Geometric Properties	Loading
$E = 3000\, kN/cm^2$	$h = 0.5 - 2.5\, m$	$p = 1000\, kN/m^2$
$G = 1300\, kN/cm^2$	$r = 5\, m$	
$\mu = 0.154$	$D = 10\, m$	

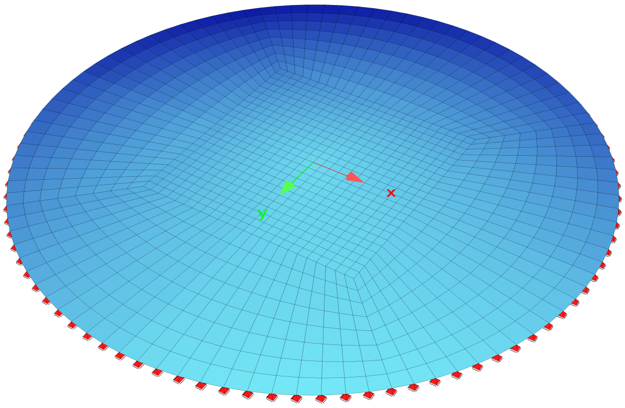

Figure 45.2: FEM model

The maximum bending moment is calculated at the middle of the plate, as $M_x = M_y = 4932.244$

$[kNm/m]$ with a deviation of 0.08 %.

Table 45.2: Results

h $[m]$	h/D	Analytical u_z $[mm]$	SOF. u_z $[mm]$	$\lvert e_r \rvert$ [%]
0.50	0.05	137.413	137.440	0.02
1.00	0.10	17.609	17.618	0.05
1.50	0.15	5.431	5.437	0.11
2.00	0.20	2.418	2.421	0.14
2.50	0.25	1.321	1.324	0.23

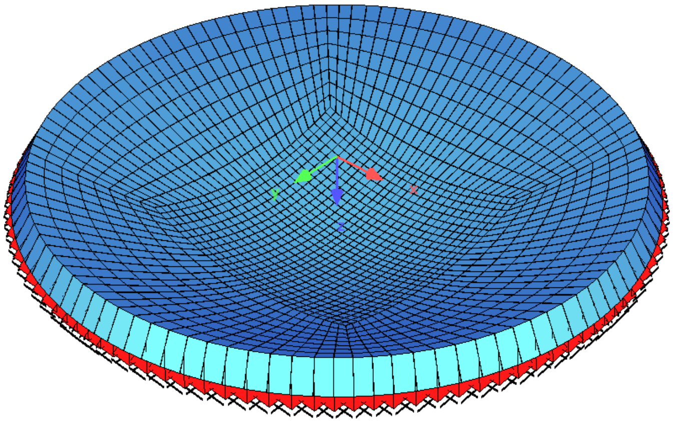

Figure 45.3: Displacements

45.4 Conclusion

The example allows the verification of the calculation of thick plates. It has been shown, that the calculated results are in very good agreement with the analytical solution even for thicker plates.

45.5 Literature

[47] *VDI 6201 Beispiel: Softwaregestütze Tragwerksberechnung - Beispiel Dicke Platte, Kategorie 1: Mechanische Grundlagen*. Verein Deutscher Ingenieure e. V.

[48] F. U. Mathiak. *Ebene Flächentragwerke Teil II, Grundlagen der Plattentheorie*. Hochschule Neubrandenburg. 2011.

46 BE43: Panel with Circular Hole

Overview	
Element Type(s):	C3D
Analysis Type(s):	STAT
Procedure(s):	
Topic(s):	
Module(s):	ASE
Input file(s):	structured_mesh.dat , unstructured_mesh.dat

46.1 Problem Description

The problem consists of a rectangular panel with a circular hole in its middle, loaded by a constant linear load p on the vertical edges, as shown in Fig. 46.1. The system is modelled as a plane stress problem and the maximum stress at the edge of the hole is determined and verified for various meshes [49].

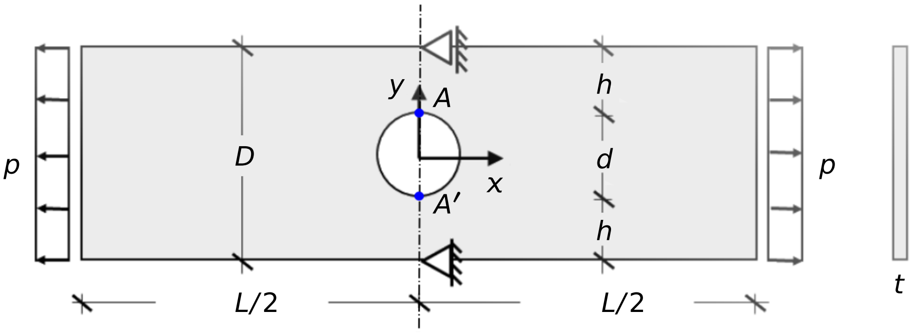

Figure 46.1: Problem Description

46.2 Reference Solution

The maximum stress $\sigma_{A,xx,max}$ resulting from a load p, at the edge of the hole can be determined at points A and A' across a vertical cut, visualised in Fig. 46.1, as follows [50] [51]:

$$\sigma_{A,xx,max} = K_t \cdot \sigma_{xx,nom} \tag{46.1}$$

where

$$P = p \cdot D = 1000 \qquad [kN] \tag{46.2}$$

$$\sigma_{xx,nom} = \frac{P}{t \cdot (D-d)} = 33.33 \qquad [N/mm^2] \tag{46.3}$$

$$K_t = 3.000 - 3.140 \cdot (d/D) + 3.667 \cdot (d/D)^2 - 1.527 \cdot (d/D)^3 \,, \qquad (0 < d/D < 1) \qquad (46.4)$$

46.3 Model and Results

The properties of the model are defined in Table 46.1. Plane stress conditions are assumed, with two degrees of freedom, u_x, u_y, per node, and a line load $p = 200.0\ kN/m$ is applied at both vertical ends. The length of the panel is considered to be large enough in order to avoid any disturbances in the area of the hole, due to the loaded ends. Due to symmetry conditions only one fourth of the panel is modelled.

Table 46.1: Model Properties

Material Properties	Geometric Properties	Loading
$E = 2.1 \cdot 10^5\ MPa$	$L = 15.00\ m$	$p = 200.0\ kN/m$
$\nu = 0.30$	$D = 5.00\ m$, $d = 2.00\ m$	
	$h = 1.50\ m$, $t = 0.01\ m$	

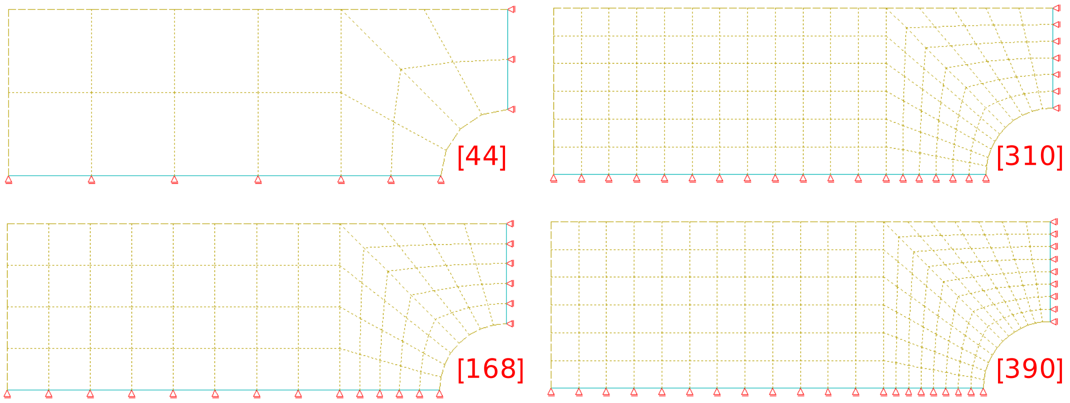

(a) Structured Meshing

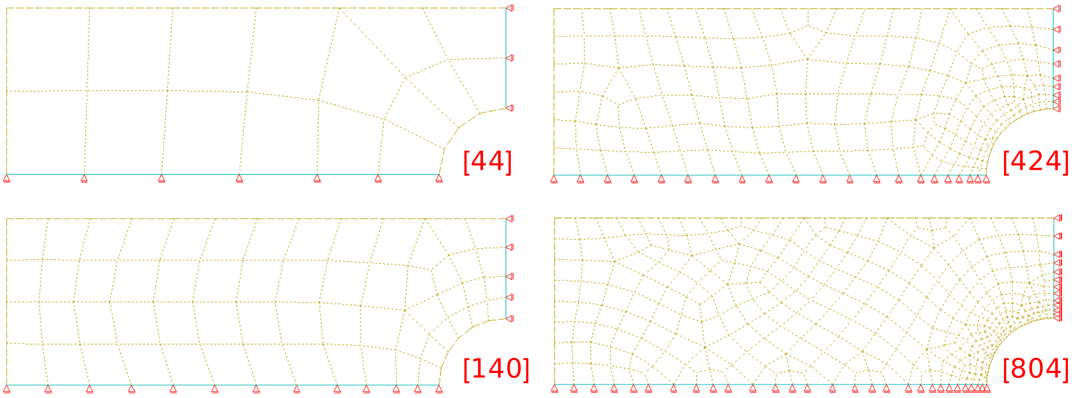

(b) Unstructured Meshing

Figure 46.2: FEM Models

Four manually structured meshes, with refinement around the hole area, are considered, shown in Fig. 46.2(a), with increasing number of quadrilateral elements and the convergence behaviour is evaluated. For the sake of comparison, unstructured meshes, shown in Fig. 46.2(b), are also considered. The number of degrees of freedom for every mesh is given in the red brackets. The results are presented in Fig 46.3 where they are compared to the analytical solution calculated from the formulas presented in Section 46.2. For the case of structured meshing two element formulations are considered. The first one, represented by the red curve, corresponds to the 4-node regular conforming element whereas the second, represented by the purple curve corresponds to the non-conforming element with six functions. The blue curve represents the unstructured meshing.

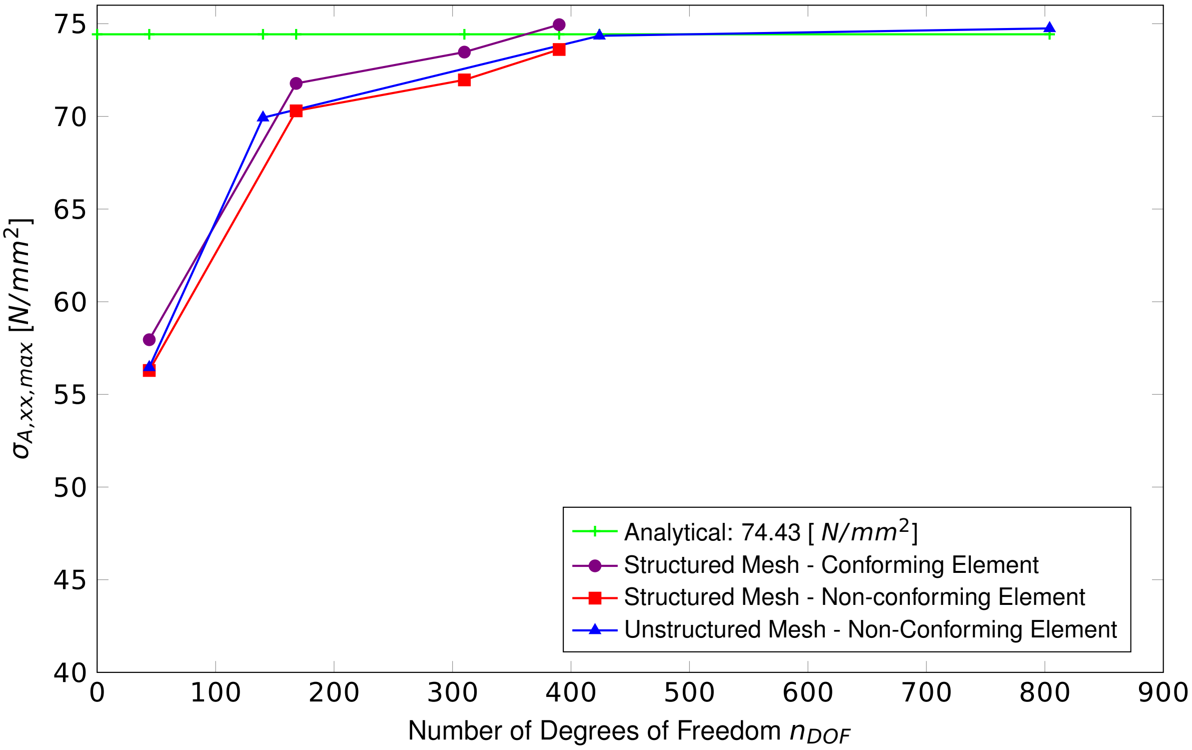

Figure 46.3: Convergence Diagram

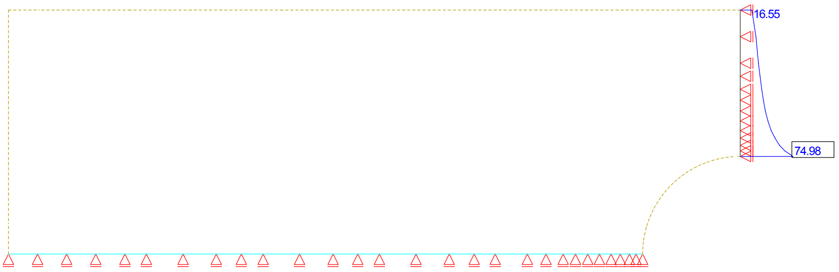

Figure 46.4: Maximum Stresses $\sigma_{xx,max}$

The regular 4-node element is characterised through a bilinear accretion of the displacements and rotations. This element is called conforming, because the displacements and the rotations between elements do not have any jumps. The results at the gravity centre of the element represent the actual internal force variation fairly well, while the results at the corners are relatively useless, especially the ones at the edges or at the corners of a region. On the other hand the non-conforming elements, are based one the idea of describing more stress states through additional functions that their value is zero at all nodes. As a rule, these functions lead to a substantial improvement of the results, however, they violate the continuity of displacements between elements and thus they are called non-conforming.

46.4 Conclusion

The example allows the verification of the calculation of plane stress problems and the convergence behaviour of quadrilateral elements. For both types of elements, the calculated results convergence rather fast to the predetermined precise analytical solution, within acceptable tolerance range. Furthermore, it is evident that the unstructured mesh, which is a more often choice in practice, gives results which are in very good agreement with the analytical solution.

46.5 Literature

[49] *VDI 6201 Beispiel: Softwaregestütze Tragwerksberechnung - Beispiel Scheibe mit kreisförmigem Loch - Konvergenztest für Scheibenelemente, Kategorie 1: Mechanische Grundlagen*. Verein Deutscher Ingenieure e. V.

[50] C. Petersen. *Stahlbau. Grundlagen der Berechnung und baulichen Ausbildung von Stahlbauten*. Vieweg, 1997.

[51] W. D. Pilkey. *Formulaes for Stress, Strain and Structural Matrices*. Wileys & Sons, 1994.

47 BE44: Undrained Elastic Soil Layer Subjected to Strip Loading

Overview	
Element Type(s):	C2D
Analysis Type(s):	STAT
Procedure(s):	
Topic(s):	SOIL
Module(s):	TALPA
Input file(s):	soil_layer_el_undr.dat

47.1 Problem Description

The example concerns the behavior of the rectangular soil layer subjected to an uniform strip loading of intensity p acting on the surface. Base of the soil is rigidly fixed while the sides are laterally constrained. Geometry, load and boundary conditions are depicted in Fig. 47.1. The soil material is elastic, isotropic and saturated with water. Two soil conditions have been analyzed - drained and undrained. The drained and undrained displacements and stresses obtained by the finite element method are compared with the analytical solution.

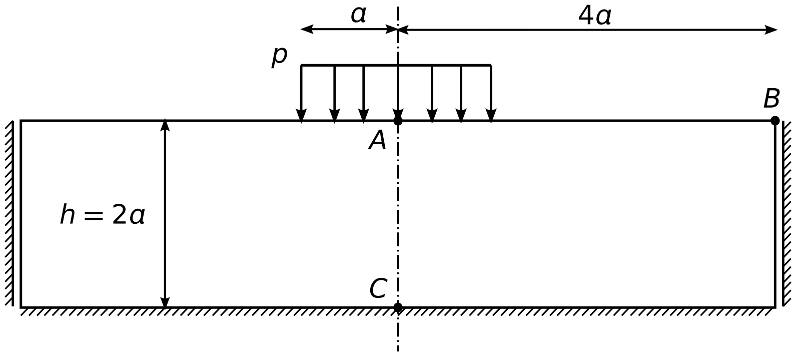

Figure 47.1: Problem Definition

47.2 Reference Solution

The analytical solution to the problem obtained using a Fourier series analysis is provided in [52].

47.3 Model and Results

Elastic, isotropic soil under drained and undrained conditions has been analyzed. Material, geometry and loading properties are summarized in Table 47.1. The undrained soil condition is considered with the help of the method based on the undrained effective stress (σ') analysis using effective material parameters. G and ν' are effective soil parameters, while B represents the Skempton's B-parameter. Self-weight is not taken into consideration.

Table 47.1: Model Properties

Material	Geometry	Loading
G, $\nu' = 0.3$	a	p
$B = 0.998$	$h = 4a$	
$\rho = 0.0\ kg/m^3$		

Finite element mesh of the model is shown in Fig. 47.2. Mesh is regular and consist of quadrilateral finite elements.

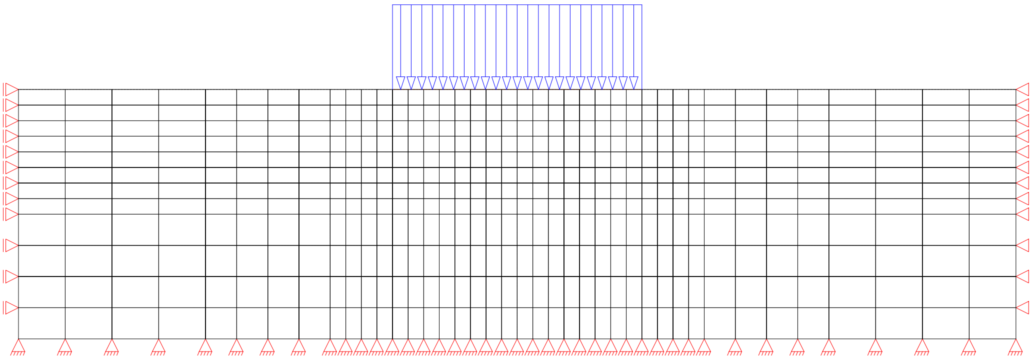

Figure 47.2: Finite Element Model

The drained and undrained vertical displacement of the surface nodes along the $A-B$ line are compared with the analytical solution from [52] and depicted in Fig. 47.3.

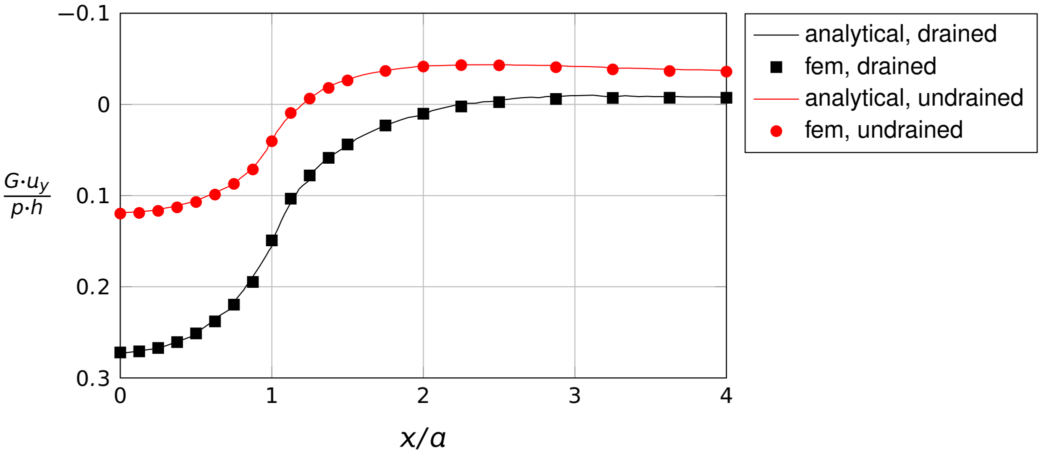

Figure 47.3: Vertical displacement u_y of the surface

The drained and undrained horizontal and vertical total stresses ($\sigma = \sigma' + p_{we}$) in the nodes along the vertical $A-C$ line have been computed and compared with the analytical ones, as show in Figures 47.4a and 47.4b.

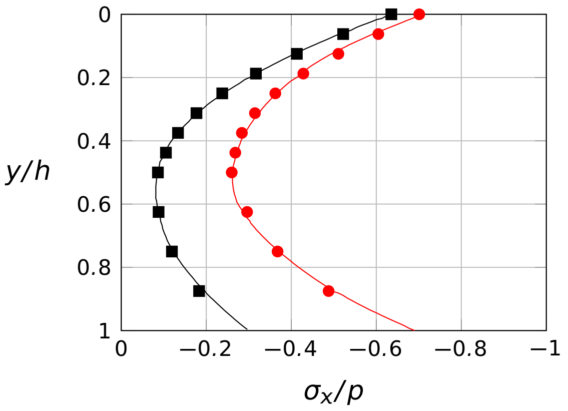

(a) Horizontal stress σ_x (b) Vertical stress σ_y

Figure 47.4: Stresses beneath footing center

Pore excess pressure (p_{we}) distribution for the undrained condition along the center line ($A - C$) is shown in Fig. 47.5.

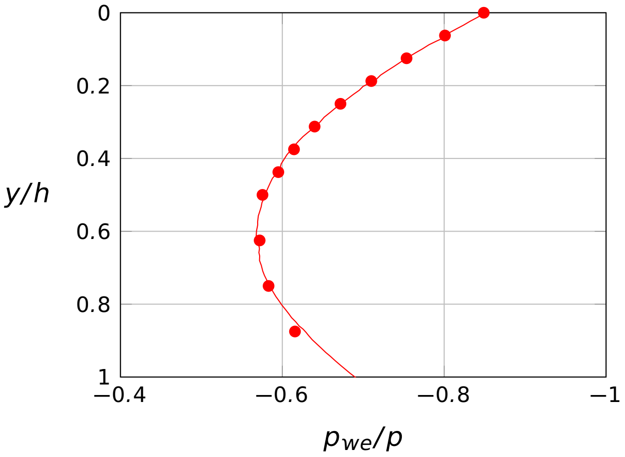

Figure 47.5: Excess pore pressure p_{we} beneath footing centre

47.4 Conclusion

This example verifies that the drained and undrained displacements and stresses obtained by the finite element method are in a good agreement with the analytical solution.

47.5 Literature

[52] J.R. Booker, J.P. Carter, and J.C. Small. “An efficient method of analysis for the drained and undrained behaviour of an elastic soil”. In: *International Journal of Solids and Structures* 12.8 (1976), pp. 589 –599.

48 BE45: One-Dimensional Soil Consolidation

Overview

Element Type(s):	C2D
Analysis Type(s):	STAT
Procedure(s):	
Topic(s):	SOIL
Module(s):	TALPA
Input file(s):	soil_1d_consolidation.dat

48.1 Problem Description

In the following example a one-dimensional consolidation problem has been analyzed. The soil layer is subjected to an uniform loading of the intensity p_0 acting on the surface. Base of the soil is rigidly fixed while the sides are laterally constrained. Only the soil surface is allowed to drain. Geometry, load and boundary conditions are depicted in Fig. 48.1. The soil material is elastic, isotropic and saturated with water. The surface settlements and pore excess pressures for the two extreme cases (time zero and time infinity) of the consolidation process are compared to the analytical solution.

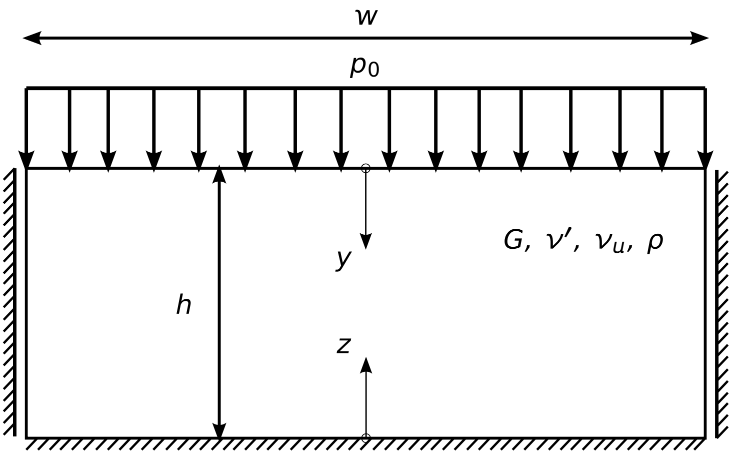

Figure 48.1: Problem Definition

48.2 Reference Solution

The analytical solution to the problem was given by Terzaghi in 1925 [53]. The solution assumes that the soil is saturated with water, the soil and water are non-deformable, the volume change takes place only on the account of the water drainage and the Darcy's filtration law applies. Then the differential equation of the one-dimensional process of consolidation for the excess water pressure p_{we} can be written as [54]:

$$\frac{\partial p_{we}}{\partial t} = c_v \frac{\partial^2 p_{we}}{\partial z^2}, \tag{48.1}$$

where:

$c_v = k \cdot E_s / \gamma_w$	coefficient of consolidation,
E_s	stiffness modulus,

k	coefficient of permeability,
γ_w	unit weight of water,
h	soil thickness,
$z = h - y$	elevation.

Taking into account the initial and boundary conditions for the problem illustrated by Fig. 48.1

$$t = 0 \quad \text{and} \quad 0 \leq z < h \quad \Rightarrow \quad p_{we} = p_0, \tag{48.2a}$$

$$0 \leq t \leq \infty \quad \text{and} \quad z = 0 \quad \Rightarrow \quad \frac{\partial p_{we}}{\partial z} = 0, \tag{48.2b}$$

$$0 \leq t \leq \infty \quad \text{and} \quad z = h \quad \Rightarrow \quad p_{we} = 0, \tag{48.2c}$$

$$t = \infty \quad \text{and} \quad 0 \leq z \leq h \quad \Rightarrow \quad p_{we} = 0, \tag{48.2d}$$

the Eq. 48.1 can be analytically solved for p_{we} as a function of the time t and the elevation $z = h - y$

$$\frac{p_{we}(t,z)}{p_0} = \frac{4}{\pi} \cdot \sum_{j=0}^{\infty} \frac{1}{2j+1} \cdot \sin\left((2j+1)\frac{\pi}{2}\frac{z}{h}\right) \cdot e^{-(2j+1)^2 \pi^2/4 \cdot T_v} \tag{48.3}$$

where:

p_0	surface pressure,
$T_v = c_v/h^2 \cdot t$	time factor.

With the known change of excess pore pressure with respect to time, the settlement due to consolidation $s(t)$ at time t can be determined

$$s(t) = \frac{p_0 h}{E_s} \cdot \left[1 - \frac{8}{\pi^2} \cdot \sum_{j=0}^{\infty} \frac{1}{(2j+1)^2} \cdot e^{-(2j+1)^2 \pi^2/4 \cdot T_v}\right]. \tag{48.4}$$

For the time infinity, the excess pore pressures will completely dissipate (see Eq. 48.2d) and the final settlements due to consolidation s_∞ will be

$$s_\infty = s(t = \infty) = \frac{p_0 h}{E_s}. \tag{48.5}$$

48.3 Model and Results

Elastic, isotropic soil under undrained and drained conditions has been analyzed. Material, geometry and loading properties are summarized in Table 48.1. The undrained soil condition is considered with the help of the method based on the undrained effective stress (σ') analysis using effective material parameters. G and ν' are effective soil parameters, while B represents the Skempton's B-parameter. Self-weight is not taken into consideration.

Table 48.1: Model Properties

Material	Geometry	Loading
G, $\nu' = 0.0$	h	p_0
$B = 0.998$	$w = h$	
$\rho = 0.0\ kg/m^3$		

Finite element mesh of the model is shown in Fig. 48.2. Mesh is regular and consist of quadrilateral finite elements.

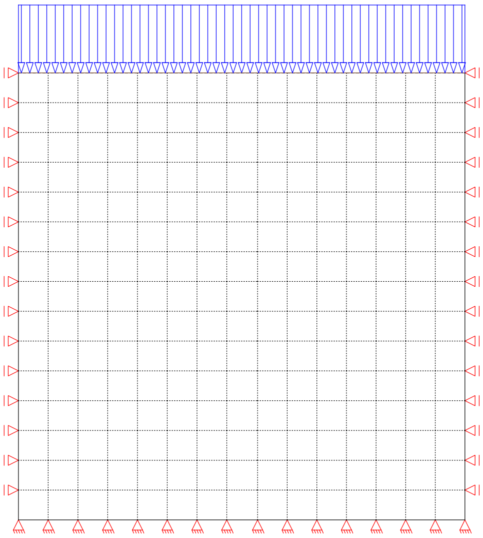

Figure 48.2: Finite Element Model

The results are summarized in the Table 48.2. Final settlement of the surface of the soil due to consolidation s_∞ is compared to the analytical solution given by Eq. 48.5. The excess water pressures p_{we} for the time zero ($T_v = 0$, undrained) and time infinity ($T_v = \infty$, drained) are compared to the analytical solutions from Eqs. 48.2a and 48.2d.

Table 48.2: Results

		$T_v = 0$		$\lvert e \rvert$	$T_v = \infty$		$\lvert e \rvert$
		SOF.	Ref.	$[-]$	SOF.	Ref.	$[-]$
$s(T_v) \cdot E_s/(p_0 h)$	$[-]$		–		1.0	1.0	0.0
$p_{we}(T_v)/p_0$	$[-]$	0.994	1.000	0.006	0.000	0.000	0.000

48.4 Conclusion

The example verifies that the settlements and excess pore pressures for initial ($t = 0$) and finial ($t = \infty$) time of the consolidation process obtained by the finite element method are in a good agreement with the analytical solution.

48.5 Literature

[53] K. Terzaghi. *Erdbaumechanik auf bodenphysikalischer Grundlage*. Leipzig (usw.): F. Deuticke, 1925.

[54] K. Terzaghi. *Theoretical Soil Mechanics*. Wiley, 1948.

49 BE46: Material Nonlinear Analysis of Reinforced Concrete Beam

Overview

Element Type(s):	B3D, SH3D
Analysis Type(s):	STAT, MNL
Procedure(s):	
Topic(s):	
Module(s):	STAR2, ASE
Input file(s):	nonl_rein_conc.dat

49.1 Problem Description

The problem consists of a single span beam of reinforced concrete, subjected to a single load P in the middle of the span, as shown in Fig. 49.1. The material nonlinear behaviour of the beam is examined and compared to test results.

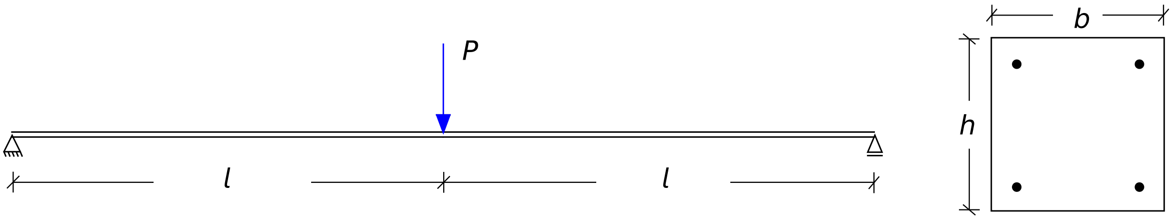

Figure 49.1: Problem Description

49.2 Reference Solution

Materially nonlinear analysis is utilised more and more for the structural design in concrete construction. It is often overlooked that for such analysis, both in-depth knowledge of the computational algorithms as well as the behavior of the concrete in cracked condition, are required. The following simple example will serve for verification of material nonlinear calculations of reinforced concrete beams. It will also highlight the unavoidable variations in practice. Therefore, the individual test results are given below and not only the mean values. The load-displacement curves of seven identical concrete beams, which were prefabricated almost at the same time and under the same controlled conditions, are graphed below. As a reference solution, these load-displacement curves of the test beams are used.

49.3 Model and Results

The properties of the model [55] are defined in Table 49.1. The simply supported beam is shown in Fig. 49.1, as well as the dimensions and the reinforcement of the beams. The total length of the span is $l_{total} = 3.0\ m$. The square rectangular cross-section with edge lengths of $20\ cm$ is reinforced by four longitudinal bars of $\oslash\ 10\ mm$ and stirrups of $\oslash\ 6\text{-}15\ cm$. For this example the stirrups are not influential and can be neglected. The load is applied at the midspan and the beam is loaded to failure. Self weight is accounted for. The material properties of the concrete, $B\ 35$ or equivalently a $C\ 35$, were determined on a total of twelve cylinders $\oslash\ 150/300$, and are given in Table 49.1. The concrete cover of the longitudinal reinforcement is $c_{v,l} = 2.4\ cm$. The reinforcing steel is a $BST\ 500\ S$, following a stress-strain law, as shown in Fig. 49.2.

The results are presented in Fig. 49.4. The deflection in the middlespan is recorded and plotted versus the load. The expectance is for the numerical calculations to fall into the gray shaded area, which bounds the curves of seven tests beams. Of particular importance, are the onset of cracking, the slope after the completion of the cracking and by the yielding of the reinforcement, as well as the limit load.

SOFiSTiK results are presented by the three additional curves included in the original figure.

For beam elements: (a) yellow color with triangles for concrete $C\ 35$, (b) red color with circles for concrete $B\ 35$. For quad elements: (c) green color with squares for concrete $C\ 35$.

Strain mm/m	Stress N/mm²
0.00	0.0
1.07	213.0
2.00	395.9
3.04	517.0
4.04	539.4
5.00	551.7
6.10	560.9
7.10	566.2
10.07	574.9
20.01	589.4
40.09	604.1
50.06	605.6
55.05	604.4
58.19	512.2

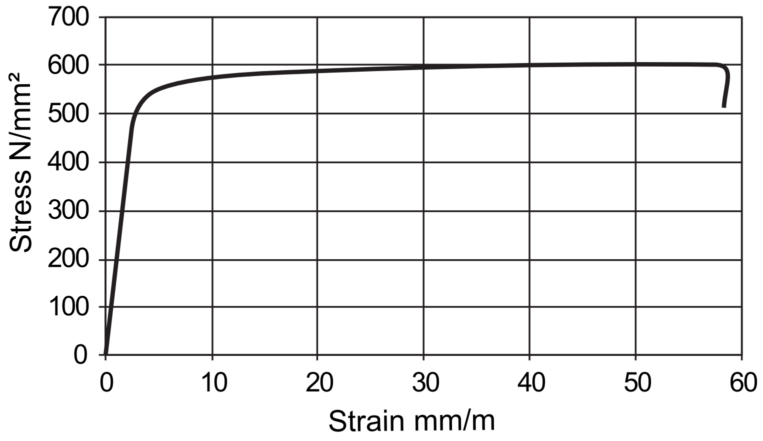

Figure 49.2: Stress-Strain Curve for Reinforcing Steel

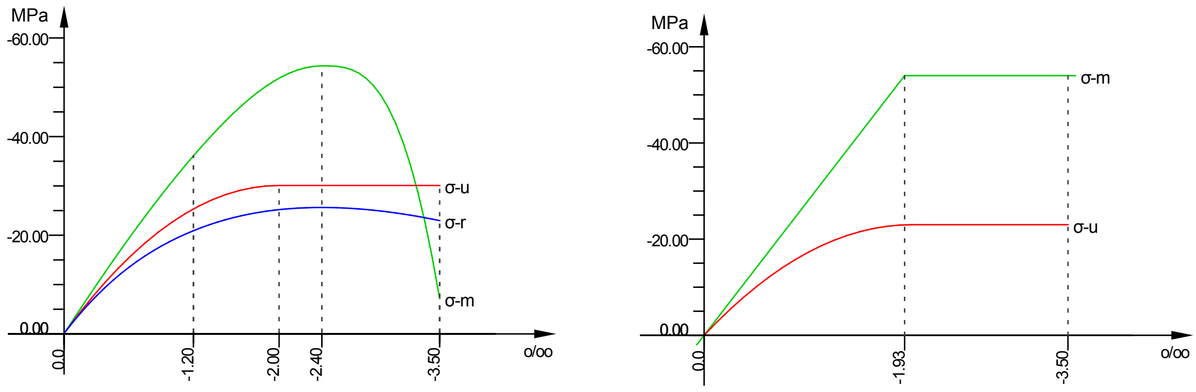

C 35 B 35

Figure 49.3: Stress-Strain Curve for Concrete

Table 49.1: Model Properties

Material Properties		Geometric Properties	Loading
Concrete	Steel	$b = h = 20.0\ cm$	$P = 1\ kN$
$B\ 35$ or $C\ 35$	$BST\ 500S$	$l = 3.0\ m$	until failure
$\rho = 2320\ kg/m^3$		$c_{v,l} = 2.4\ cm$	
$f_{cm} = 54.0\ MN/m^2$		4 bars $\oslash\ 10\ mm$	

Table 49.1: (continued)

Material Properties	Geometric Properties	Loading
$E = 28000\ MN/m^2$		

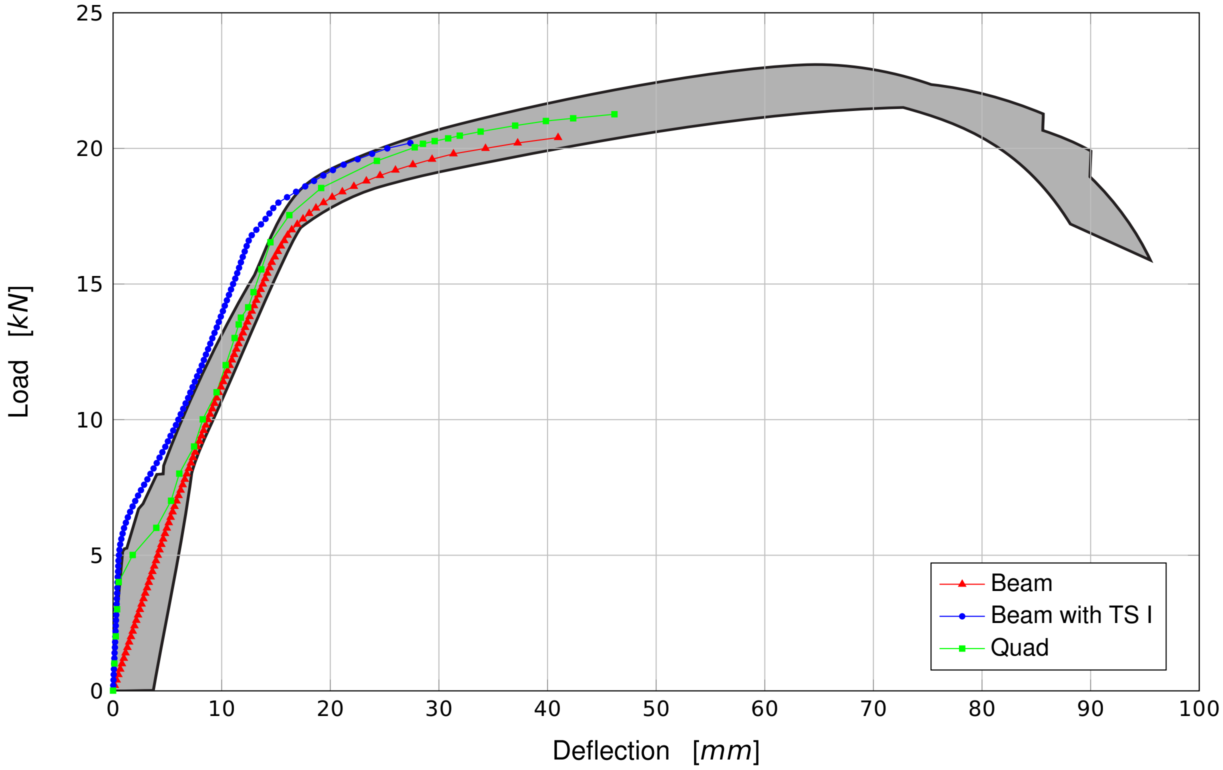

Figure 49.4: Load-Displacement Curves

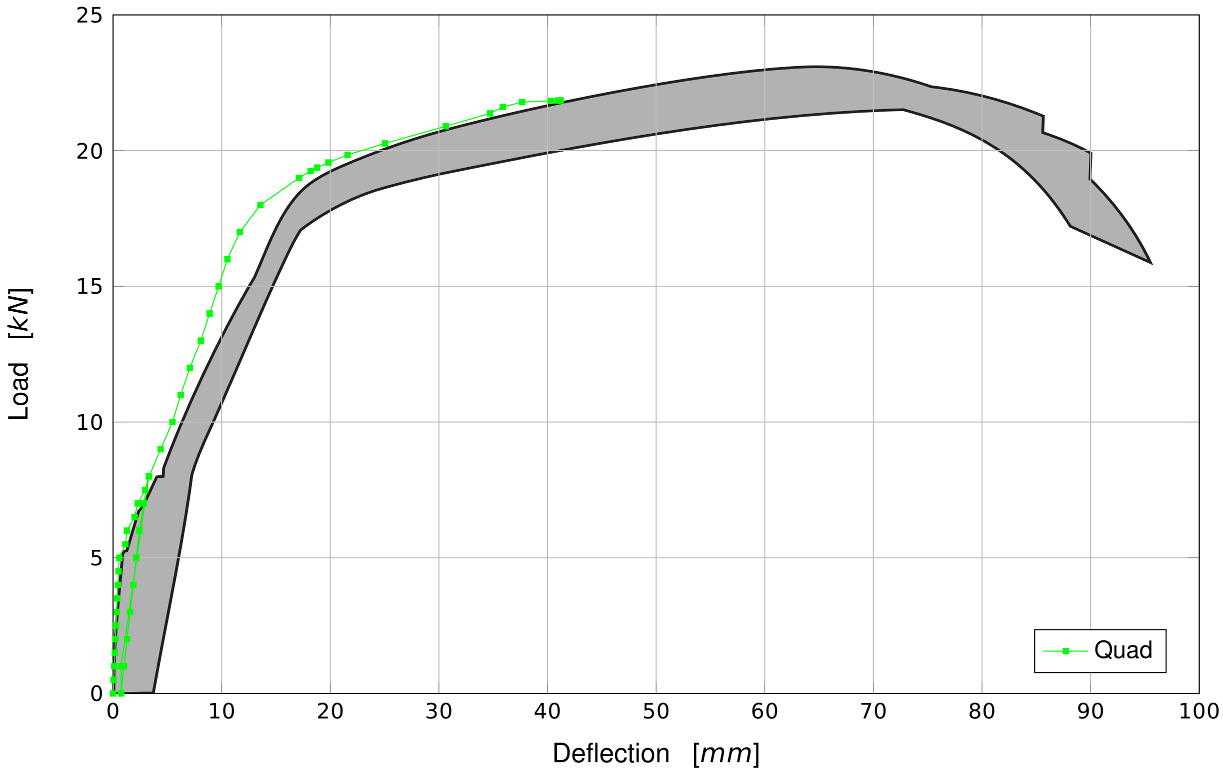

Figure 49.5: Load-Displacement Curves with reloading

49.4 Conclusion

This example examines the material nonlinear analysis of reinforced concrete beams. It has been shown that the behaviour is captured accurately.

49.5 Literature

[55] *VDI 6201 Beispiel: Softwaregestütze Tragwerksberechnung - Beispiel Stofflich nichtlineare Berechnung von Stahlbetonbalken, Kategorie 1: Mechanische Grundlagen*. Verein Deutscher Ingenieure e. V.

50 BE47: Pushover Analysis: SAC LA9 Building

Overview

Element Type(s):	B3D
Analysis Type(s):	MNL
Procedure(s):	EIGE
Topic(s):	EQKE
Module(s):	ASE, SOFiLOAD
Input file(s):	pushover_sac_la9.dat

50.1 Problem Description

In this example a pushover analysis of a moment resisting frame structure is performed. The pushover curve is identified and compared to the reference solution, as described in Chopra [56].

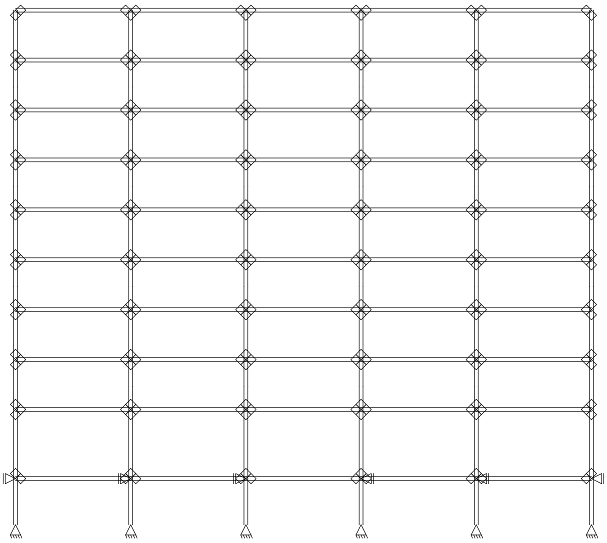

Figure 50.1: Problem Description

50.2 Reference Solution

In this Benchmark the interest is focused in the retrieval of the pushover curve. The steps involved in this process are described schematically in Figure 50.2. Important is the definition of the pushover lateral load case pattern. The pushover analysis is performed by subjecting the structure to this monotonically increasing load pattern of lateral forces. Here the first three eigenmodes of the structure will be used. Choosing the characteristic force and displacement of the structure, a so called *pushover curve* of the multi-degree-of-freedom (MDOF) system can be obtained. The force, here denoted as V_b, is usually *base-shear*, while the displacement is a displacement of the characteristic point on the structure u_{cnod}, also called the *roof displacement* and the *control node displacement*.

50.3 Model and Results

The properties of the model are presented in Table 50.1 and Figure 50.3. The model utilised in this Benchmark consists of the benchmark structure for the SAC project, as has been described by Gupta

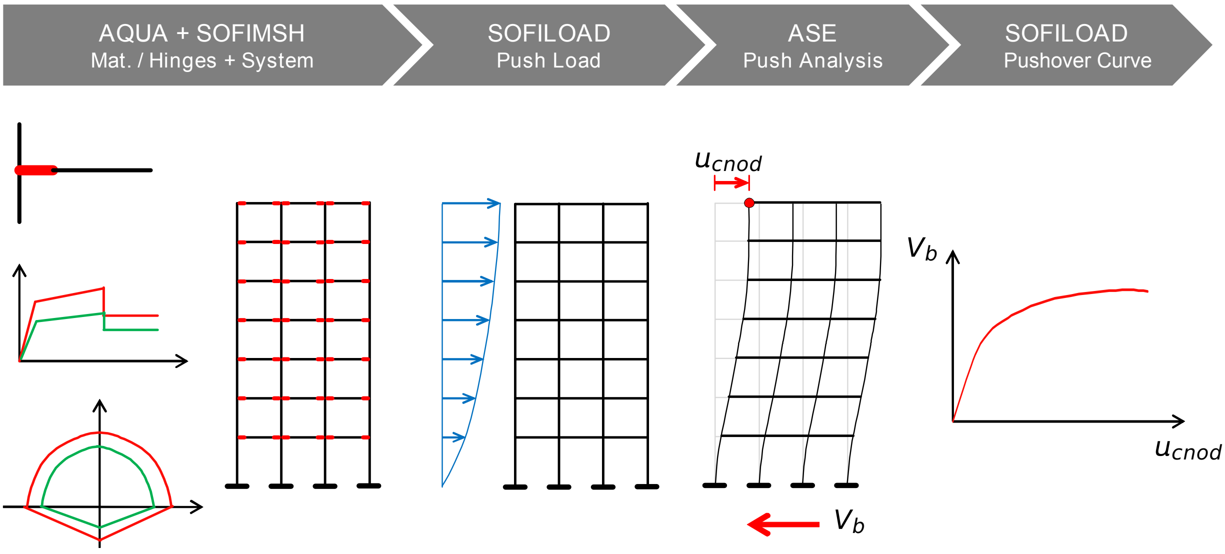

Figure 50.2: Pushover curve determination workflow

and Krawinkler [57], Chopra and Goel [56] and FEMA [58].

“The 9-story structure, was designed by Brandow & Johnston Associates for the SAC2 Phase II Steel Project. Although not actually constructed, this structure meets seismic code and represents typical medium-rise buildings designed for the Los Angeles, California, region. The building is square in plan and rises nine floors above ground in elevation. The bays are $9.15\ m$ on center, in both directions, with five bays each in the north-south (N-S) and east-west (E-W) directions. The buildingâ€™s lateral load-resisting system is composed of steel perimeter moment-resisting frames (MRFS) with simple (simple hinged connection) framing on the farthest south E-W frame. The columns are steel wide-flange sections. The levels of the 9-story building are numbered with respect to the ground level, with the ninth level being the roof. The building has a basement level, denoted B-1. The column lines employ two-tier construction, i.e., monolithic column pieces are connected every two levels beginning with the first level. Column splices, which are seismic (tension) splices to carry bending and uplift forces, are located on the first, third, fifth, and seventh levels at $h_s = 1.83\ m$ above the center-line of the beam to column joint. The column bases are modeled as pinned and secured to the ground (B-1). Concrete foundation walls and surrounding soil are assumed to restrain the structure at the ground level from horizontal displacement. The floor system is composed of steel wide-flange beams in acting composite action with the floor slab. Each frame resists one half of the seismic mass associated with the entire structure. The seismic mass of the structure is due to various components of the structure. The model is based on centerline dimensions of the bare frame in which beams and columns extend from centerline to centerline. The strength, dimension, and shear distortion of panel zones are neglected.” [56]

“Shear deformations in beam and column elements are neglected. Plastic zones in beams and columns are modeled as point hinges. The hysteretic behavior at plastic hinge locations is described by a bilinear moment-rotation diagram. All elements have 3% strain hardening. Expected rather than nominal yield strength values are used ($49.2\ ksi$ for $A\ 36$ steel and $57.6\ ksi$ for $A\ 50$ steel). Viscous damping 2% is used in first mode and at $T = 0.2\ sec$.” [58]

Table 50.1: Model Properties

Material	Geometry
$A\ 50$	$l = 9.15\ m$
$A\ 36$	$h_b = 3.65\ m$, $h_g = 5.49\ m$

Table 50.1: (continued)

Material	Geometry
	$h_f = 3.96\,m$, $h_s = 1.83\,m$

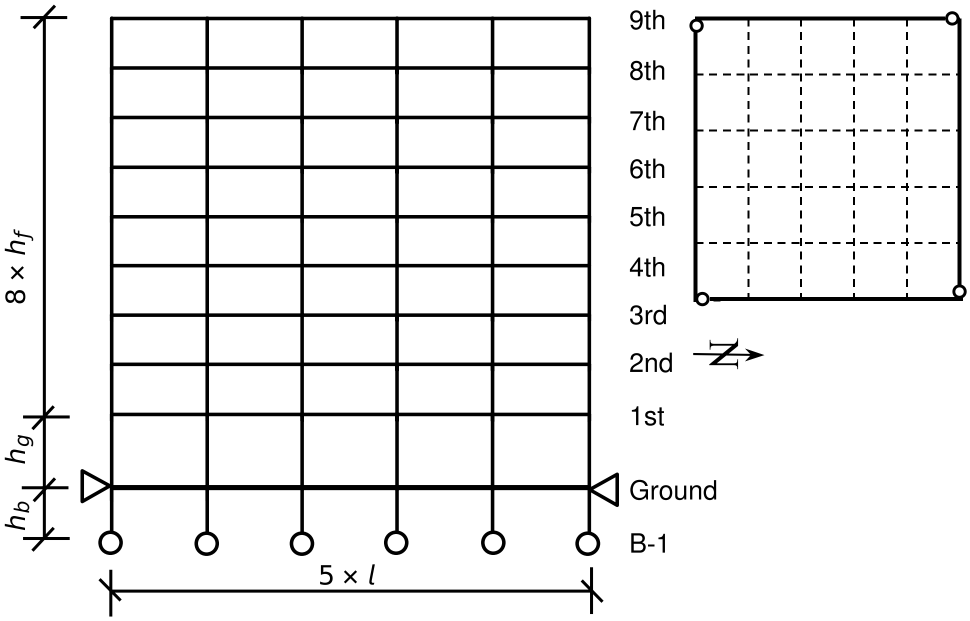
$8 \times h_f$
h_g
h_b
9th
8th
7th
6th
5th
4th
3rd
2nd
1st
Ground
B-1
$5 \times l$

Figure 50.3: Model Description

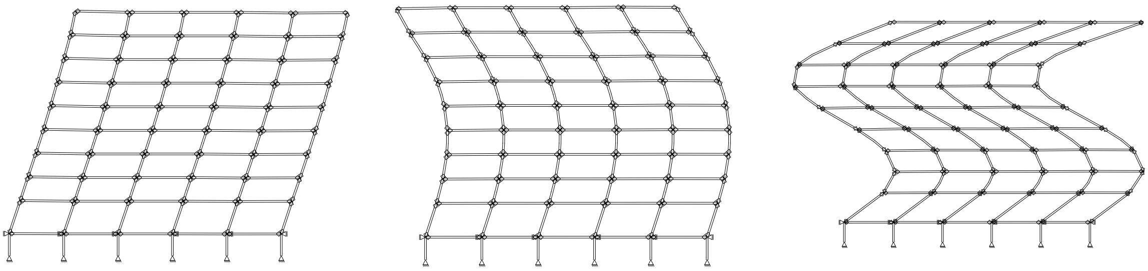
(a) Mode 1

(b) Mode 2

(c) Mode 3

Figure 50.4: Eigenmodes

Table 50.2: First three natural-vibration periods

Periods	Ref. [56]	SOF.
T_1	2.27	2.26
T_2	0.85	0.85
T_3	0.49	0.49

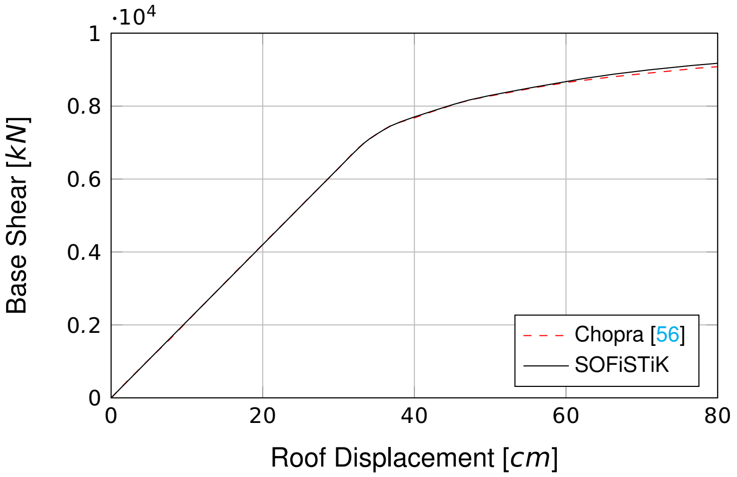

(a) Mode 1 Pushover Curve

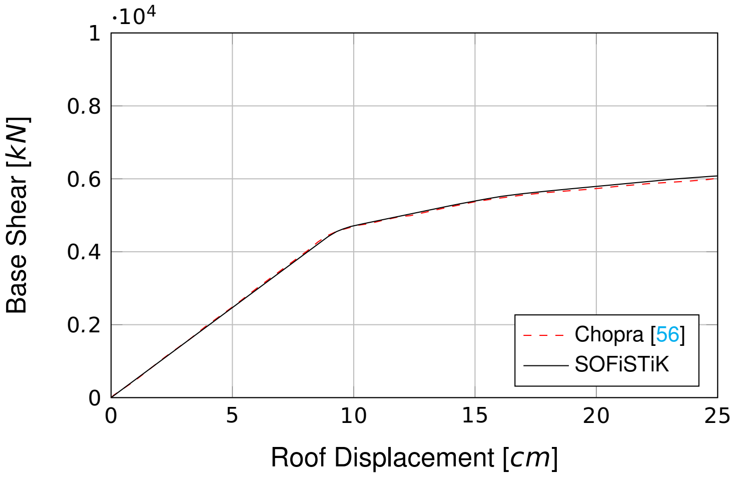

(b) Mode 2 Pushover Curve

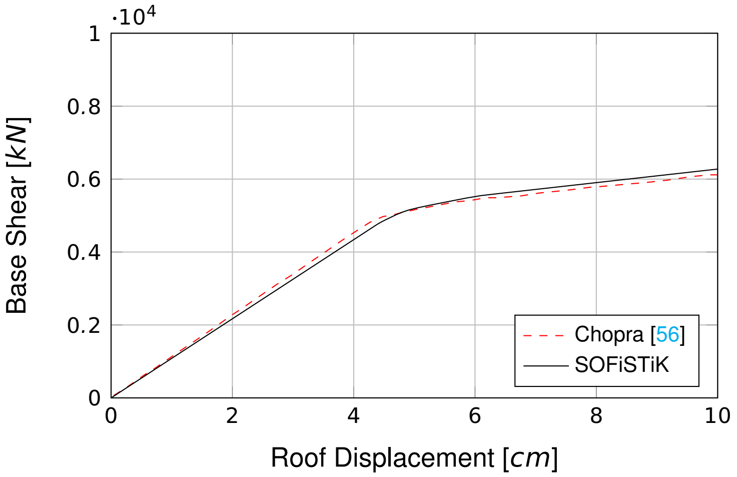

(c) Mode 3 Pushover Curve

Figure 50.5: Pushover Curves

The first three vibration modes and periods of the building for linearly elastic vibration are shown in Figure 50.4. The vibration periods are 2.26, 0.85, and 0.49 sec, respectively. The force distributions of these first three modes are used in the pushover analysis in order to retrieve the pushover curves. The pushover curves for the first three eigenmodes, are presented in Figures 50.5. The hinge formation distribution for each pushover analysis, corresponding to approximatelly the last load case depicted in each pushover curve, is presented in Figures 50.6.

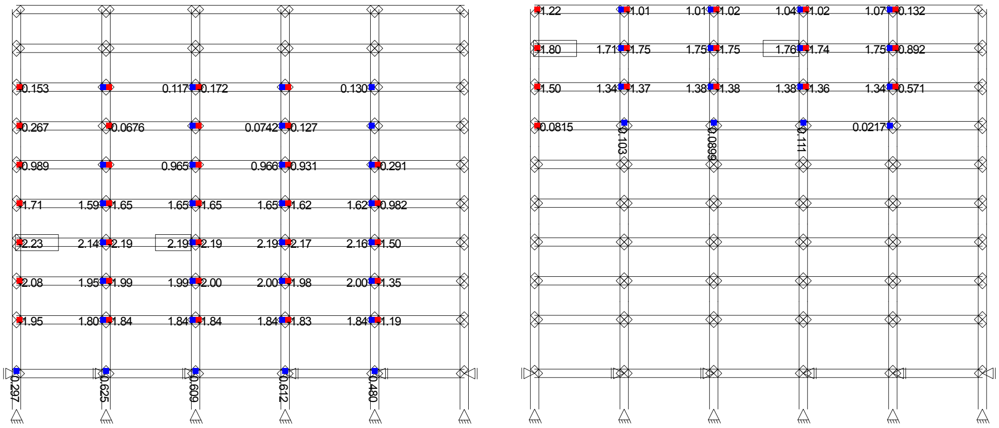
0.153
0.117
0.172
0.130
0.267
0.0676
0.0742
0.127
0.989
0.965
0.966
0.931
0.291
1.71
1.59
1.65
1.65
1.65
1.65
1.62
1.62
0.982
2.23
2.14
2.19
2.19
2.19
2.19
2.17
2.16
1.50
2.08
1.95
1.99
1.99
2.00
2.00
1.98
2.00
1.35
1.95
1.80
1.84
1.84
1.84
1.84
1.83
1.84
1.19
0.297
0.625
0.609
0.612
0.480
1.22
1.01
1.01
1.02
1.04
1.02
1.07
0.132
1.80
1.71
1.75
1.75
1.75
1.76
1.74
1.75
0.892
1.50
1.34
1.37
1.38
1.38
1.38
1.36
1.34
0.571
0.0815
0.103
0.0899
0.111
0.0217

(a) Mode 1

(b) Mode 2

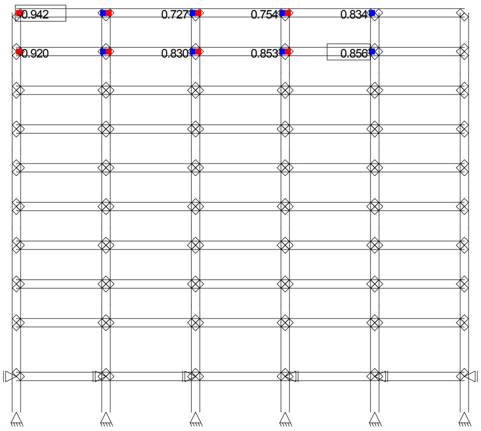
0.942
0.727
0.754
0.834
0.920
0.830
0.853
0.856

(c) Mode 3

Figure 50.6: Hinge distribution

50.4 Conclusion

This example adresses the determination of the pushover curve for a benchmark structure. It has been shown that the results obtained are in a good agreement with the reference given by Chopra [56].

50.5 Literature

[56] A.K. Chopra and R. K. Goel. *A Modal Pushover Analysis Procedure to Estimate Seismic Demands for Buildings: Theory and Preliminary Evaluation*. Tech. rep. PEER Report 2001/03. Pacific Earthquake Engineering Research Center - University of California Berkeley, 2001.

[57] A. Gupta and H. Krawinkler. *Seismic Demands for Performance Evaluation of Steel Moment Resisting Frame Structures*. Tech. rep. Report No. 132. The John A. Blume Earthquake Engineering Center, 1999.

[58] Prepared for the SAC Joint Venture Partnership by Helmut Krawinkler. *State of the Art Report on Systems Performance of Steel Moment Frames Subject to Earthquake Ground Shaking*. Tech. rep. FEMA-355C. Federal Emergency Management Agency (FEMA), 2000.

51 BE48: Triaxial Consolidated Undrained (CU) Test

Overview	
Element Type(s):	CAXI
Analysis Type(s):	MNL
Procedure(s):	LSTP
Topic(s):	SOIL
Module(s):	TALPA
Input file(s):	triaxial_cu_test.dat, triaxial_cu_test_200.dat

51.1 Problem Description

In this example a consolidated undrained (CU) triaxial test on a loose Hostun-RF sand is simulated. The specimen is subjected to different levels of triaxial confining stresses and the results are compared to those of the experimental tests and numerical simulations, as described in Wehnert [59].

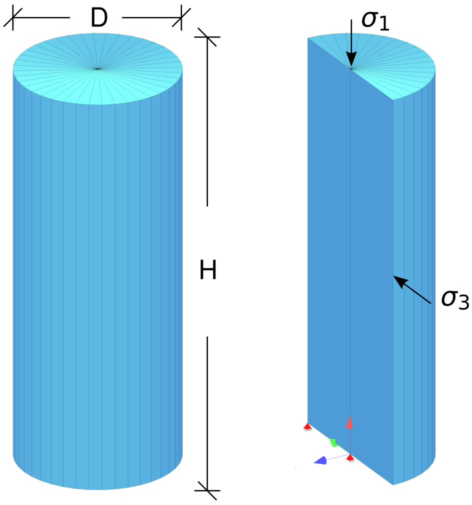

Figure 51.1: Problem Description

51.2 Reference Solution

In this example two soil models are utilised, the Mohr-Coulomb (MC) and the Hardening Soil (HS) model. Further details on these two models can be found in Benchmarks 20 and 21.

The choice of the appropriate model for the soil is of a significant importance. For example, MC model can significantly overestimate the undrained shear strength for a normally consolidated soil. More advanced models can provide better estimate for the undrained strength than the MC model. In particular, the HS model is able to represent the change of the excess pore water pressure occurring under undrained shear loading conditions, providing more realistic effective stress paths and values for undrained shear strength. However, the results of the analysis with the Hardening Soil model are very sensitive to the used model parameters and the choice of the dilatancy model. Therefore, in this example for the HS model different dilatancy formulations are tested and their influence on the result examined.

A well-established stress dilatancy theory is described by Rowe [60], where the so-called mobilized dilatancy angle ψ_m is defined as

$$\sin\psi_m = \frac{\sin\varphi_m - \sin\varphi_{cs}}{1 - \sin\varphi_m \sin\varphi_{cs}} \tag{51.1}$$

Therein, the critical state friction angle φ_{cs} marks the transition between contractive (small stress ratios with $\varphi_m < \varphi_{cs}$) and dilatant (higher stress ratios with $\varphi_m > \varphi_{cs}$) plastic flow. The mobilized friction angle φ_m in Equation 51.1 is computed according to

$$\sin\varphi_m = \frac{\sigma'_1 - \sigma'_3}{2c \cdot \cot\varphi - \sigma'_1 - \sigma'_3} \tag{51.2}$$

At failure, when $\varphi_m \equiv \varphi$, also the dilatancy angle reaches its final value $\psi_m \equiv \psi$. Accordingly, from Equation 51.1 the critical state friction angle can be derived as

$$\sin\varphi_{cs} = \frac{\sin\varphi - \sin\psi}{1 - \sin\varphi \sin\psi} \tag{51.3}$$

It has been recognized that in some cases the Rowe's model for dilatancy angles (Eq. 51.1) can overestimate the contractive behavior of the soil at low mobilized friction angles, $\varphi_m < \varphi_{cs}$. As a remedy, several researchers have developed modified formulations based on the original Rowe's model. Some of these models which are implemented in SOFiSTiK are described below.

One of the models which does not require additional input parameters is the model according to Soreide [61] which modifies the Rowe's formulation by using the scaling factor $\sin\varphi_m / \sin\varphi$

$$\sin\psi_m = \frac{\sin\varphi_m - \sin\varphi_{cs}}{1 - \sin\varphi_m \sin\varphi_{cs}} \cdot \frac{\sin\varphi_m}{\sin\varphi} \,. \tag{51.4}$$

Wehnert [59] proposed a model based on a lower cut-off value ψ_0 for the modification of the Rowe's formulation from Eq. 51.1 at low mobilized friction angles

$$\sin\psi_m = \begin{cases} \sin\psi_0 & ; \quad 0 < \psi_m \le \psi_m^{Rowe} \\ \dfrac{\sin\varphi_m - \sin\varphi_{cs}}{1 - \sin\varphi_m \sin\varphi_{cs}} & ; \quad \psi_m^{Rowe} < \psi_m \le \psi \end{cases} \,. \tag{51.5}$$

This dilatancy model obviously requires a specification of an additional parameter, ψ_0.

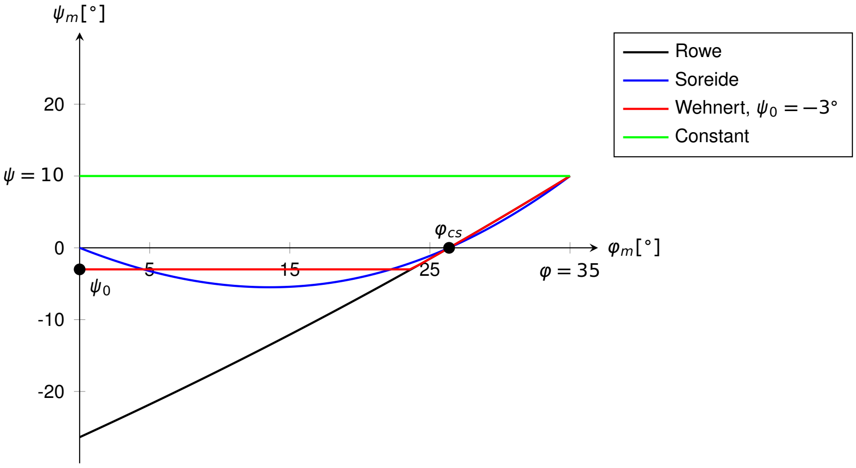

Figure 51.2: Comparison of models for mobilized dilatancy angle ψ_m implemented in SOFiSTiK for $\varphi = 35°$ and $\psi = 10°$

51.3 Model and Results

The properties of the model are presented in Table 51.1. Two material models are considered: the Mohr-Coulomb and the Hardening Soil, which is combined with the different dilatancy models as described by the formulations presented in Section 51.2. For the model according to Wehnert (Eq. 51.5) additional parameter, dilatancy ψ_0 at low stress ratios, is used. The undrained calculation is conducted in the form of effective stresses with effective shear parameters (c', φ') and stiffness parameters. Skempton's parameter $B \approx 0.9832$ (corresponding undrained Poisson's ratio is $\nu_u = 0.495$) is considered to describe the incompressibility of the pore water and saturated soil [59].

The analysis is carried out using an axisymmetric model. Two confining stress levels are considered, $\sigma_c = 200$ and $300\ kPa$. The undrained triaxial test on loose Hostun-RF sand is used as a reference. More information about the Hostun-RF sand can be found in Wehnert [59].

Table 51.1: Model Properties

Material		Geometry	Loading
$E = 60.0\ MN/m^2$	$E_{s,ref} = 16.0\ MN/m^2$	$H = 0.09\ m$	Phase I:
$\nu_{ur} = 0.25$	$E_{50,ref} = 12.0\ MN/m^2$	$D = 0.036\ m$	$\sigma_1 = \sigma_3 = \sigma_c =$
$\gamma = 0.0\ MN/m^3$	$m = 0.75$		$= 200, 300\ kPa$
$c' = 0.01\ kN/m^2$	$R_f = 0.9$		Phase II:
$\varphi' = 34°$	$K_0 = 0.44$		$\sigma_3 = \sigma_c = 200, 300\ kPa$
$\psi = 2°$	$B = 0.9832$		$\sigma_1 = \sigma_a > \sigma_c$
$\psi_0 = -4°$			

The results, as calculated by SOFiSTiK, are presented in Figures 51.3 - 51.9 (MC, HS-Rowe, HS-Cons, HS-Soreide and HS-Wehnert). Figures 51.3 - 51.8, also include the results of the numerical simulations and of the experimental tests from Wehnert [59] (Wehnert, Exp. 1 and Exp. 2). On a $p - q$ diagram, apart from the effective stress paths (ESP), the total stress paths (TSP) as well as the Mohr-Coulomb failure condition (MC failure) based on the used shear parameters, c' and φ', are displayed.

First the numerical simulation results by Wehnert [59] are compared to the results from the laboratory tests (Exp. 1 and Exp. 2). Although the oedometer and the drained triaxial tests (see also Benchmark 49) show good agreement with the results from the laboratory tests, the results from the undrained triaxial tests show deviation from the experimental results (see Figs. 51.3 - 51.8)[1]. The difference comes mainly as a result of the used dilatancy model (Eq. 51.5) and the choice of the model parameters, i.e. the peak dilatancy angle ψ and the lower cut-off dilatancy angle ψ_0.

Comparing the results of the development of the deviatoric stress q and the excess pore water pressure p_{we} between the experiment and the calculation, one can notice a considerable difference, both for the confining stress level of $200\ kPa$ as well as for the level of $300\ kPa$ (Figs. 51.4, 51.5, 51.7 and 51.8). As explained in [59], the test sample with confining stress of $200\ kPa$ behaves significantly more dilatant than the sample with the confining stress of $300\ kPa$. Since only one material model has been used to model the soil, only one peak dilatancy angle can be used to represent the dilatancy effects of both test cases. This peak dilatancy angle of $\psi = 2°$ represents therefore a compromise, leading to a underestimation of the results for a test with a smaller confining stress level and to overestimation of the results with larger confining stress level at higher mobilized friction angels.

Further differences arise from the chosen dilatancy model and the used lower cut-off dilatancy angle $\psi_0 = -4°$[2]. Due to the presence of the negative mobilized dilatancy angle ($\psi_m < 0$) at low stress levels, the soil has the tendency to decrease its volume (contraction) under increase of the deviatoric stress q (shear). However, since the soil is under undrained conditions, the volumetric strains cannot develop, and as a result the excess pore pressure increases under shear. The increase of the excess pore pressure means that the effective stresses will reduce (ESP lines curve to the left in the $p-q$ plot, Figs. 51.3 and 51.6). With the increase of the stress level, the contractive behavior turns to dilatant, meaning that the negative rate of excess pore pressures (pore water under-pressure) will arise, excess pore pressures decrease and hence the effective stresses increase. This transition from contractant to dilatant behavior occurs when the mobilized friction angle φ'_m becomes larger than the phase transition angle φ'_f which is approximately equal to the critical state friction angle φ'_{cs} (see Fig. 51.2). As further noted by Wehnert [59], due to the fact that mobilized dilatancy angle at low stress levels is slightly heigher and kept constant ($\psi_m = \psi_0$ for $0 \leq \psi_m \leq \psi_m^{Rowe}$, Eq. 51.5), the pore water under-pressures are overestimated.

Next the SOFiSTiK results obtained using the same soil model and dilatancy formulation as in [59] (HS-Wehnert) can be compared with the reference numerical simulation results (Wehnert). They show good agreement.

Finally, in other to illustrate the effect that the chosen dilatancy model can have on the results of the undrained soil, the results of the computation using the hardening soil model with different dilatancy formulations from Section 51.2 are included.

---

[1] Note also that the experimental test results for different samples of the same soil deviate significantly from each other.

[2] The used value $\psi_0 = -4°$ is much higher than the values obtained from experimental tests, which range from $-13°$ to $-21°$. The reason for choosing this higher value is due to the fact that the experimental test used to obtain the dilatancy parameters involve not only shear but also some normal stress application to the test samples [59].

51.3.1 Hostun-RF Sand, $\sigma_c = 200\ kN/m^2$

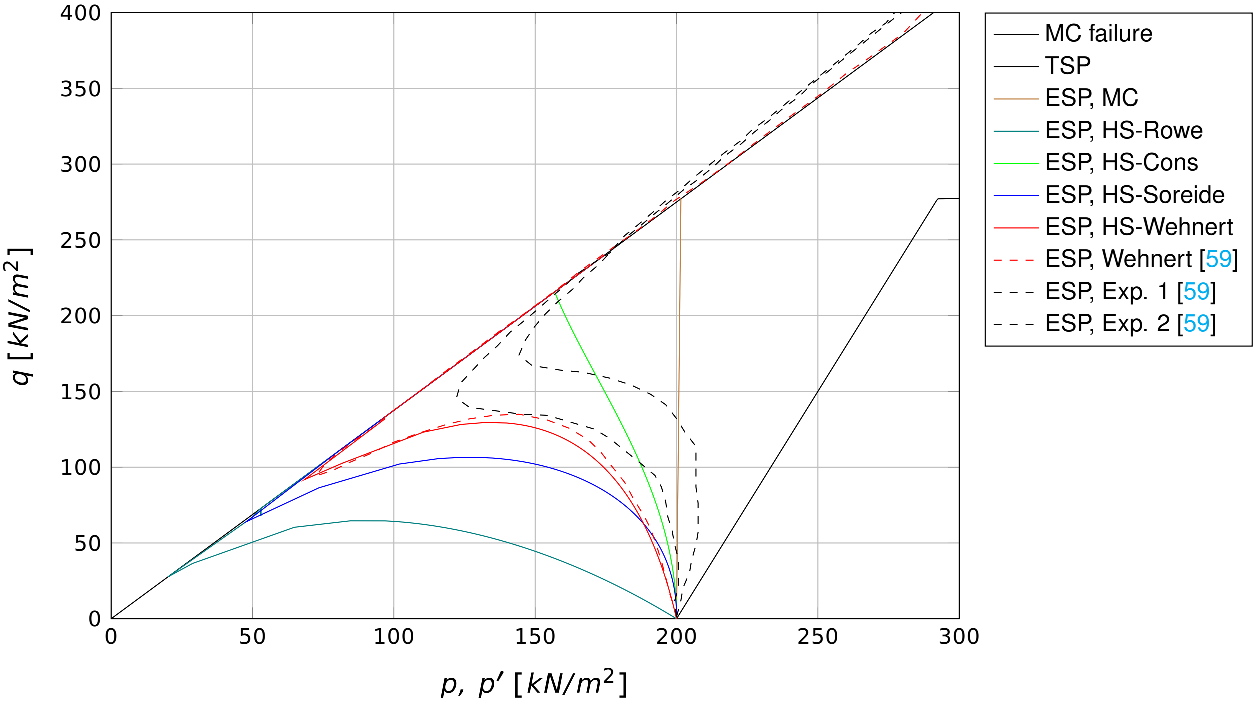

Figure 51.3: Effective stress path curve (q-p)

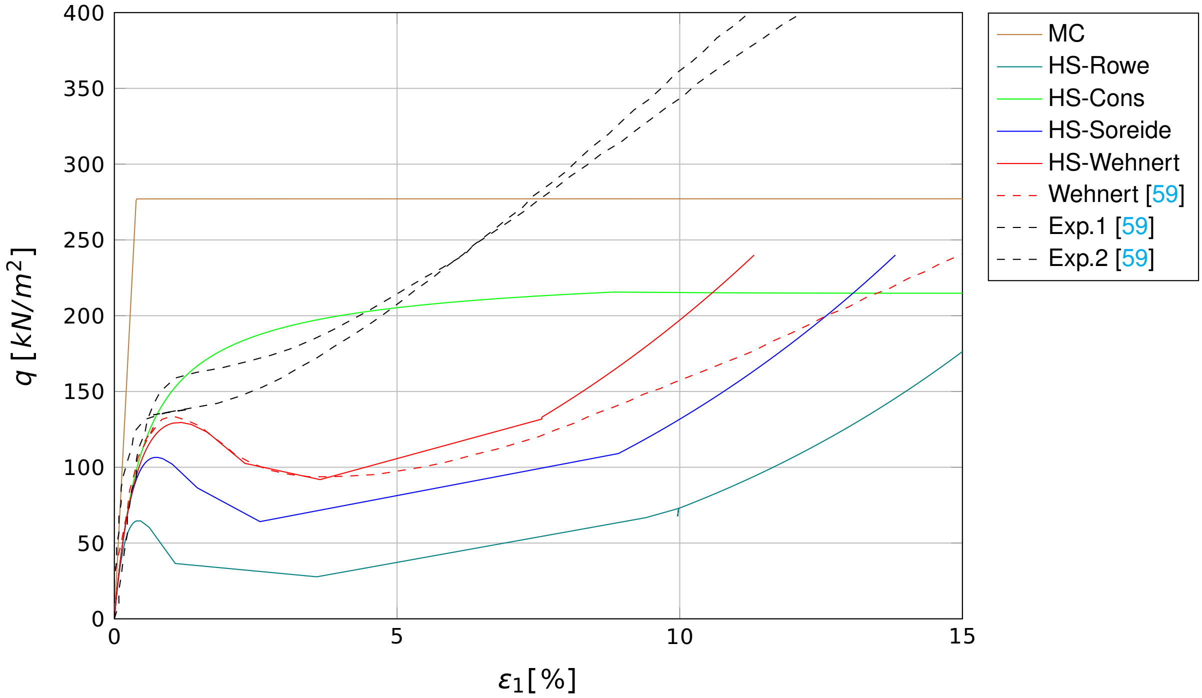

Figure 51.4: Deviatoric stress - axial strain curve (q-ε_1)

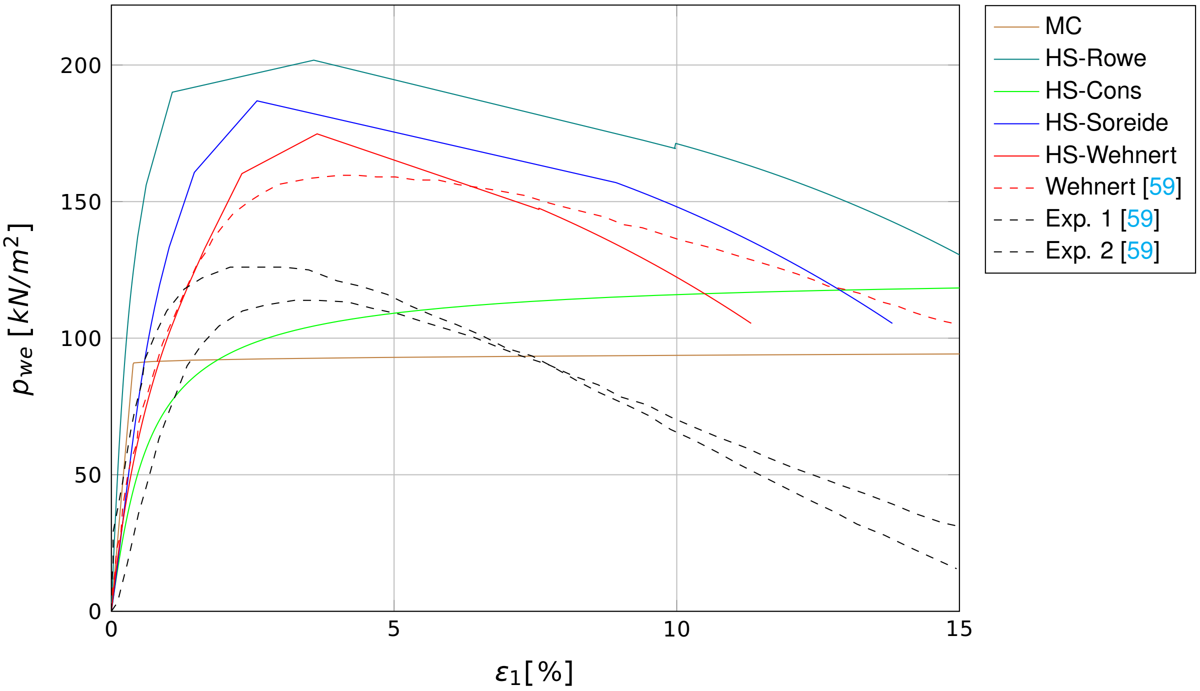

Figure 51.5: Excess porewater pressure - axial strain curve (p_{we}-ε_1)

51.3.2 Hostun-RF Sand, $\sigma_c = 300\ kN/m^2$

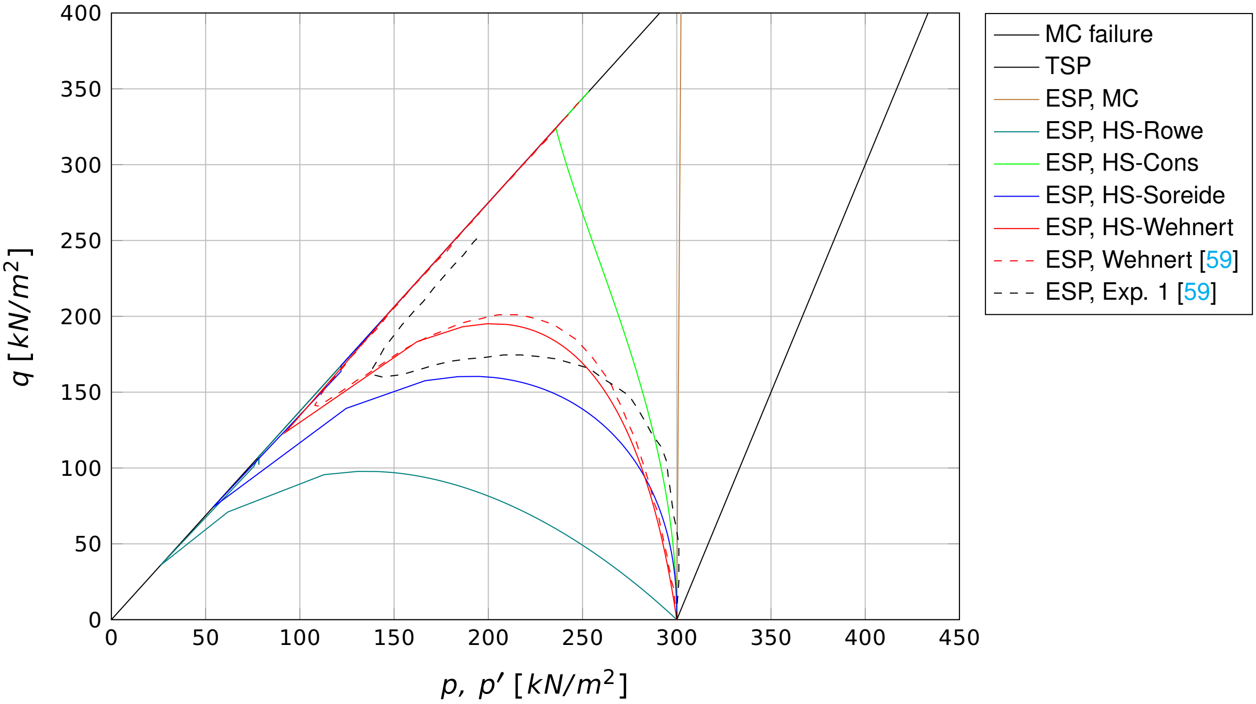

Figure 51.6: Effective stress path curve (q-p)

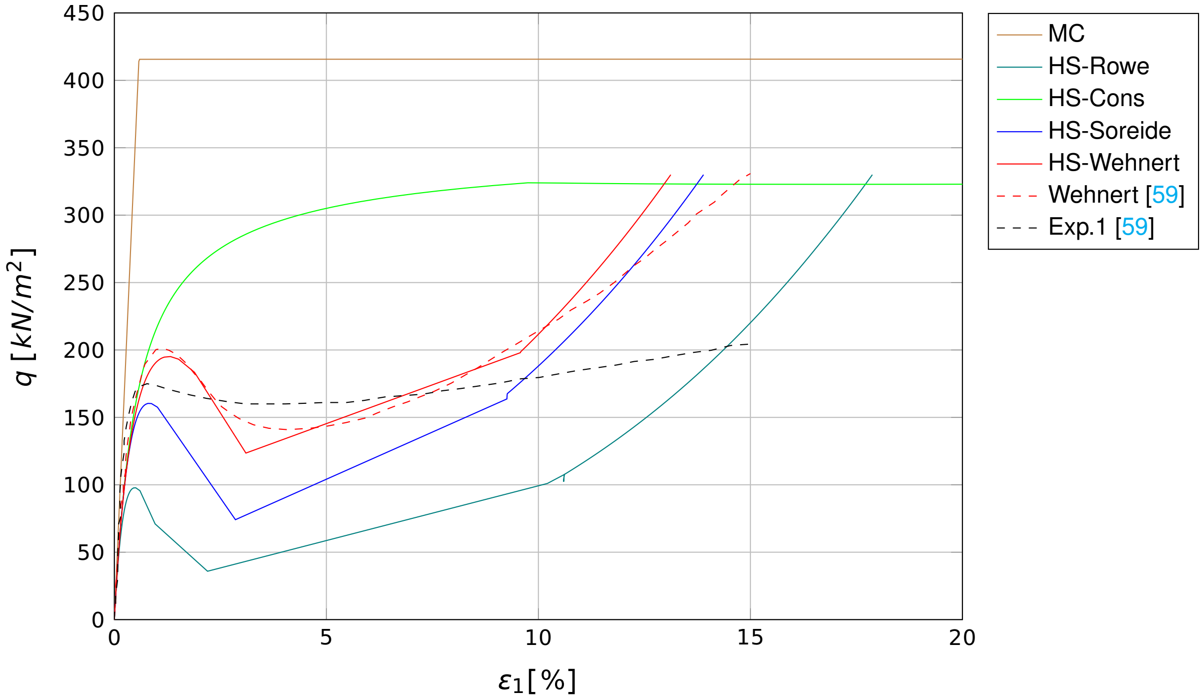

Figure 51.7: Deviatoric stress - axial strain curve (q-ε_1)

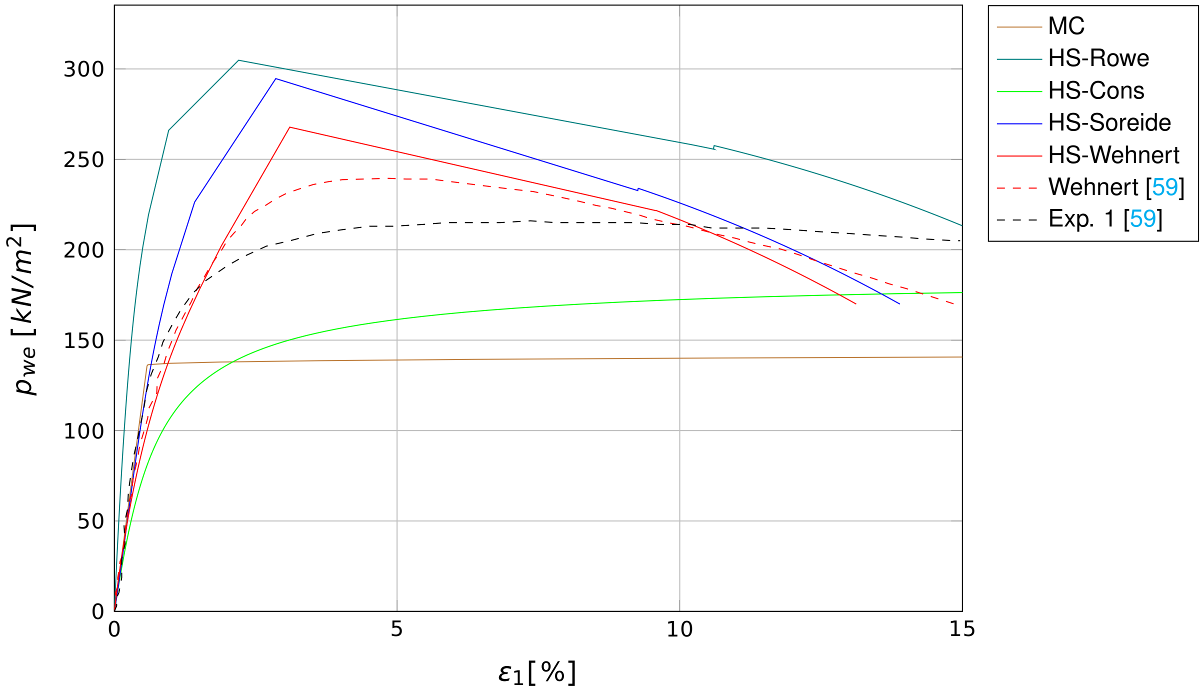

Figure 51.8: Excess porewater pressure - axial strain curve (p_{we}-ε_1)

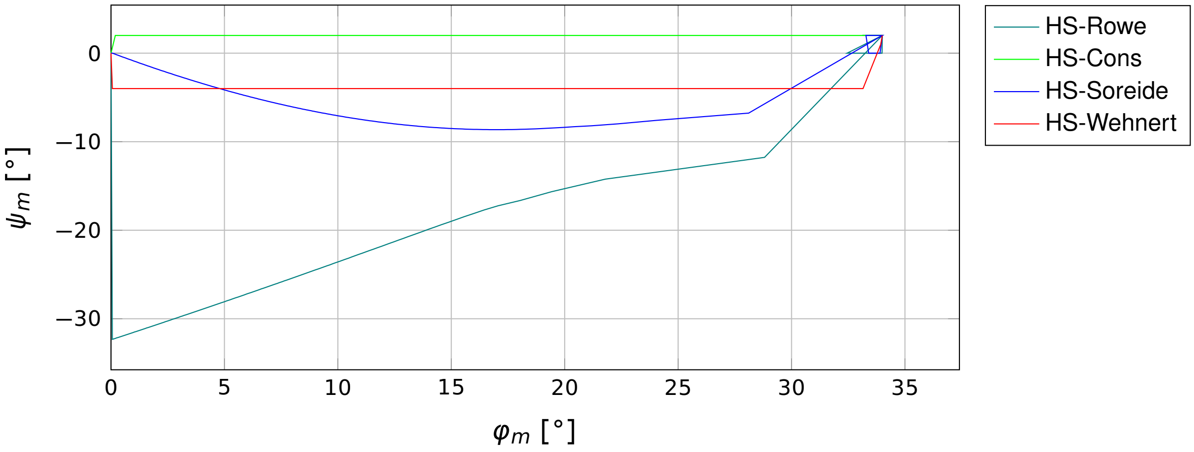

Figure 51.9: Mobilised dilatancy angle - friction angle curve (ψ_m-φ_m)

51.4 Conclusion

This example concerning the consolidated undrained triaxial test of a loose sand soil verifies that the Hardening Soil material model in combination with an appropriate choice of model parameters and dilatancy model is able to capture important behavior characteristics of the undrained soil. The numerical results are in a good agreement with the reference solution provided by Wehnert [59].

51.5 Literature

[59] M. Wehnert. *Ein Beistrag zur dreainerten und undrainerten Analyse in der Geotechnik.* Institut für Geotechnik, Universität Stuttgart: P. A. Vermeer, 2006.

[60] P.W. Rowe. “The stress-dilatancy relation for static equilibrium of an assembly of particles in contact”. In: *Proceedings of the Royal Society of London. Series A. Mathematical and Physical Sciences* 269.1339 (1962), pp. 500–527.

[61] O. K. Soreide. “Mixed hardening models for frictional soils”. PhD thesis. NTNU Norges teknisk-naturvitenskapelige universitet, 2003.

52 BE49: Triaxial Drained Test

Overview	
Element Type(s):	CAXI
Analysis Type(s):	MNL
Procedure(s):	LSTP
Topic(s):	SOIL
Module(s):	TALPA
Input file(s):	triaxial_d_test.dat, triaxial_d_test_100.dat

52.1 Problem Description

In this example a drained (D) triaxial test on a loose Hostun-RF sand is simulated. The specimen is subjected to different levels of triaxial confining stresses and the results are compared to those of the experimental tests and numerical simulations, as described in Wehnert [59].

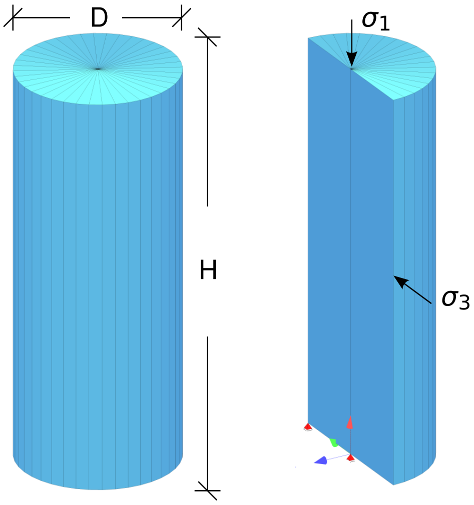

Figure 52.1: Problem Description

52.2 Reference Solution

In this example, the same triaxial test described in Benchmark 48 is examined, but for the case of a drained sample. Two soil models are utilised, the Mohr-Coulomb (MC) and the Hardening Soil (HS) model with different dilatancy configurations. Further details on the material models can be found in Benchmarks 48.

52.3 Model and Results

The properties of the model are presented in Table 52.1. Two material models are considered: the Mohr-Coulomb and the Hardening Soil, which is combined with the different dilatancy configurations as described by the formulations presented in Section 52.2 in Benchmark 48.

The analysis is carried out using an axisymmetric model. Two confining stress levels are considered,

$\sigma_c = 100$ and $300\ kPa$. The drained triaxial test on loose Hostun-RF sand is used as a reference. More information about Hostun-RF sand can be found in Wehnert [59] and Benchmark 48.

Table 52.1: Model Properties

Material		Geometry	Loading
$E = 60.0\ MN/m^2$	$E_{s,ref} = 16.0\ MN/m^2$	$H = 0.09\ m$	Phase I:
$\nu_{ur} = 0.25$	$E_{50,ref} = 12.0\ MN/m^2$	$D = 0.036\ m$	$\sigma_1 = \sigma_3 = \sigma_c =$
$\gamma = 0.0\ MN/m^3$	$m = 0.75$		$= 100, 300\ kPa$
$c' = 0.01\ kN/m^2$	$R_f = 0.9$		Phase II:
$\varphi' = 34°$	$K_0 = 0.44$		$\sigma_3 = \sigma_c = 100, 300\ kPa$
$\psi = 2°$	$B = 0.9832$		$\sigma_1 = \sigma_a > \sigma_c$
$\psi_0 = -4°$			

The results, as calculated by SOFiSTiK, are presented in Figures 52.2 - 52.8 (MC, HS-Rowe, HS-Cons, HS-Soreide and HS-Wehnert). Figures 52.2 - 52.7, also include the results of the numerical simulations and of the experimental tests from Wehnert [59] (Wehnert, Exp. 1 and Exp. 2). On a $p - q$ diagram the Mohr-Coulomb failure condition (MC failure) based on the used shear parameters, c' and φ', is also displayed.

If we first analyse the reference curves from Wehnert [59], we will notice, that the agreement between the numerical simulation and the experimental tests is quite good.

Comparing the SOFiSTiK results for the HS model with the dilatancy model acc. to Wehnert (HS-Wehnert) with the reference numerical results from Wehnert [59], we can notice that the stress paths p-q are captured exactly for both σ_c-stress levels. Accordingly, the deviatoric stress q versus the axial strain ϵ_1 curve fits very well to the reference results. For the case of the strain curves some deviation in results is identified and it seems that the Soreide dilatancy model shows better agreement with the simulation results from Wehnert.

52.3.1 Hostun-RF Sand, $\sigma_c = 100\ kN/m^2$

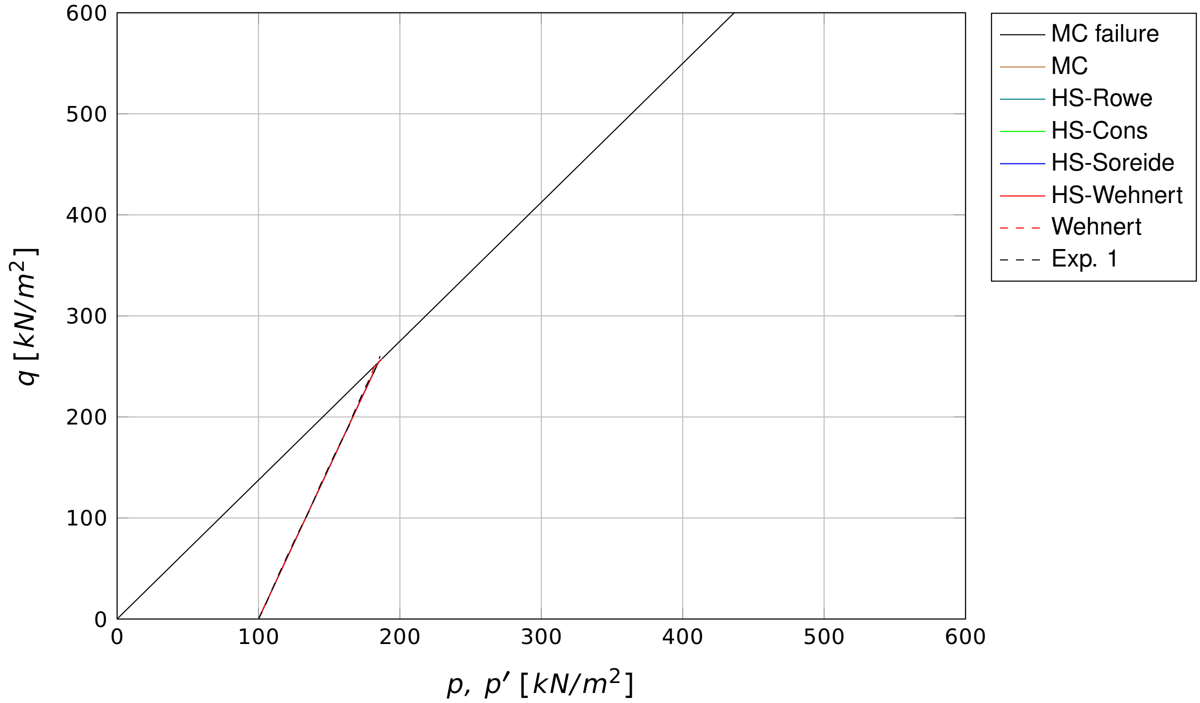

Figure 52.2: Effective stress path curve (q-p)

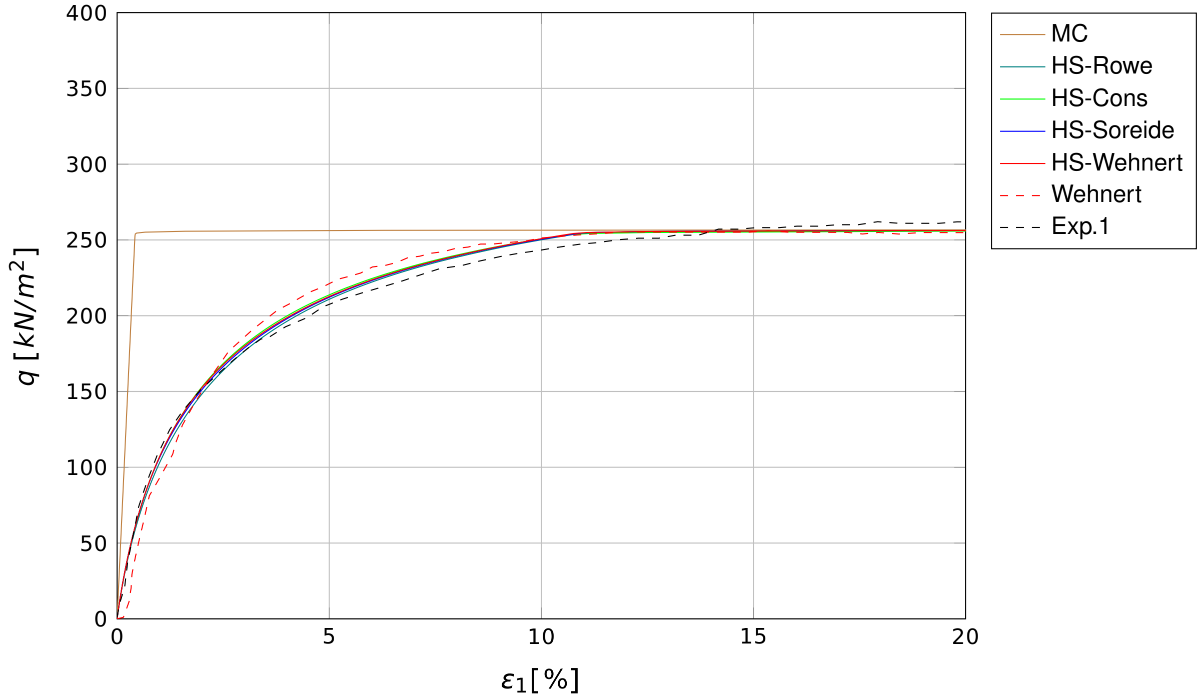

Figure 52.3: Deviatoric stress - axial strain curve (q-ε_1)

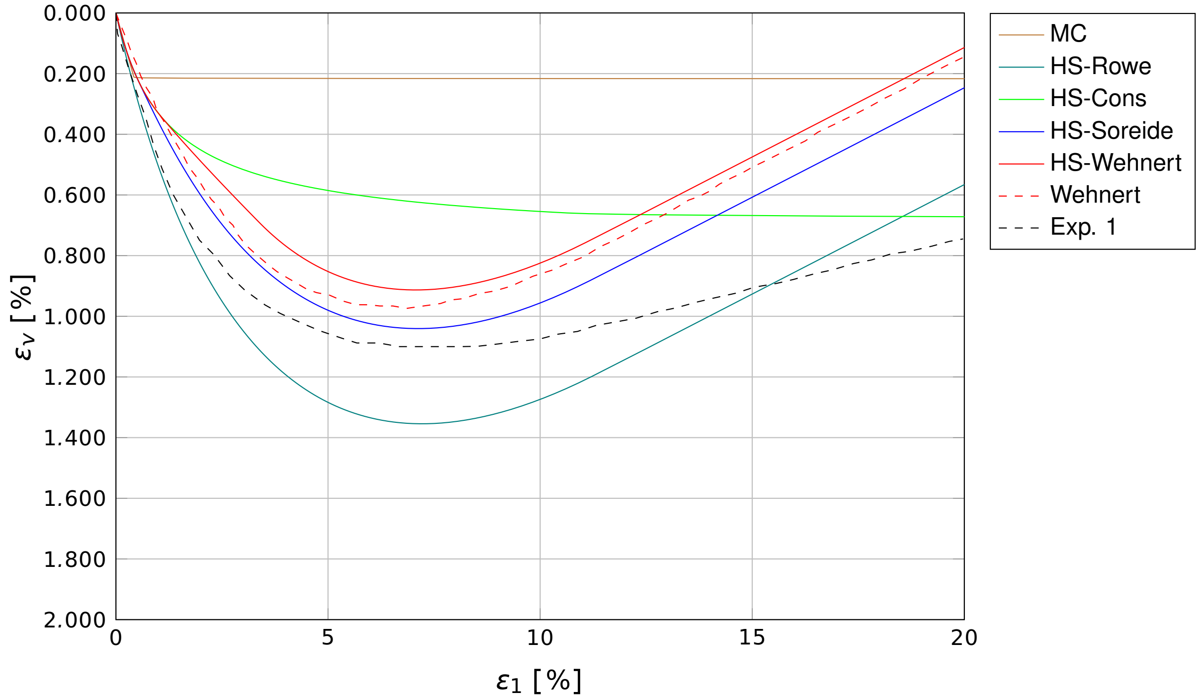

Figure 52.4: Volumetric strain - axial strain curve (ε_v-ε_1)

52.3.2 Hostun-RF Sand, $\sigma_c = 300\ kN/m^2$

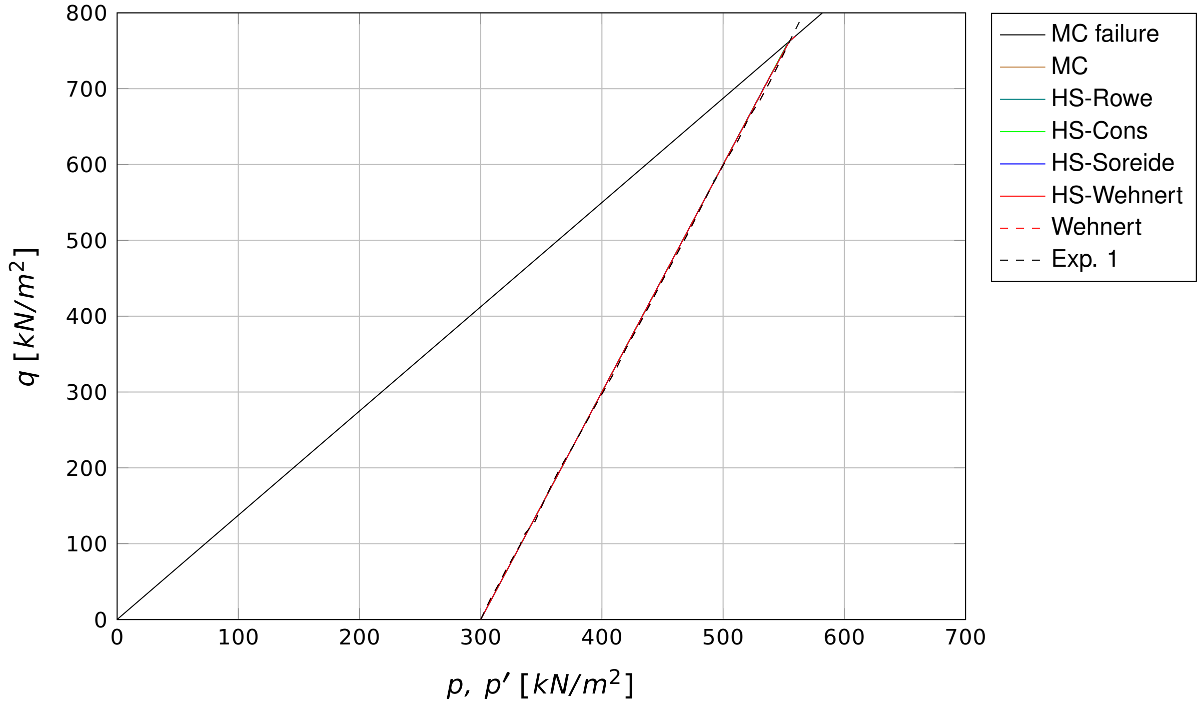

Figure 52.5: Effective stress path curve (q-p)

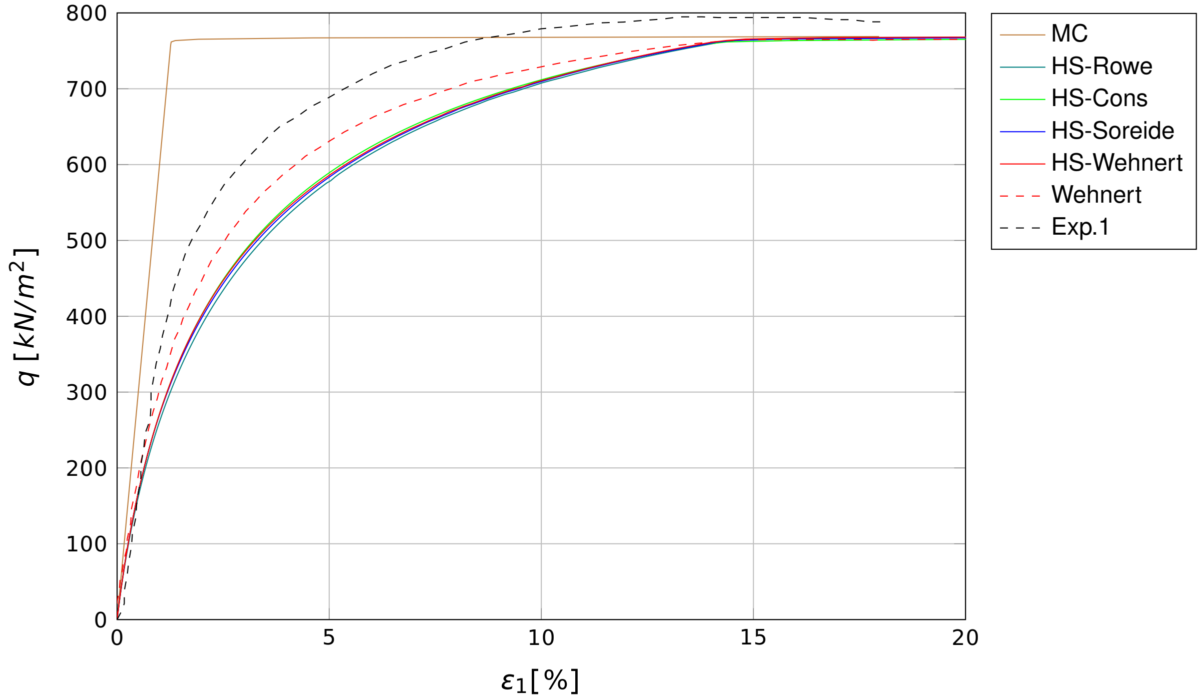

Figure 52.6: Deviatoric stress - axial strain curve (q-ε_1)

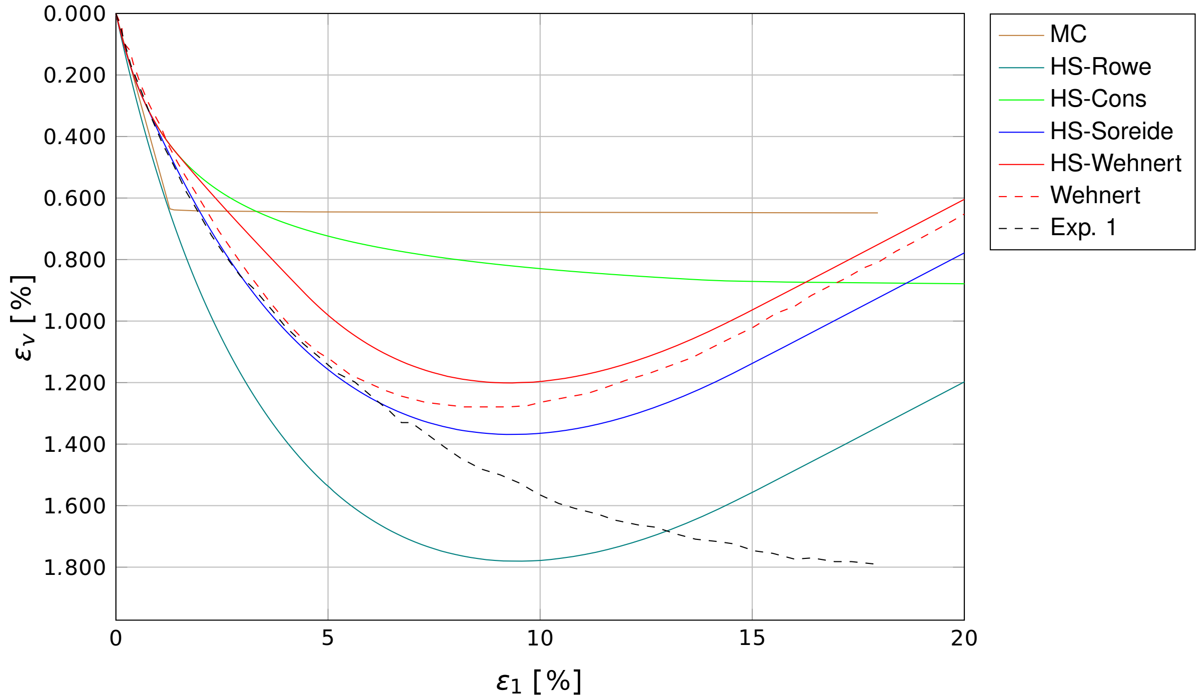

Figure 52.7: Volumetric strain - axial strain curve (ε_v-ε_1)

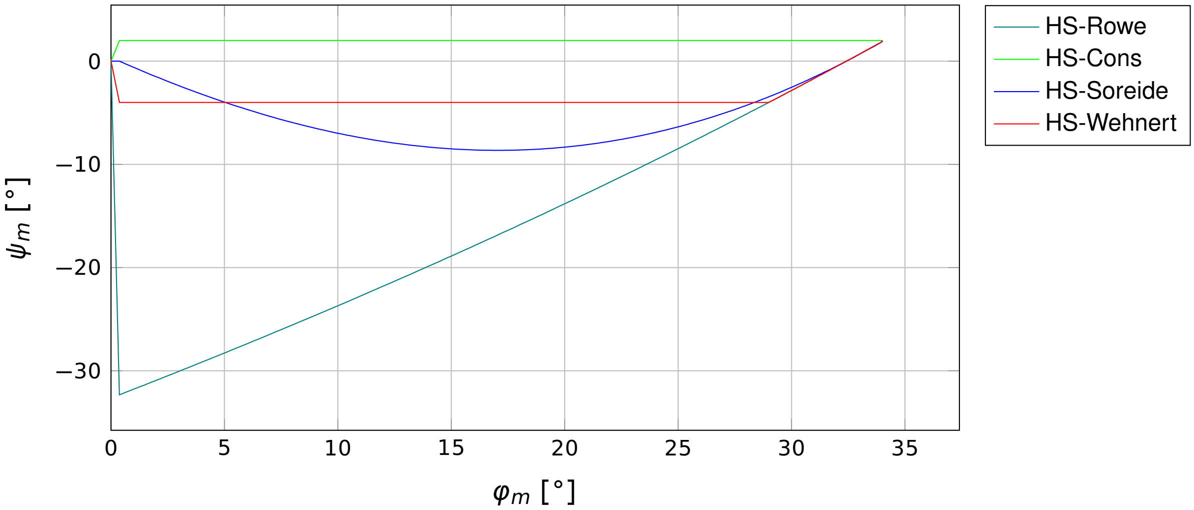

Figure 52.8: Mobilised dilatancy angle - friction angle curve (ψ_m-φ_m)

52.4 Conclusion

This example, concerning the triaxial test of a loose consolidated undrained sand soil, verifies that the results obtained by the Hardening Soil material model with a cut-off in the dilatancy are in a good agreement with the solution given by Wehnert [59].

52.5 Literature

[59] M. Wehnert. *Ein Beistrag zur dreainerten und undrainerten Analyse in der Geotechnik.* Institut für Geotechnik, Universität Stuttgart: P. A. Vermeer, 2006.

53 BE50: A Circular Cavity Embedded in a Full-Plane Under Impulse Pressure

Overview	
Element Type(s):	C2D
Analysis Type(s):	DYN
Procedure(s):	
Topic(s):	SOIL
Module(s):	DYNA
Input file(s):	sbfem_2d_cric_cavity.dat

53.1 Problem Description

This example addresses a circular cavity with radius r_0 embedded in a full-plane subjected to a radial pressure $p(t)$ (Fig. 53.1). The full-plane is assumed to be elastic, homogeneous, isotropic, without material damping which stretches to infinity and it is modeled with the help of the Scaled Boundary Finite Elements (SBFE). Plane-strain condition is considered. Load is in a form of a triangular impulse and applied on the cavity wall (Fig. 53.1b). Radial displacement response of the cavity wall has been computed and compared to the analytical solution.

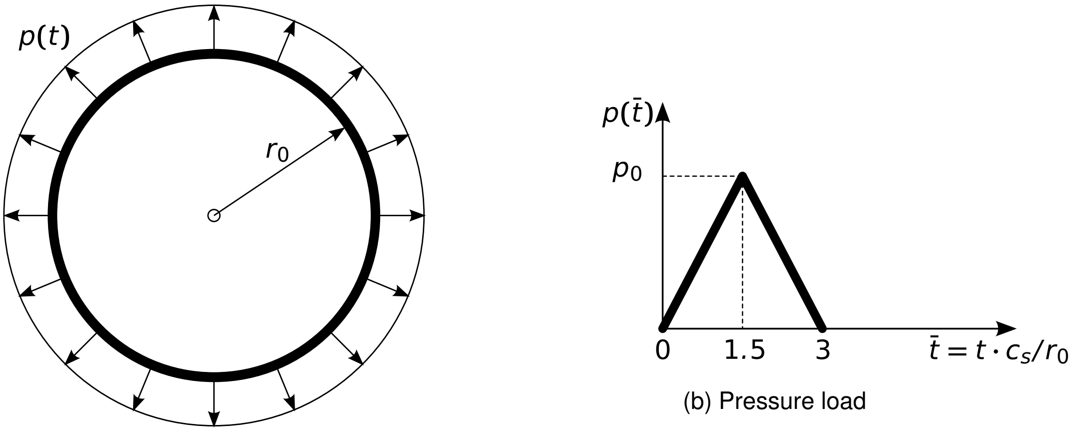

(a) Circular cavity embedded in a full-plane

(b) Pressure load

Figure 53.1: Problem Definition

53.2 Reference Solution

This problem is essentially a one dimensional problem which has an analytical solution [62]. The force-displacement relationship for this problem in frequency domain is given by

$$P(\omega) = S^{\infty}(\omega) \cdot u_r(\omega) \; , \tag{53.1}$$

where $\omega = 2\pi f$ represents the circular frequency, $P(\omega)$ is the *total force* applied on the cavity wall, $u_r(\omega)$ is the radial displacement and $S^{\infty}(\omega)$ is the dynamic-stiffness coefficient.

The dynamic-stiffness coefficient for this particular problem has an analytical expression and it reads

$$S^{\infty}(a_0) = \frac{2\pi G_0}{1-2\nu} \cdot \left[2(1-\nu)\frac{\lambda-1-F}{\lambda} - 2\nu + 2(1-\nu)\frac{H^{(2)}_{F+1}(\lambda a_0)}{H^{(2)}_{F}(\lambda a_0)} a_0 \right] , \tag{53.2}$$

where

G_0	shear modulus,
ν	Poisson's ratio,
ρ	mass density,
$c_s = \sqrt{G/\rho}$	shear wave velocity,
$c_p = c_s\sqrt{(2-2\nu)/(1-2nu)}$	P-wave velocity,
$a_0 = \omega r_0/c_p$	dimensionless frequency,
$\lambda = 2/(2-\alpha)$	coefficient,
α	non-homogeneity parameter of elasticity ($\alpha = 0$ for the homogeneous case),
$H^{(2)}_k$	the second kind Hankel function of the order k,
$F = \sqrt{(\lambda-1)^2 - \lambda^2\frac{\nu(\alpha+1)-1}{1-\nu}}$	order of the Hankel function.

The static-stiffness coefficient K^{∞} is used to non-dimensionlize displacement response

$$K^{\infty} = \frac{2\pi G_0}{1-2\nu} \cdot \left[\alpha(1-\nu) - 2\nu + \sqrt{(\alpha(1-\nu)-2\nu)^2 + 4 - 8\nu} \right] . \tag{53.3}$$

The radial displacement response in frequency domain $u_r(\omega)$ is obtained by first making the Fourier transformation of the total triangular impulse load $P(\omega)$ (Fig. 53.1b) and then dividing it with the dynamic-stiffness coefficient $S^{\infty}(\omega)$ (Eq. 53.1). Finally the displacement response is transformed in the time domain ($u_r(t)$) using the inverse Fourier transformation.

53.3 Model and Results

Material, geometry and loading properties of the model are summarized in the Table 53.1. The plane-strain model of the full-pane is assumed to be elastic, homogeneous ($\alpha = 0$) and isotropic.

Table 53.1: Model Properties

Material	Geometry	Loading	Integration parameters
$c_s, \rho, \nu = 0.3$	r_0	$P(t) = 2\pi r_0 p(t)$	$\Delta t = 0.04 \cdot r_0/c_p$
$G_0 = \rho c_s^2$		$P_0 = 2\pi r_0 p_0$	$M, N, \theta = 1.4$

Load and the finite element model of the structure are depicted in Fig. 53.2. The structure is comprised solely of the 2-node line scaled boundary finite elements and the load is applied directly to the nodes of the boundary.

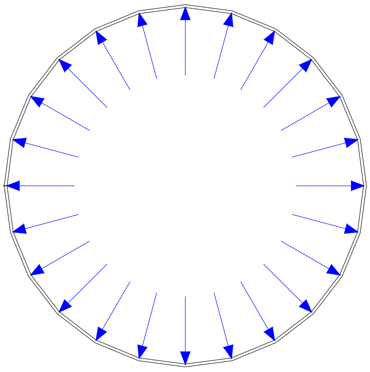

Figure 53.2: Finite Element Model

The transient radial displacement response of the cavity wall $u_r(t)$ has been computed using the Scaled Boundary Finite Element Method (SBFEM) in the time domain. The integration of the governing equations of the SBFEM is performed using the original discretization scheme (*const*) [62][63] and the extrapolation scheme from [64] based on the parameters M, N and θ [1].

The results in dimensionless form are plotted in Fig. 53.3 together with the analytical solution. The numerical results show excellent agreement with the analytical solution for all three cases.

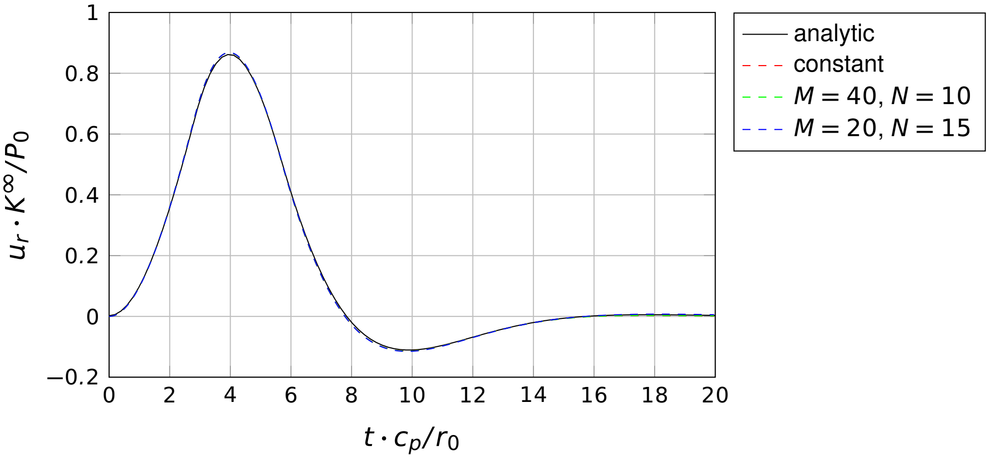

Figure 53.3: Radial displacement response

53.4 Conclusion

The example verifies the accuracy of the SBFEM method in modeling unbounded domain problems. The integration scheme for the solution of the governing equations of the SBFEM in time domain based on the work from [64] provides the solution with high computational efficiency and little loss of accuracy compared to the original method from [63].

---

[1] For the full description of the scheme based on the extrapolation parameter θ and the meaning of the integration parameters M, N and θ consult [64].

53.5 Literature

[62] M.H. Bazyar. “Dynamic Soil-Structure Interaction Analysis Using the Scaled Boundary Finite-Element Method”. PhD thesis. Sydney, Australia: The University of New South Wales, School of Civil and Environmental Engineering, 2007.

[63] J.P. Wolf and C. Song. *Finite-Element Modelling of Unbounded Media*. Chichester, UK: John Wiley and Sons, 1996.

[64] B. Radmanović and C. Katz. “A High Performance Scaled Boundary Finite Element Method”. In: *IOP Conference Series: Materials Science and Engineering* 10 (2010).

54 BE51: Pushover Analysis: Performance Point Calculation by EC8 Procedure

Overview	
Element Type(s):	
Analysis Type(s):	
Procedure(s):	
Topic(s):	EQKE
Module(s):	SOFiLOAD
Input file(s):	pushover-pp-ec8.dat

54.1 Problem Description

The following example is intended to verify the Eurocode 8 (EC8) procedure for the calculation of the performance point (illustrated schematically in Fig. 54.1), as implemented in SOFiSTiK. The elastic demand and capacity diagrams are assumed to be know.

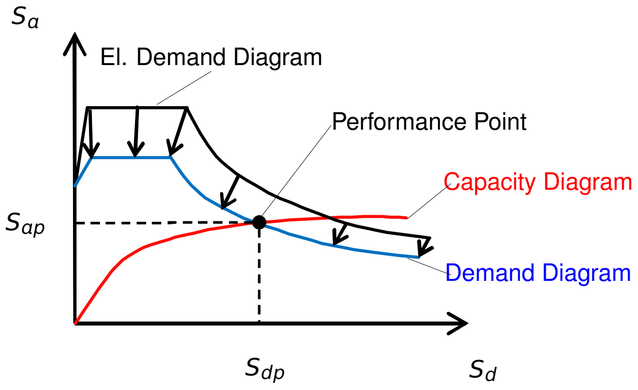

Figure 54.1: Determination of the performance point PP (S_{dp}, S_{ap})

54.2 Reference Solution

The reference solution is provided in [65].

Assuming that the elastic demand diagram (5% elastic response spectrum in ADRS format[1]) and the capacity diagram are known, it is possible to determine the performance point PP (S_{dp}, S_{ap}) (Fig. 54.1). The procedure comprises of a series of trial calculations (trial performance points PP_t $(S_{dp,t}, S_{ap,t})$), in which the equivalent *inelastic* single degree of freedom system (SDOF), represented by the capacity diagram, is idealized with the equivalent inelastic SDOF system with a bi-linear force-deformation relationship. The response in form of the performance point PP is then calculated from the *inelastic* response spectrum (demand diagram). The computation stops when the performance point PP is within a tolerance of a trial performance point PP_t. Detailed description of this procedure can be found in [66], [67], [65] and [37].

In the reference example [65] the bi-linear idealization of the capacity is assumed to be independent of the performance point and it is performed at the beginning of the analysis. This eliminates the need for the iterations and the solution of the problem can be obtained in a single calculation step.

---

[1] ADRS = Spectral Acceleration S_a - Spectral Displacement S_d format

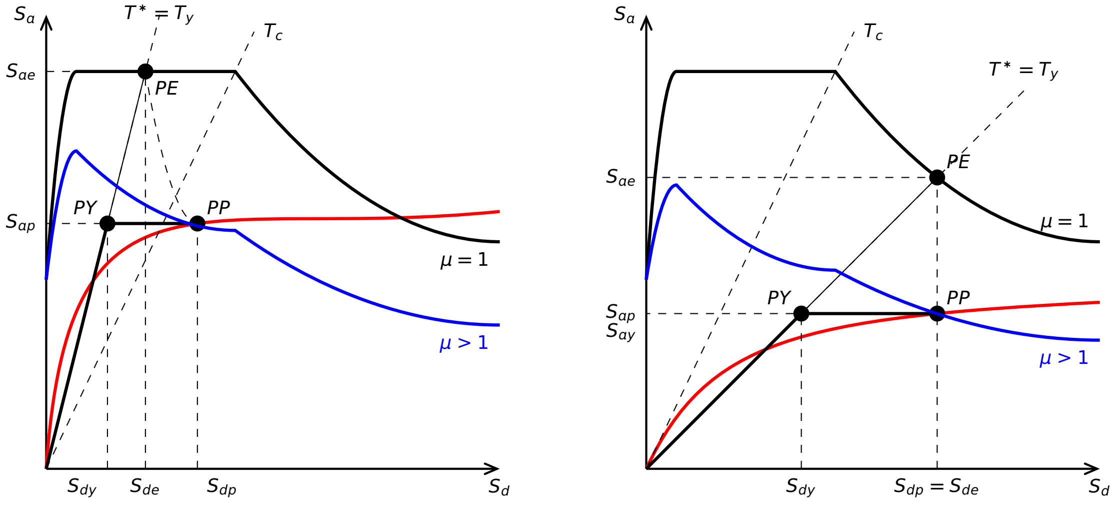

(a) Short period range, $T^* < T_C$ (b) Medium and long range, $T^* > T_C$

Figure 54.2: Determination of the performance point PP for the equivalent SDOF system

Hence in this example it is assumed that the bi-linear idealization of the capacity diagram is already known, which means that the point PY (S_{dy}, S_{ay}) is given. The procedure to calculated the performance point is illustrated in Fig. 54.2 and can be summarized as follows [37]:

1. Determine the period of the idealized system $T^* = T_y$ from the known PY (S_{dy}, S_{ay}):

$$T^* = T_y = 2\pi \cdot \sqrt{\frac{S_{dy}}{S_{ay}}} \; ; \tag{54.1}$$

2. Calculate the elastic spectral response PE (S_{de}, S_{ae}) of the idealized equivalent SDOF system with the period $T^* = T_y$ from the given 5%-damped elastic response spectrum (Fig. 54.2);

3. Calculate the yield strength reduction factor R_y:

$$R_y = \frac{S_{ae}}{S_{ay}} \; ; \tag{54.2}$$

4. Calculate ductility μ:

$$\mu = \begin{cases} (R_y - 1) \cdot \dfrac{T_C}{T^*} + 1 & \text{for} \quad T^* < T_C \\ R_y & \text{for} \quad T^* \geq T_C \end{cases} \; ; \tag{54.3}$$

5. Determine the performance point PP (S_{dp}, S_{ap}) from the inelastic design spectrum:

$$S_{dp} = \mu \cdot S_{dy} = \mu \cdot \frac{S_{de}}{R_y} \; , \tag{54.4a}$$

$$S_{ap} = \frac{S_{ae}(T^*)}{R_y} \; . \tag{54.4b}$$

54.3 Model and Results

In order to verify the analysis procedure for the determination of the performance point, a test case has been set up in such a way that it comprises of a SDOF with a unit mass and a non-linear spring element. It is obvious that for such an element the quantities governing the transformation from the original system to the equivalent inelastic SDOF system must be equal to one, i.e.

$$\phi_{cnod} = 1 \quad ; \quad \Gamma = 1 \quad ; \quad m = 1 \, , \tag{54.5}$$

where ϕ_{cnod} is the eigenvector value at control node, Γ is the modal participation factor and m is the generalized modal mass. Writing now the equations which govern the conversion of the pushover curve to capacity diagram, we obtain [37]

$$S_d = \frac{u_{cnod}}{\phi_{cnod} \cdot \Gamma} = u_{cnod} \, , \tag{54.6a}$$

$$S_a = \frac{V_b}{\Gamma^2 \cdot m} = V_b \, , \tag{54.6b}$$

where V_b is the base shear and u_{cnod} is the control node displacement.

Since the original system is a SDOF system, V_b and u_{cnod} are nothing else but the force in spring P and the displacement of the unit mass u, respectively. It follows further that the force-displacement work law assigned to the spring element corresponds to the capacity diagram in ADRS format, with the force P and displacement u equal to S_a and S_d, respectively.

The bi-linear idealization of the capacity diagram used in the reference example is defined by two points, whose coordinates are listed in the Table 54.1 [2]. According to the analysis above, these points can be used to define the force- displacement work law $P - u$ of the non-linear spring element (Fig. 54.3).

Table 54.1: Model Properties [65]

Capacity Diagram		Elastic Demand
Point	$(S_d[mm],\ S_a[m/s^2])$	5%-Damped Elastic Response Spectrum
A	$(61, 3.83)$	$a_g = \{0.60g, 0.30g, 0.16g\}$
B	$(\infty, 3.83)$	$S_A = 1.0, S_B = 2.5, k_1 = 1.0$
		$T_B = 0.15s, T_C = 0.60s, T_D = 3.00s$

---

[2] Not that the point A is nothing else but the point PY (S_{dy}, S_{ay}).

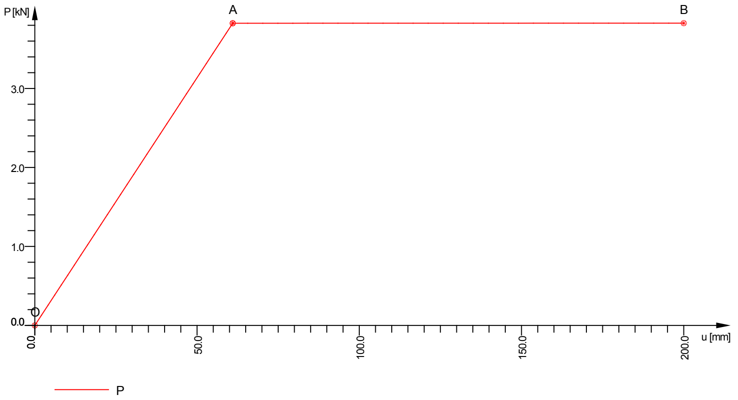

Figure 54.3: Force-displacement work law of the non-linear spring

The elastic demand is a 5%-damped elastic response spectrum, whose properties are summarized in Table 54.1. Three levels of peak ground acceleration a_g have been taken into an account. The shape of the spectrum and the meaning of the parameters specified in Table 54.1 are shown in Figure 54.4.

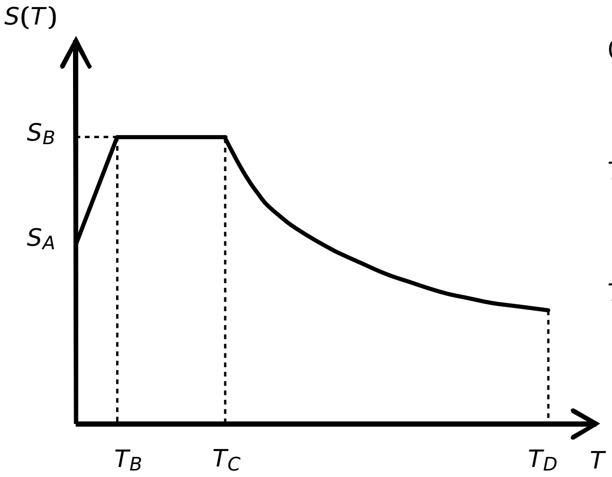

$0 \leq T \leq T_B$:

$$S = S_A + \frac{T}{T_B} \cdot (S_B - S_A)$$

$T_B \leq T \leq T_C$:

$$S = S_B$$

$T_C \leq T \leq T_D$:

$$S = S_B \cdot \left(\frac{T_C}{T}\right)^{k_1}$$

Figure 54.4: 5%-Damped Elastic Response Spectrum (El. Demand Diagram)

The outcome of the analysis is shown in Figures 54.5 to 54.7.

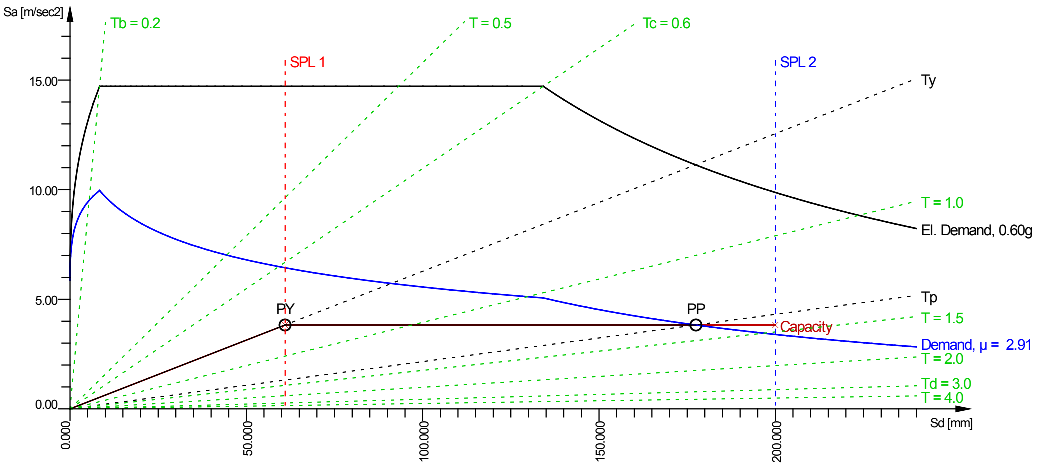

Figure 54.5: Capacity-Demand-Diagram ($a_g = 0.60g$)

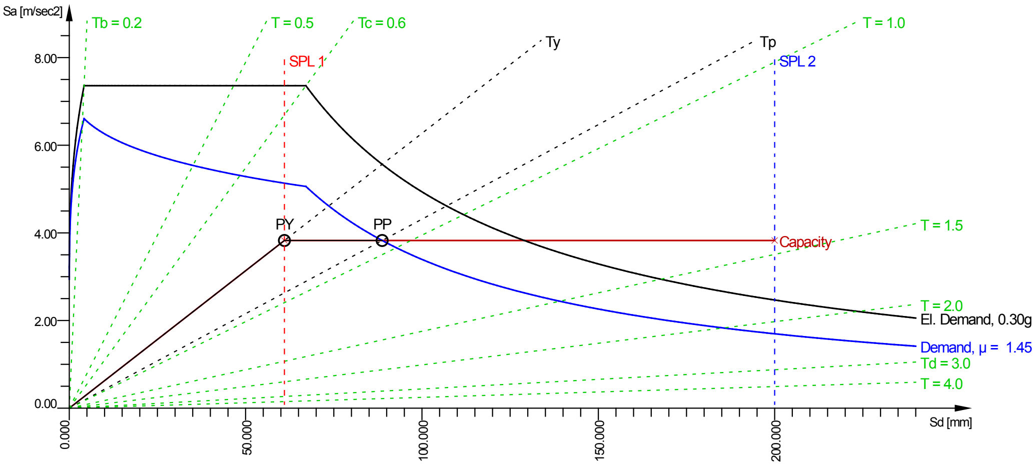

Figure 54.6: Capacity-Demand-Diagram ($a_g = 0.30g$)

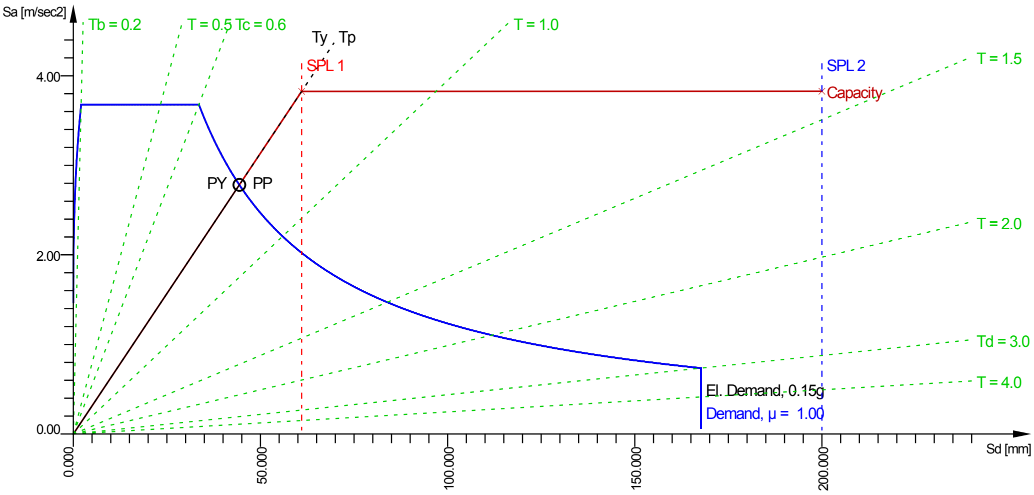

Figure 54.7: Capacity-Demand-Diagram ($a_g = 0.15g$)

The results of the SOFiSTiK calculation and the comparison with the reference solution are summarized in Table 54.2.

Table 54.2: Results

a_g		μ	R_{yp}	T_y	S_{dy}	S_{dp}	S_{ap}
$[g]$		$[-]$	$[-]$	$[s]$	$[mm]$	$[mm]$	$[m/s^2]$
0.60	SOF.	2.9	2.9	0.79	61	177	3.83
	Ref. [65]	2.9	2.9	0.79	61	177	3.83
	$\lvert e\rvert$ $[\%]$	0.0	0.0	0.0	0.0	0.0	0.0
0.30	SOF.	1.5	1.5	0.79	61	89	3.83
	Ref. [65]	1.5	1.5	0.79	61	89	3.83
	$\lvert e\rvert$ $[\%]$	0.0	0.0	0.0	0.0	0.0	0.0
	SOF.	1.0	1.0	0.79	44	44	2.78

Table 54.2: (continued)

a_g		μ	R_{yp}	T_y	S_{dy}	S_{dp}	S_{ap}
$[g]$		$[-]$	$[-]$	$[s]$	$[mm]$	$[mm]$	$[m/s^2]$
0.15	Ref. [65]	1.0	1.0	0.79	44	44	2.76
	$\lvert e \rvert$ $[\%]$	0.0	0.0	0.0	0.0	0.0	0.7

μ	displacement ductility factor
R_{yp}	reduction factor due to ductility at performance point
T_y	period associated with yielding point
S_{dy}, S_{dp}	spectral displacements at yielding and performance point
S_{ap}	pseudo spectral acceleration at performance point

The results are in excellent agreement with the reference solution.

54.4 Conclusion

Excellent agreement between the reference and the results computed by SOFiSTiK verifies that the procedure for the calculation of the performance point according to Eurocode 8 is adequately implemented.

54.5 Literature

[37] *SOFiLOAD Manual: Loads and Load Functions*. Version 2018-0. SOFiSTiK AG. Oberschleißheim, Germany, 2017.

[65] P. Fajfar. “A Nonlinear Analysis Method for Performance-Based Seismic Design”. In: *Earthquake Spectra* 16.3 (2000), pp. 573–592.

[66] EN1998-1:2004. *Eurocode 8: Design of structures for earthquake resistance, Part 1: General rules, seismic actions and rules for buildings*. CEN. 2004.

[67] P. Fajfar. “Capacity Spectrum Method Based on Inelastic Demand Spectra”. In: *Earthquake engineering and structural dynamics* 28.9 (1999), pp. 979–993.

55 BE52: Verification of Wave Kinematics

Overview	
Element Type(s):	
Analysis Type(s):	
Procedure(s):	
Topic(s):	WAVE
Module(s):	SOFiLOAD
Input file(s):	stokes.dat

55.1 Problem Description

This benchmark is concerned with the validation of wave kinematics of regular nonlinear Stokes 5th order wave theory. In Fig. 55.1 the properties of a wave can be visualised.

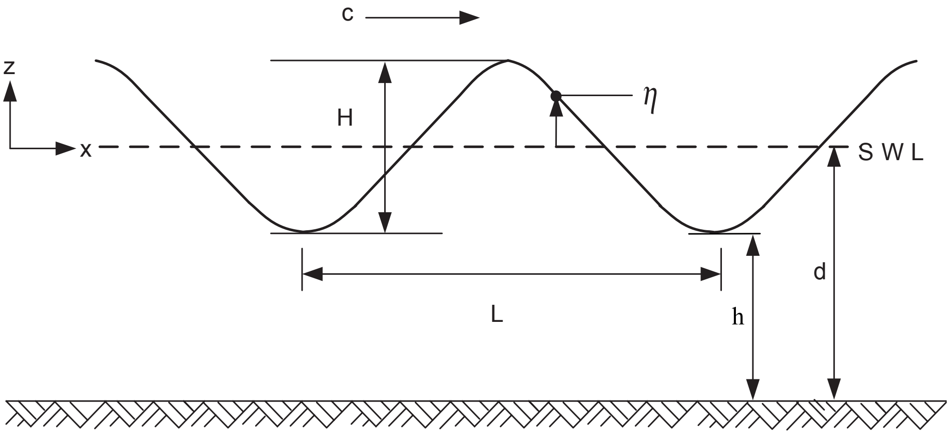

Figure 55.1: Wave

55.2 Reference Solution

The reference solution is provided in [68]. This article investigates the solution of the dispersion relation of Stokes fifth order wave theory, which is governed by two coupled nonlinear equations in two variables, through a Newton-Raphson iterative scheme. Different waves are investigated and their wave profile and horizontal velocitiy is computed and plotted. The interest of this benchmark focuses on the provided solution for the corrected coefficient in the original expression for C_2 (the factor $+2592$ should be replaced by -2592), which is employed also from SOFiSTiK. For more information on this correction please refer to Nishimura & al. (1977), Fenton (1985) [69], Bhattacharyya (1995) [68] and SOFiLOAD manual [37].

55.3 Model and Results

The properties of the considered wave are defined in Table 55.1.

Table 55.1: Model Properties

Wave Properties		
$d = 107\,ft$	$H = 70\,ft$	$T = 16.30\,s$

The wave profile, i.e. the phase angle θ versus the surface elevation η, is computed and shown in Fig 55.2 and the horizontal velocity under the wave crest versus the elevation from the seabed $(z - d)$, in Fig 55.3. Both results are compared to the reference solution, as peresented in Bhattacharyya (1995) [68].

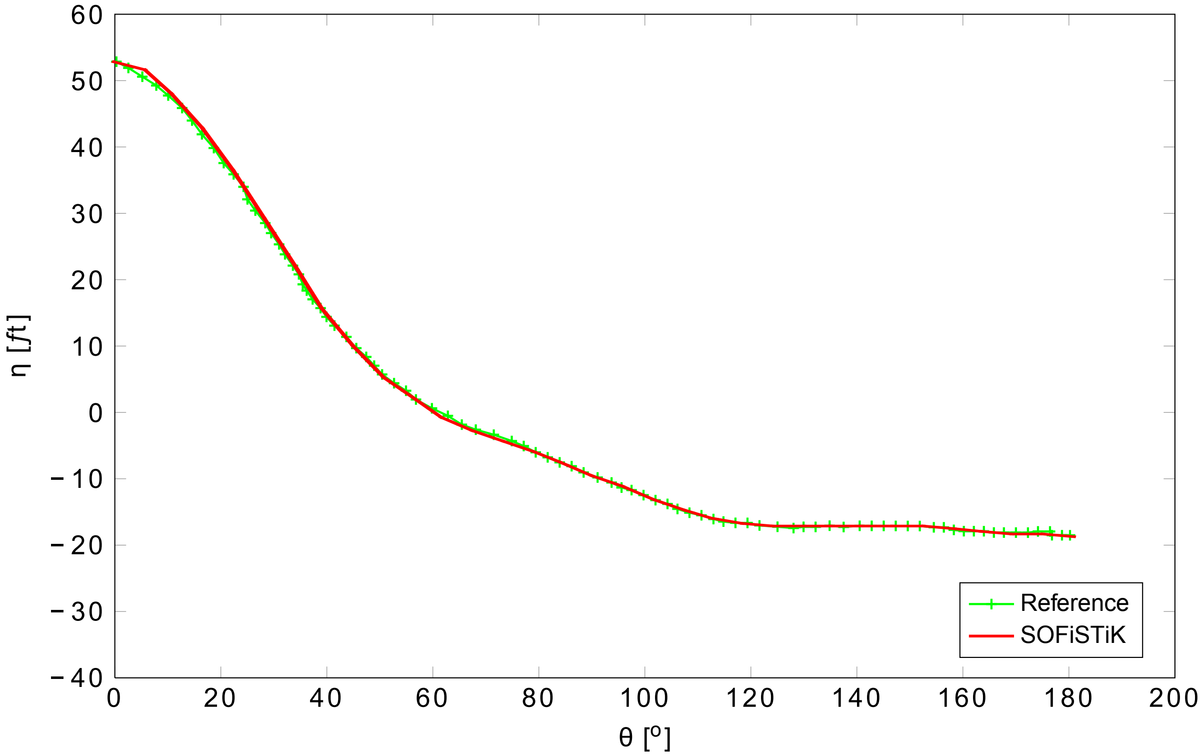

Figure 55.2: Wave profile

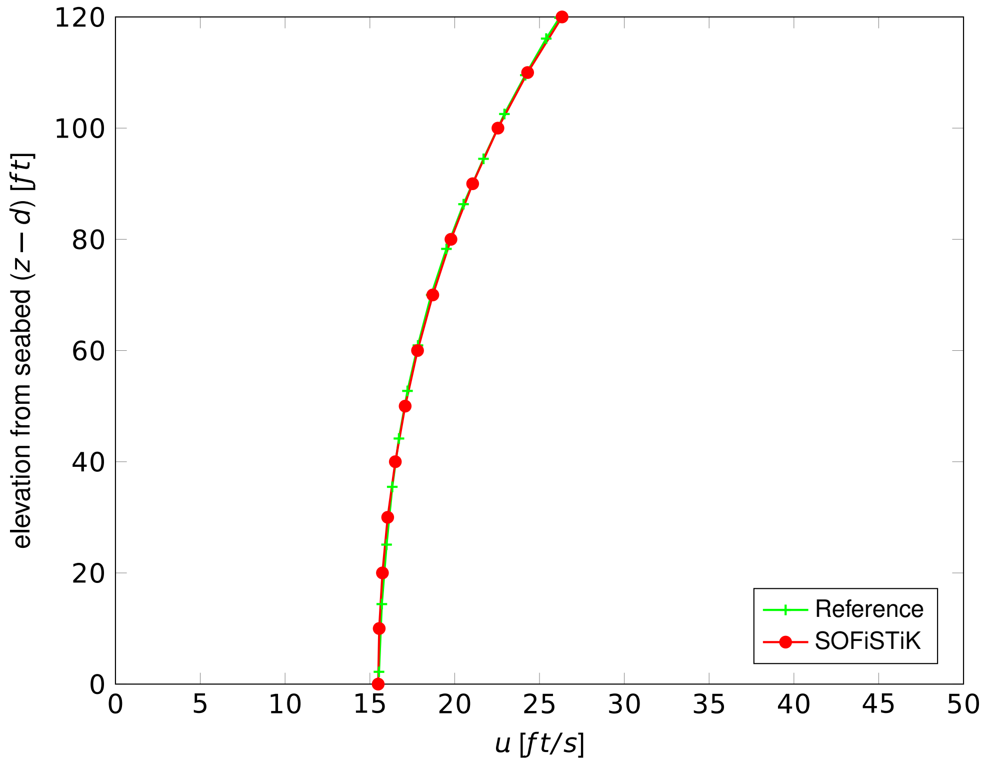

Figure 55.3: Horizontal velocity under wave crest

55.4 Conclusion

The very good agreement between the reference and the results computed by SOFiSTiK verifies that the Stokes fifth order wave theory is adequately implemented.

55.5 Literature

[37] *SOFiLOAD Manual: Loads and Load Functions*. Version 2018-0. SOFiSTiK AG. Oberschleißheim, Germany, 2017.

[68] S. K. Bhattacharyya. “On two solutions of fifth order Stokes waves”. In: *Applied Ocean Research* 17 (1995), pp. 63–68.

[69] J. D. Fenton. “A fifth order Stokes theory for steady waves”. In: *J. Waterways, Port, Coastal & Ocean Engineering* 111(2) (1985), pp. 216–234.

56 BE53: Verification of Wave Loading

Overview	
Element Type(s):	
Analysis Type(s):	
Procedure(s):	
Topic(s):	WAVE
Module(s):	SOFiLOAD
Input file(s):	wave_loading.dat

56.1 Problem Description

This benchmark is concerned with the validation of wave loading on a structure. In this example the linear Airy wave theory with Wheeler stretching is applied to one exemplary wave on a monopile, as presented in Fig. 56.1. The surface elevation and the accumulated forces produced by the wave theory are compared with the results calculated by WaveLoads. WaveLoads is a well-known software developed within the research project GIGAWIND at Hannover University for calculating wave induced loading on hydrodynamically transparent structures [70].

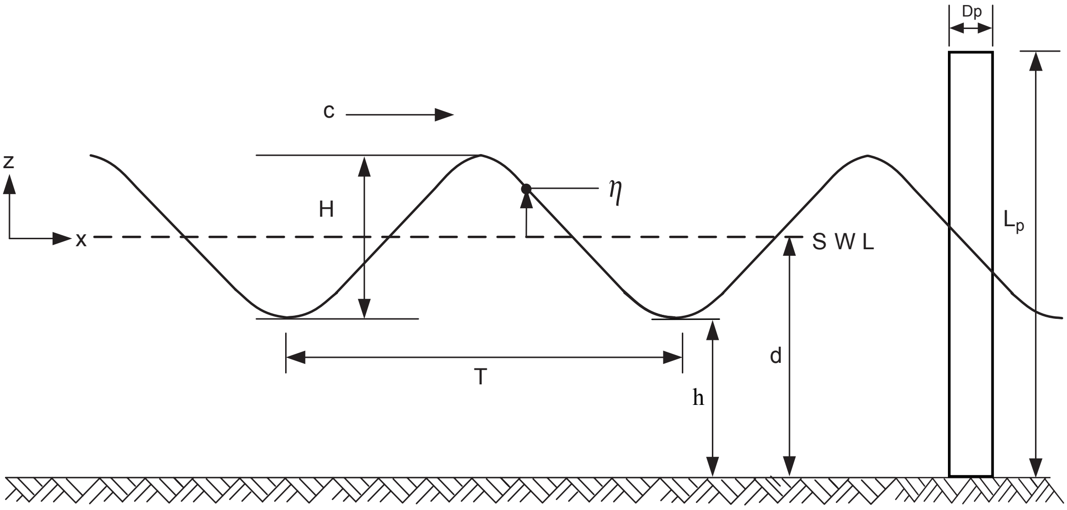

Figure 56.1: Wave

56.2 Reference Solution

The reference example is calculated with WaveLoads. Further information on the model can be found in the WaveLoads manual [70]. This benchmark aims at verifying three important components: the Airy wave theory, the Wheeler stretching scheme and the Morison equation [37].

56.3 Model and Results

The properties of the considered wave and the structure are defined in Table 56.1. The wave profile, i.e. the surface elevation η over time of one period, is computed and shown in Fig 56.2 and the accumulated forces over time of one period, in Fig 56.3. Both results are compared to the calculated reference solution [70].

Table 56.1: Model Properties

Wave Properties	Structure Properties
$d = 34\,m$	$D_p = 6\,m$
$H = 17.5\,m$	$L_p = 54\,m$
$T = 15\,s$	$C_m = 2.0$
$SWL = 0\,m$	$C_d = 0.7$

The pile is modeled with 500 elements as in the reference example. The Wheeler stretching is applied. The calculated wave length is $L = 246.013\,m$ and the calculated depth criterion $d/L = 0.138$ indicates that the examined case falls into finite water.

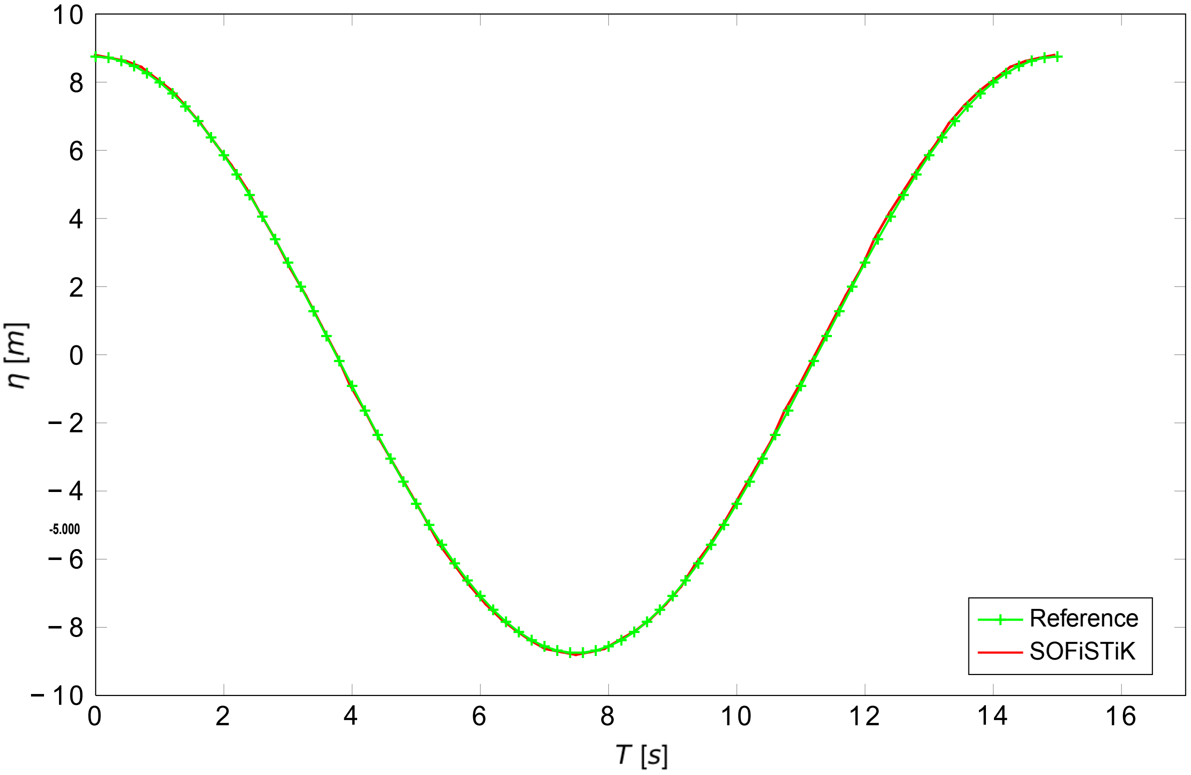

Figure 56.2: Wave profile

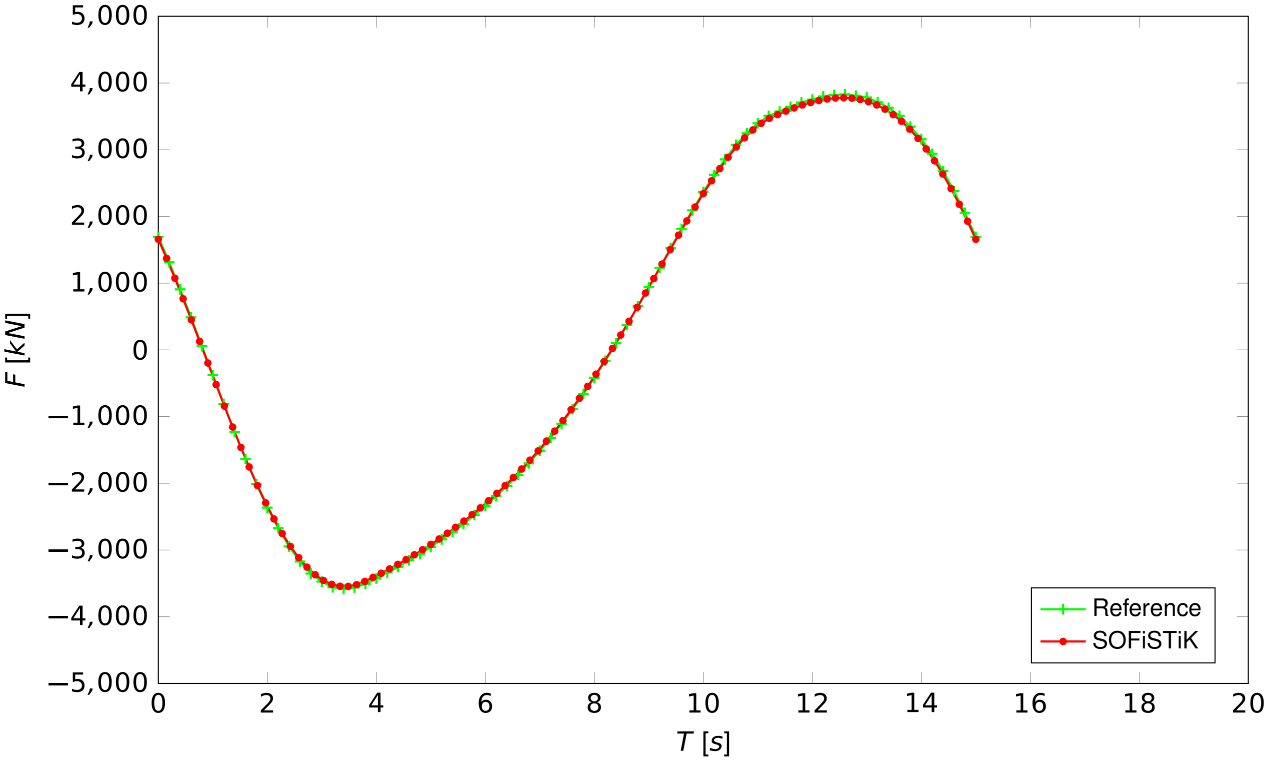

Figure 56.3: Accumulated Force for Airy linear wave theory in combination with Wheeler Stretching

56.4 Conclusion

The very good agreement between the reference and the results computed by SOFiSTiK verifies that the linear Airy wave theory, the Wheeler stretching scheme and the Morison equation are adequately implemented.

56.5 Literature

[37] *SOFiLOAD Manual: Loads and Load Functions*. Version 2018-0. SOFiSTiK AG. Oberschleißheim, Germany, 2017.

[70] K. Mittendorf, B. Nguyen, and M. Blümel. *WaveLoads - A computer program to calculate wave loading on vertical and inclined tubes*. ISEB - Fluid Mechanics Institute, University of Hannover. 2005.

57 BE54: Equivalent Linear Temperature Load

Overview

Element Type(s):
Analysis Type(s):
Procedure(s):
Topic(s): Fire and temperature
Module(s): SOFiLOAD
Input file(s): eqv_linear_temp_load.dat

57.1 Problem Description

The following example is focused on verifying the effects of the nonlinear temperature gradient along the height of a beam's cross section. A simply supported beam (Figure 57.1a) is analyzed with the corresponding temperature distribution (heating and cooling profiles) in the cross section (Figure 57.1b). The internal stresses due to the nonlinear temperature gradient can be divided into stresses due to uniform and linear temperature component and into remaining self-equilibrating eigenstresses [71].

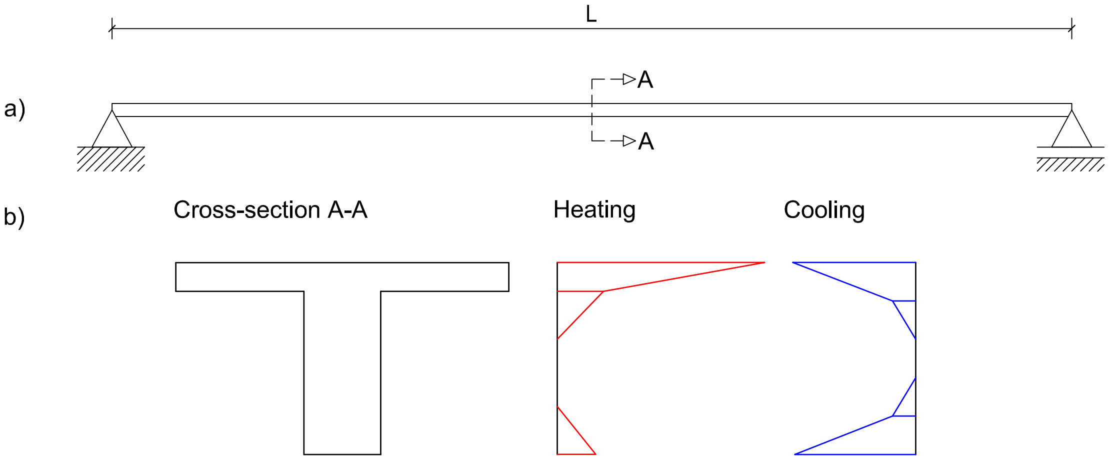

Figure 57.1: (a) Simply supported beam; (b) Cross section with corresponding heating and cooling profiles

57.2 Reference Solution

The reference solution is calculated analytically from the stress distribution corresponding to the restrained conditions, which is obtained by multiplying the assigned temperature profile with the coefficient of thermal expansion α_t and the modulus of elasticity E [72, 73] :

$$\sigma^T(z) = -E\alpha_t \Delta T(z), \tag{57.1}$$

Stress due to the restraining axial force is derived by integrating the stresses $\sigma^T(z)$ multiplied with the corresponding width $b(z)$ over the cross section height and dividing the value with the cross-section area *A* [72, 73]. The same stress value can be obtained by multiplying the equivalent uniform (constant) temperature component ΔT_{eq} with the coefficient of thermal expansion and the modulus of elasticity (Figure 57.2b):

$$\sigma_{cons} = \frac{1}{A}\int_0^h \sigma^T(z)b(z)dz = -E\alpha_t\Delta T_{eq} \tag{57.2}$$

Stresses due to the restraining moment are calculated by taking moments around the centroid of the cross section and dividing the values with the section modulus [72, 73]. Correspondingly, the linear temperature distribution multiplied with the coefficient of thermal expansion and the modulus of elasticity (Figure 57.2c) yields the same stress values. Hence, the equivalent linear temperature component $\Delta T_{z,eq}$ can be derived from the following expression:

$$\sigma_{line} = \frac{1}{I/h}\int_0^h \sigma^T(z)b(z)(z-\bar{z})dz = -E\alpha_t\Delta T_{z,eq} \tag{57.3}$$

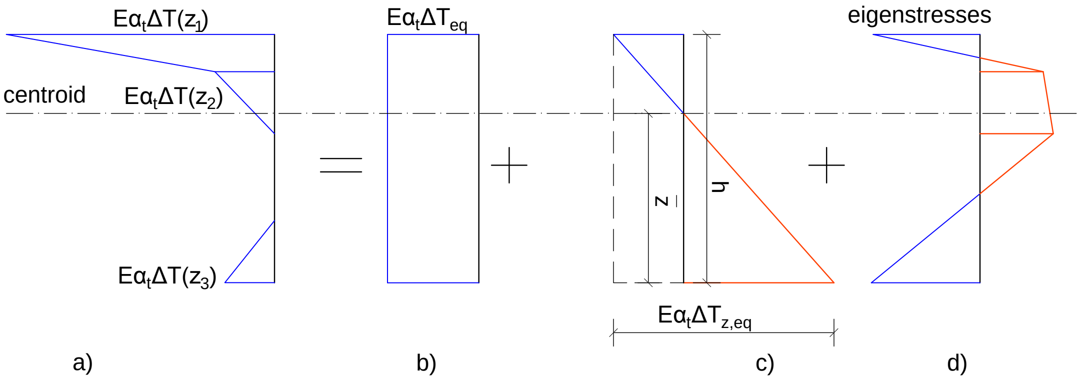

Figure 57.2: (a) Restrained stresses; (b) Stresses due to the equivalent uniform temperature; (c) Stresses due to the equivalent linear temperature; (d) Self-equilibrating eigenstresses

In case of a simply supported beam, it is free to expand and bend. Therefore, the corresponding strain distributions are generated. The differences between the restrained stress distribution and that which result in axial and bending strains, are trapped in the section and are known as self-equilibrating eigenstresses [73].

57.3 Model and Results

Two different cross-sections with the corresponding nonlinear temperature gradient are investigated: a concrete T-beam and a composite cross-section. The used material properties for concrete and steel are presented in Table 1. The implemented geometry and the temperature loading profiles for both heating and cooling conditions are shown in Figure 3. The beam's length is chosen to be 10 m. Reference solution for the same concrete T-beam cross-section, material properties and heating conditions can be found in [73].

Table 57.1: Material Properties

Type of cross section	Material properties	
T-beam	$E_{conc} = 35000\,MPa$	
	$\alpha_{t,conc} = 1.2 \times 10^{-5}\,K^{-}$	
Composite cross section	$E_{conc} = 35000\,MPa$	$E_{steel} = 210000\,MPa$
	$\alpha_{t,conc} = 1.2 \times 10^{-5}\,K^{-}$	$\alpha_{t,steel} = 1.2 \times 10^{-5}\,K^{-}$

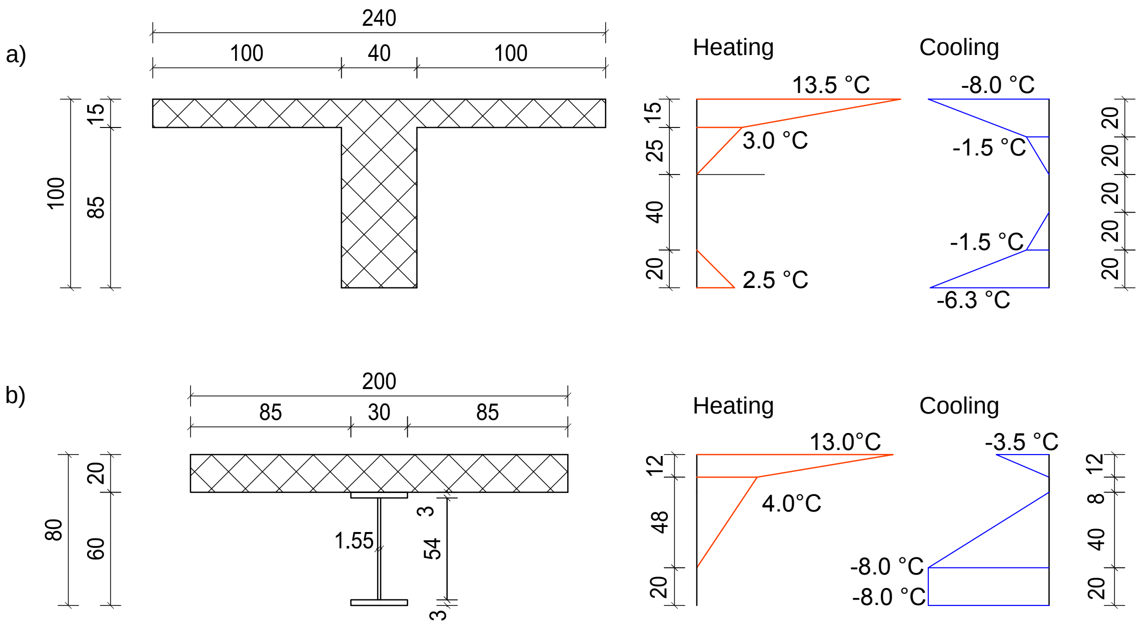
a)
240
100
40
100
15
100
85
Heating
13.5 °C
3.0 °C
2.5 °C
15
25
40
20
Cooling
-8.0 °C
-1.5 °C
-1.5 °C
-6.3 °C
20
20
20
20
20
b)
200
85
30
85
20
80
60
1.55
3
54
3
Heating
13.0°C
4.0°C
12
48
20
Cooling
-3.5 °C
-8.0 °C
-8.0 °C
12
8
40
20

Figure 57.3: (a) T-beam concrete cross section - geometry [cm] with assigned temperature profiles; (b) Composite cross section - geometry [cm] with assigned temperature profiles

The calculated values of the equivalent uniform and linear temperature component are compared with the reference values in Table 2.

Table 57.2: Results

			ΔT_{eq} $[°C]$	$\Delta T_{z,eq}$ $[°C]$
T-beam	Heating	SOF.	4.600	−11.096
		Ref.[73]	4.600	−11.096
		$\lvert e_r \rvert$ [%]	0.00	0.00
	Cooling	SOF.	−3.544	4.704
		Ref.	−3.544	4.704
		$\lvert e_r \rvert$ [%]	0.00	0.00

Table 57.2: (continued)

			ΔT_{eq} $[°C]$	$\Delta T_{z,eq}$ $[°C]$
Composite	Heating	SOF.	5.111	−9.740
		Ref.	5.111	−9.740
		$\lvert e_r \rvert$ [%]	0.00	0.00
	Cooling	SOF.	−2.047	−7.371
		Ref.	−2.047	−7.371
		$\lvert e_r \rvert$ [%]	0.00	0.00

Calculated eigenstresses for a simply supported beam with the T-beam cross-section are shown in Figure 57.4. Results for the temperature heating profile calculated in [73] correspond nicely with the SOFiSTiK calculated eigenstresses (Figure 57.4a).

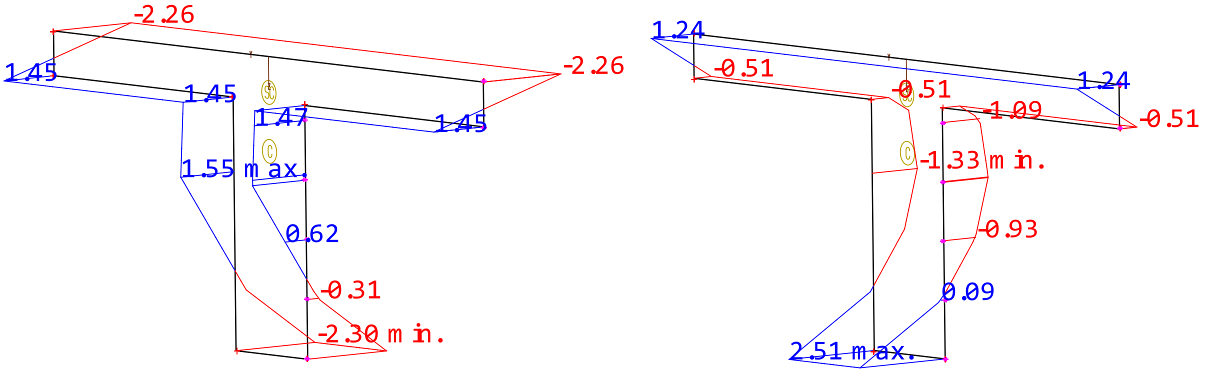

(a) For the heating profile

(b) For the cooling profile

Figure 57.4: Eigenstresses for the T-beam cross-section in N/mm^2

57.4 Conclusion

An excellent agreement between the reference solution and the numerical results calculated by SOFiSTiK verifies that the effects of the nonlinear temperature gradient are adequately taken into account.

57.5 Literature

[71] M.M. Elbadry and A. Ghali. “Nonlinear temperature distribution and its effects on bridges”. In: *International Association of Bridge and Structural Engineering Proceedings* (1983), pp. 66–83.
[72] L.A. Clark. *Concrete Bridge Design to BS 5400*. Construction Press, 1983.
[73] D.L. Keogh and E. O´Brien. *Bridge Deck Analysis*. CRC Press, 2005.

58 BE55: Design elements and SOFiSTiK T-beam Philosophy

Overview

Element Type(s):	B3D, SH3D
Analysis Type(s):	Linear
Procedure(s):	
Topic(s):	Design Elements
Module(s):	ASE, DECREATOR
Input file(s):	designElements_tbeamphilosophy.dat

58.1 Problem Description

This verification sets a benchmark for Design Elements in SOFiSTiK 2018 at the analysis level. Results are compared with those of the existing SOFiSTiK T-Beam Philosophy, and a reference analytical solution.

58.2 Reference Solution

As an example, the solution of the bending moment at the middle support $M_{y,s}$ of a two span continuous T-beam system shown in figure 58.1 is considered. The effective width of the beam is the determining parameter. The exact analytical value of the support moment is given by:

$$M_{y,s} = \frac{wl^2}{8} \tag{58.1}$$

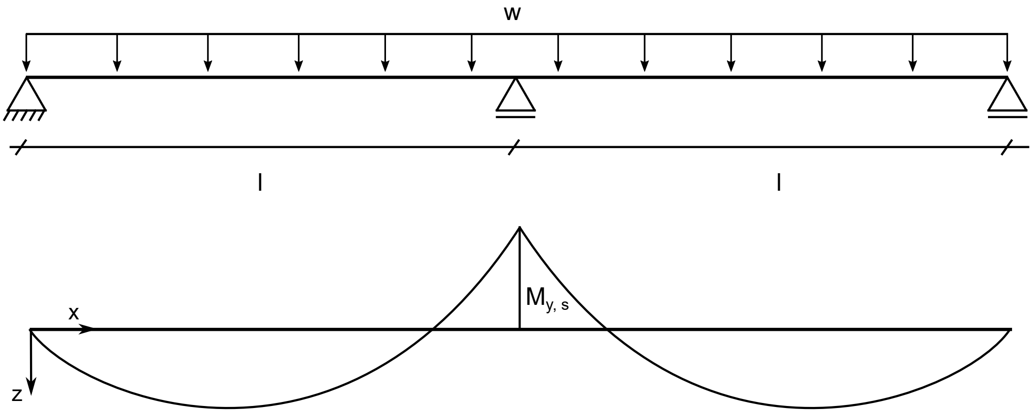

Figure 58.1: Reference system: continuous beam and its bending moment distribution

For bending design of a T-beam, analysis can be done in the module ASE using the SOFiSTiK T-beam Philosophy [74, 75, 76, 77]. Accordingly, the resulting bending moment $M_{y,Tbeam}$ is calculated by multiplying the effective width b_{eff} with the nodal value of the plate elements that is computed by averaging some of the nodal values of the plates the at the support (eg. $m_{y,avg.} = (m_1 + m_2 + m_3)/3$), then adding the remaining moment carried by the beam element $M_{y,beam}$. That is:

$$M_{y,Tbeam} = M_{y,beam} + m_{y,avg.} \cdot b_{eff} \tag{58.2}$$

58.3 Model and Results

The wide flange of the continuous T-beam is modeled with quad elements. In addition, a centric beam with a T-cross section is embedded at the center of the flange. A uniformly distributed area load is then applied over the flange. To supplement the comparison, three variations of this model are made, in which only the effective width is altered.

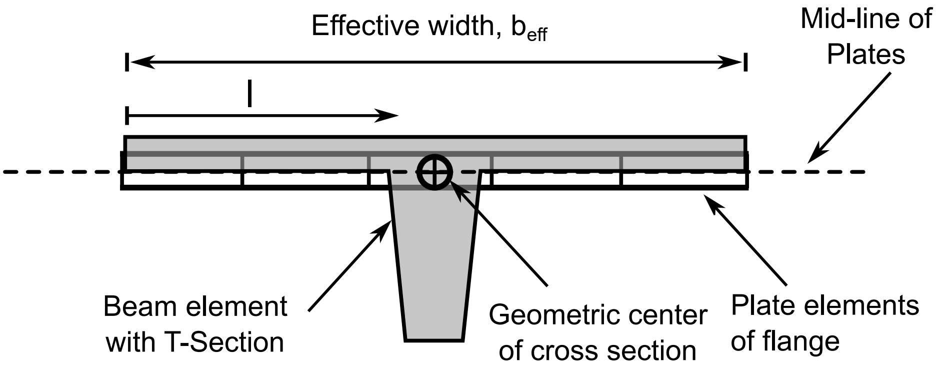
Effective width, b_{eff}
l
Mid-line of Plates
Beam element with T-Section
Geometric center of cross section
Plate elements of flange

Figure 58.2: Sectional layout of a T-beam FE-model according to the T-beam Philosophy in SOFiSTiK

In contrast to the SOFiSTiK T-Beam Philosophy stated in equation 58.2, the bending moment calculation by Design Elements takes the integral of all the nodal values covered within the effective width, then adds the remaining beam moment. This improves the approximation, and can be put as:

$$M_{y,Tbeam} = M_{y,beam} + \int_0^{b_{eff}} m_{y,p}(l)\, dl \tag{58.3}$$

Figure 58.3 illustrates this difference.

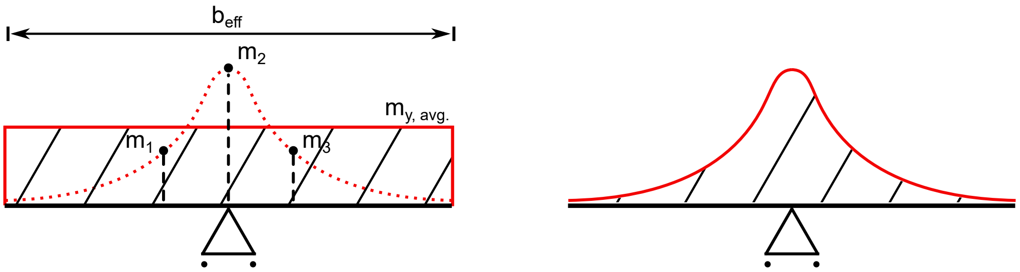

Figure 58.3: Consideration of the actual support bending moment distribution across the plate elements in T-beam Philosophy (left) and Design Elements

As a result, applying the T-beam Philosophy on a model with a larger effective width, the error in the support bending moment is more pronounced (see table 58.1). However, the results of the Design Elements, as one may expect, remain well approximate for all effective widths. In this example, larger widths were so chosen that the deviations could clearly be illustrated.

Table 58.1: Comparison of support moments for varying effective widths

Effective Widths $b_{eff,i}$ $[m]$	1.0	2.0	4.0
Ref. $[kNm]$	-32.4	-64.8	-129.6
SOF. T-Beam Phil. $[kNm]$	-32.2	-66.2	-148.8
$\lvert e \rvert$ $[\%]$	0.6	2.0	10.0
Design Elements $[kNm]$	-32.0	-64.0	-129.3
$\lvert e \rvert$ $[\%]$	1.2	1.2	0.2

58.4 Conclusion

In case of a flexural design of a finite element structural model consisting T-beams, the results using the Design Elements and the SOFiSTiK T-beam Philosophy match that of the exact analytical solution up to a certain effective width. The design elements however always ensure more approximate results regardless of the effective width.

58.5 Literature

[74] C. Katz and J. Stieda. *Praktische FE-Berechnungen mit Plattenbalken*. Bauinformatik 1, 1992.
[75] W. Wunderlich, G. Kiener, and W. Ostermann. *Modellierung und Berechnung von Deckenplatten mit Unterzügen*. Bauingenieur, 1994.
[76] J. Bellmann. *Vorgespannte schiefwinklige Plattenbalkenbrücke*. 7. SOFiSTiK Seminar, 1994.
[77] C. Katz. *Neues zu Plattenbalken*. 7. SOFiSTiK Seminar, 1994.

59 BE56: Interface element

Overview	
Element Type(s):	C2D
Analysis Type(s):	MNL
Procedure(s):	
Topic(s):	Interface Element
Module(s):	SOFIMSHC, TALPA
Input file(s):	interface_elements.dat

59.1 Problem Description

The following example is focused on verifying the interface element which can be used to model the contact behaviour in a geotechnical model. In the example according to [78] interface elements are simulating the contact between a long elastic block on a rigid foundation. The block is subjected to pressure p at one vertical side, while being restrained at the other end, and no strain is permitted in the y direction (Figure 59.1).

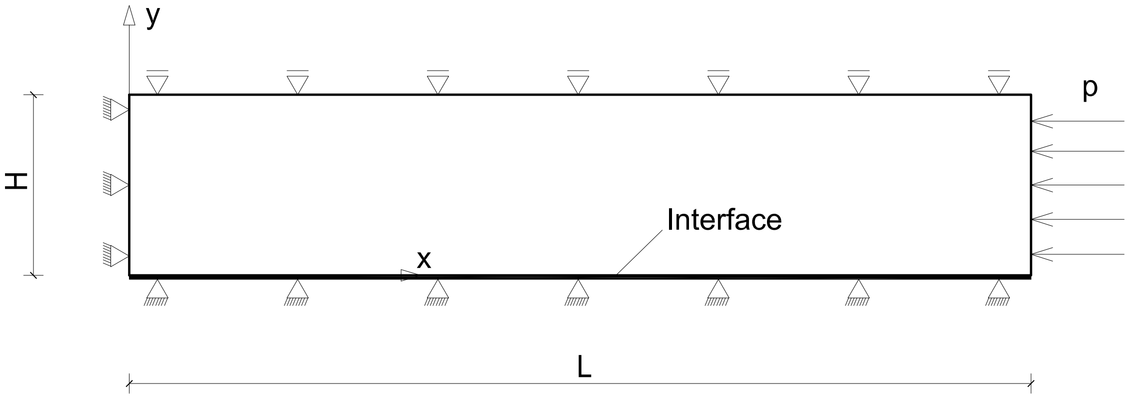

Figure 59.1: Long elastic block on a rigid foundation

59.2 Reference Solution

The distribution of shear stress along the interface between $x = 0$ and $x = x_1$, where x_1 is the point at which the shear stress reaches its maximum level, is given analytically by [78]:

$$\tau(x) = \frac{k_s m_v}{\alpha} \cdot \frac{e^{\alpha x} - e^{-\alpha x}}{e^{\alpha x_1} - e^{-\alpha x_1}} \cdot \left[pH - \tau_{max}(L - x_1) \right] \tag{59.1}$$

where

$m_v = \frac{(1+\nu)(1-2\nu)}{E(1+\nu)}$

$\alpha = \sqrt{\frac{k_s m_v}{H}}$

k_s	shear stiffness parameter,

ν	Poisson’s ratio,
E	Elastic modulus,
p	pressure applied at $x = L$,
τ_{max}	maximum shear stress (cohesion)
H	height of the elastic block,
L	length of the elastic block

For the slipping portion of the block, between $x = x_1$ and $x = L$, the shear stress is constant, i.e. $\tau = \tau_{max}$.

The point $x = x_1$ is calculated iteratively by applying the Newton Raphson iterative scheme for the following equation [78, 79]:

$$\frac{e^{\alpha x} + e^{-\alpha x}}{e^{\alpha x_1} - e^{-\alpha x_1}} + \alpha(L - x_1) - \frac{p\alpha H}{\tau_{max}} = 0 \tag{59.2}$$

59.3 Model and Results

Material, geometry and loading properties of the model are summarized in the Table 59.1. To satisfy the required condition of no strain in the y direction the normal stiffness of the interface elements, i.e. the elastic constant normal to the interface surface c_s is defined with a relatively high value. Plane strain conditions are assumed, and nonlinear analysis is performed with loading being increased in increments of 2.5 kPa up to 400 kPa.

Table 59.1: Model Properties

Material	Geometry	Loading
Elastic block:		Increments of 2.5 kPa
$E = 100\ MPa$, $\nu = 0.0$	$L = 10.0\ m, H = 1.0\ m$	up to 400 kPa
Interface elements:		
$k_s = c_t = 10^4\ kN/m^3$	Thickness of $0.01\ m$	
$\tau_{max} = coh = 30\ kN/m^2$		
$c_s = 10^7\ kN/m^3$		

The shear stress distribution along the interface length is plotted in Figure 59.2, and verified with respect to the formulas provided in Section 59.2 for the loading levels of 100, 200, 300 and 400 kPa. Furthermore, the longitudinal displacement distribution at the bottom of the elastic block is compared with the results of the finite element analysis provided by [78] (Figure 59.3).

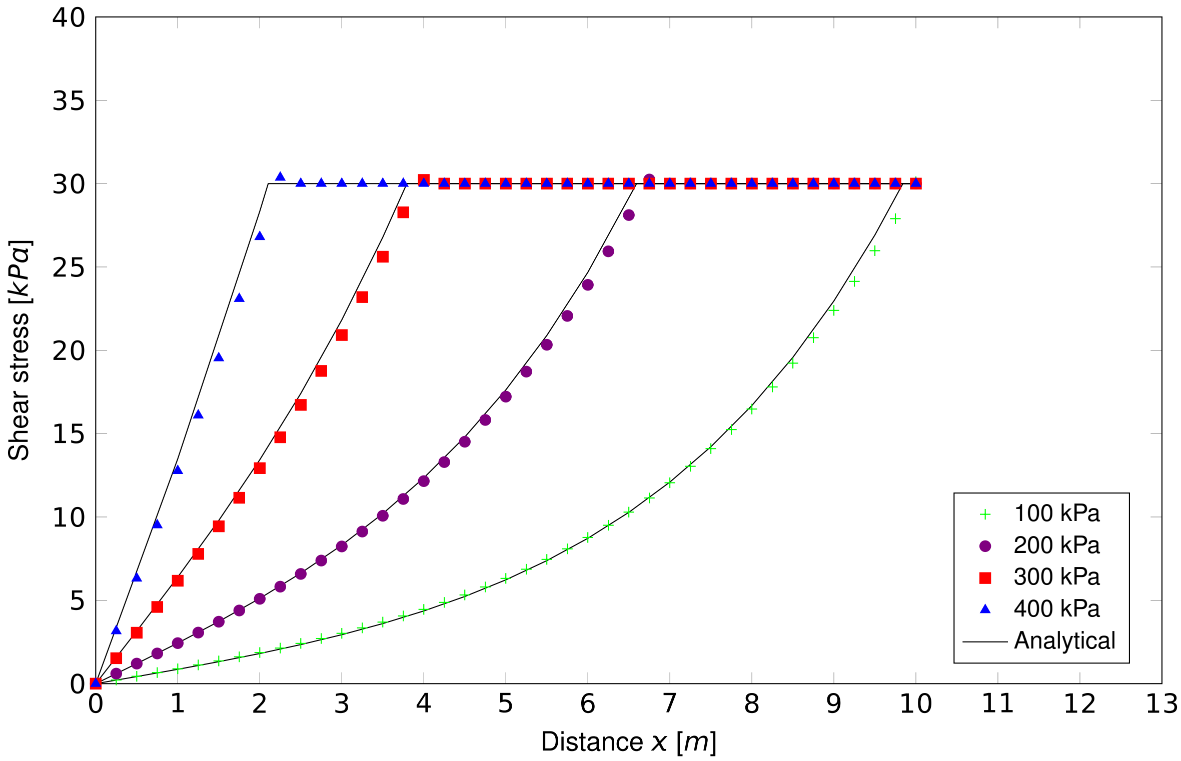

Figure 59.2: Interface shear stress distribution

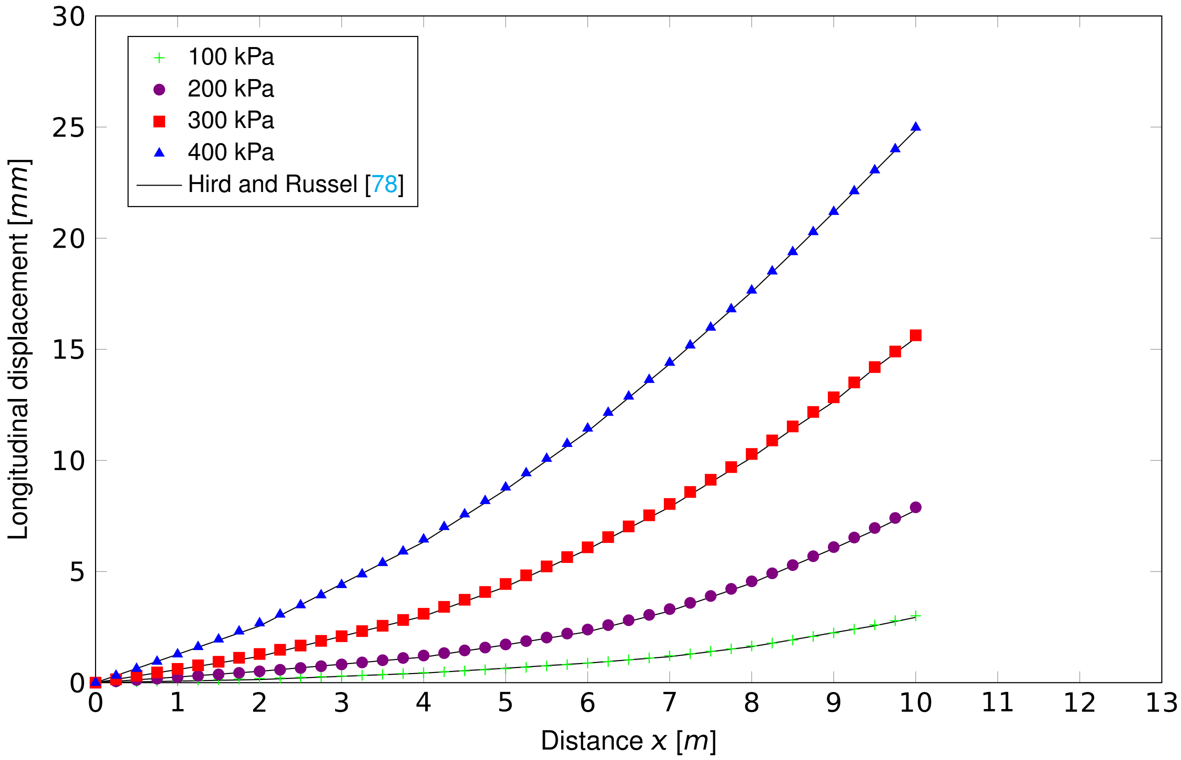

Figure 59.3: Longitudinal displacement distribution at the bottom of the elastic block

When comparing the numerical results in Figure 59.2 with the analytical solution a slight difference can be noticed. It should be noted that the analytical solution provided in Section 59.2 is not exact since it is based on the assumption that the normal stresses are constant along the height of the elastic block

[78]. In reality, the normal stress will be higher near the unrestrained upper boundary compared to the lower one, which can be seen in Figure 59.4 for a distance of 2 m from the restrained vertical face of the elastic block.

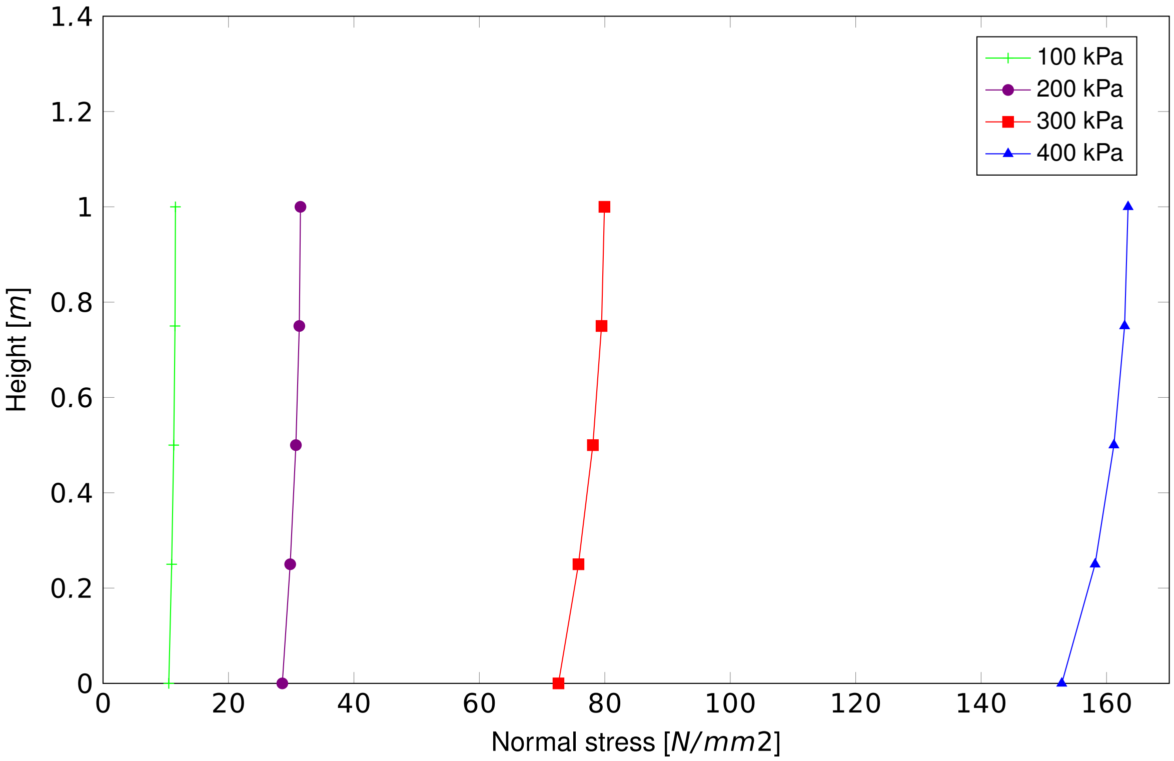

Figure 59.4: Stress distribution along the height of the block, at $x = 2.0$ [m]

59.4 Conclusion

A good agreement between the reference solution and the numerical results calculated by SOFiSTiK verifies the implementation of the interface element.

59.5 Literature

[78] C.C. Hird and D. Russell. “A Benchmark for Soil-Structure interface Elements”. In: *Computers and Geotechnics* (1990).

[79] R.C. Barros et al. “A Benchmark for Soil-Structure interface Elements”. In: *Proceedings of the XXXVIII Iberian Latin-American Congress on Computational Methods in Engineering* (2017).

60 BE57: Response Spectrum Analysis of a Simply Supported Beam

Overview	
Element Type(s):	
Analysis Type(s):	
Procedure(s):	
Topic(s):	EQKE
Module(s):	DYNA
Input file(s):	response_spectrum_analysis.dat

60.1 Problem Description

The following example is focused on the results of a response spectrum analysis of a simply supported beam, with the problem description defined by [80]. A simple beam with a rectangular cross section, shown in Fig.60.1a, is subjected to a vertical movement of its supports according to the acceleration history shown in Fig.60.1b. The acceleration changes linearly from g to $-g$ within a time period of $2t_d$, and is zero afterwards, with g being the gravitational acceleration.

The response of the system is determined based only on the first eigenmode. Therefore, modal superposition is not carried out in this example. Furthermore, zero damping of the system is assumed.

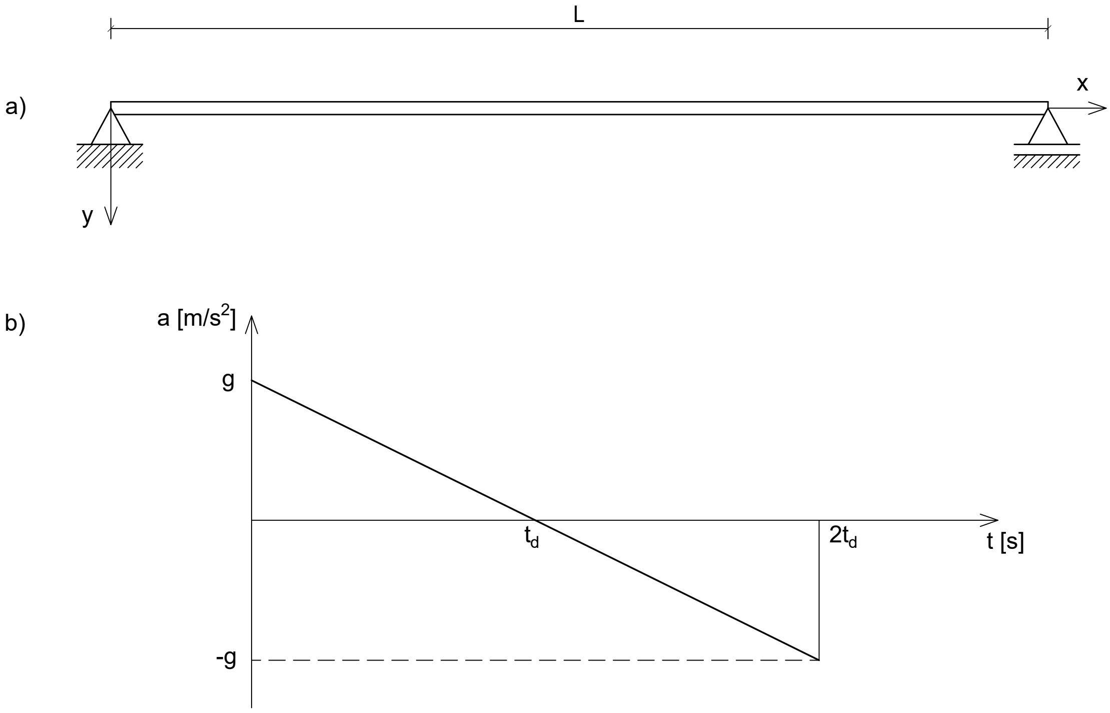

Figure 60.1: (a) Simply supported beam; (b) Acceleration history

The acceleration of a mass in a SDOF spring-mass system subjected to the base acceleration history from Fig.60.1b is defined as follows [80], for $t \leq 2t_d$:

$$\ddot{u} = g\left(1 - \cos\omega t + \frac{\sin\omega t}{\omega t_d} - \frac{t}{t_d}\right) \tag{60.1}$$

and for $t > 2t_d$:

$$\ddot{u} = \ddot{u}_{t=2t_d}\cos\omega(t - 2t_d) + \dot{u}_{t=2t_d}\frac{\sin\omega(t - 2t_d)}{\omega} \tag{60.2}$$

where ω is the circular eigenfrequency.

60.2 Reference Solution

In the first step of the response spectrum analysis, the eigenfrequency of the first eigenmode is calculated as follows [80]:

$$f = \frac{\pi}{2l^2}\sqrt{\frac{EI_y}{m}} \tag{60.3}$$

where l is the length and m is the mass per unit lenght of the beam, and EI_y is the bending stiffness.

Based on the calculated eigenfrequency, the maximum relative displacement of the equivalent SDOF system, $u_{max,0}$, is determined from the corresponding response spectrum [80]. Subsequently, the maximum beam deflection is calculated [80]:

$$u_{max} = \Gamma u_{max,0} \tag{60.4}$$

The shape function for the first eigenmode $\Phi(x)$ is given by [80]

$$\Phi(x) = \sin\frac{\pi x}{l} \tag{60.5}$$

, and the modal participation factor Γ is calculated as:

$$\Gamma = \frac{\int_0^l m\Phi(x)dx}{\int_0^l m[\Phi(x)]^2 dx} = \frac{4}{\pi} \tag{60.6}$$

The bending moment is defined as follows [80]:

$$M_x = -EI_y\frac{\partial^2 u(x)}{\partial x^2} \tag{60.7}$$

where $u(x)$ is the beam deflection for the first eigenmode

$$u(x) = u_{max}\sin\frac{\pi x}{l} \tag{60.8}$$

Therefore, the maximum bending moment in the middle of the span is computed as:

$$M_{y,max} = \frac{EI_y \pi^2}{l^2} u_{max} \tag{60.9}$$

60.3 Model and Results

Material, geometry and loading properties of the beam model defined in a plane system are summarized in Table 60.1.

Table 60.1: Model Properties

Material Properties	Geometric Properties	Loading
$E = 206842\, MPa$	$l = 6.096\, m$	$g = 10\, m/s^2$
$\rho = 104730\, kg/m^3$	$h = 35.56\, mm$	$t_d = 0.1\, s$
	$b = 3.7026\, mm$	

The response spectrum values are calculated as maximum acceleration values, in the units of g, from the Equations 60.1 and 60.2 as a function of the eigenperiod. For the purpose of this example, only the values in the proximity of the system´s first eigenperiod are taken as the input points of the response spectrum. The selected points are listed in Table 60.2 and also shown on the graph of the response spectrum, which is plotted as a function of the eigenfrequency in Figure 60.2.

Table 60.2: Calculated points of the response spectrum

Eigenfrequency [Hz]	Eigenperiod [s]	Max. acceleration [g]
5.00	0.20	2.000000
5.50	0.181818	1.818181
6.00	0.166667	1.666667
6.05	0.165289	1.652893
6.10	0.163934	1.639344
6.15	0.162602	1.626016
6.50	0.1538461	1.538461
7.00	0.142857	1.428571

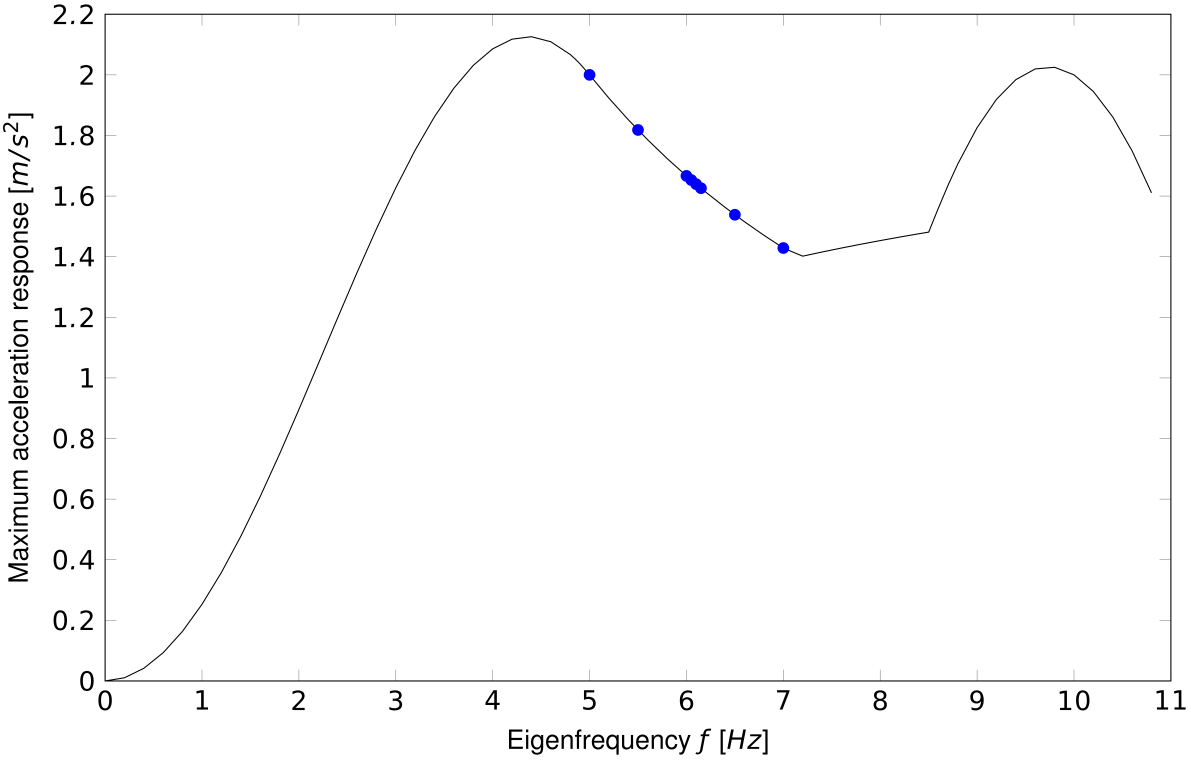

Figure 60.2: The response spectrum and the selected input points

The calculated values of the eigenfrequency f of the first mode, and the maximum deflection u_{max} and the bending moment $M_{y,max}$ in the middle of the span as a result of the response spectrum analysis, are compared with the reference values in Table 60.3.

Table 60.3: Results

	SOF.	Ref. [80]
f $[Hz]$	6.12	6.10
u_{max} $[mm]$	14.15	14.22
$M_{y,max}$ $[kNm]$	108.03	108.41

60.4 Conclusion

A very good agreement between the reference solution and the numerical results calculated by SOFiSTiK verifies the implementation of the response spectrum analysis.

60.5 Literature

[80] J.M. Biggs. *Structural Dynamics*. McGraw-Hill, 1964.

61 BE58: Automatic computation of spring constant values in BDK

Overview	
Element Type(s):	B3D
Analysis Type(s):	
Procedure(s):	
Topic(s):	
Module(s):	BDK
Input file(s):	automatic_spring_constant.dat

61.1 Problem Description

The problem consists of three steel members, as shown in Fig. 61.1. Member 1 is subjected to a compressive load P. Its displacements and torsional rotations at the lower end are fixed and there are pinned supports in the middle and at the top. Moreover, the top of member 1 is rigidly connected to the rest of the structure. In order to determine the buckling resistance of member 1 in BDK, the spring constant values are computed automatically at node 1, 2 and 3 using the literal AUTO in the CVA, CVE and CVM input.

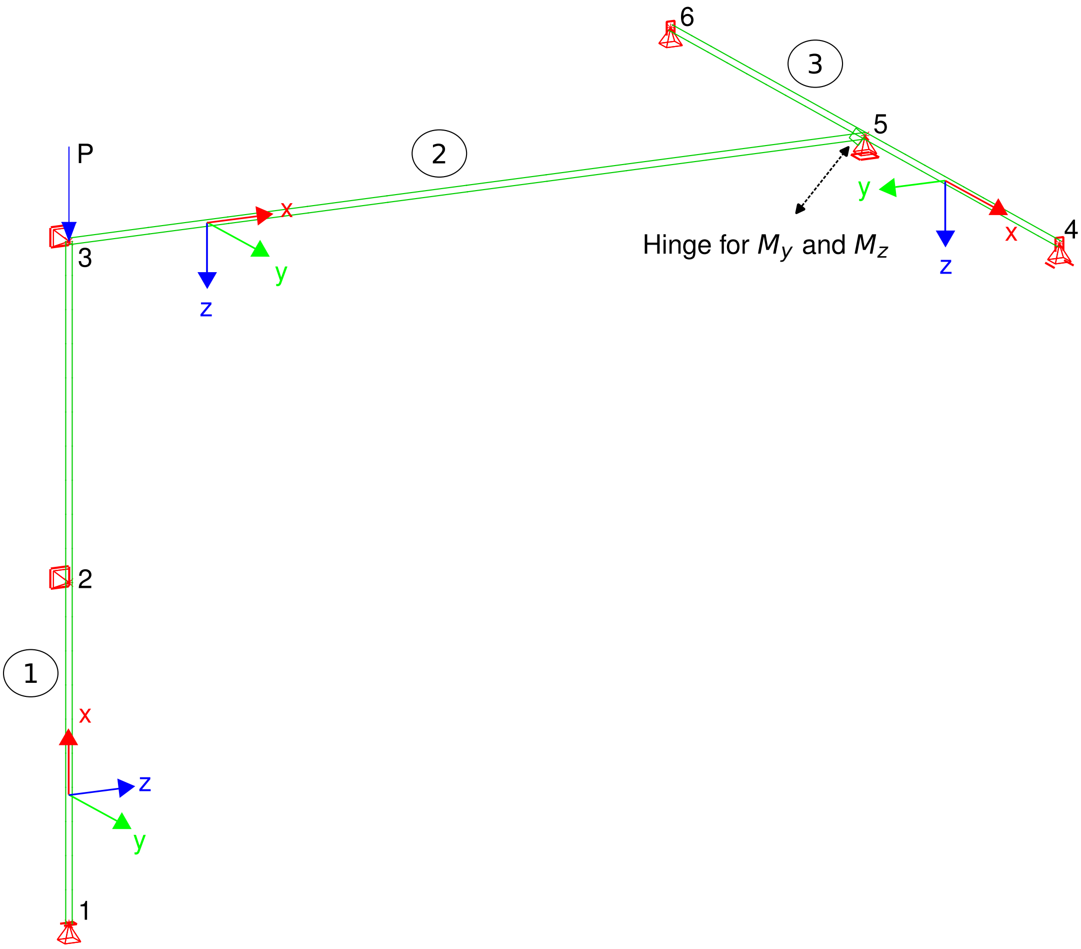

Figure 61.1: Problem Description

61.2 Reference Solution

Based on the approach described in [81], the reference values of the spring constants at node 3 are calculated from the stiffness of the connected beams 2 and 3 in consideration of the boundary conditions:

Table 61.1: Model Properties

Analytical Solution	
$CY = \dfrac{48 E I_{z3}}{l_3^3}$	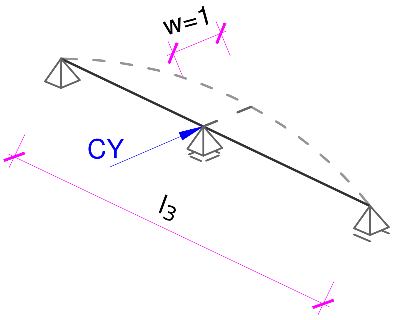

Table 61.1: (continued)

Analytical Solution

$$DX = \frac{3EI_{z2}}{l_2}$$

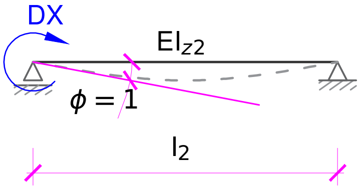

$$DY = \frac{3EI_{y2}}{l_2}$$

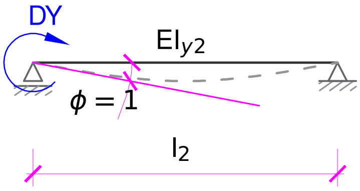

$$DZ = \frac{1}{\frac{l_2}{GI_{T2}} + \frac{l_3}{12EI_{y3}}}$$

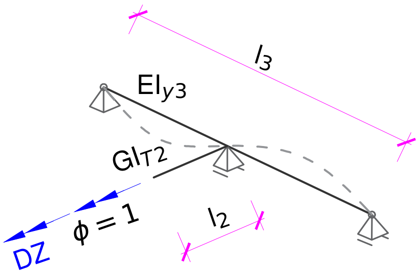

61.3 Model and Results

The properties of the model are listed in Table 61.2. Standard cross-sections and a standard steel material are used.

Table 61.2: Model Properties

	Member 1	Member 2	Member 3
Material	S 355	S 355	S 355
Cross-Section	RHS 260x180x10	SHS 180x10	HEA 220
A $[cm^2]$	83	67	64
I_T $[cm^4]$	8933.0	5142.4	28.2
I_y $[cm^4]$	7740.2	3193.0	5410.8
I_z $[cm^4]$	4350.3	3193.0	1954.6
Length [m]	8	10	10

The spring constant values provided by SOFiSTiK agree very well with the reference, as shown in Table 61.3. There are only small differences, which can be mainly attributed to longitudinal and shear deformations considered by SOFiSTiK but not in the reference.

Table 61.3: Spring constant values

	Ref.	SOF.	e_r [%]
CZ [kN/m]	197.0	196.5	0.28
DX [kNm/rad]	2011.6	2009.7	0.09
DY [kNm/rad]	2011.6	2009.7	0.09
DZ [kNm/rad]	403.1	402.9	0.03

61.4 Conclusion

This example verifies the spring constant values that are computed automatically in BDK. It has been shown that they are determined accurately from a linear analysis. However, it should be made sure that connected beams are not or only insignificantly subjected to compressive forces because they can lead to a considerable reduction of the bending stiffness [81]. In those cases, as illustrated in Figure 61.2, a global analysis that takes second order effects and imperfections into account can be used to verify the structural stability as described in [82].

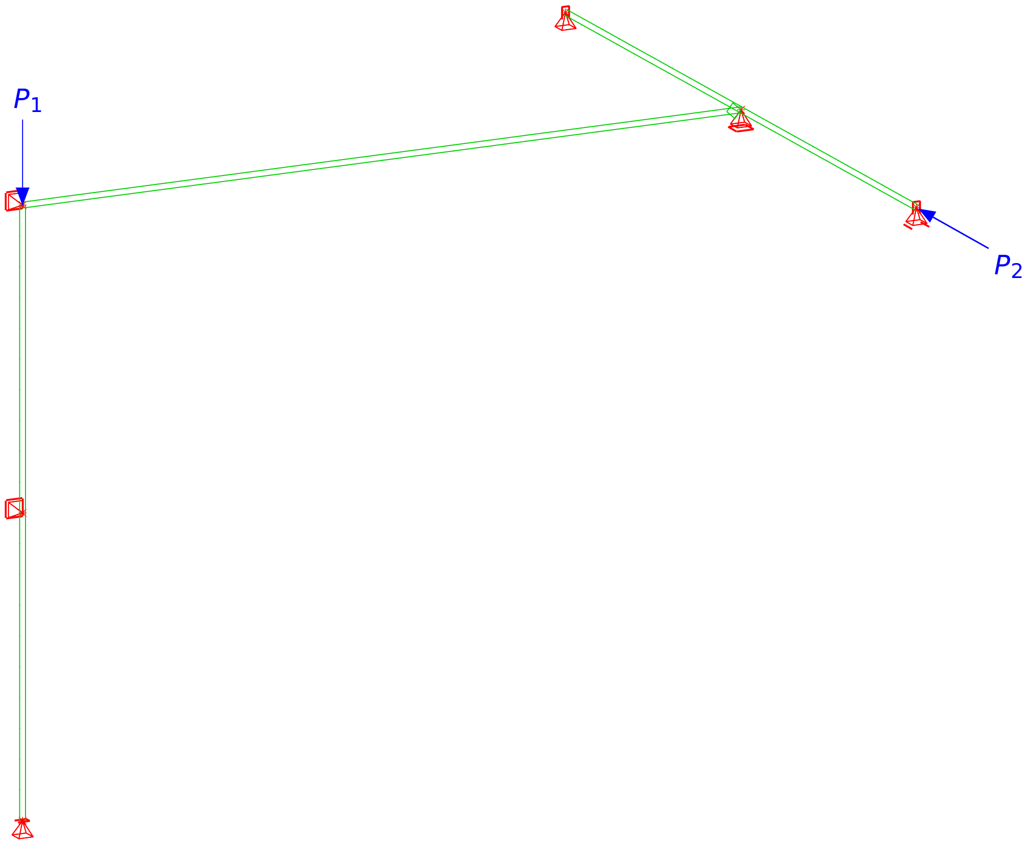

Figure 61.2: Example with 2^{nd} Order Effects

61.5 Literature

[81] C. Petersen. *Statik und Stabilität der Baukonstruktionen*. 2nd. Vieweg, 1982.

[82] U. Kuhlmann and F. Jörg. *Stahlbaunormen - DIN EN 1993-1-1: Allgemeine Bemessungsregeln und Regeln für den Hochbau, in Stahlbau-Kalender 2020*. Ernst & Sohn, 2020.